UPSCALING REACTIVE TRANSPORT IN POROUS MEDIA: LABORATORY VISUALIZATION AND STOCHASTIC MODELS

by

Peter M. Oates

B.S. Earth and Environmental Engineering (2000)
Columbia University

M.Eng. Environmental Engineering (2001)
M.I.T.

Submitted to the Department of Civil and Environmental Engineering in partial fulfillment
of the requirements for the degree of

DOCTOR OF PHILOSOPHY
AT THE
MASSACHUSETTS INSTITUTE OF TECHNOLOGY

June 2007

Signature of Author ____________________
Department of Civil and Environmental Engineering
May 25th, 2007

Certified by ____________________
Charles F. Harvey
Thesis Supervisor
Professor of Civil and Environmental Engineering

Accepted by ____________________
Professor Daniele Veneziano
Chairman, Departmental Committee for Graduate Students

UPSCALING REACTIVE TRANSPORT IN POROUS MEDIA: LABORATORY VISUALIZATION AND STOCHASTIC MODELS

by
Peter M. Oates

Submitted to the Department of Civil and Environmental Engineering on May 25th, 2007 in partial fulfillment of the requirements for the degree of Doctor of Philosophy in the field of Hydrology.

ABSTRACT

Solute transport models are essential tools for understanding and forecasting chemical concentrations in groundwater. Advection-dispersion based models can adequately predict spatial averages of conservative solute concentrations without using explicit maps of pore structures or variations in hydraulic conductivity. However, coupling advection-dispersion based transport models to chemical reaction models is inaccurate because it implicitly assumes complete mixing. Mixing in natural porous media is a slow process that can control the overall rate of chemical reactions, and the lack of mixing causes concentrations to be spatially variable. This thesis develops and experimentally validates a new solute transport modeling framework that approximates the correct amount of chemical reaction and provides concentration probability density functions, which are needed to address laws and regulations based on maximum contaminant levels.

To study solute mixing and reaction in porous media, we conducted highly detailed lab-scale experiments by digitally imaging the movement of colored dye tracers and colorimetric chemical reactions through illuminated clear homogeneous and heterogeneous porous media. The resulting sequence of solute concentration maps demonstrates the problem of conventional solute transport models and shows that concentrations can be well approximated with Beta distributions.

Conservative Beta distributions can be modeled with partial-differential equations for concentration mean and variance. These conservative distributions can then be transformed into joint reactant distributions, which produces product and remaining reactant distributions. This upscaling approach is verified by modeling the product and reactant means, variances, and distributions in heterogeneous media and product means in homogeneous media from our lab-scale experiments.

We found that (co)variance production-destruction balances can approximate aqueous species covariance matrixes, which are necessary to form multivariate reactant distributions of complex reactive transport scenarios. Alternatively, these second moments can be used in upscaled reaction expressions derived from a second order Taylor series expansion. Incomplete mixing, parameterized by variance and covariance, causes an upscaled reaction rate to be almost an order of magnitude smaller compared to the conventional reaction rate that implicitly assumes complete mixing. Finally, manipulating the flow field to be perpendicular to its original direction would increase the rate of reactive mixing by an order of magnitude. Thus generating a transient flow field would be a practical way to accelerate natural attenuation and bioremediation.

Thesis Supervisor: Charles F. Harvey
Title: Professor of Civil and Environmental Engineering

ACKNOWLEDGMENTS

DEDICATED TO MY PARENTS PETER AND NANCY
TO WHOM I OWE EVERYTHING

TO MY SISTER KATE FOR NOT LETTING ME BE COMPLETELY ENGULFED BY SCIENCE

TO WLBC AND THE LATE NIGHTS OF PHILOSPHY THAT HELPED PUT ME HERE

TO CHRISSY "POD" KAVANAUGH WHOSE LOVE AND SUPPORT HELPED ME FINISH.

TO MY ADVISROR CHARLIE. YOUR GOOD NATURE MADE 6 YEARS POSSIBLE AND FUN. OH, AND YOU'RE PRETTY SMART TOO.

TO PETE SHANAHAN. THANK YOU FOR ALWAYS HAVING TIME AND A SMILE. I'VE ALWAYS FELT YOU'VE BEEN IN MY CORNER.

TO PHIL GSCHWEND AND LYNN GELHAR. ITS BEEN AN HONOR A PRIVILEGE WORKING WITH YOU.

TABLE OF CONTENTS

LIST OF FIGURES AND TABLES

Chapter 2

Chapter 3

Chapter 4

Chapter 5

Chapter 6

Chapter 1. Introduction

1.1 Motivation and Background

Water is the most ubiquitous biological compound and it is imperative for life. Only 0.5% of the world's freshwater is available for consumption. Of this small fraction, groundwater composes 96% of the available water, and this important resource is vulnerable to contamination. For example, the USA reported groundwater contamination from leaking underground storage tanks (LUSTs), landfills, septic systems, and hazardous waste sites. As of 1996, more than 300,000 releases from LUSTs had been confirmed (USEPA, 1998b). Fertilizers, pesticides, and agricultural chemical facilities also contribute as non-point sources to the contamination of groundwater. With the world's water demand increasing, it is necessary to understand how chemicals move and change in groundwater in order to protect groundwater sources and bodies of water that interact with groundwater.

When chemicals move through aquifers, they undergo both biotic and abotic reactions with other dissolved chemicals and with the porous matrix itself. A desirable reaction that removes contaminants from the aquifer is biodegradation in which microorganisms transform harmful chemicals into safe byproducts. For example, bacteria can metabolize the toxic chemical benzene, present in LUST spills, with oxygen and transform it into carbon dioxide and water:

$$C_6H_6 + 7.5\,O_2 \rightarrow 6CO_2 + 3H_2O \qquad (1)$$

These types of multi-component redox reactions occur during natural attenuation and can be facilitated during enhanced bioremediation. Effective biodegradation depends on many variables, but it is essential to have contaminant and electron acceptors/donors simultaneously present. In a typical contaminant spill, the electron acceptors/donors are quickly used up leaving contaminant degradation to occur only at the interface of the contaminant plume and freshwater where new electron acceptors/donors can mix with the contaminant substrate. What controls the overall biodegradation reaction rate is the slower of the chemical kinetic reaction rate and the rate that components are mixed together.

Suarez and Rifai (1999) compiled a database of first-order chemical kinetic degradation rates of common groundwater contaminants. The mean degradation rates of m-xylene and PCE (tetrachloroethylene) under aerobic and anaerobic conditions are 0.058 day^{-1} (number of studies = 90) and 0.05 day^{-1} (number of studies = 50), respectively. This indicates chemical reaction kinetics occur on the time scale of $(0.058)^{-1} \approx 17$ days and $(0.05)^{-1} \approx 20$ days. However, all of these first-order reaction rates are representations of multi-component reactions, such as equation 1, which assumes that the electron acceptor (*e.g.*. oxygen) or donor (*e.g.* hydrogen) are not limiting.

In natural porous media, the rates of contaminant and electron acceptor/donor mixing can be much slower than reaction rates and can therefore control the overall rate of chemical reaction. Several researchers have agreed that transverse mechanical dispersion dominates mixing (*e.g.*. Dagan and Fiori, 1997; Cirpka *et al.*, 1999; Cirpka and Kitanidas, 2000) and we verify this in Chapter 3. Recent advancements in measuring transverse dispersion by Cirpka *et al.* (2006) have revealed that at typical groundwater flow velocities, transverse dispersion is only slightly larger than molecular diffusion for steady-sate flow. The mean distance, λ, of diffusion/dispersion, D, is given as a function of the time scale for diffusion/dispersion t_D:

$$\lambda = \sqrt{t_D D} \qquad (2)$$

For the time scales calculated from Suarez and Rifai (1999), in order for chemical reaction kinetics to affect significantly the overall rate of chemical transformation compared to the rates of mixing, chemical components would have to mix over a mean distance of about $\sqrt{(20\,day)(10^{-9}m^2/s)(86400\,s/day)}$ = 4 cm. Even if mechanical transverse dispersion were two orders of magnitude larger, the mean distance of mixing would be 0.5 m. In natural porous media, the scale over which hydraulic conductivity values correlate, which determines how far chemical reactants have to mix, is usually on the scale of 10's to 100's of meters (Gelhar, 1993). This typically causes the overall chemical reaction rates to be governed by mixing.

Mixing and reaction are critical to: 1) natural attenuation; 2) enhanced bioremediation; and 3) in-situ chemical oxidation scenarios. Furthermore, fluid mixing in aquifers addresses a very fundamental issue: chemical concentrations. Not only do small-scale concentrations drive biogeochemical reactions but EPA laws and regulations are written in terms of MCL or maximum contaminant levels. Slow mixing causes concentrations to be spatially variable with maximum concentration levels well above spatial averages.

Natural porous medium are undoubtedly heterogeneous at all scales making it extremely challenging to construct models that accurately predict the small-scale concentrations that govern chemical reactions. In many cases, groundwater solute transport models based on the advection-dispersion equation (*ADE*) adequately predict spatial averages of conservative solute concentrations without using explicit maps of pore structures or maps of small-scale variations in hydraulic conductivity. However, coupling the advection-dispersion equation to chemical reaction models is inaccurate because it implicitly assumes complete mixing. Furthermore this approach only provides information about mean concentrations and not the regulated maximum concentrations. The slow mixing that can control chemical reaction rates and the lack of mixing that can lead to spatially variable concentrations needs to be accounted for in reactive transport models.

1.2 Thesis Overview

1.2.1 Objective.

The goal of this thesis is to understand mixing and reaction in porous media and to develop a reactive transport modeling framework that approximates the correct amount of chemical reaction and concentration probability density functions.

1.2.2 Tasks.

In order to study and model mixing and reaction in porous media, we conducted laboratory visualization and numerical experiments. Specific tasks were:

1) Find a colorimetric reaction suitable for optical quantification of mixing and reaction in illuminated clear laboratory chambers filled with clear porous media.
2) Conduct conservative and reactive experiments in homogeneous and heterogeneous laboratory chambers.
3) Construct MODFLOW, MT3D, and RT3D numerical models to investigate reactive transport scenarios not conducted with laboratory experiments.
4) Use results to understand mixing and reaction and develop and validate a new reactive transport modeling framework.

1.2.3 Thesis Structure.

- *Chapter 1* is a comprehensive overview of the thesis. It covers the thesis motivation and summarizes the research findings.
- *Chapter 2* provides the details of the Tiron/molybdate colorimetric reaction that was used for optical quantification of mixing and chemical reaction in our laboratory chambers.
- *Chapter 3* covers the homogeneous and heterogeneous conservative and reactive transport experiments and compares the results against conventional modeling approaches.
- *Chapter 4* develops the concentration fluctuation Beta *pdf* ($CF\text{-}\beta$) modeling framework for reactive transport and validates it against the data from Chapter 3.
- *Chapter 5* extends the $CF\text{-}\beta$ modeling framework to address more complex reactive transport scenarios, proposes how to measure the key modeling parameter at a field site, and proposes an approach to enhance favorable mixing and reaction in the subsurface.
- *Chapter 6* discusses future research directions.

1.3 Summary of Findings

1.3.1 Chapter 2. A Colorimetric Reaction to Quantify Fluid Mixing.

In order to study mixing and reaction in porous media we conducted laboratory visualization experiments in illuminated clear porous media. We needed a chemical reaction that consists of two colorless reactants that mix to rapidly form colored, stable, and soluble products. These colored products can then be digitally imaged and quantified using light absorbance as they move through the illuminated clear porous media. We found the colorimetric reaction of Tiron (1,2-Dihydroxybenzene, 3,-5-disulfonic acid) and molybdate suitable for optical quantification of chemical reaction during fluid mixing in laboratory chambers. We developed a mathematical model to describe the two-step complexation reaction and determined the two equilibrium constants for this reaction. We also provide methods for relating light absorbance to product concentration, which allows our digital images to be quantitative.

1.3.2 Chapter 3. Imaging Colorimetric Reactions in Spatially Homogeneous and Heterogeneous Material.

To characterize solute mixing and reaction in porous media, we conducted highly detailed lab-scale experiments by digitally imaging the movement of colored dye tracers and colorimetric chemical reactions through illuminated chambers containing: (1) homogeneous media, in which spreading is largely caused by mechanical dispersion; (2) heterogeneous media with mild differences in hydraulic conductivity, in which spreading is accurately predicted by a Fickian macro-dispersion model; and finally (3) highly heterogeneous media in which solute spreading is better described by a mass-transfer model. By analyzing the resulting sequence of solute concentration maps, we show how solute transport models based on the advection-dispersion and mass-transfer equations adequately predict spatial averages of conservative solute concentrations without using explicit maps of pore structures or maps of small-scale variations in hydraulic conductivity. However, we observe the conventional coupling of conservative transport models to chemical reaction models incorrectly predicts the amount of chemical reaction because reactants are not well mixed at small scales. The experimental results demonstrate that Darcy-scale chemical segregation dominates incomplete mixing at the pore scale. A key result for constructing reactive transport models is that the small-scale distribution of solute concentrations is distinctly non-Gaussian, and that concentration distributions are very well approximated by Beta distributions.

1.3.3 Chapter 4. Development and Experimental Validation of the Concentration Fluctuation Beta-*pdf* (*CF-β*) Model.

Building on the observation that small-scale concentrations are Beta distributed, we sought to model these distributions with partial-differential equations for conservative concentration mean and variance. Then, the conservative distributions can be transformed into joint reactant distributions by applying a mixing line and all the small-scale reactions can be calculated. This produces product and remaining reactant distributions, which can be integrated to calculate the expected amount of chemical reaction. The full distributions are useful for assessing laws and regulations based on maximum concentration levels. This approach is verified for mildly heterogeneous media by modeling the product and reactant means, variances, and distributions from the experiments of Chapter 3 and for homogeneous media by modeling the product means from the experiments of Chapter 3, Gramling *et al.* (2002), and Raje and Kapoor (2000). This reactive transport approach works without maps of hydraulic conductivity fields or pore structures but requires experimental calibration to determine the variance-length scale, a length scale that characterizes variance destruction and reactive mixing.

1.3.4 Chapter 5. Production-Destruction Balances, Taylor Series, and Practical Considerations for the *CF-β* Model.

At this stage in development, the *CF-β* approach works for modeling equilibrium reactions, reactions with chemical kinetics much faster than mixing rates, and when there is no difference in chemical sorption between the chemical species in the reaction. These restrictions arise because, 1) we can currently model only the variance of total reactants because it is a conservative quantity and, 2) non-differential sorption allows for the covariance between species to be calculated from a mixing line. Reactive transport situations undergoing rate-limited reactions with reactants having different retardation factors is an important and practical scenario (*e.g.* Oya and Valocchi, 1998). The difficulty for applying the *CF-β* framework to these types of complex reactive transport scenarios is in determining the reactant variances and covariances. Numerous unclosed terms arrive from perturbation analysis when chemical reactions are included in variance and covariance budgets. This chapter explores macro-dispersive and mechanical-dispersive (co)variance production-destruction balances to approximate these second moments.

Velocity fluctuations shear and distort fluid interfaces. This produces (co)variance and at the same time establishes mechanical-dispersive transverse concentration gradients that destroy (co)variance. The rates of (co)variance production and destruction asymptotically balance each another for both conservative and reactive flows. This balance leads to the following relationship to approximate an m-by-n aqueous species covariance matrix as a function of the variance length scale χ_L, macro-dispersivites A_{ij}, and species mean gradients:

$$\sigma^2_{C_m C_n} \approx 2\chi_L A_{ij}\left(\frac{\partial \overline{C}_m}{\partial x_i}\right)\left(\frac{\partial \overline{C}_n}{\partial x_j}\right) \qquad (3)$$

We found this relationship to asymptotically hold for the following scenarios based on our experimental data: variance of a conservative tracer, covariance of two conservative tracers, covariance of two conservative species with differential sorption, variance of A and P for the $A+B \rightarrow P$ reaction, and the variance of the Tiron/molybdate product. It also holds for the variances and covariance of oxygen and hydrocarbon undergoing a double-Monod rate-limited reaction where hydrocarbon sorbs with a retardation factor (R_H = 1.0, 1.2, 1.5, 4.0) determined in numerical simulations.

Production-destruction balances can provide the necessary statistical moments to form multivariate reactant distributions to upscale complex reactive transport scenarios. Alternatively, we found that these second-order moments can be used in an upscaled reaction expression derived from a second-order Taylor series expansion. Incomplete mixing, parameterized by variance and covariance, caused the upscaled double-Monod reaction rate to be almost an order of magnitude smaller compared to the conventional double-Monod reaction rate that implicitly assumes complete mixing.

We propose the decisive variance length-scale can be measured in the field with a reactive breakthrough curve as it was for the lab-scale experiments of Raje and Kapoor (2000), or possibly from a breakthrough curve of conservative concentration variance. Finally, manipulating the flow field to be perpendicular to its original direction would increase variance destruction and reactive mixing by an order of magnitude. Thus, generating a transient flow field would be a practical way to accelerate natural attenuation and bioremediation.

References:

1. Cirpka, O. A., Frind, E. O., and Helmig, R. 1999a. Numerical simulation of biodegradation controlled by transverse mixing. *Journal of Contaminant Hydrology*. 40(2), 159–182.
2. Cirpka, O. A., Olsson, A., Q. Ju, Q., Rahman, M. A. and Grathwohl, P. 2006. Determination of transverse dispersion coefficients from reactive plume lengths. *Ground Water*. 44(2), 212-221.
3. Cirpka, O. A., and Kitanidis., P. K. 2000. Characterization of mixing and dilution in heterogeneous aquifers by means of local temporal moments. *Water Resources Research*. 36 (5), 1221-1236.
4. Dagan, G. and Fiori, A. 1997. The influence of pore-scale dispersion on concentration statistical moments in transport through heterogeneous aquifers. *Water Resources Research*. 33(7), 1595-1605.
5. Gelhar, L.W. 1993. Stochastic Subsurface Hydrology. New Jersey, Prentice-Hall Inc.
6. Gramling, C. M. Harvey, C. F., Meigs, L. C. 2002. Reactive transport in porous media: A comparison of model prediction with laboratory visualization. *Environmental Science and Technology*. 36(11), 2508-2514.
7. Oya, S., and Valocchi, A. J. 1998. Transport and biodegradation of solutes in stratified aquifers under enhanced in situ bioremediation conditions. *Water Resources Research*. 34(12), 3323–3334.
8. Raje, D. S., and Kapoor, V. 2000. Experimental Study of Reaction Kinetics in Porous Media. *Environmental Science and Technology*. 34(7), 1234-1239.
9. Suarez, M. P. and Rifai, H. S. 1999. Biodegradation Rates for Fuel Hydrocarbons and Chlorinated Solvents in Groundwater. *Bioremediation Journal*. 3(4), 337-362.
10. U.S. Environmental Protection Agency (USEPA). (1998). "National water quality inventory: 1996 Report to Congress, ground water chapters [online]." Office of Water, Washington, D.C., http://www.epa.gov/OW/resources/9698/chap6.html.

Chapter 2. A Colorimetric Reaction to Quantify Fluid Mixing

Abstract: We found the colorimetric reaction of Tiron (1,2-Dihydroxybenzene-3,-5 disulfonic acid) and molybdate suitable for optical quantification of chemical reaction during fluid-fluid mixing in laboratory chambers. This reaction consists of two colorless reagents that mix to rapidly form colored, stable, soluble products. These products can be digitally imaged and quantified using light absorbance to study fluid-fluid mixing. Here we provide a model and equilibrium constants for the relevant complexation reactions. We also provide methods for relating light absorbance to product concentrations. Practical implementation issues of this reaction are discussed and an example of imaged absorbances for fluid-fluid mixing in heterogeneous porous media is given.

2.1 Introduction.

Understanding chemical reaction during fluid-fluid mixing is important for environmental processes (Beven et al., 1994), the chemical industry (Sterback and Tausk, 1965), pharmaceutical engineering (Hickey and Ganderton, 2001), process industries (Harnby et al., 1985), and the field of medicine (Omurtag et al., 1996; International Union of Biochemistry. 1964) among other disciplines. Reactive mixing results from molecular diffusion across complex fluid-fluid interfaces (Ottino, 1990).

To better understand this molecular-scale phenomenon, researchers have developed non-invasive optical measurement techniques. The two leading methods are laser-induced-fluorescence, where the fluorescence of a reaction product is measured (e.g. Koochesfahani *et al.*, 1985), and absorption imaging, where the amount of light absorbance is related to chemical concentration by Beer's Law (Tidwell and Glass, 1994; Zhang *et al.*, 1995; Gramling, 2002). As pointed out by Zhang *et al.* (1995), planar-laser-induced-fluorescence (PLIF) is an excellent technique but involves a relatively complex setup; requiring laser equipment and cylindrical and spherical mirrors to separate the laser into a plane. This light plane is able to able to give a 2-D concentration profile at a selected location in the mixing vessel. However, experimental times are typically short to avoid changes in the fluorescent signal due to temperature variation (eg. Kling and Mewes, 2003). Absorption imaging involves a simpler setup by pairing a colorimetric chemical reaction with a charge-coupled device (CCD) camera and digital image processing to quantify the 2D absorption field (Tidwell and Glass, 1994; Zhang *et al.*, 1995; Gramling, 2002). Experimental times can typically be much longer implying this technique maybe more suitable for studying slower flows (Zinn *et al.*, 2004). Absorption imaging is a quasi-2D technique that is unable to resolve concentration detail in the third spatial dimension but it does provide the correct spatial average of the molecular product formed. Whether the correct spatial average of product formation given by absorption imaging or a plane giving detailed concentration information in the third dimensional is more valuable depends on what questions the researchers are trying to answer.

To study reactive mixing with light absorption imaging, a reaction is needed where two initially colorless reagents react to form a colored, stable, soluble, quantitative product. Ideally, this reaction should happen at circumneutral pH, not involve hazardous chemicals, and be unreactive with other materials used in the study. Unfortunately, this type of reaction is very hard to find (Breidenthal, 1981). Several reactions have been used for flow visualization: ozone and nitric oxide for turbulent jet studies (Shea, 1977); photochemically-induced colorimetric reactions for hydrodynamic instabilities at reactive interfaces (Avnir and Kagan, 1984); iron(II) and nitric acid for studying multi component convection (Pojman *et al.*, 1991); electrically-induced iodate-arsenous-acid reaction to produce iodine in the presence of starch (Bockmann and Miller, 2000); phenolphthalein and base, which is probably the most commonly used reaction to study fluid-fluid mixing (e.g. Menisher *et al.*, 2000; Fox and Gex, 1956; Zhang *et al.*, 1995; Breidenthal, 1981); and recently Gramling *et al.* (2002) used a complexation reaction of copper sulfate and EDTA.

We found that all of the above-mentioned reactions had undesirable characteristics for studying fluid-fluid mixing. While the phenolphthalein reaction contains many of the desired attributes (Breidenthal, 1981), the colored product is unstable and fades back to colorless (Nicholson, 1989); thus, it only allows for the calculation of a lower mixing bound (Breidenthal, 1981). Gramling *et al.* (2002)

overcame this problem of color stability by using a copper sulfate-EDTA reaction that forms a dark blue complex, but the copper sulfate reagent is initially light blue, making it impossible to distinguish between reagent and low product concentration. While an ideal reaction may not exist, we sought to improve the colorimetric reaction used for absorption imaging. In addition to the above-mentioned reactions, we also considered starch and iodine, leuco crystal violet and hydrogen peroxide, manganese and periodate, but they all failed to meet one or more of the aforementioned requirements. We found the colorimetric reaction of Tiron (1,2-Dihydroxybenzene-3,-5disulfonic acid) and molybdate suitable to quantifiably study the mixing of two fluids.

In the first section of this paper, we give the background on Tiron, molybdate, and their complexation reaction. Next, we present a specific chemical recipe and its properties relevant to study fluid-fluid mixing, cover the governing reaction equations, and model the reaction to fit two chemical equilibrium constants. Then we discuss how light absorbance captured by a digital camera relates to product concentration. Finally, we discuss some practical implementation issues and then give an example of imaged absorbance of this reaction used to study mixing in transparent heterogeneous porous media.

2.2 Tiron, Molybdate, and Their Reaction.

1,2-Dihydroxybenzene-3,-5disulfonic acid:

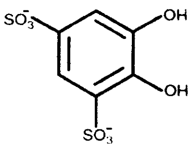

was named Tiron for its use as a chelatometric indicator for both titanium and iron (Yoe and Armstrong, 1947). Tiron is easily soluble in water, slightly soluble in alcohol, and insoluble in nonpolar organic solvents. The ionization constants for the two hydroxyl groups are $pKa_1=7.66$ and $pKa_2=12.6$ (Schwarzenback and Willi, 1951). Aqueous solutions are colorless (Atkinson and McBride, 1957; Will and Yoe, 1953) and have been reported to remain stable for a year (Atkinson and McBride, 1957). However, tiron easily oxidizes in alkaline solutions to turn colored (Atkinson and McBride, 1957), and we found it to slightly photooxidize after sitting exposed to light after about a week. Tiron forms colored complexes with: Fe^{+3}, MoO_4^{-2}, OsO_5^{-2}, Cu^{+2}, UO_2^{+2}, VO^{+2}, Ti^{+4} (Will and Yoe, 1953) and many rare earth metals (Taketatsu and Toriumi, 1970, 1971); it forms colorless complexes with: Al^{+3}, Ca^{+2}, Ce^{+3}, Sn^{+4}, Zr^{+4}, Th^{+4}, Hg^{+2}, WO_4^{-2}, Pb^{+2}; and Tiron reduces Ag^{+} and $AuCl_4^{-}$ to the metallic state (Will and Yoe, 1953).

Molybdate oxo species polymerize depending on the concentration and pH of the solution (Aveston *et al.,* 1964; Mitchell, 1990). Under conditions of a pH between 0.9 and 6.0 and molybdate concentrations greater than 10^{-3} M, MoO_4^{2-} anions form $[Mo_7O_{24}]^{-6}$ and $[Mo_8O_{26}]^{-4}$ polymeric species. Below a pH of 0.9, molybdate precipitates as MoO_3. Above a pH of 7, it forms "molybdenum blues", which is a blue mixture of molybdenum(VI) and molybdenum(V) oxyhydroxides, typically represented as $[Mo_3^{6+}Mo_3^{5+}O_{18}H]^{-}$. However, between a pH of 6 and 7, molybdate exists as mono-anions, which are clear in solution (Mitchell, 1990). When the molybdate ion hydrates, it can act acidic (the exact degree of protonation is pH dependent; $pKa_1=4.24$, $pKa_2=8.24$ (Flaschka, H. A., Barnard, 1967)):

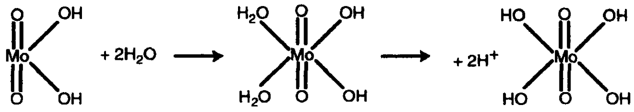

The final product can be described as the tetrahydroxo complex of the molybdenyl(VI) cation, MoO_2^{2+}, which will complex with anionic chelating agents (Flaschka, H. A., Barnard, 1967).

Dozens of polyphenolic compounds have been reported to react with molybdenum (Flaschka and Barnard, 1967) via the chelating agent displacing the molybdate hydroxo ligands (see below) to form a stronger complex (Schwarzenback, 1957). The general structure of the polyphenolic-molybdenum chelate is given by Halmekoski (1959):

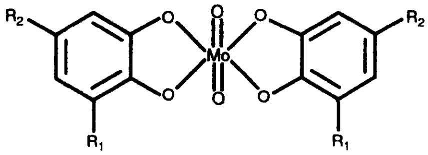

In the case of Tiron, the two R groups (R_2 and R_1) are sulfonate groups ($-SO_3^-$), which are responsible for the high water solubility of Tiron and its complexes. Tiron was found to be the most stable molybdate ligand of EDTA, NTA, or 5-sulfosalicylic acid (Chabarek *et al.*, 1959) and the complexation occurs instantaneously to produce a color that is stable for at least three weeks (Will and Yoe, 1953). Furthermore, Will and Yoe (1953) recommended this reaction for the spectrophotometeric determination of molybdate. Two tiron-molybdate species with a metal to ligand ratio of 1:1 and 1:2 have been reported (Sommer, 1962). The first complexation reaction can be written as:

$$Ti + Mo \rightleftharpoons MoTi \quad (1)$$

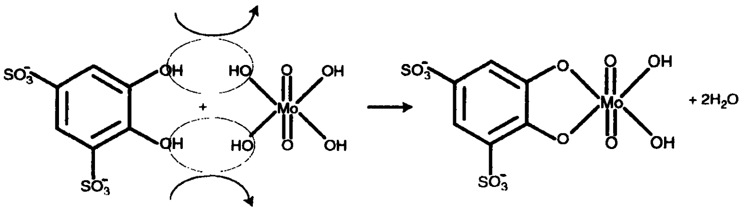

where *Ti* is the molar concentration of Tiron; *Mo* is the molar concentration of molybdate; and *MoTi* is the molar concentration of the 1:1 complex. This dehydration can produce H_3O^+ or OH^- as well as H_2O depending on the pH of the solution (Flaschka and Barnard, 1967). In a well buffered solution, this first reaction can be expressed with the equilibrium expression:

$$K_1 = \frac{[MoTi]}{[Mo][Ti]} \tag{2}$$

where K_1 is the first equilibrium constant (liters/mol). This first product then undergoes an additional reaction with Tiron to produce the complex in the form reported by Halmekoski, (1959):

$$MoTi + Ti \rightleftharpoons MoTi_2 \tag{3}$$

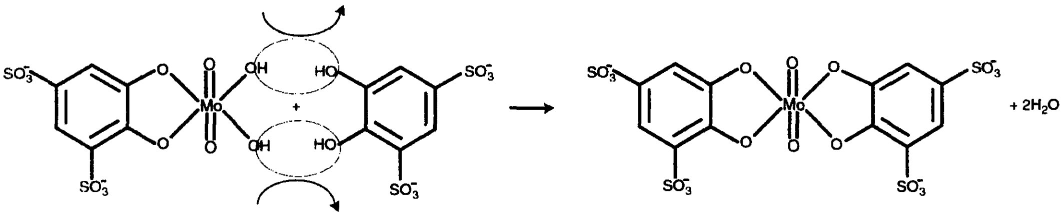

where $MoTi_2$ is the second chelate formed. The second equilibrium expression follows:

$$K_2 = \frac{[MoTi_2]}{[MoTi][Ti]} \tag{4}$$

where K_2 is the second equilibrium constant (liters/mol).

Mixing two clear solutions of 0.05M Tiron and 0.025M molybdate buffered at pH 6.1 (see below) forms a red wine color, which progressively appears orange and then yellow as the products are diluted. The colored products strongly absorb in the violet and blue region of the spectrum, transmit the yellow and red wavelengths, and the absorbance of green light increases with product concentration. The red-to-yellow color-shift occurs because green and red light transmitted together appear yellow (Serway and Faughn, 1995). Thus, at low concentrations, the product solution transmits green, yellow, and red; the combination of green and red with the yellow give the solution a yellow appearance. However, as product concentrations increase, the complexes absorb more of the green wavelengths. Without green light, the transmitted wavelengths progressively appear redder and the solution changes from yellow to orange to red.

2.3 A Chemical Recipe to Study Fluid Mixing in Laboratory Chambers.

We chose reagent concentrations of 0.05M Tiron (added as a disodium salt) and 0.025M molybdate (added as ammoniummolybdate) in order for a digital camera to record the colored product absorbances with a dynamic range of over one and one-half orders of magnitude in a clear tank approximately 0.7 cm thick. A pH of 6.1 was chosen so molybdate would predominantly exist in the mono-anionic form allowing the diffusion coefficients of all reacting species to be explicitly calculated and accounted for in a model if desired. Additionally, at pH 6.1, alkaline-induced oxidation of Tiron is minimized, reducing absorbance artifacts. We used a 0.13 M succinate buffer (added as succinic acid) to ensure no spatial or temporal pH changes, which would make the observed color more difficult to understand, as the reaction is pH sensitive. Succinate was chosen because its second pKa is 5.64, close to the desired pH, and it had no adverse effects on the reaction. Finally, sodium chloride was added to the molybdate solution to equalize its density to the tiron solution.

In summary, the species concentrations in the two solutions buffered at a pH of 6.1 were:

- **Tiron Solution:** 0.05 M *Ti* (pKa_1=7.66, pKa_2=12.6); 0.356 M *Na*; 0.13 M *Succinate* ($pKa_1 = 4.21$, $pKa_2 = 5.64$).
- **Molybdate Solution:** 0.025 M *Mo* (pKa_1=4.24, pKa2=8.24); .0215 M NH_4 (pKa = 9.25); 0.477 M *Na*; and 0.192 M *Cl*, 0.13 M *Succinate*

We also investigated the viscosity of the two solutions and calculated the diffusion coefficients of all the species involved, as these factors might be important for reactive transport situations. Using a Cannon-Fenske Routine Viscometer in triplicate, we found no distinguishable difference between the kinematic viscosity of the tiron, molybdate, or product solution (equal volumes of 0.05 M Tiron with 0.025 molybate). The average viscosity of the three solutions was 0.9798 ± 0.0017 mm^2/s at 25° C (H_2O = 1.1526 mm^2/s), where the uncertainty is in the range of our experimental error. The self diffusion coefficients not found in the literature were calculated by the method of Hayduk and Laudie (1974), which relates the molecular diffusion in water (cm^2/s) to the species molar volume calculated by the method of Fuller *et al.* (1966). The self diffusion coefficients for the species considered are given in Table 1.

Table 1

2.4 Tiron and Molybdate Reaction Model.

At a pH of 6.1, the predominant species and their charges are: Na^+ (over 96% of the cations by concentration are sodium and we considered it the only cation in system); Ti^{-2} (> 97% diprotonated); Mo^{-1} (> 98% mono-prononated); and 74% $Succ^{2-}$ and 26% $SuccH^-$. These will be the species considered in the model. The colorimetric reactions can be modeled as (the specifics of the reaction will be developed below):

$$\begin{aligned} Mo^{-1} + Ti^{-2} &\rightleftharpoons MoTi^{-3} + 2H_2O \\ MoTi^{-3} + Ti^{-2} &\rightleftharpoons MoTi_2^{-4} + OH^- + H_2O \end{aligned} \tag{5}$$

We assumed that because of succinate's pKa's and high concentration, it is the only species to react with the OH⁻ and that the reaction occurs rapidly.

$$SuccH^{-1} + OH^- \rightleftharpoons Succ^{-2} + H_2O \tag{6}$$

The rapid reaction assumption was supported by the experimental observation that the pH did not change during the reaction. If the colorimetric reaction is rapid and produces OH⁻ as supported by the literature and experimental observation in an unbuffered solution at pH = 6.1, the quenching of OH⁻ must also be instantaneous or the pH would change. Therefore, because $MoTi_2^{-4}$ is equal to the amount of OH^- produced, we can assume:

$$\begin{aligned} SuccH^{-1} &= \left(SuccH^{-1}\right)_0 - MoTi_2^{-4} \\ Succ^{-2} &= \left(Succ^{-2}\right)_0 + MoTi_2^{-4} \end{aligned} \tag{7}$$

Where $SuccH_0^{-1}$ and $SuccH_0^{-2}$ are the initial concentration of protonated and unprotonated succinate respectively.

When the concentrations are mixed, mass balances for the total molybdate, Mo_T, and the total tiron, Ti_T, can be written:

$$\begin{aligned} Ti_T &= Ti + MoTi + 2 * MoTi_2 \\ Mo_T &= Mo + MoTi + MoTi_2 \end{aligned} \tag{8}$$

Combining equation 8 with equations 2 and 4 redefines the two equilibrium expressions:

$$K_1 = \frac{\left[MoTi\right]}{\left[Mo_T - MoTi - MoTi_2\right]\left[Ti_T - MoTi - 2 * MoTi_2\right]} \tag{9}$$

$$K_2 = \frac{\left[MoTi_2\right]}{\left[MoTi\right]\left[Ti_T - MoTi - 2 * MoTi_2\right]} \tag{10}$$

Equations 9 and 10 can be solved simultaneously to obtain independent analytic solutions for each of the complexes:

$$\begin{aligned} \left[MoTi\right] &= f\left(\left[Ti_T\right], \left[Mo_T\right], K_1, K_2\right) \\ \left[MoTi_2\right] &= f\left(\left[Ti_T\right], \left[Mo_T\right], K_1, K_2\right) \end{aligned} \tag{11}$$

The solutions found using Matlab are too lengthy for presentation in this paper. Because Beer's Law is additive, the linear absorbance, A_l, of the two products can be expressed as:

$$-log\left(\frac{T}{T_0}\right) = A_l = \varepsilon_1\left[MoTi\right] + \varepsilon_2\left[MoTi_2\right] \tag{12}$$

where T/T_0 is the fraction of light transmitted; and ε_1 and ε_2 are coefficients that include the transmittance path length (1 cm in our experimental tank) and the corresponding molar absorptivity of the compound. It is expected that the complexed species with two tirons absorbs more light because it has more delocalized electrons (larger antenna to absorb light).

2.5 Equilibrium Constants.

The two stock reagent solutions described above were combined in incrementally increasing ratios of Mo:Ti to make thirty samples with identical total volumes (actual concentrations of Mo_T and Ti_T can be read from Figure 1). The resulting absorbances were measured with a Beckman DU 640 spectrophotometer at 580 nm with a 1 cm cuvette. The cuvette containing the product was placed in front of a sophisticated light box designed to give a constant source of diffuse white light (see Detwiler *et al.*, 1999 for details). An Optronics MagnaFire 10 bit (1024 x 1024 pixel) digital camera (designed for quantitative scientific imaging) was placed 2 ft in front of the cuvette on the opposite side of the light box to take digital images with an exposure time of ~0.6 seconds. The resulting images were processed with IP Lab to convert pixel intensities towards the center of the cuvette into normalized absorbances according to Beer-Lambert Law:

$$\frac{A_i}{A_{\max}} = \frac{\log(I_i) - \log(I_{blank})}{\log(I_{\max}) - \log(I_{blank})} \tag{13}$$

Where A_i is the absorbance of the *i*th product solution, $A_{\max}$ is the maximum product absorbance, I_i is the measured light intensity of *i*th product solution, I_{blank} is the measured light intensity of the blank solution, $I_{\max}$ is the measured light intensity of the max product solution. The resulting normalized absorbances varied little over the cuvette and an average value was used. Replicate absorbances were created with a different brand of chemical reagents (originally Sigma and then Fluka) on a different day to produce absorbances within 5% of each other.

Utilizing equations 11 and 12, a Gauss-Newton non-linear least squares minimization was used to fit K_1, K_2, ε_1, and ε_2 to the observed absorbance at 580 nm. Different initial guesses were used for the same estimation to confirm that the parameters converged to a unique value. Conventional methods were used to calculate the standard deviations on each of the fitted parameters from the Jacobian matrix (derivatives of residuals with parameter values) at the solution and the residuals (Milton and Arnold, 1995). The model gave an excellent fit to the data (Figure 1) to produce the following parameter values: $K_1 = 3.4 \pm 0.8 \times 10^3$ liter/mol, $K_2 = 7.5 \pm 1 \times 10^2$ liter/mol, $\varepsilon_1 = 4.3 \pm 2$ liters/(mol*cm), $\varepsilon_2 = 83 \pm 1$ liters/(mol*cm).

Figure 1

These fitted K values should be applicable to a wide range of combinations of molybdate and tiron concentrations over a wide range of wavelengths as long as the pH is maintained at 6.1. A parameter sensitivity analysis was conducted by determining the change to sum of the squared residuals caused by decreasing each of the following parameters by 5%: Mo_T, Ti_T, K_1, K_2, ε_1, and ε_2. The parameter rank from most sensitive to least sensitive including the resulting % change of the sum of squared residuals is: ε_2 (520%), Ti_T (410%), Mo_T (360%), K_2 (11%), K_1 (2.2%), ε_1 (1%). At a pH of 6.1 and a wavelength of 580 nm, absorbance is dominated by the $MoTi_2$ species. If the model is simplified (incorrectly) by setting the absorbance of *MoTi* to zero, then the best fit has a 15% higher root mean square error, although the total error is still very low. However, treating $MoTi_2$ as the only absorbing species may serve to be a good first approximation.

2.6 Imaged Absorbance versus Monochromatic Absorbance.

Digital cameras that record polychromatic absorption provide a practical tool for studying spatial patterns of color-changing reactions in experimental tanks. The observed color-shift from yellow to orange to red led us to investigate the relationship between the recorded polychromatic absorption and the monochromatic absorbance predicted by Beer's law. We found that this relationship is nonlinear, but very well described by an exponential function (Figure 2):

Figure 2

This result is explained by considering absorbance curves over the full visible spectrum on the spectrophotometer. Fifteen samples were prepared as previously described, and the concentrations of *MoTi* and $MoTi_2$ were calculated using the best-fit equilibrium constants. Then the absorbance over the visual spectrum, which is what the digital camera observes, was compared to the absorbance at 580 nm (Figure 3).

Figure 3

Beer's law is valid for monochromatic light and states that absorbance is linear with concentration. However, non-linear behavior is often observed at high absorbance values because of measurement limitations and an increase in the refractive index as the solution becomes more concentrated. For the *MoTi* and $MoTi_2$, shorter wavelengths are significantly transmitted at low product concentrations and they make up a portion of the observed light as seen by the digital camera. However, as the product concentration increases the shorter wavelengths plateau while the higher wavelengths are still absorbed in proportion to the concentration, implying that at high concentrations the short wavelengths are below the detection limit, which also verifies the progressively redder appearance of the product solution (see section 2). Therefore, the plateauing absorbance of lower, but not higher, wavelengths with increasing product concentration explains the non-linear behavior of digitally imaged camera absorbances and concentrations. The wave-like appearance of the higher absorbance values is systematic with the crests having predominantly *MoTi* and the troughs having predominantly $MoTi_2$. This implies the ratio of *MoTi* to $MoTi_2$ molar absorbtivities (ε_1 and ε_2) at the lower wavelengths (and higher absorbances) is higher than the implemented value determined at 580 nm. The only importance of this is *MoTi* does seem to have a more significant absorbance in the visible spectrum than determined from the fit at 580 nm. Because Beer's law is valid for monochromatic light, we can transform camera absorbances, A/A_O, into linear absorbances, A_l, through the following relationship (see Figure 2):

$$A_l = \kappa_1 * (e^{\kappa_2 * A/A_O} - 1) \tag{14}$$

where κ_1 and κ_2 are fitted coefficients. Using known concentrations of Tiron and molybdate, pixel-by-pixel calibration curves to fit κ_1 and κ_2 (equation 13) can be constructed from linear absorbances, such as at 580 nm, and digitally imaged absorbances of the physically system containing the known amount of product. These pixel-by-pixel calibration curves allows for absorbances captured by the digital camera to be converted into experimental linear absorbances, which can then be compared with modeled linear absorbances calculated from modeled product concentrations.

2.7 Practical Implementation: An Example of Imaged Absorbances for Mixing in Heterogeneous Porous Media.

We have presented a colorimetric reaction and relevant properties to fluid mixing, that starts with two colorless reagents that upon mixing instantly form colored, stable, soluble, quantitative products that can be modeled and used to assess fluid mixing. However, before implementing this reaction, there are some practical issues worth addressing. At a concentration of 0.05 M and pH of 6.1, Tiron has a very slight absorbance, which may be non-negligible if the path length is above a few centimeters. Additionally, if a fluid-fluid system is being studied at slow flow rates and is constantly exposed to light, Tiron may photo-oxidize and turn slightly colored. There are several alternatives to overcome these Tiron absorbance artifacts. First, if the path length of the system is longer than 1 cm, the tiron and molybdate concentrations can be decreased because the absorbance of both the colored product and tiron vary linearly with path length. The decrease in product concentration will directly offset the increase in path length and would still be visible to the digital camera over one and one-half orders of magnitude. Additionally, if explicitly modeling the diffusion of each species is unimportant (and there are no concerns with molybdate polymerizing), the pH of the solution could be lowered to minimize Tiron absorption as long as new K_1 and K_2 are determined. For experiments run for several days, photo-oxidation can be minimized by shutting off the light source or blocking it with an opaque barrier between snapshots. Additionally, tiron solutions should be stored in the dark to minimize photo-oxidation. Lastly, because Tiron complexes with many metals (see first section), metals must be absent from the fluid-fluid system. For example, we found that trace amounts of iron our system react with Tiron to form a deep purple color. Iron was subsequently removed by magnetic separation. With these issues resolved, this reaction can be very useful for studying fluid-fluid mixing.

For example, we used the tiron-molybdate reaction to image fluid-fluid mixing in heterogeneous porous media. Assuming solutes are not sorbing to the porous media, mixing in porous media is a result of hydrodynamic dispersion (pore-scale and local velocity variations), which leads to the spreading and stretching of solute plume interfaces. This stretching itself does not mix solutes, but it greatly enhances the surface areas for solutes to diffuse. Concentrations C are calculated by modeling reactive transport with a hydrodynamic dispersion coefficient D from the advection-dispersion-equation:

$$\frac{\partial C}{\partial t} = D\frac{\partial^2 C}{\partial x^2} - v\frac{\partial C}{\partial x} \qquad (15)$$

where v is the average linear velocity. This model implicitly averages reacting concentrations at the pore scale and larger length scales in heterogeneous formations; this incorrectly assumes complete mixing and leads to an over prediction of mixing and reaction (e.g. Kapoor *et al.*, 1997; Ginn *et al.*, 1995; Miralles-Wilhelm et al., 1997; Gramling *et al.*, 2002; Jose *et al.*, 2004). To help resolve these issues and create up-scaled models of reactive transport in heterogeneous porous media, we used the experimental setup described by Gramling *et al.* (2002) and the tanks of heterogeneous porous media created by Zinn *et al.*, (2004) with the Tiron-molybdate reaction (Figure 4):

Figure 4

In this setup, a clear heterogeneous tank (40 x 20 x 0.65 cm) had spatially varying hydraulic conductivity from large glass beads (2.1 mm) packed in 2.5 cm diameter circular inclusions that contained smaller glass beads (0.9 mm) resulting in a hydraulic conductivity ratio of 6, with slower velocities moving through the small circles. The tank was initially saturated with the Tiron solution and a molybdate solution (see section 3 for solution concentrations) was injected with an ISCO model 500D syringe pump at a flow rate of 4.1 ml/min. The chamber was mounted in front of a sophisticated light box designed to give a constant source of diffuse white light (see Detwiler *et al.*, 1999 for details). A 14-bit liquid-cooled CCD (charge-coupled device) camera was placed on the opposite side of the tank at a distance of ~10 ft, which gave a spatial resolution of ~0.3 mm while still capturing the entire 20 x 40 cm absorbance field, which ultimately produced ~750,000 absorbance values per time snap shot. Images were taken every minute with an exposure time of ~0.7 s. IP Lab was used to process the images to convert pixel intensities into normalized absorbance according to equation 13 (figure 5):

Figure 5

The normalized camera imaged absorbances were transformed to a linear absorbance by constructing pixel-by-pixel calibration curves from six known Tiron/molybdate mixtures (table 2) to fit the exponential transform coefficients κ_1 and κ_2 ($R^2 = 0.99 \pm 0.02$) from equation 14 at every pixel. A mass balance was then performed by comparing the digitally imaged mass to the known injected mass and the total masses differed by less than 3%, indicating there is fairly low experimental error. The transform coeffecients allowed for the observed linear absorbance based on molecular scale collisions to be compared to a model-predicted linear absorbance. The modeled linear absorbance was based on a finite difference of the conventional 1D advection-dispersion-equation (equation 15) to model the mixing and reaction of Mo_T and Ti_T (equations 11 and 12). The experimental product is inherently averaged over the thickness of the tank but it does provide the correct spatial average of the molecular scale product. Next the product is spatially averaged over Y so that it can be compared to the 1-D model along X. Using a Gauss-Newton non-linear least squares minimization, the best fit dispersion coefficient 0.63 cm^2/min and average linear velocity of 0.57 cm/min does a poor job of modeling the correct amount of mixing and reaction (figure 6).

Figure 6

As can be observed from the variability in the Y-direction in figure 5, mixing is not complete as assumed by the advection-dispersion-equation. This incomplete mixing causes the discrepancy between the observed and model predicted reaction. Up-scaled models to describe reactive transport, as visualized in figure 5, do not yet exist and are the focus of our, and many other researchers' studies (e.g. Kitanidis, 1994; Kapoor and Kitanidis, 1996, 1998; Weeks and Sposito,1998; Oya and Valocchi, 1998, Cirpka *et al.*, 1999).We feel that the reaction and analysis method presented in this paper will be instrumental in understanding mixing in porous media. Ultimately, it is hoped that this reaction and analysis method will broadly help researchers in industry and academia improve their conceptual and mathematical models of fluid-fluid mixing.

Acknowledgments. We would like to thank Claudius Freiherr Von Schwerin and Lucy Meigs from Sandia National Labortories Visual Flow Lab, and Phil Gschwend for his helpful conversation. Funding: NSF and EPA STAR graduate research fellowship. The experiments performed in this paper comply with the current laws of the United States of America.

References:

1. Atkinson, G. F. and McBryde, W.A. E., *Can. J. Chem.*,35,477,1957.
2. Aveston, J. Anacker, E. W., and Johnson, J. S. 1964. Hyrdolysis of Molybdenum(VI). Ultracentrifugation, Acididty Measurements, and Raman Spectra of Polymolybdates. *Inorganic Chemistry.* 3: 735-746.
3. Avnir, D. Kagan, M. Nature. 1984, 307, 717
4. Beven, K. J., Chatwin, P. C., Millbank, J. H. Allen, C. M. 1994. Mixing and transport in the environment : a memorial volume for Catherine M. Allen (1954-1991). Chichester ; New York : J. Wiley
5. Bockman, M., Muller, C. 2000. Growth Rates of the Bouyancy-Driven Instability of an Autocatalytic Reaction Front in a Narrow Cell. Physical Review Letters. 85(12);2506-2509.
6. Breidenthal, R. 1981. Structure in turbulent mixing layers and wakes using a chemical reaction. J. Fluid Mechanics. 109;1-24.
7. Chabarek, S. Jr., Gustafson, R. L., Courntney, R. C., Martell, A. E. *J. Am. Chem. Soc.*, 81, 515, 1959.
8. Cirpka, O. A., E. O. Frind, and R. Helmig. , 1999. Numerical simulation of biodegradation controlled by transverse mixing, J. Contam. Hydrol., 40(2), 159–182.
9. Cussler, E. L., 1997. Diffusion Mass Transfer in Fluid Systems. 2nd Ed. Cambridge University Press. USA.
10. Detwiler, R. L., Pringle, S. E., Glass, R. J., 1999. Measurement of fracture aperture fields using transmitted light: An evaluation of measurement errors and

their influence on simulations of flow and transport through a single fracture. Water Resources Research. 35(9). 2605-2617..

11. Fox, E. A., Gex, V. E. 1956. AICHE J. 2(4): 539-544.
12. Fuller, E. N., Schettler, P. D., Giddings, J. C. 1966. A new method for prediction of binary gas-phase diffusion coefficients. *Ind. Eng. Chem.*, 58, 19-27
13. Ginn, T. R., C. S. Simmons, and B. D. Wood, Stochastic-convective transport with nonlinear reaction: Biodegradation with microbial growth, Water Resour. Res., 31(11), 2689–2700, 1995.
14. Garrido, J., Mafe, S., Pellicer, J. 1985. Generalization of the a finite-difference numerical method for the steady-state and transient solutions of the Nernst-Planck flux equations. *Journal of Membrane Science*, 24, 7-14.
15. Gramling, C. M., Harvey, C. F., Meigs, L. C. 2002. Reactive Transport In Porous Media: A comparison of Model Prediction and Laboratory Visualization. Environmental Science and Technology. 36(11): 2508-2514.
16. Halmekoski, J. 1959. *Ann. Acad. Sci. Fennicae, Ser.* A2, 96. 1.
17. Harnby, N., Edwards, M. F., Nienow, A. W. 1985. Mixing in the process industries (Butterworths series in chemical engineering). London ; Boston : Butterworths.
18. Hayduk, W., and Laudie. 1974. Prediction of diffusion coeffecients for non-electrolytes in dilute aqueous solutions. *AICHE J.*, 20, 611-615.
19. Hickey, A. J., and Ganderton, D. 2001. Pharmaceutical process engineering. In Drugs and the pharmaceutical sciences ; v. 112. New York : M. Dekker.
20. International Union of Biochemistry. 1964. International Colloquium on Rapid Mixing and Sampling Techniques Applicable to the Study of Biochemical Reactions: Rapid mixing and sampling techniques in biochemistry; proceedings. In Johnson Research Foundation colloquia. New York, Academic Press.
21. Jose, S.C., M.A. Rahman and Cirpka, O.A. (2004). "Large-scale sandbox experiment on longitudinal effective dispersion in heterogeneous porous media." *Water Resour. Res.* 40(12): W12415, doi: 10.1029/2004WR003363.
22. Kapoor, V., and P. K. Kitanidis. 1996. Concentration fluctuations and dilution in two-dimensionally periodic heterogeneous porous media, Transp. Porous Media, 22, 91–119.
23. Kapoor, V., and P. K. Kitanidis. 1998. Concentration fluctuations and dilution in aquifers, Water Resour. Res., 34(5), 1181–1193.
24. Kapoor, V., L. W. Gelhar, and F. Miralles-Wilhelm, Bimolecular second order reactions in spatially varying flows: Segregation induced scale-dependent transformation rates, Water Resour. Res., 33(4), 527–536, 1997.
25. Kitanidis, P. K., The concept of the dilution index, Water Resour. Res., 30(7), 2011–2026, 1994
26. Kling, K., Mewes, D., 2003. Quantitative Measurements of Micro- and Macromixing in a Stirred Vessel using Planar Laser-Induced Fluorescence. Journal of Visualization. Vol. 6, No. 2 165-173.
27. Koochesfahani, M., Dimotakis, P. 1985. A 'flip' experiment in a chemically reacting turbulent mixing layer. J Fluid Mechanics. 170: 83-112.

28. Leaist, D. 1982. Simplified Theory of Diffusion of Mixed Electrolytes with Simultaneous Chemical Reactions. *J. Chem. Soc., Faraday Trans. 1,* 78, 3069-3079.
29. Leaist, D., Curtis, N. 1999. Hartley-Crank Equations for Coupled Diffusion in Concentrated Mixed Electrolyte Solutions. The $CaCl_2$ +HCl+H_2O System. *Journal of Solution Chemistry.* 28(4): 341-366.
30. Menisher, T., Metghalchi, M., Gutoff, E. B. 2000. Mixing Studies in bioreactors. Bioprocess Engineering. 22, 115-120.
31. Milton, J. S., Arnold, J.C. 1995. Introduction to Probability and Statistics. Principles and Applications for Engineering and the Computing Sciences. Irwin/McGraw-Hill. USA.
32. Miralles-Wilhelm, F., L. W. Gelhar, and V. Kapoor, Stochastic analysis of oxygen-limited biodegradation in three-dimensionally heterogeneous aquifers, Water Resour. Res., 33(6), 1251–1263, 1997.
33. Mitchell, P.C.H. 1990. Molybdenum and Molybdenum Compounds; in Ullmann's Encyclopedia of Industrial Chemistry, 5th Edition. A16, 668.
34. Nicholson, L. 1989. Kinetics of the Fading of Phenolphthalein in Alkaline Solution. *Journal of Chemical Education,* 1989, 66, 725-726.
35. Omurtag, A., V. Stickel, R. Chevray, 1996, Chaotic Advection in a Bioengineering System, *Proc. Eleventh ASCE Engineering Conference.*
36. J.M. Ottino. Mixing, *chaotic advection*, and turbulence. Annu. Rev. Fluid Mech., 22: 207-53, 1990.
37. Oya, S., and A. J. Valocchi. 1998. Transport and biodegradation of solutes in stratified aquifers under enhanced in situ bioremediation conditions, Water Resour. Res., 34(12), 3323–3334.
38. Pojman, J.A., Nagy, I. P., Epstein, I. R. 1991. Convective Effects on Chemical Waves. 3. Multicomponent Convection in the Iron(II)-Nitric Acid System. *J. Phys. Chem.* 95, 1306-1311.
39. Schwarzenbach, G., and Willi, A., 1951. Metallindikatoren III. Die Komplexbildung der Brenzcatechin-3,5-disulfosäure (Tiron) mit dem Eisen(III)-ion. *Helv. Chim. Acta,* 34, 528.
40. Schwarzenback, G. 1957. *Die komplexometrische Titration,* Ferd. Enke Verlag, Stuttgart, p. 2.
41. Serway, R. A., and Faughn, J. S. 1995. College Physics. Saunders College Publishing. New York
42. Shea J. R. 1977. A chemical reaction in a turbulent jet. Journal of Fluid Mechanics. 81:317-333
43. Simmons, C. T., Fenstemaker, T. R., Sharp, J. M. 2001. Variable-density groundwater flow and solute transport in heterogeneous porous media: approaches, resolutions and future challenges. *Journal of Contaminant Hydrology.* 52, 245-275.
44. Sommer, L. *Z. Anal. Chem.*, 187, 263 (1962).
45. Sterbacek, Z., Tausk, P. 1965. Mixing in the chemical industry. 1st. Ed. International series of monographs in chemical engineering, v. 5. Oxford, New York, Pergamon Press.
46. Stumm, W., Morgan, J. 1996. Aquatic Chemistry: Chemical Equilibria and Rates in Natural Waters. John Wiley and Sons Inc. USA.

47. Taketatsu, T., and Toriumi, N. 1970. Spectrophotometric study and analytical application of rare earth tiron complexes-I. *Talanta* 17:465-473.
48. Taketatsu, T., and Toriumi, N. 1971. Spectrophotometric study and analytical application of rare earth tiron complexes-II. *Talanta* 18:647-649.
49. Tidwell, V. C., Glass, R. J. 1994. Water Resources Research. 30(11), 2873-2882.
50. Truc, O., Ollivier, J.P., Nilsson, L.O. 2000. Numerical simulation of multi-species transport through saturated concrete during a migration test – *MsDiff* code. *Cement and Concrete Research* 30: 1581-1592.
51. Weeks, S. W., and G. Sposito. 1998. Mixing and stretching efficiency in steady and unsteady groundwater flows, Water Resour. Res., 34(12), 3315–3322.
52. Will, F., and Yoe, J. H. *Anal. Chim. Acta,* 8, 546, 1953.
53. Yoe, J. H. and Armstrong, A. R. 1947. Colorimetric Determination of Titanium with Disodium-1,2-dihydroxybenzene-3,5-disulfonate. *Ind. Eng. Chem., Anal. Ed.,* 19: 100.
54. Zhang, S. Schneider, S.P. Collicott, S.H. 1995. Quantitative Molecular-Mixing Measurements using digital processing of absorption images. *Experiments in Fluids.* 19(5): 319-327.
55. Zinn, B., C. F. Harvey, L. Meigs, R. Haggerty, W. Peplinski, and C.Freiherr von Schwerin. 2004. "Experimental Visualization of Solute Transport and Mass Transfer Processes in Spatially Heterogeneous Porous Media," *Environmental Science and Technology*, 38(14).

Figures and Tables:

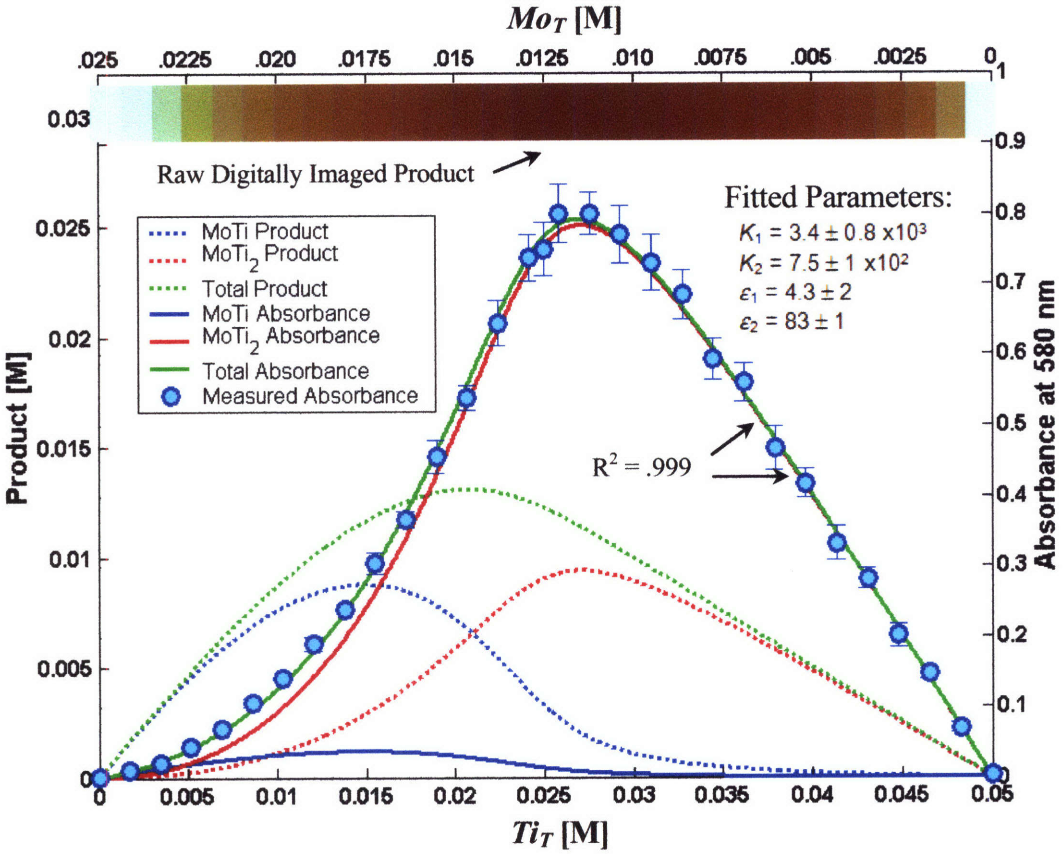

Figure 1. Modeling the Tiron-molybdate reaction to fit K_1 and K_2 at pH = 6.1. This figure is read by looking at the top and bottom x-axis of respective total Tiron and total Molybdate concentrations that formed the Product concentrations (left y-axis) and corresponding Absorbances at 580 nm (right y-axis)

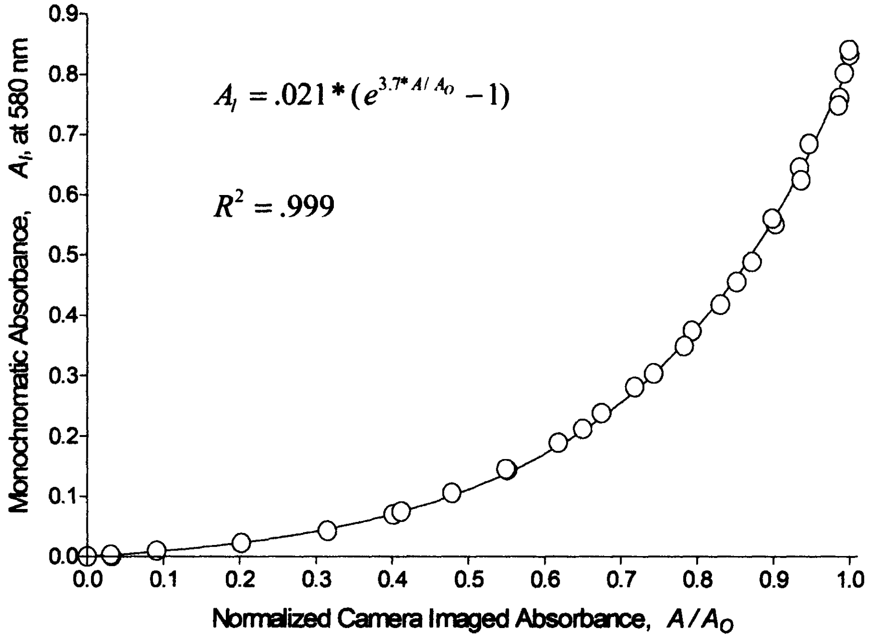

Figure 2. Monochromatic Absorbance versus Normalized Imaged Absorbance.

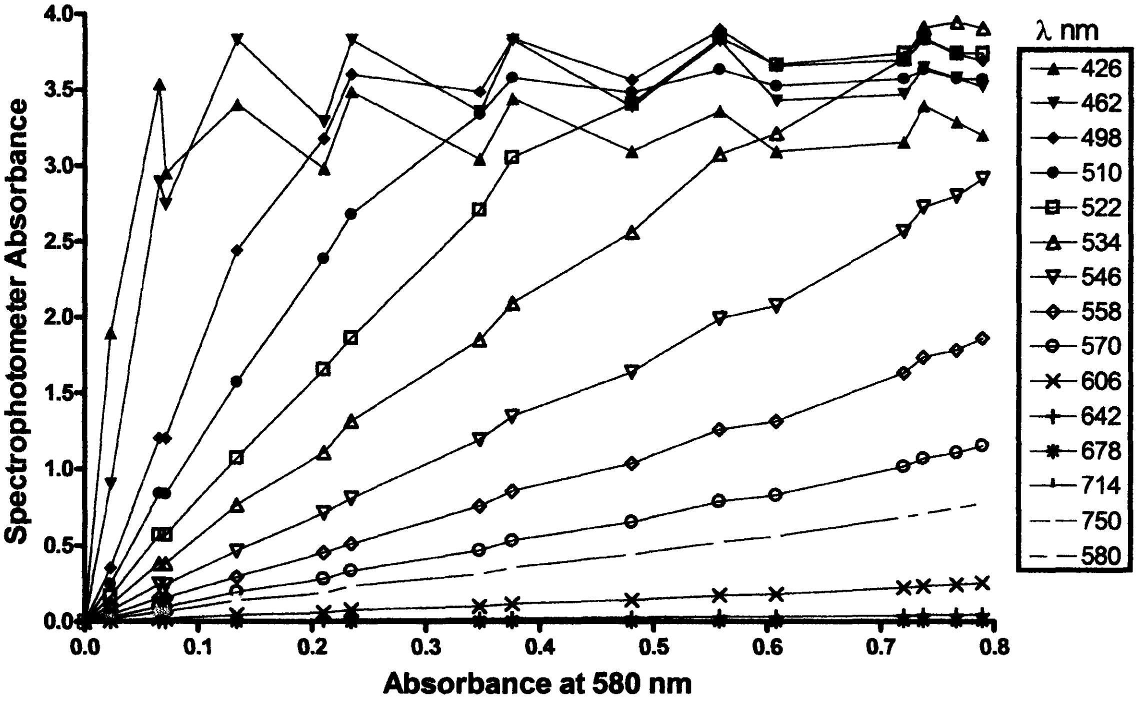

Figure 3. Comparing Absorbance over the visible spectrum as the product concentration increases.

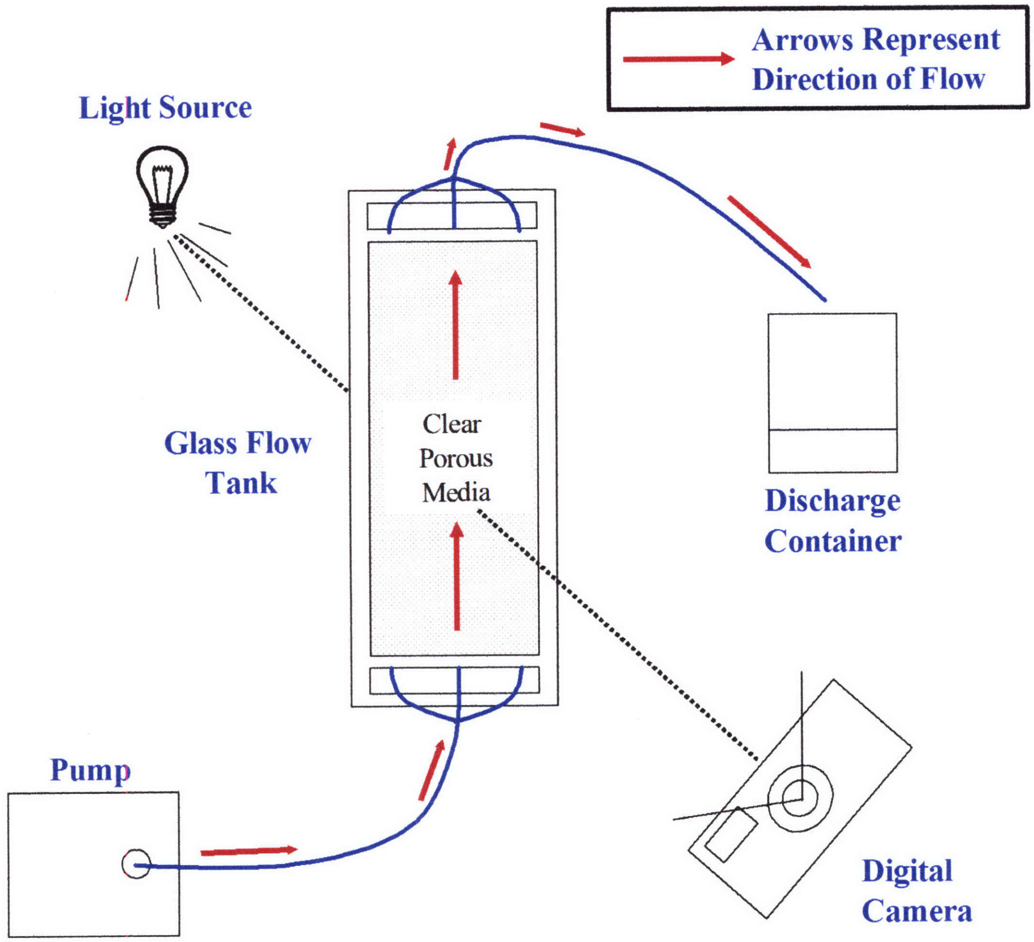

Figure 4. Experimental Setup.

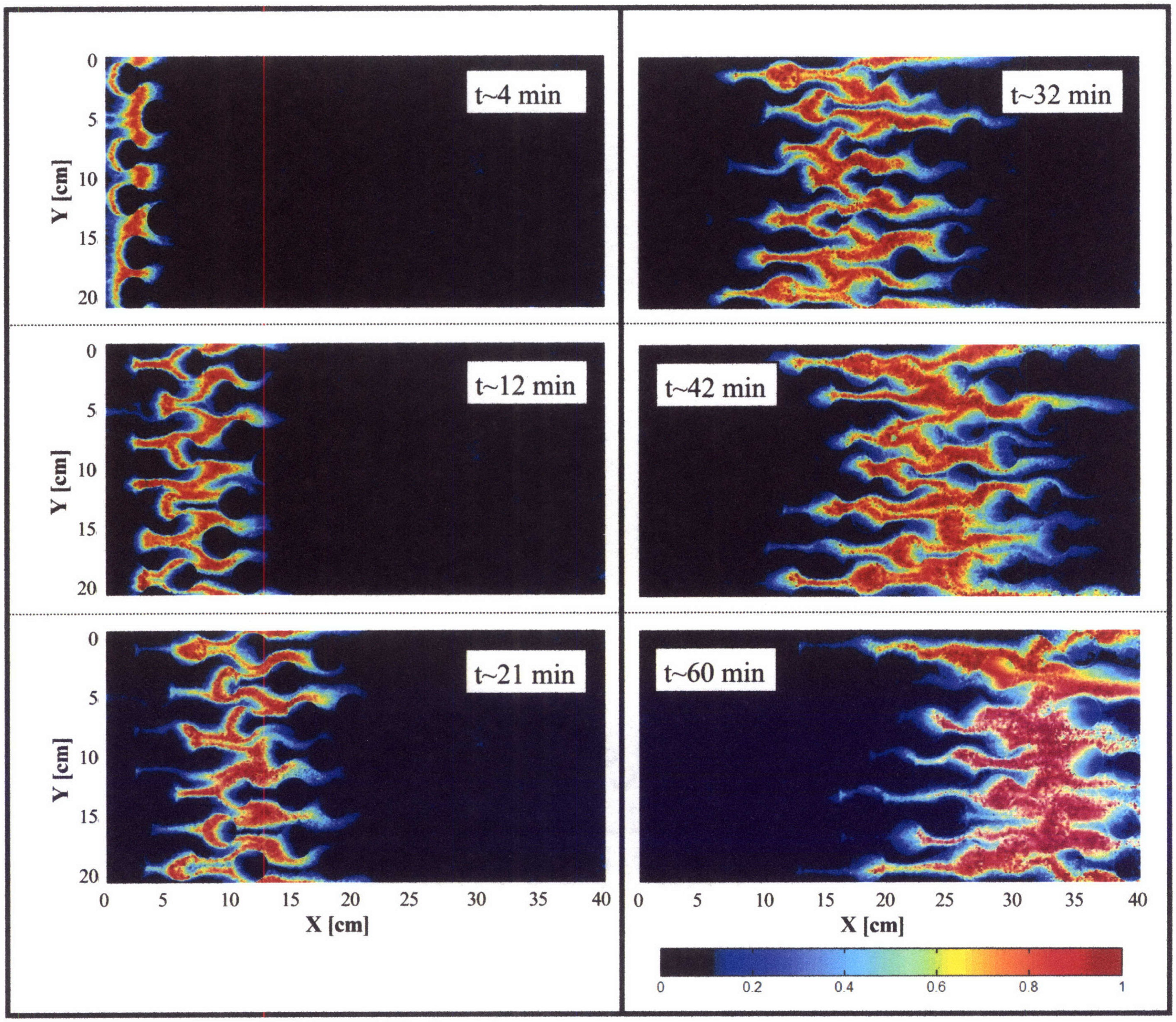

Figure 5. Imaged Absorbances of six time snap shots of fluid-fluid mixing in heterogeneous porous media, elucidated by the Tiron-molybdate reaction. Flow is from left to right.

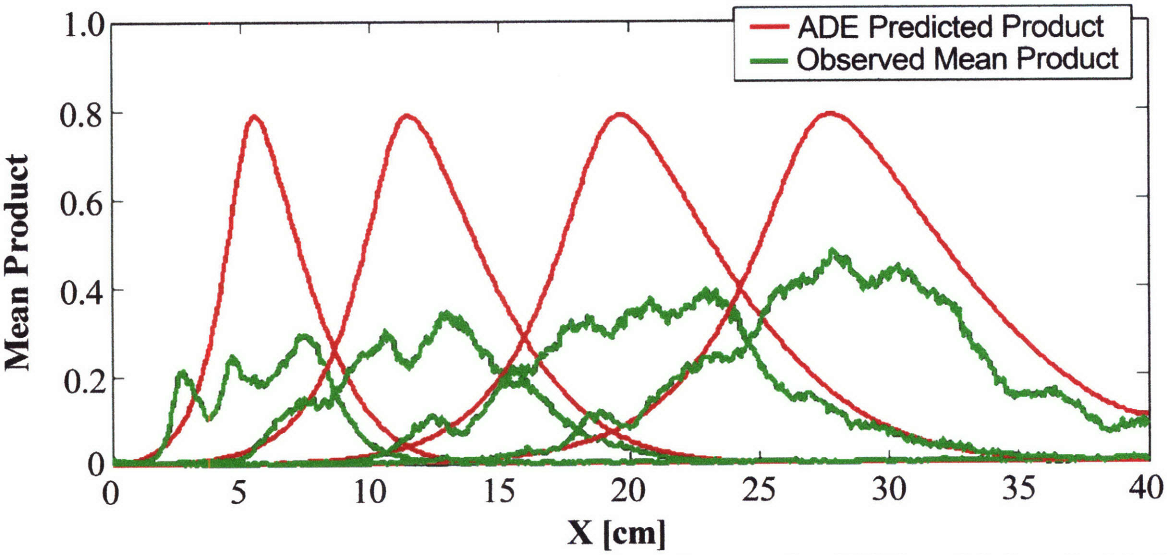

Figure 6. Comparison of coupling the advection-dispersion-equation (ADE) modeled product to the observed product at 8, 18, 32, and 46 minutes.

Table 1. Diffusion coefficients.

Species	Ti^{-2}	Mo^{-1}	$Succ^{-2}$	$SuccH^{-1}$	Cl^{-}	$MoTi^{-3}$	$MoTi_2^{-4}$	Na^{+}
Free Solution Self¥ Diffusivity [cm^2/s]	5.4 x 10^{-6}*	1.98 x 10^{-5}#	9.6 x 10^{-6}*	9.4 x 10^{-6}*	2.03 x 10^{-5}#	5.1 x 10^{-6}*	3.3 x 10^{-6}*	1.334 x 10^{-5}#

*Calculated from Hayduk and Laudie (1974) and Fuller *et al.*, (1966)

Taken from CRC

¥ For suggested recipe multiply by .98 for viscosity corrections

Table 2. Calibration Curve Solutions.

Solution #	1	2	3	4	5	6
Tiron (M)	0.05	0.0053	0.043	0.017	0.033	0.025
Molybdate (M)	0.0	0.022	0.0033	0.016	0.0083	0.0125
A_l, at 580 nm	0.0	0.047	0.26	0.40	0.64	0.83

Chapter 3. Imaging Colorimetric Reactions in Spatially Homogeneous and Heterogeneous Material

In many cases, groundwater solute transport models based on the advection-dispersion and mass-transfer equations adequately predict spatial averages of conservative solute concentrations without using explicit maps of pore structures or maps of small-scale variations in hydraulic conductivity. However, these upscaled models may incorrectly predict solute reactions because reactants are not well mixed at small scales. To characterize solute mixing in porous media, we conducted highly detailed laboratory experiments by digitally imaging the movement of colored dye tracers and colorimetric chemical reactions through illuminated chambers containing: (1) homogeneous media, in which spreading is largely caused by mechanical dispersion; (2) heterogeneous media with mild differences in hydraulic conductivity, in which spreading is accurately predicted by a Fickian macro-dispersion model; and finally (3) highly heterogeneous media, in which solute spreading is better described by a mass-transfer model. By analyzing the resulting sequence of solute concentration maps, we quantify how the conventional coupling of conservative solute transport models to chemical reaction models over-predicts chemical reaction. The experimental results demonstrate that Darcy-scale chemical segregation dominates incomplete mixing at the pore-scale. A key result for constructing reactive transport models is that the small-scale distribution of solute concentrations is distinctly non-Gaussian, and that concentration distributions are very well approximated by Beta distributions.

3.1. Introduction.

Understanding how chemicals move and change in porous media is fundamental to the study of geochemical weathering, diagenesis, and mineral deposition as well as to the design and management of schemes for aquifer remediation, nuclear waste disposal, and carbon-dioxide sequestration. In this sequence of papers we attempt to address the disparity between representations of large-scale solute migration and representations of local well-mixed biogeochemical reactions. This gap exists because solute transport models that predict large-scale solute migration and spreading do not describe the local distributions of concentrations that drive geochemical reactions, and, likewise, sophisticated biogeochemical models that accurately represent transformations within well-mixed solutions rarely attempt to represent the physical processes that mix solutes and thereby drive solute reactions. In this paper, we describe lab-scale experiments that directly image reactive transport and provide detailed quantification of small-scale solute mixing and reaction.

Several theoretical studies (e.g. Ginn *et al.*, 1995; Kapoor *et al.*, 1997; Miralles-Wilhelm *et al.*, 1997; Cirpka and Kitanidis, 2000; Robinson and Viswanathan, 2003) have suggested mixing and reaction are much less than predicted by a large-scale models of dispersive mixing (figure 1).

Figure 1.

For example, to model their biostimulation field data, Semprini and McCarty (1991) had to greatly reduce the dispersion coefficient from the value fit to a conservative tracer. Sturman *et al.* (1995) reviewed existing bioremediation laboratory and field data and pointed out several remediation cases in which pollutant removal was less effective in the field than predicted by laboratory experiments. They attributed this to a problem associated with incomplete mixing in heterogeneous aquifers. Raje and Kapoor (2000) showed that breakthrough curves of a rate-limited bimolecular reaction in homogeneous porous media are overestimated by assuming complete pore-scale mixing. Gramling *et al.* (2002) conducted colorimetric experiments in a transparent homogeneous porous media to demonstrate that actual reaction is overestimated by coupling dispersion and chemical reaction. Jose and Cirpka (2004) and Jose *et al.* (2004) conducted tank experiments to show that the effective-dispersion coefficient that predicts the correct total amount of product formed from the mixing of two reactants is less than the macro-dispersion coefficient. In order to predict and understand how conservative and reactive concentrations behave without explicitly mapping pore structures and hydraulic conductivity fields, which is highly impractical, unresolved small-scale mixing has to be understood and parameterized in reactive transport models.

In this first of three papers, we begin by describing the laboratory methods used for imaging conservative and reactive transport in porous-media-filled chambers. We then compare our high resolution data to predictions made by advection-dispersion and first-order mass-transfer equations coupled to chemical reaction models. We find that this upscaled modeling approach adequately predicts conservative solute transport but not reactive solute concentrations because of incomplete mixing at small scales. We assess the upscaling error caused by pore-scale solute segregation to Darcy-scale solute segregation in heterogeneous porous media, and then we investigate how different initial reactant concentrations affect the accuracy of upscaled predictions. Incomplete small-scale mixing creates solute concentration distributions that may not be adequately described by Gaussian distributions. We show that the small-scale concentration distributions are accurately described by Beta distributions. Models of small-scale concentration distributions are necessary for upscaling non-linear reactions, and the results presented in this paper serve as a basis for developing a reactive transport modeling approach in the accompanying paper.

3.2. Laboratory Visualization Methods.

3.2.1 Experimental chambers.

Three glass-walled experimental chambers were filled with glass beads. One chamber (30 x 5 x 0.65 cm) contained uniform-sized beads (0.4 mm) as described by Gramling *et al.* (2002), and hence has spatially homogeneous conductivity. Two different chambers (40 x 20 x 0.65 cm), described by Zinn et al. (2004), had spatially variable hydraulic conductivity. Each of these chambers contained large glass beads (2.1 mm diameter) packed around circular inclusions (2.5 cm diameter) containing smaller glass beads (0.9 mm or 0.135 mm diameter). Because the inclusions were filled with small beads, they had much lower conductivity. The first chamber, with inclusions filled with 0.9 mm beads, had a contrast in conductivity of 6. In this chamber, conservative solute transport followed classical advective-dispersive behavior. The second chamber with inclusions filled with much smaller beads (0.135 mm) had a conductivity ratio of 300, and transport through this tank was reproduced accurately by advective-mass-transfer equations (Zinn *et al.*, 2004).

3.2.2 Light absorption imaging.

Non-invasive light absorption imaging of solutes was used for each of the three chambers. This technique relates digital images of a colored solute to concentration through

Beer's Law (*e.g.* Oates and Harvey, 2006). Experiments with conservative solutes were conducted by imaging a blue dye, FD&C Blue#1, at 25 mg/l as it moved through the illuminated tanks with a 14-bit digital camera (spatial resolution of 0.3 mm) and measuring breakthrough curves with a photometer (figure 2) (Zinn *et al.*, 2004).

Figure 2.

For the reaction experiments, a clear chemical reactant was pumped into the tanks displacing another clear chemical reactant. When the two reactants mix, they produce colored complexes, which we quantified with the same light absorption method (Oates and Harvey, 2006).

3.2.3 The colorimetric reaction: Tiron and molybdate complexation.

The complexations of Tiron and molybdate (Tiron solution: 0.05 M Tiron, 0.356 M sodium, and 0.13 M succinate; Molybdate Solution: 0.025 M molybdate, 0.0215 M ammonium, 0.477 M sodium, 0.192 M chloride, and 0.13 M succinate) were used as the colorimetric reaction (Oates and Harvey, 2006). Tiron and molybdate are both initially clear and they react to produce two colored products (1:1 and 2:1 Tiron to molybdate products), which create absorbance linear with the sum of the concentrations weighted by their respective molar absorbances. In these papers we will use the term "product" to refer to light absorbance at 580 nm (Oates and Harvey, 2006).

3.2.4 Batch sorption experiments.

Zinn *et al.* (2004) tested FD&C Blue#1 with the chamber components and demonstrated that the dye did not sorb. As Tiron, molybdate, and the glass beads are all negatively charged, we did not anticipate significant sorption, but we ran batch sorption experiments to ensure that sorption could be considered negligible. Six different Tiron/molybdate mixtures (table 1) were placed in sealed glass Erlenmeyer flasks containing glass beads and the O-rings, metal screens, and glue used to construct the low-conductivity inclusions in the heterogeneous tanks. After recording the absorbance at 580 nm, the flasks were stored in the dark for one week and the absorbance at 580 nm was measured again and found to be indistinguishable. Thus we concluded that neither Tiron, molybdate, nor their product were significantly sorbing.

3.2.5 Image processing and analysis.

The captured images were processed with IPlab by applying Beer's Law to every pixel (approximately 250,000 pixels for the homogeneous tank and 750,000 for the heterogeneous tanks) to quantify the temporal evolution of the entire two-dimensional absorbance field, which is equal to the normalized concentration field for the conservative tracer (Tidwell and Glass, 1994; Zhang *et al.*, 1995; Gramling *et al.*, 2002):

$$\frac{A}{A_O} = \frac{\log(T) - \log(T_{blank})}{\log(T_{\max}) - \log(T_{blank})} \qquad (1)$$

where A is the absorbance; A_O is the absorbance of the maximum concentration (25 mg/l FD&C Blue#1 or colored product from 0.025 M Tiron and 0.0125 M molybdate solution); T is the light transmittance; T_{blank} is the light transmittance of the tank filled with water; and T_{max} is the transmittance of the tank with the maximum colored concentration. The normalized camera-imaged absorbance, A/A_O of the Tiron/molybdate product is nonlinear with chemical concentration and was transformed to the absorbance at 580 nm, A_l, which is linear with respect to concentration, by constructing pixel-by-pixel calibration curves (Oates and Harvey, 2006). The product of six known Tiron/molybdate mixtures (table 1) was imaged in the tanks with the digital camera and then measured by the spectrophotometer at 580 nm.

Table 1.

The resulting six camera absorbances A/A_O were compared with the six linear spectrophotometer absorbances, A_l at 580 nm, to fit the coefficients κ_1 and κ_2 ($R^2 = 0.99 \pm 0.02$) at every pixel (Oates and Harvey, 2006):

$$A_l = \kappa_1 * (e^{\kappa_2 * A/A_O} - 1) \tag{2}$$

Using equation 2 and the pixel-specific transform coefficients, all camera absorbances A/A_O were converted to linear absorbances A_l that vary linearly with concentration. The evolution of the observed absorbances can then be compared to modeled absorbances to assess the validity of reactive transport models. To assure the accuracy of the visualization technique, mass balances were performed for both the FD&C Blue#1 and Tiron/molybdate product on all three tanks by comparing the known injected mass to the mass calculated from the digital images.

3.3. Transport and Reaction Models.

3.3.1 Conservative transport.

To model the conservative tracer (FD&C Blue #1) in the homogeneous and heterogeneous media we applied the conventional 1-D advection-dispersion equation (*ADE*) and included rate-limited mass transfer for the highly heterogeneous conductivity field:

$$\frac{\partial C}{\partial t} = -v\frac{\partial C}{\partial x} + D\frac{\partial^2 C}{\partial x^2} - \beta\frac{\partial S}{\partial t} \tag{3}$$

where C is the mass per mobile volume, v is the average linear velocity, D is the hydrodynamic dispersion coefficient (mechanical dispersion for homogeneous media and macro-dispersion for heterogeneous media), β is the ratio of immobile to mobile volume, and S is the mass per immobile volume. Mass transfer is approximated as a rate-limited process representing diffusion or very slow advection (*e.g* Zinn et al., 2004):

$$\frac{\partial S}{\partial t} = \alpha\left(C - S\right) \tag{4}$$

where α is a rate coefficient. For the homogeneous and mildly heterogeneous case α and β are equal to zero.

A constant flux boundary was used for the inflow side of the chamber and zero gradient was applied at the outflow:

$$-D\frac{\partial C}{\partial x} + vC = vC_O \qquad x = 0, t \tag{5}$$

$$\frac{\partial C}{\partial x} = 0 \qquad x = L, t \tag{6}$$

where C_O is the initial concentration; and L is the tank length. The initial concentrations of tracer and reactant were uniform everywhere and the two coupled equations (3 and 4) were solved numerically by a central-in-space Crank-Nicholson finite difference scheme with Matlab.

3.3.2 Tiron/molybdate reaction.

Oates and Harvey (2006) discuss the Tiron/molybdate reaction as it applies to absorption imaging in detail. Here we describe the relevant aspects of this reaction for constructing a reactive-transport model. Briefly, Tiron, Ti, and molybdate, Mo, undergo an instantaneous two step complexation governed by two equilibrium expressions:

$$\begin{aligned} &Mo + Ti \rightleftharpoons MoTi; \qquad && K_1 = \frac{[MoTi]}{[Mo][Ti]} \\ &MoTi + Ti \rightleftharpoons MoTi_2; \qquad && K_2 = \frac{[MoTi_2]}{[MoTi][Ti]} \end{aligned} \tag{7}$$

The concentrations of the two colored products, $MoTi$ and $MoTi_2$, can be calculated from the concentration of total Tiron $[Ti_T,]$ the concentration of total molybdate $[Mo_T,]$ with the two equilibrium constants ($K_1 = 3.4 \pm 0.8 \times 10^3$ liter/mol and $K_2 = 7.5 \pm 1.0 \times 10^2$ liter/mol):

$$\begin{aligned} &[Ti_T] = [Ti] + [MoTi] + 2[MoTi_2] \\ &[Mo_T] = [Mo] + [MoTi] + [MoTi_2] \\ &[MoTi] = f([Ti_T],[Mo_T],K_1,K_2) \\ &[MoTi_2] = f([Ti_T],[Mo_T],K_1,K_2) \end{aligned} \tag{8}$$

where $f(\ )$ represent analytical solutions found in Matlab that are too lengthy for presentation (Oates and Harvey, 2006). Because Beer's Law is additive, the linear absorbance, A_l, of the two colored products can be expressed as:

$$A_l = \varepsilon_1 \left[MoTi \right] + \varepsilon_2 \left[MoTi_2 \right] \tag{9}$$

Where ε_1 and ε_2 are coefficients that depend on the transmittance path length (1 cm) and the corresponding molar absorptivity of the compound (at 580 nm, $\varepsilon_1 = 4.3 \pm 2.0$ liter/(mol*cm), $\varepsilon_2 = 83 \pm 1$ liter/(mol*cm)).

An important property of the Tiron/molybdate reaction is that the concentration of product can always be calculated from the concentrations of total Tiron Ti_T and total molybdate Mo_T (equation 8). Because neither Tiron, molybdate, nor their products sorb to our porous media, total Tiron and total molybdate are conserved quantities and will be transported through the chamber like a conservative tracer. For example, when a solution of molybdate displaces a solution of Tiron from the mildly heterogeneous chamber, the total concentrations of tiron and molybdate are mirror-image solutions to the advection-dispersion equation:

$$\frac{Mo_T}{Mo_{T,O}} = \frac{1}{2} erfc\left(\frac{x - vt}{2\sqrt{D_x t}}\right); \qquad \frac{Ti_T}{Ti_{T,O}} = 1 - \frac{1}{2} erfc\left(\frac{x - vt}{2\sqrt{D_x t}}\right) \tag{10}$$

because,

$$\frac{Ti_T}{Ti_{T,O}} = 1 - \frac{Mo_T}{Mo_{T,O}} \tag{11}$$

In other words, Ti_T and Mo_T lie along a mixing line and represent fractions of each fluid present. This mixing line concept holds true for any pair of conservative solutes if they do not sorb (or they have the same equilibrium linear sorption coefficient) and if dispersion dominates diffusion (or the chemicals have the same diffusion coefficients). Mixing lines also hold for rate-limited mass transfer if mass-transfer is driven by advection or if the two species have the same diffusion coefficient.

Because of this conservative behavior, reactive transport of Tiron and molybdate can be modeled from a conservative tracer by the following steps:

1) The mixing line concept is used to find concentrations of total Tiron and total molybdate from a conservative solute C/C_O:

$$\begin{aligned} &Mo_T / Mo_{T,O} = C/C_O; \;\; Ti_T / Ti_{T,O} = 1 - C/C_O; \\ &where\ Mo_{T,O} = 0.025\, M\ and\ Ti_{T,O} = 0.05\, M \end{aligned} \tag{12a}$$

2) The chemical equilibrium equations are solved to determine product concentrations:

$$\begin{aligned} [MoTi] &= f([Ti_T],[Mo_T],K_1,K_2) \\ [MoTi_2] &= f([Ti_T],[Mo_T],K_1,K_2) \end{aligned} \tag{12b}$$

3) The linear absorbance is calculated from the reaction product concentrations:

$$A_l = \varepsilon_1 [MoTi] + \varepsilon_2 [MoTi_2] \tag{12c}$$

This modeled linear absorbance is then compared to the observed linear abbsorbance to assess the accuracy of coupling the advective-dispersion and rate-limited-mass-transfer equations to chemical reaction for homogeneous and heterogeneous porous media.

3.4. Results and Discussion.

3.4.1 Conservative tracer and Tiron/molybdate product images.

The experimental results were captured as 250,000 conservative and reactive concentration values in homogeneous porous media and 750,000 concentration values in the heterogeneous porous media per image (figure 3).

Figure 3.

Comparing the known injected mass to the mass calculated from the digital images resulted in less than a 1% difference for the homogeneous tank and less than 3% for both heterogeneous tanks for both the conservative tracer and reaction product. These results demonstrate how non-invasive absorption imaging can provide highly detailed reactive concentration data in homogeneous and heterogeneous porous media.

3.4.2 Homogeneous Porous Media: Comparison of Experimental Results to Conventional Transport Models.

The reactive-transport experiments in the tank filled with uniformly sized beads provide information about pore-scale mixing because the Darcy-scale velocity field is nearly uniform. The results of these experiments corroborate the findings of Raje and Kapoor (2000) and Gramling *et al.* (2002) that pore-scale segregation reduces mixing and reaction. The tracer experiment (figure 4-A) is well fit by the advection-dispersion equation (equation 3 with $\beta = 0$) with a longitudinal dispersion coefficient of 0.15 [cm^2/min] (mechanical dispersivity of 0.35 [mm], comparable to the mean bead size of 0.4 [mm]) and a mean velocity of 4.3 cm/min. However, coupling this model with the chemical equilibrium equations (equations 8 and 9) significantly overestimates the total and peak product formed (figure 4-B), indicating pore-scale segregation of reactants.

Figure 4

Flow was stopped at 298 seconds when the reactive front was ~3/4 of the distance across the tank to test the hypothesis that the observed product would increase with time because diffusion would complete pore-scale mixing. Over the forty-three minutes after stopping the flow, product concentrations in the reactive front increased towards the concentrations predicted by the *ADE*-reaction model, indicating that molecular diffusion mixed reactants that were segregated at the pore-scale. The mean distance of diffusion over forty-three minutes is approximately 0.5 millimeter (below our experimental resolution), which is comparable to the mean bead size. This demonstrates that chemical reactants are segregated in neighboring pores.

3.4.3 Mildly Heterogeneous Porous Media.

3.4.3.1 Comparison of experimental results to conventional transport models. We fit the *ADE* (equation 3 with $\beta = 0$) to the breakthrough curve of the conservative tracer to estimate a dispersion coefficient. The *ADE* gave an excellent fit to the conservative tracer breakthrough curve in the mildly heterogeneous tank with a dispersion coefficient of 0.63 cm^2/min (macro-dispersivity of 1.1 cm) for a mean velocity of 0.57 cm/min (figure 5).

Figure 5.

Using these fit coefficients, the *ADE* gives a very good prediction of the space-time evolution of the mean tracer concentration (averaged over the Y direction) across the heterogeneous tank. However the *ADE* has no capability to describe the observed variability around the mean concentration as indicated by the observed large standard deviation (figure 6-A).

Figure 6.

Reaction product concentrations predicted by coupling the *ADE* to the chemical reaction model (equations 8 and 9) significantly overestimate the total and peak product (averaged over Y) and do not capture the observed large standard deviation (figure 6-B). Simulations indicate that the overestimation of reaction would be much greater in finer grained material. In contrast to the large gravel-sized beads we used in our tanks, fine-grained material would have less mixing and reaction because mechanical dispersion would be reduced. If the log conductivity variance (ratio of high to low conductivity) was held constant while reducing both bead sizes, the macro-dispersive spreading would remain the same but the reduced mechanical dispersion would reduce mixing and reaction and result in thin but distorted ribbons of product. This affect is easily demonstrated by adjusting the variance length-scale in the $CF\text{-}\beta$(concentration fluctuation Beta-*pdf*) model we develop in the next paper (see next paper) to account for a reduction in mechanical-dispersivities proportional to a reduction in grain size (figure 6-B, compare red and black line). In this calculation we reduced the mechanical dispersion by a factor of 10 and the overestimation in product is dramatic. Although the modeling approach is developed in the next paper, we include the result in this paper to show that product formation can be grossly overestimated even though the *ADE* gives an excellent fit to the conservative breakthrough curve (figure 5) and the lab-scale chemical reaction is well understood (Oates and Harvey, 2006).

3.4.3.2 Relative importance of pore-scale mixing. In heterogeneous porous media, there is reactant segregation at both the pore-scale and at the scale of conductivity variations. We used the detailed two-dimensional images of the conservative FD&C Blue#1 tracer to assess the relative importance of pore-scale mixing in mildly heterogeneous porous media by applying equations 12a through 12c to every pixel of the conservative tracer data. Because the pixel dimensions (0.3 mm) are greater than the pore sizes, the imaged concentration fields represent an average pore-volume concentration, and the reaction products calculated from these average concentrations approximate the product that would be produced if there was complete pore-scale mixing. Therefore, pore-scale segregation of reactants can be assessed by comparing the true product (figure 7-A) to the product simulated based on the assumption of complete pore-scale mixing (figure 7-B).

Figure 7

Figures 7-A and 7-B look very similar. However, figure 7-B shows that there is a solid red band of product in the middle of he very deformed reaction front as a result of complete pore-scale mixing. If spatial averaging was done in such a way as to follow the twist and turns of the product front, the comparison of true and complete pore-scale mixing would resemble the product front in the homogenous chamber (figure 4-B). However, most chemical segregation is at the scale of conductivity variations, which is why the average concentrations between the true product and the simulated product that assumes complete pore-scale mixing are so similar (figure 7-C).

3.4.3.3 Simulated A+B→P reaction and the effects of initial concentration differences.

In this section we investigate how a generic bimolecular reaction would have behaved in our mildly heterogeneous tank and use this reaction to assess how different initial concentrations would affect upscaling errors. The mixing line approach (section 3.3) can be used for irreversible reactions as long as the chemical reaction rate is much faster than the rate of mixing. In this case, the reaction goes to completion and the product is equal to the limiting reactant. Koussis *et al.* (2003) studied and concluded that the instantaneous assumption is generally valid for many reactions except for initial plume development close to the contaminant source or during high flow velocities and these concepts have been discussed by Ham *et al.* (2004). The consequences of slow mixing relative to faster kinetic rates is that kinetic expressions such as the commonly used Michaelis-Menten or Monod models can be replaced by assuming that multi-component reactions are controlled by the limiting reactant. Thus, a generic bimolecular reaction with reactants A and B and product P (*e.g.* Kapoor *et al.,* 1997; Ciprka *et al.*, 1999; Gramling *et al.,* 2002; Ham *et al.*, 2004):

$$A + B \rightarrow P \tag{13}$$

can be modeled from the concentrations of a conservative tracer C, as long as A and B do not sorb differently, by applying the following steps:

1) Apply a mixing line to calculate total reactant concentrations A_T and B_T, which are conserved quantities:

$$A_T / A_{T,O} = C / C_O; \quad B_T / B_{T,O} = 1 - C / C_O; \tag{14a}$$

2) Calculate the product concentration to be equal to the limiting reactant:

$$P = minimium\left(A_T, B_T\right) \tag{14b}$$

3) Calculate the remaining reactants A and B as the total concentration minus that converted into product:

$$A = A_T - P; \quad B = B_T - P \tag{14c}$$

Many studies have examined this generic reaction (*e.g.* Kapoor *et al.,* 1997; Ciprka, 1999; Gramling *et al.,* 2002) under the condition that the initial reactant concentrations $A_{T,O}$ and $B_{T,O}$ are equal. However, initial reactant concentrations are usually different in field problems. For example, oxygen concentrations are approximately 8 mg/l when in equilibrium with air, while benzene has a solubility of around 1800 mg/l. Therefore, if oxygenated water (reactant $B_{T,O}$) were flushed into a benzene plume (reactant $A_{T,O}$), the ratio of initial concentrations of $A_{T,O}$ to $B_{T,O}$ would be 225 (assuming the two plumes are saturated or equally diluted). A scenario of oxygen and ethanol could have an even larger initial concentration ratio.

To simulate the $A+B \rightarrow P$ reaction with different initial concentrations the initial concentrations of $A_{T,O}$ and $B_{T,O}$ are adjusted in equation 14a. We will refer to the ratio of $A_{T,O}$ to $B_{T,O}$ as R_{AB}. We showed in section 3.4.3.2 that pore-scale segregation causes only a slight difference between this simulated reaction and actual reaction. However, we find that scaling our conservative data by more than 20 to simulate reaction of a different initial concentration makes noise significant, which is undesirable. To overcome our noise limitations we applied the *CF-β* approach to simulate the $A+B \rightarrow P$ reaction (Chapter 4) and compared it to the *ADE* predicted product for different values of R_{AB}. All of the *ADE* and *CF-β* predictions were made using parameters fit from the reaction experiments in the mildly heterogeneous chamber. When the initial concentration ratio $R_{AB} = 20$ (concentration of $A_{T,O} = 20$ in the domain with concentration $B_{T,O} = 1$ entering the domain) both the macro-dispersion predicted product and the mean of the small-scale product are shifted backwards towards B when compared to the $R_{AB} = 1$ case (figure 8).

Figure 8.

When $R_{AB} = 20$, the discrepancy between the *ADE* and the averaged small-scale product is no longer symmetric. The *ADE*-predicted product accurately models the leading edge of the reaction front where reactant concentrations are different, but poorly predicts the following edge where reactant concentrations are similar. When $R_{AB} = 1/20$ (concentration of $A_{T,O} = 1/20$ in the domain with concentration $B_{T,O} = 1$ entering the domain) we see a mirror image of $R_{AB} = 20$ (figure 8). Additionally, the percent over-estimation of the *ADE*-predicted total product (product integrated over space) compared to the *CF-β* total product changes and generally increases as the initial concentration ratio differs further from 1 (figure 9)

Figure 9.

This demonstrates that upscaling problems become more important as initial concentrations differ for the $A+B \rightarrow P$ reaction.

3.4.4 Highly Heterogeneous Porous Media.

3.4.4.1 Comparison of conservative experimental results to conventional transport model. The rate-limited mass-transfer model (equations 3 and 4) closely fit the breakthrough curve for the conservative solute in the highly heterogeneous tank (figure 10) with the following parameter values: v of 0.13 cm/min, D of 0.061 (dispersivity of 0.46 cm), α of 0.001 [min^{-1}], and a β of 0.7 [(immobile volume)/(mobile volume)]. In addition to the observed concentration variability in the macro-dispersive front (the part of the front that can be modeled with the ADE), there was less but still significant variability during the rate-limited mass transfer tailings (concentrations modeled by rate-limited mass transfer).

Figure 10

Dispersion was lower than in the mildly heterogeneous media because concentrations in the macro-dispersion front did not experience the velocity fluctuations in the circular inclusions because of the large difference in hydraulic conductivity. The estimated values for the rate coefficient, α, and the ratio of immobile to mobile volume, β, are physically reasonable. Zinn *et al.* (2004) calculated the internal velocity v_{in} through the circular inclusions as 0.0016 cm/min, which implies the characteristic length L of the immobile domain is 1.6 cm from the expression for advective mass transfer, $\alpha = v_{in} / L$. This distance is the same as the harmonic average of the distance across the circular inclusions given by $4R/\pi$, where R is the radius of the inclusion. The estimated value of β, 0.7, is also close to the volume of circles divided by the volume of surrounding media ~ 0.5.

3.4.4.2 Simulated A+B→P reaction compared to conventional model predictions and the effects of initial concentration differences. During the Tiron/molybdate reaction experiment in the highly heterogeneous chamber, density affected flow in the low-permeability inclusions (figure 11) due to a difference in diffusion coefficients between products and reactants (Oates *et al.*, 2007).

Figure 11.

The effects were not noticeable in the other experiments because of the short residents times compared to the highly heterogeneous experiments. As a result of the density affected flow, so we did not use these experiments to quantify upscaling reactive transport in highly heterogeneous porous media (figure 11). Instead, we used our conservative tracer data from the highly heterogeneous experiment to simulate reaction in the same way we used our conservative tracer data from the mildly heterogeneous chamber to assess pore-scale mixing in (section 3.4.3.2)

We investigated upscaling reactive transport in highly heterogeneous porous media by simulating the bimolecular $A+B \rightarrow P$ reaction with equal and different initial concentrations (equations 14a-14c) using the imaged conservative concentrations C/Co at every pixel. We did not exceed a factor of 20 in the initial concentration difference in order to avoid introducing excessive noise when scaling our data. With this method, we obtained the detailed space-time evolution of product and reactant concentration profiles. The only difference between this approach and a true reaction experiment is pore-scale mixing, which we found relatively unimportant in a macro-dispersion front and we believe is unimportant in highly heterogeneous media. For the purpose of our simulations, we considered A to exist in the domain and B to be entering; these initial conditions apply to all the analysis to follow. The spatial averages of the simulated bimolecular reaction (equations 14a-14c) were then compared to predicted product behavior calculated from the upscaled *ADE* and rate-limited mass-transfer model (equations 3 and 4). For the case of $R_{AB} = 1$, there is an overestimation of product in the dispersion front (shown to the left of the Y-axis in figure 12) but the average amount of reaction behind the dispersion front is accurately predicted by the mass-transfer model (figure 12).

Figure 12.

When R_{AB} is greater than 1, as shown for $R_{AB} = 5$, $R_{AB} = 10$, and $R_{AB} = 20$ in figure 12, the spatially averaged product concentrations agree with the *ADE* and rate-limited-mass-transfer model predicted product concentrations at the leading part of the reaction front where reactant concentrations are different, but poorly represents the tailing region where reactant concentrations are similar (figure 12). Conversely, when R_{AB} is less than 1, the estimation of the lead part of the reaction front is poor but the estimation of the tailing front improves (not shown). In general, for highly-heterogeneous porous media, the large variations in hydraulic conductivity tremendously distort the interface between the two reacting fluids and set up an extremely large surface area for transverse mixing to generate large amounts of mixing and reaction.

3.4.5 Incomplete Mixing.

Generally, the observed product is less than the *ADE* and *ADE*-mass-transfer modeled product because reactants are not completely mixed at small-scales. Even though the upscaled *ADE* and *ADE*-mass-transfer models accurately predict conservative solute spreading (figure 13-A,-B,-C top row), concentrations are not completely mixed at small-scales.

Figure 13

In the homogeneous tank, the lack of mixing is evident by the incomplete product formation, which can be seen by the spotty areas of red product (figure 13-A, bottom-left). The lack of mixing is dramatically evident in the macro-dispersion front as shown by comparing the spatial pattern of the observed product (figure 13-B, bottom-left) to the *ADE* predicted product (figure 13-B, bottom-right), which clearly shows that in the area of *ADE* predicted mixing there is chemical reactant segregation. In highly heterogeneous porous media, reactant segregation occurs from mass transfer occurring in small thin tails coming out of spatially variable local immobile inclusions (figure 13-C bottom-left).

Generally for the 1 to 1 stoichiometric reaction of $A+B \rightarrow P$, product formation is most overestimated where the reactant concentrations are equal because any fluctuation away from the mean will always result in the limiting reactant being lower. For example, consider a case where the mean of $A_T = 0.5$ and the mean of $B_T = 0.5$; reacting the mean concentrations will produce a P of 0.5 (see equation 14b). However if the means are decomposed into $A_{T,1} = 0.3$ and $A_{T,2} = 0.7$ and from the mixing line the paired reactants are $B_{T,1} = 0.7$ and $B_{T,2} = 0.3$, these small-scale reactions would produce $P_1 = 0.3$ and $P_2 = 0.3$. Then taking averages would produce a mean P of 0.3 versus a predicted value 0.5. This demonstrates how similar reactant concentrations can have high discrepancies between the small-scale reactions and performing reactions based on spatially averaged concentrations. Conversely, when mean concentrations are substantially different such that the mean of $A_T = 0.2$ and the mean of $B_T = 0.8$, reacting the means would produce a P of 0.2. If these means are decomposed into $A_{T,1} = 0.0$ and $A_{T,2} = 0.4$ with $B_{T,1} = 1.0$ and $B_{T,2} = 0.6$, they would produce $P_1 = 0.0$ and $P_2 = 0.4$. Then taking averages would produce a mean P of 0.2 versus a predicted value 0.2 demonstrating how different concentrations can have very low discrepancies between the true local reactions and performing reactions based on spatially averaged concentrations. The reason for this is when concentrations are different, the limiting reactant is still fully consumed whether it is the true small-scale values or the mean value so long as the small-scale concentrations do not fluctuate around the mean so much that they are no longer the limiting reactant. If they are no longer the limiting reactant, then upscaling error is introduced. For different stochiometries, the same principles apply but should be different by a ratio of the stochiometry. For example, if the reaction was $A+2B \rightarrow P$, we would expect the biggest discrepancy between observed and predicted product where mean B concentrations are two times mean A concentrations.

3.4.6 Concentration distributions and the Beta distribution.

As a result of the incomplete mixing, concentration distributions exist in any unresolved volume of porous media and they should be accounted for when considering both conservative and reactive transport. Before examining concentration distributions in our experimental results, it is useful to consider the concentration distribution of a typical contaminant pulse. For a pulse injection, the particle positions for a Fickian process produce a normal or Gaussian distribution (figure 14-A).

Figure 14

In this case, the Gaussian pulse has been normalized by its maximum concentration to keep concentrations between 0 and 1. We wish to determine the concentration probability density function (*pdf*) of the concentration profile for a distance of $\pm 4\sigma$ around the mean. Recognizing that normalizing the distance between -4σ and the mean at x=vt represents a cumulative density function (*cdf*) (i.e. the relative volume of water containing each concentration value) we can differentiate the distribution to analytically calculate the concentration *pdf* (see appendix for derivation):

$$f_{C/C_{\max}} = \frac{i}{4\sqrt{2}\left(C/C_{\max}\right)\sqrt{\log\left(C/C_{\max}\right)}} \tag{15}$$

The most important feature to recognize is that even though particle positions are normally distributed, the concentration *pdf* is highly non Gaussian and has a bimodal shape (figure 14-B).

Based on the first two moments, the Beta distribution is capable of reproducing bimodal behavior (initial stage of mixing), a uniform distribution (early stages of mixing), asymptotically approaching a Gaussian distribution (later stages of mixing), and finally a delta function around the mean if the system is ever completely mixed. Thus, the Beta distribution is a natural choice to represent concentration *pdfs* in porous media, and it has been used to model the similar process of turbulent mixing (Frankel *et al.*, 1991; Frankel *et al.*, 1992; Girimaji, 1991). The Beta distribution is:

$$f_{C/C_O} = \frac{\Gamma(a+b)}{\Gamma(a)\Gamma(b)}\left(C/C_O\right)^{a-1}\left(1-C/C_O\right)^{b-1} \tag{16}$$

Where f_{C/C_O} is the probability density of normalized concentrations C/C_O, Γ is the gamma function, and a and b are shape parameters calculated from the concentration mean and variance:

$$a=\overline{C/C_O}\left(\frac{\overline{C/C_O}\left(1-\overline{C/C_O}\right)}{\sigma^2_{C/C_O}}-1\right); \qquad b=\left(1-\overline{C/C_O}\right)\left(\frac{\overline{C/C_O}\left(1-\overline{C/C_O}\right)}{\sigma^2_{C/C_O}}-1\right) \tag{17}$$

Typically the initial concentration C_O is the maximum concentration C_{max} but if there were not the case, then concentrations would have to be normalized by C_{max} to ensure the values ranged between 0 and 1.

Integrating the *pdf* of a Gaussian pulse bound by 4σ (equation 15) produces the mean and variance (see appendix):

$$\overline{C/C_{\max}}=\frac{1}{4}\sqrt{\frac{\pi}{2}}erf\left(2\sqrt{2}\right) \tag{18}$$

$$\sigma^2_{C/C_{\max}}=\frac{1}{32}\left(4\sqrt{\pi}erf\left(4\right)-\pi erf\left(2\sqrt{2}\right)^2\right) \tag{19}$$

where *erf* is the error function. A Beta distribution with the same mean and variance as a pulse's *pdf* bound by $\pm 4\sigma$ (equation 15) is virtually identical (figure 14-B), demonstrating the versatility and usefulness of the Beta distribution for modeling concentration *pdfs* in porous media. The Gaussian pulse may be thought of representing many repeated fingers in a macro-dispersive front that have been smoothed out by transverse dispersion, and it is therefore expected that the Beta distribution will be useful for modeling concentration *pdfs* in our experimental macro-dispersion front.

Looking along a few slices of Y in the macro-dispersion front in our experimental results (figure 15-A-B-C):

Figure 15.

where the colored squares show the location of the corresponding colored distributions, it is evident that there is not a uniform concentration value (i.e. a dirac delta of the mean value) as predicted by the *ADE*, but rather a distribution of concentrations. For a given mean and variance, we found that the space-time evolution of these conservative distributions are very well described by Beta distributions. We used the empirical mean and variance over y at a given x to generate Beta distributions which were then compared to the observed *pdf* for the same location and the results were found to be in good agreement for the mildly heterogeneous results (figure 15-A,-B,-C). The agreement for the highly heterogeneous results was equally as good although the distributions were generally tighter (not shown).

To quantitatively compare how well the Beta distributions matched at a given (x,t) we calculated the root-mean-square-error of Beta *cdf* compared to the observed *cdf* along the dispersion front at a given time for the mildly heterogeneous chamber and along the entire domain for the highly heterogeneous chamber. Then all the root-mean-square errors were averaged at a given time and reported as solute passed through both heterogeneous mediums (figure 16).

Figure 16.

The full space-time evolution of the conservative concentration distributions can be approximated as a Beta distribution with only a 3-4 percent root-mean-square error on average.

The fact that solute concentrations are distributed over many values at unresolved spatial scales has important implications for understanding and upscaling reactive transport. For non-linear reactions, each concentration or pair of concentrations in the distribution or joint distribution will react differently, which is why it is not appropriate to first average the reactants and then calculate chemical reaction based on the mean reactant values. The small-scale specific reactions have to be calculated first before any averaging is applied if the reaction is non-linear. There are several types of non-linear reactions encountered in practice (table 2-A) that would be affected by incomplete mixing.

Table 2.

For the simplest linear reactions, mean reactions are adequately modeled by calculating chemical reaction based on mean reactant concentrations (table 2-B). However, reactant and product distributions still exist for linear reactions. These distributions are useful to know to help answers important questions like what is the probability that the concentration will exceed their regulated MCL.

3.4.7. Maximum Contaminant Levels versus Spatial Averages.

EPA laws and regulations are in terms of MCLs or maximum contaminant levels. Slow mixing in porous media causes concentrations to be spatially variable with maximum concentrations to be well above spatial averages. If there was a similar concentration profile of figure as 15-A at a larger scale (hypothetical scaling shown in green), two wells right next to each other could measure very different concentrations. The green square shows the x value where the *ADE* very accurately predicts a mean of $C/C_O = 0.5$. However, even though this is the correct mean, because of incomplete mixing, different concentrations outside the mean exist and in this case, the mean value is actually the least likely concentration for a well to experience. It is much more likely that a well would see almost no concentration or a very high concentration. This implies that it would be more appropriate to model contaminant transport situations such that point locations such as wells or control planes have less then a 5% (hypothetical) chance of seeing a threshold concentration value as opposed to making decisions based on mean values. Furthermore it suggests that transport models calibrated with sampling wells could be erroneous if sampling wells are insufficiently refined.

3.5. Conclusions.

Molecules must collide before they can react, and collisions result from molecular diffusion across complex fluid interface. In natural porous media these interfaces may have very complex spatial structures at all scales. Here we describe the results of an experimental method that combines visual light absorption imaging and colorimetric chemical reactions to create very accurate and high-resolution images of changing concentrations during reaction in spatially homogeneous and heterogeneous media. Data from physical experiments are extremely valuable because they enable testing of hypotheses concerning reactive transport without the assumptions and artifacts of numerical simulations.

Previous work with conservative tracers in similar experimental chambers (Gramling *et al.*, 2002; Zinn, *et al.*, 2004) shows that the advection-dispersion and mass-transfer models can accurately predict spatially-averaged conservative solute spreading in homogeneous, mildly heterogeneous, and highly heterogeneous media. Here we show that these approaches do not accurately represent reactive transport because these upscaled transport models do not consider small-scale concentration variability and reactant segregation.

We find pore-scale segregation of reactants consistent in magnitude to the findings of Gramling *et al.* (2002). However, as theorized by Jose and Cirpka (2004) our experiments show that pore-scale chemical segregation is relatively unimportant for reactive transport in heterogeneous porous media because chemical segregation is dominated by hydraulic conductivity variations at a larger scale. We also explore how differences in mean reactant concentrations moderate reactive transport. Upscaling error is greatest where the mean concentrations are similar, thus reactive transport may be most inhibited in either the leading edge of a plume or within the plume core depending on the initial or boundary concentrations of reactants. Also, highly heterogeneous porous media can cause large amounts of mixing and reaction, but upscaling error from spatially variable immobile domains is dependent on initial reactant concentrations.

A key finding from these experiments is that the local distribution of solutes concentrations is not Gaussian. Even in mildly heterogeneous porous material, where concentration profiles have a Gaussian shape, the distribution of concentrations is decidedly not Gaussian. Instead, we find concentration distributions are accurately fit by Beta distributions. This experimental result, that concentration distributions are Beta and not Gaussian, has important implications for understanding reactant mixing and hence constructing reactive transport models. These implications are explored in the second paper of this three-part series.

Appendix.

For a pulse injection that undergoes Fickian spreading, the concentration evolution can be described by the following equation, which is essentially a normal distribution:

$$C(x,t) = Co\frac{1}{\sqrt{4\pi v_x A_x t}} e^{-\frac{(x-v_x t)^2}{4 v_x A_x t}} \tag{A-1}$$

The maximum concentration occurs at x = $v_x t$ which means:

$$C_{\max}(x,t) = Co\frac{1}{\sqrt{4\pi v_x A_x t}} \tag{A-2}$$

To keep concentrations normalized such that they fall between 0 and 1 equation A-1 is divided by equation A-2:

$$C/C_{\max}(x,t) = e^{-\frac{(x-v_x t)^2}{4 v_x A_x t}} \tag{A-3}$$

The spatial location of the concentrations is obtained by solving for the concentrations location:

$$x = v_x t + 2i\sqrt{v_x A_x t}\sqrt{\log\left(C/C_{\max}\right)} \tag{A-4}$$

Arbitrarily choosing a cutoff of 4σ $\left(\sigma = \sqrt{2tA_x v_x}\right)$, and making use of symmetry, the concentration distribution is bounded between the spatial locations:

$$vt - 4\sqrt{2 v_x A_x t} \le x \le vt \tag{A-5}$$

The concentrations at these locations are constant:

$$C/C_{\max}\left(x = vt - 4\sqrt{2 v_x A_x t}, t\right) = 1/e^8 \tag{A-6}$$

$$C/C_{\max}\left(x = vt, t\right) = 1 \tag{A-7}$$

The spatial location of the concentrations is converted into to cumulative density functions by subtracting the distance of -4σ to evaluate the selected part of the domain and then normalizing by 4σ such that cumulative frequencies are:

$$F\left(C/C_{\max}\right)=\frac{v_x t+2i\sqrt{v_x A_x t}\sqrt{\log\left(C/C_{\max}\right)}-\left(v_x t-4\sqrt{2v_x A_x t}\right)}{4\sqrt{2v_x A_x t}}\Rightarrow$$

$$F\left(C/C_{\max}\right)=\frac{i\sqrt{\log\left(C/C_{\max}\right)}}{2\sqrt{2}}+1 \tag{A-8}$$

The *pdf* is then given by the differentiating with respect to $C/C_{\max}$:

$$f_{C/C_{\max}}=\frac{i}{4\sqrt{2}\left(C/C_{\max}\right)\sqrt{\log\left(C/C_{\max}\right)}} \tag{A-9}$$

The first three moments are found by integrating over the *pdf*:

$$0th=\int_{1/e^8}^{1}\frac{i}{4\sqrt{2}\left(C/C_{\max}\right)\sqrt{\log\left(C/C_{\max}\right)}}dC/C_{\max}=1 \tag{A-10}$$

$$1st=\int_{1/e^8}^{1}\frac{i}{4\sqrt{2}\left(C/C_{\max}\right)\sqrt{\log\left(C/C_{\max}\right)}}C/C_{\max}dC/C_{\max}=\frac{1}{4}\sqrt{\frac{\pi}{2}}Erf\left(2\sqrt{2}\right) \tag{A-11}$$

$$2nd=\int_{1/e^8}^{1}\frac{i}{4\sqrt{2}\left(C/C_{max}\right)\sqrt{log\left(C/C_{max}\right)}}\left(C/C_{max}\right)^2dC/C_{max}=\frac{1}{8}\sqrt{\pi}Erf\left(4\right) \tag{A-12}$$

From the moments, the mean and the variance can be calculated:

$$\overline{C/C_{\max}}=\frac{1}{4}\sqrt{\frac{\pi}{2}}Erf\left(2\sqrt{2}\right) \tag{A-13}$$

$$\sigma^2_{C/C_{\max}}=\frac{1}{32}\left(4\sqrt{\pi}Erf\left(4\right)-\pi Erf\left(2\sqrt{2}\right)^2\right) \tag{A-14}$$

References

1. Cirpka, O. A., Frind, E. O., and Helmig, R. 1999. Numerical simulation of biodegradation controlled by transverse mixing. Journal of Contaminant Hydrology. 40(2), 159–182.
2. Cirpka, O. Kitanidis, P.K. 2000. An advective-dispersive stream tube approach for the transfer of conservative-tracer data to reactive transport. *Water Resources Research.* 36(5), 1209-1220.
3. Frankel, S. H., Madnia, C. K. and Givi, P. 1991. Modeling of the unmixedness in homogeneous reacting turbulence. *Chem. Eng. Comm.* 104, 117-125.
4. Frankel, S.H., Madnia, C.K. and Givi, P. 1992. Modeling of the reactant conversion rate in a turbulent shear flow. *Chem. Eng. Comm.* 113, 197-209.
5. Ginn, T. R., Simmons, C. S. and Wood., B. D. 1995. Stochastic-convective transport with nonlinear reaction: Biodegradation with microbial growth. *Water Resources Research.* 31(11), 689–2700.
6. Gramling, C. M. Harvey, C. F., Meigs, L. C. 2002. Reactive transport in porous media: A comparison of model prediction with laboratory visualization. *Environmental Science and Technology.* 36(11), 2508-2514.
7. Ham, P. A. S., Schotting, R. J., Prommer, H., Davis, G. B. 2004. Effects of hydrodynamic dispersion on plume lengths for instantaneous bimolecular reactions. *Advances in Water Resources.* 27, 803-813.
8. Jose, S. C., and Cirpka, O. A. 2004. Measurement of mixing-controlled reactive transport in homogeneous porous media and its prediction from conservative tracer test data. *Environmental Science and Technololgy.* 38(7), 2089-2096.
9. Jose, S. C., Rahman, M. A. and Cirpka, O.A. 2004. Large-scale sandbox experiment on longitudinal effective dispersion in heterogeneous porous media. *Water Resources Research.* 40(12), W12415, doi: 10.1029/2004WR003363.
10. Kapoor, V., Gelhar, L. W., and Miralles-Wilhelm, F. 1997. Bimolecular second order reactions in spatially varying flows: Segregation induced scale-dependent transformation rates. *Water Resources Research.* 33(4), 527–536.
11. Miralles-Wilhelm, F., Gelhar, L. W., and Kapoor, V. 1997. Stochastic analysis of oxygen-limited biodegradation in three-dimensionally heterogeneous aquifers. *Water Resources Research.* 33(6), 1251–1263.
12. Oates P. M. and Harvey, C.F. 2006. A colorimetric reaction to quantify fluid mixing. *Experiments in Fluids.* 41, 673–683. DOI 10.1007/s00348-006-0184-z.
13. Oates P.M., Freiherr von Schwerin, C., Harvey, C.F. and Meigs, L. 2007. Induced Density Fingering by Solute Reaction in Porous Media. *Journal of Fluid Mechanics.* (In preperation).
14. Raje, D. S. and Kapoor, V. 2000. Experimental study of bimolecular reaction kinetics in porous media. *Environmental Science and Technology.* 34 (7), 1234-1239.
15. Robinson, B.A., Viswanathan, H.S. 2003. Application of the theory of micromixing to groundwater reactive transport models. *Water Resources Research.* 39(11), 1313.
16. Semprini, L. and P.L. McCarty. 1991. Comparison between model simulation on field results for in-situ biorestoration of chlorinated aliphatics: Part 1. Biostimulation of the methanotrophic bacteria. *Ground Water.* 29(3), 365-374.

17. Sturman, P.J., Stewart, P.S., Cunningham, A.B., Bouwer, E. J., and Wolfram, J. H. 1995. Engineering scale-up of in situ bioremediation processes: A review. *Journal of Contaminant Hydrology*. 19, 171-203.
18. Tidwell, V. C., Glass, R. J. 1994. X-ray and visible light transmission for laboratory measurement of two-dimensional saturation fields in thin slab systems. *Water Resources Research*. 30(11), 2873-2882.
19. Zhang, S., Schneider, S. P., Collicott, S. H. 1995. Quantitative Molecular-Mixing Measurements using digital processing of absorption images. *Experiments in Fluids*. 19(5), 319-327.
20. Zinn, B., Harvey, C. F., Meigs, L., Haggerty, R., Peplinski, W., and Freiherr von Schwerin, C. 2004. Experimental Visualization of Solute Transport and Mass Transfer Processes in Spatially Heterogeneous Porous Media. *Environmental Science and Technology*. 38(14), 3916-3926.

Figures.

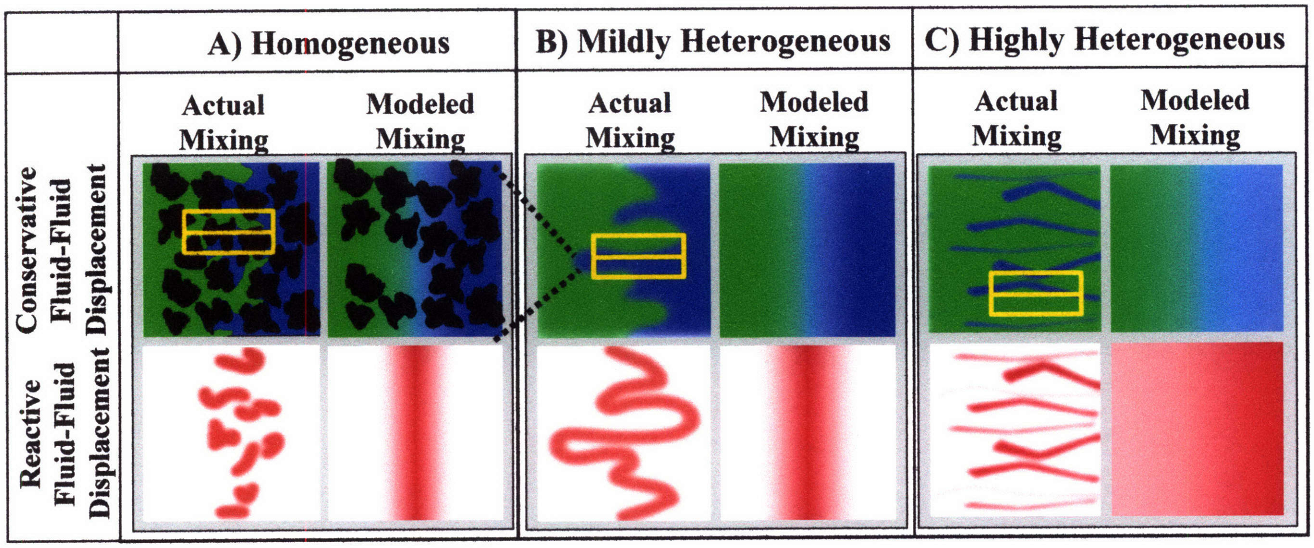

Figure 1. Flow is from left to right. A) In both homogenous and heterogeneous porous media, mechanical dispersion has incomplete mixing from solute movement through some pores but not though adjacent pores. This small scale chemical reactant segregation (shown by yellow boxes) is not captured by applying conventional conservative transport equations that assume complete mixing (product shown in red). B) In mildly heterogeneous porous media, local velocity variations cause solute spreading or macro-dispersion which appears as mixing at larger scales but potential reactants remain spatially separate. C) When concentrations slowly come out of local immobile regions in highly heterogeneous media, rate-limited mass-transfer models assume that concentrations tailing the dispersive front are uniformly mixed when infact chemical segregation exists.

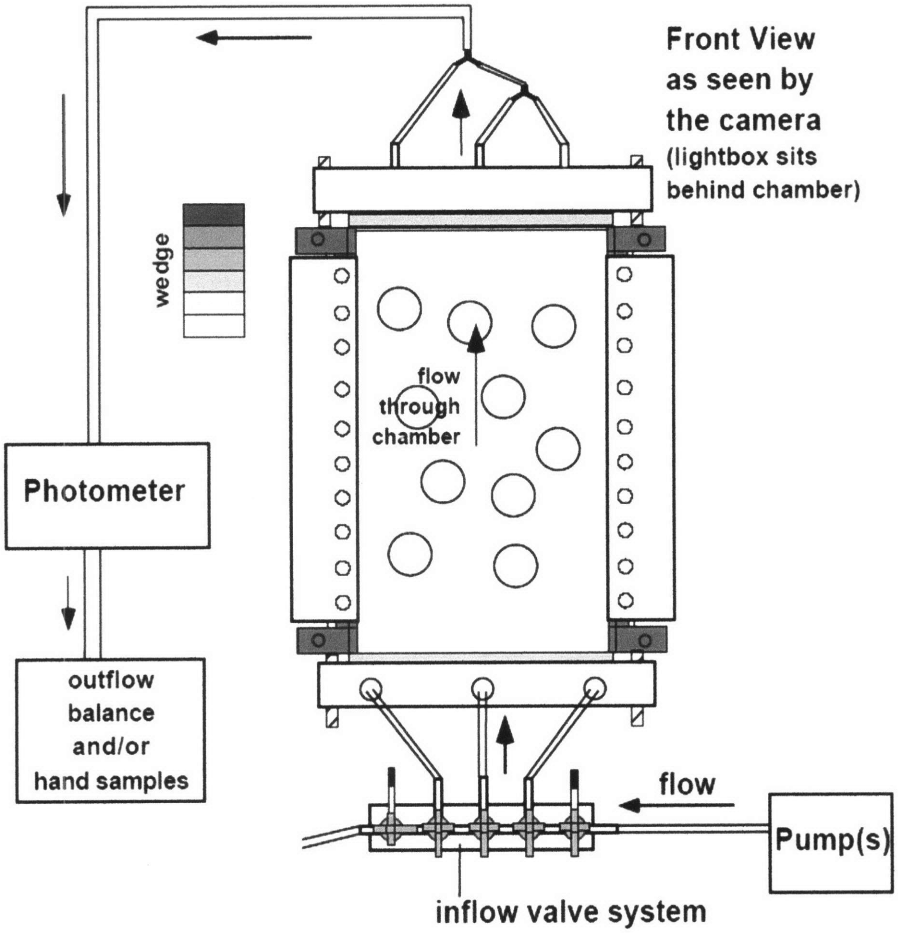

Figure 2. Experimental chamber filled with porous media. Contains circular inclusions of low conductivity.

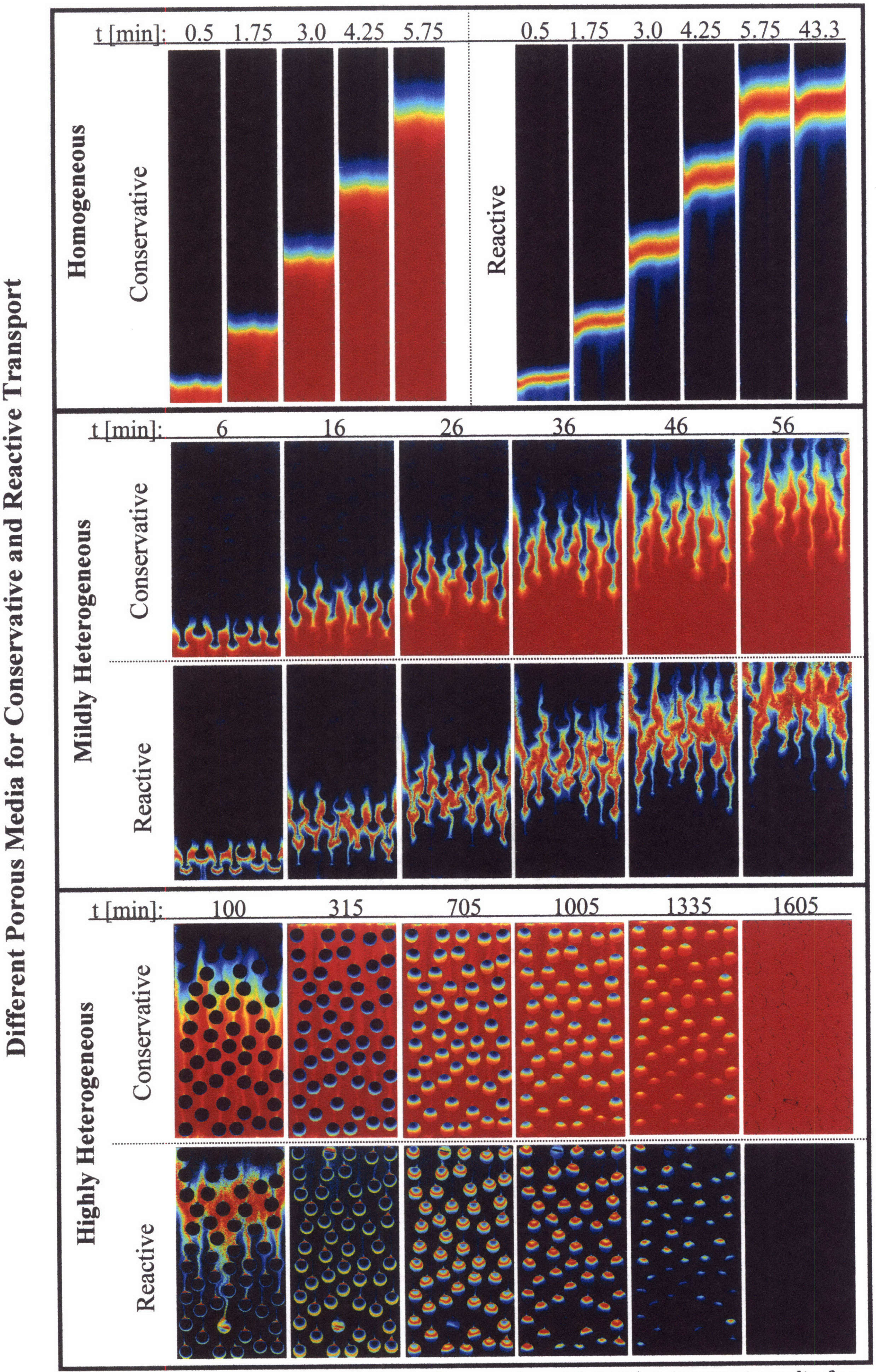

Figure 3. Flow is from top to bottom. Conservative and reactive transport results for homogeneous (mechanical-dispersion) 30 x 5 cm, mildly heterogeneous (macro-dispersion) 40 x 20 cm, and highly heterogeneous porous media (mass transfer) 40 x 20 cm.

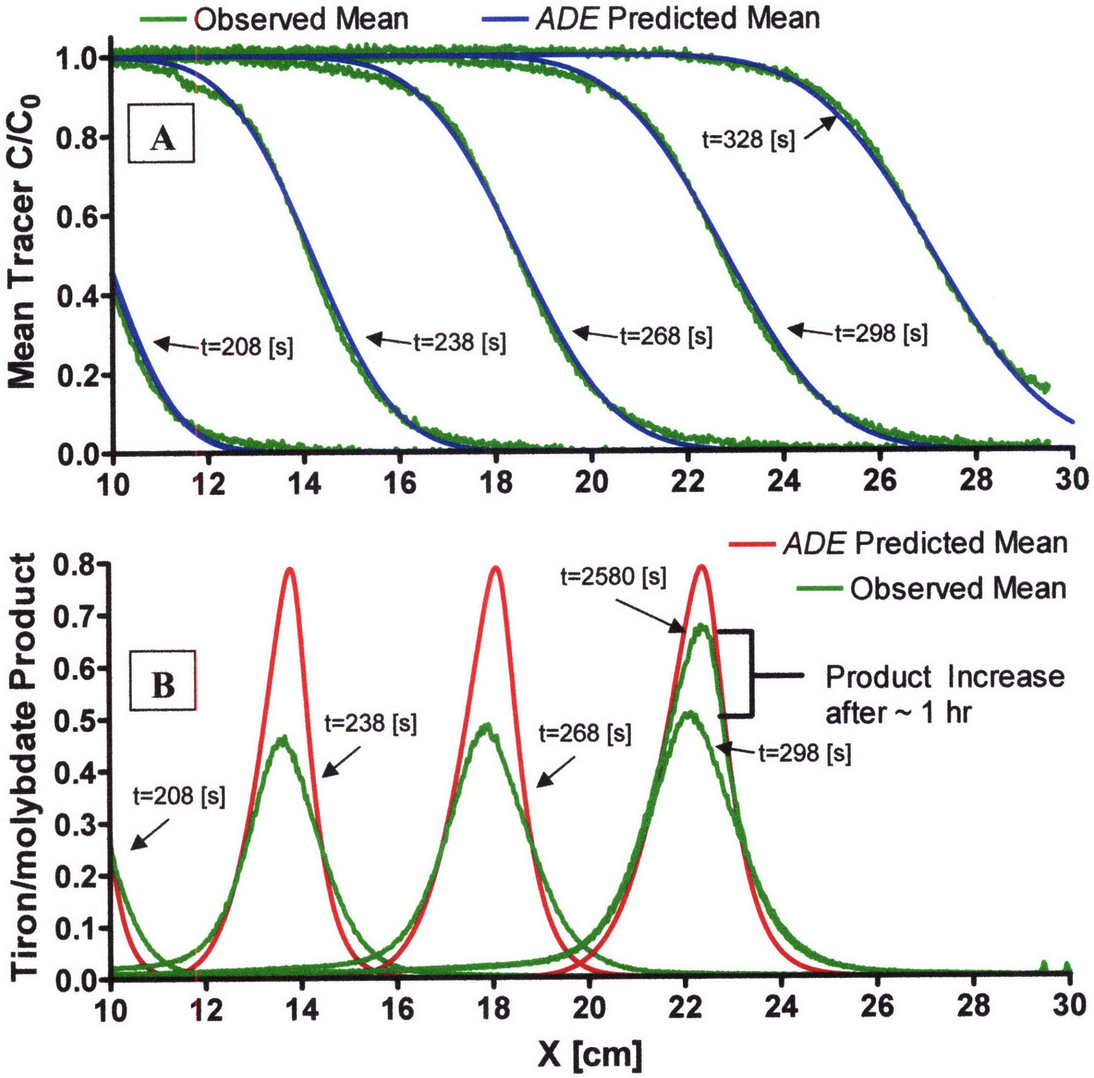

Figure 4. A) Comparison of advection-dispersion-equation (ADE) predicted mean dye concentration to the observed mean dye concentration. B) Comparison of the predicted mean product from the ADE coupled to the Tiron/molybdate reaction model to observed mean product at 208, 238, 268, 298 and 2580 seconds. Flow was stopped at 298 seconds to allow diffusion to complete the pore-scale mixing. The observed jump in product concentration is shown after 43 minutes (2580 seconds).

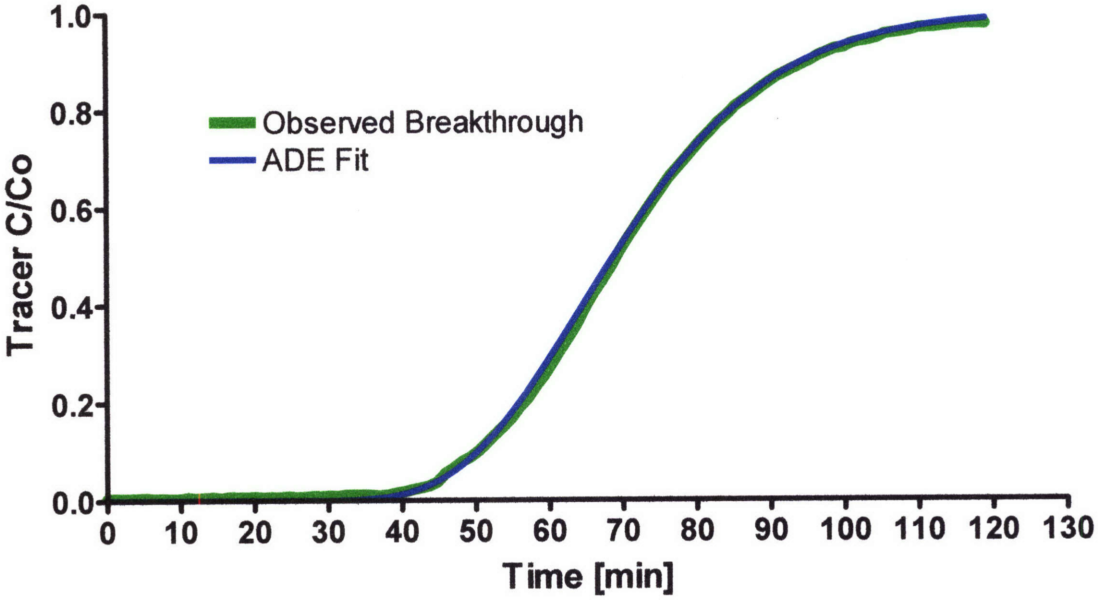

Figure 5. Concentration breakthrough curve of the mildly heterogeneous chamber modeled by the *ADE*.

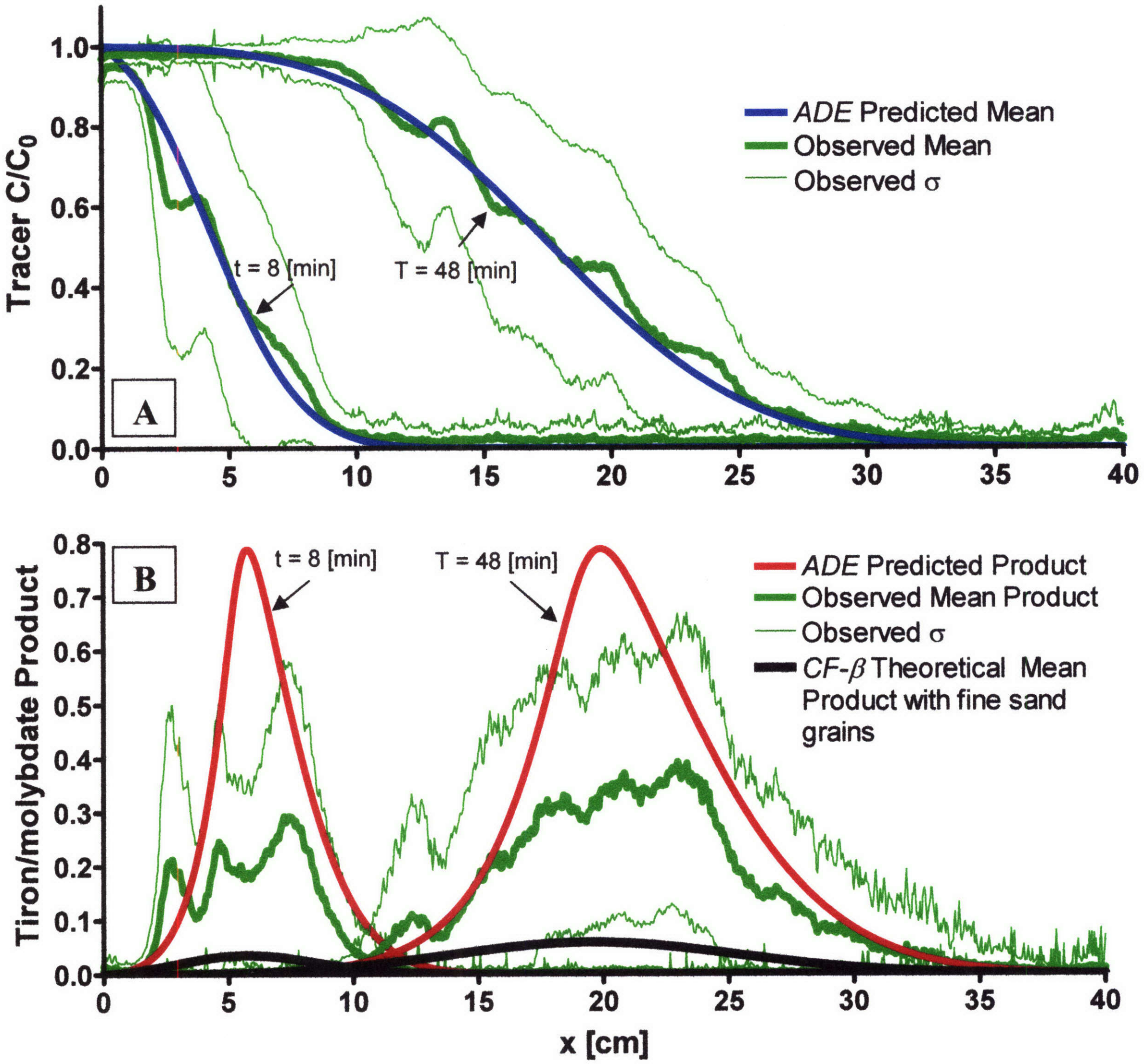

Figure 6. A) Comparison of ADE predicted mean dye concentration based the dispersion coefficient and average velocity fit from a breakthrough curve to the observed mean dye concentration shown at 8 and 46 minutes. B) Comparison of the predicted mean product from the ADE coupled to the Tiron/molybdate reaction model to observed mean product. The black line represents the theoretical mean product if the grain size and hence mechanical dispersivities in our tanks were reduced.

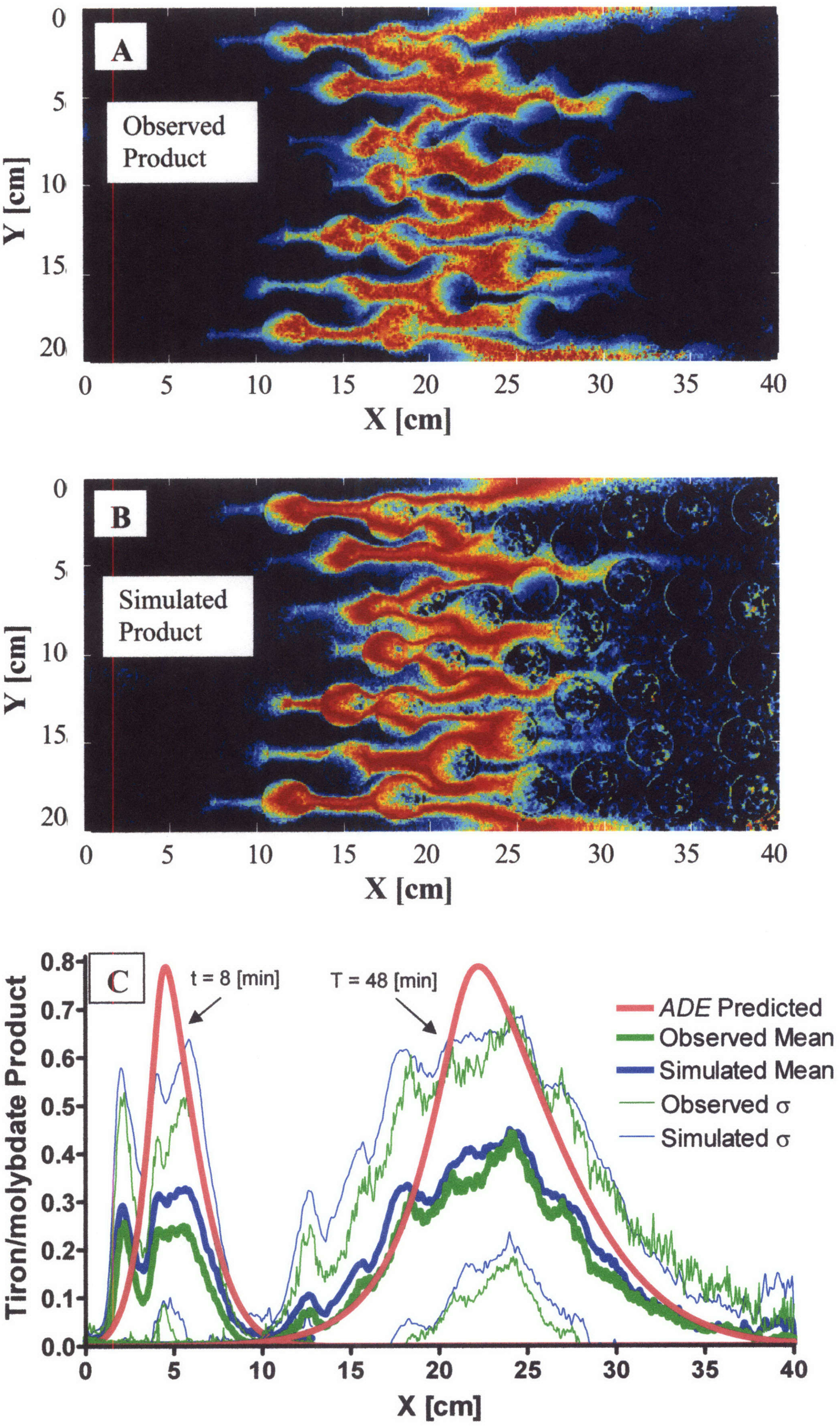

Figure 7. Assessing the importance of pore-scale mixing in the mildly heterogeneous tank by comparing A) Observed product and the B) Simulated product assuming complete pore-scale mixing at 32 minutes. C) Mean product of the ADE predicted product, observed product, simulated product for 8 and 32 minutes.

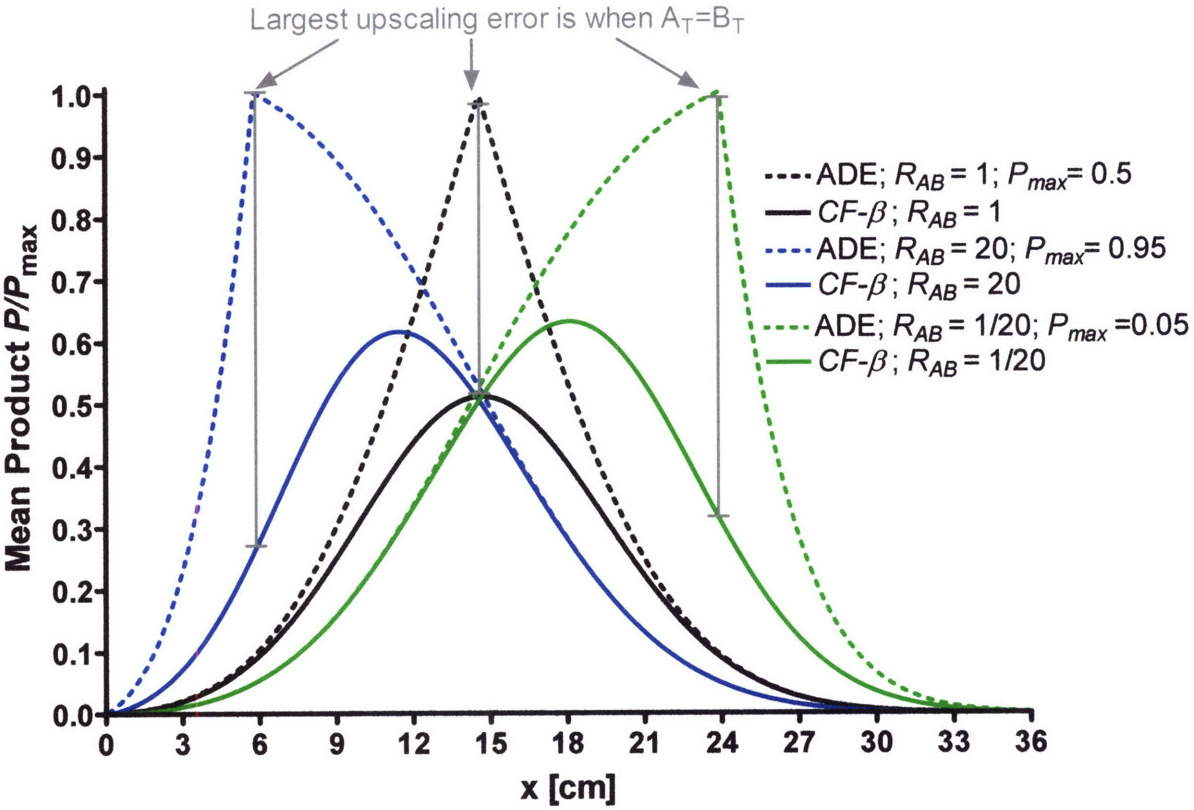

Largest upscaling error is when $A_T=B_T$

Figure 8. Effects of initial concentration difference on the ADE predicted product and mean concentration fluctuation beta *pdf* (*CF-β*) product (average of small scale product) for the $A+B\rightarrow P$ reaction.

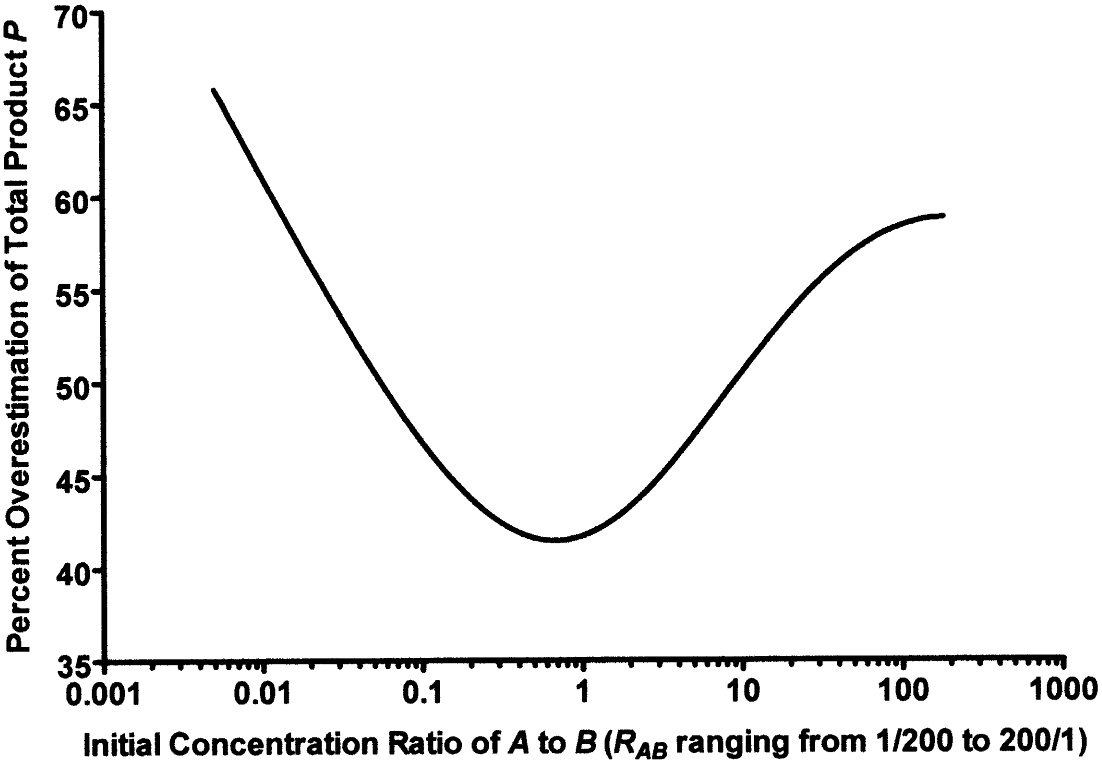

Figure 9. Percent difference in zeroth moment of *P* for the *A*+*B*→ *P* product between *ADE* predicted product and *CF-β* model as a function of different initial concentration ratios.

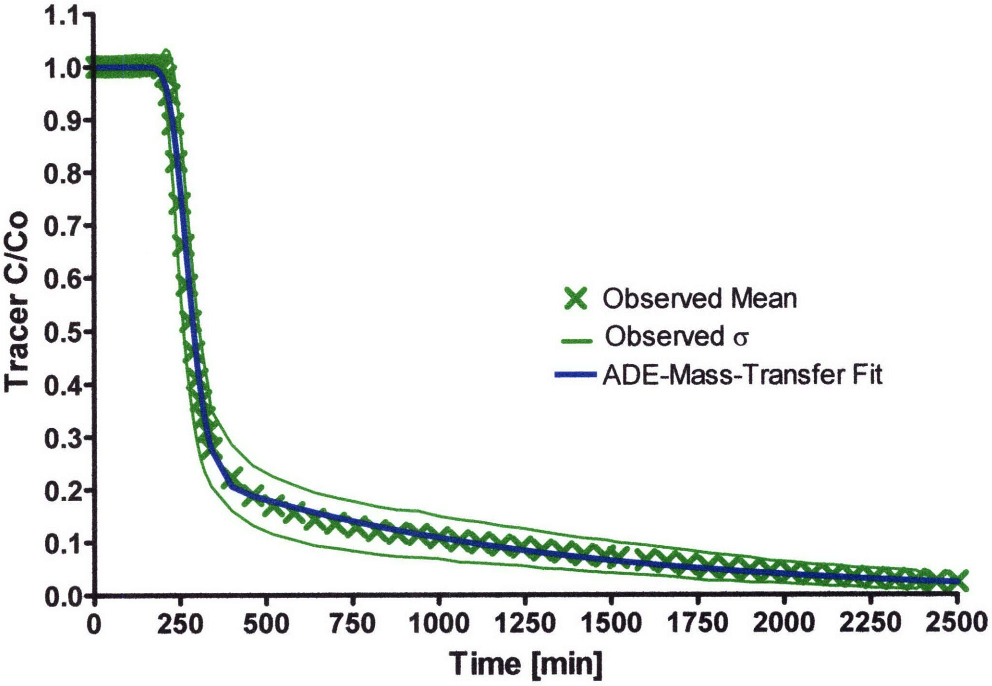

Figure 10. Breakthrough curves of conservative tracer and ADE-mass-transfer model.

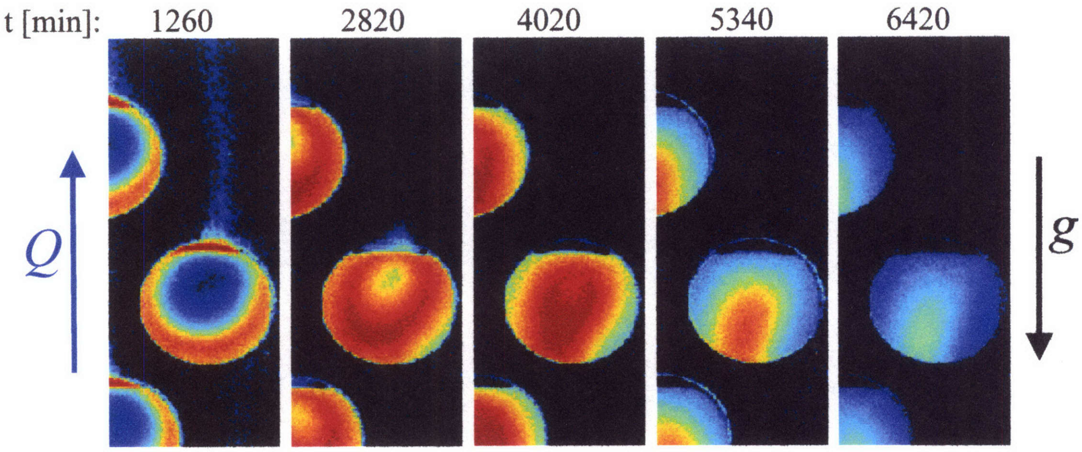

Figure 11. Observed density effects of the Tiron/molybdate reaction in the low conductivity inclusions for the highly heterogeneous chamber. Flow is upwards against gravity.

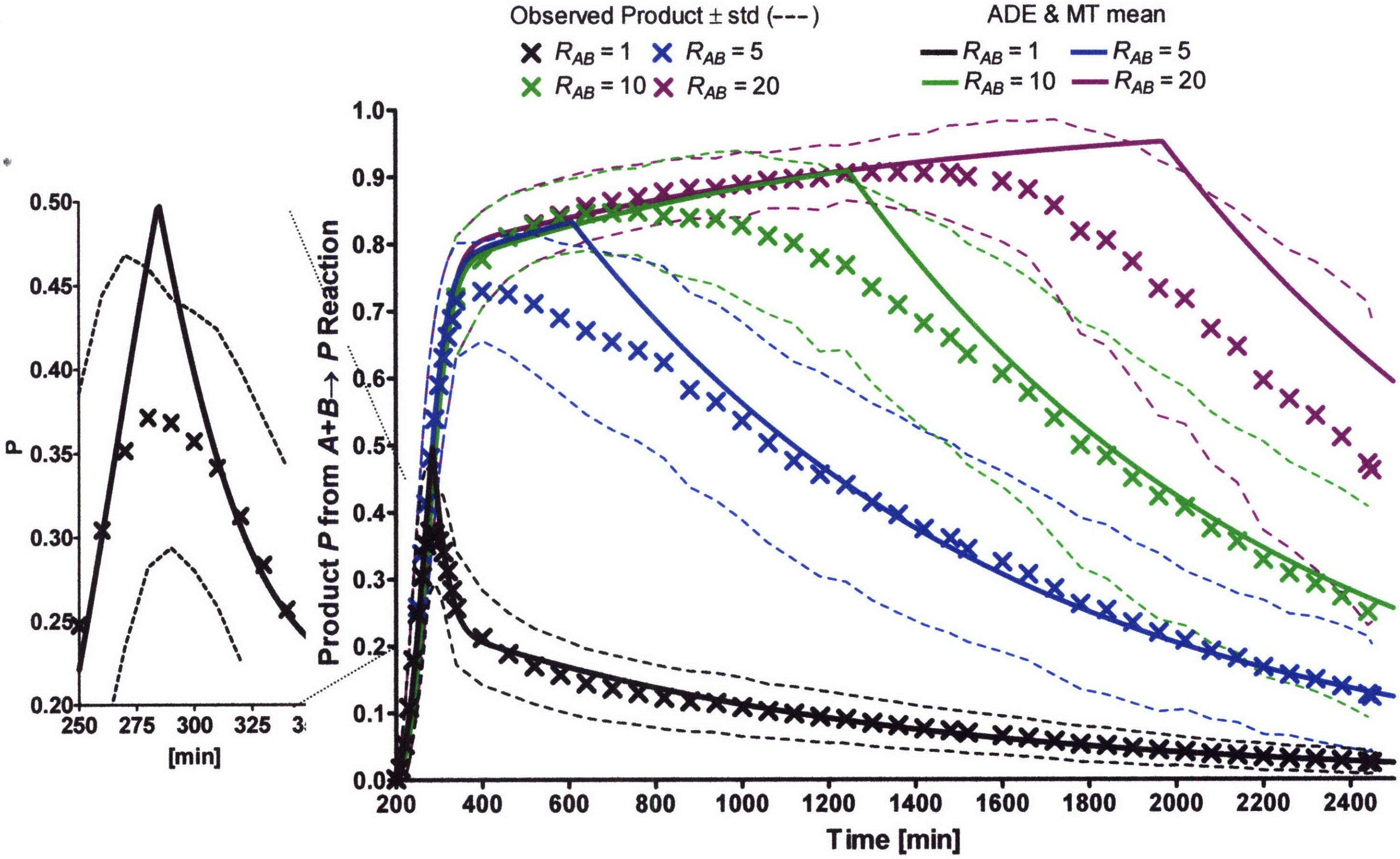

Figure 12. Observed product and ADE-mass-transfer modeled breakthrough curves. The rate-limited mass-transfer model yielded a good fit for the conservative tracer and reaction product (except for dispersion front) when initial reagent concentrations are equal. However, as the ratio of initial concentrations R_{AB} get larger problems with reaction behind the dispersive front develop.

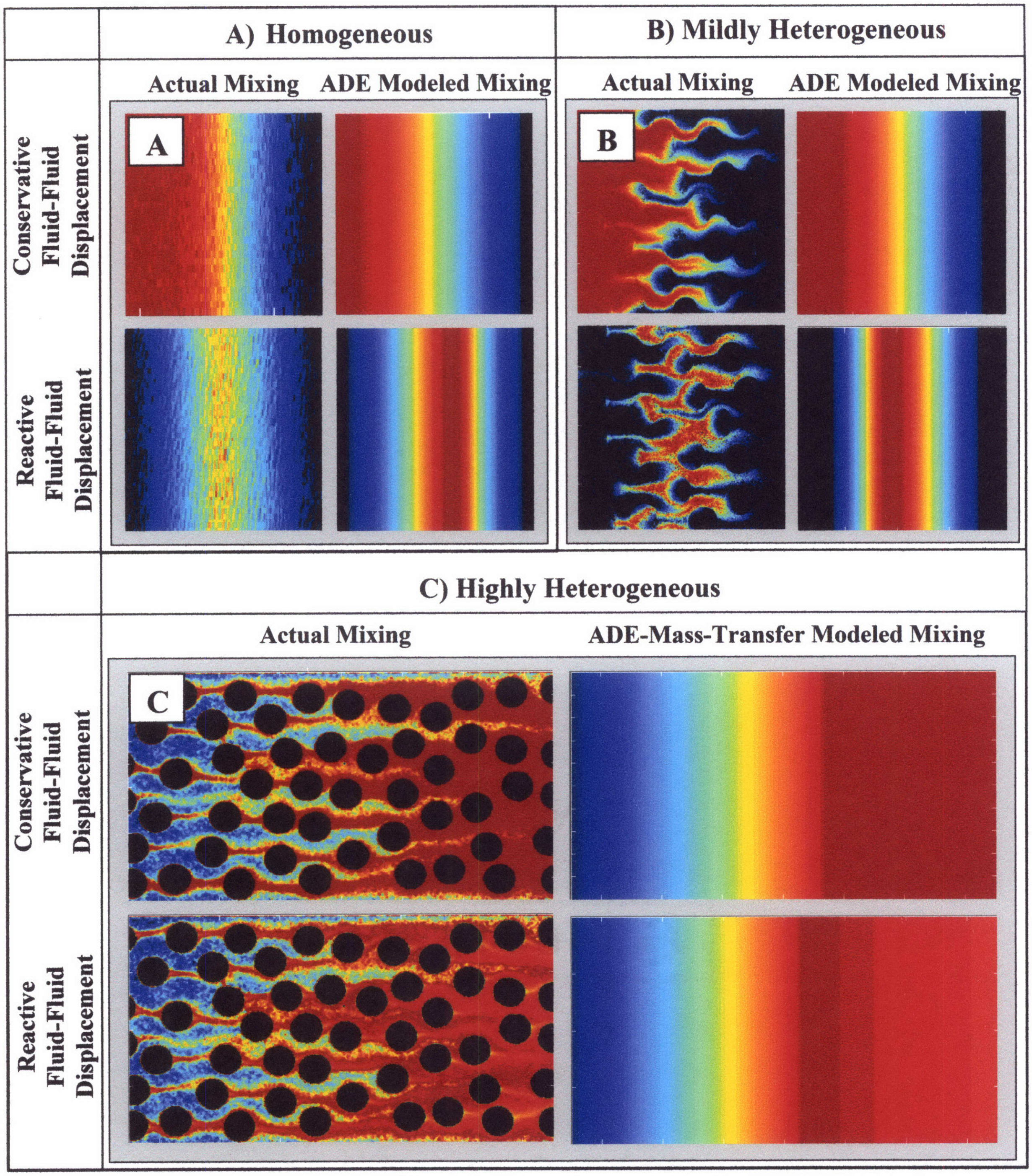

Figure 13. Top row of panels A, B, and C: experimentally observed and modeled conservative solute front for A) Homogeneous media (mechanical-dispersion) 30 x 5 cm, B) Mildly heterogeneous (macro-dispersion) 40 x 20 cm, and C) Highly-heterogeneous media (mass-transfer) 40 x 20 cm. Bottom rows of panels A, B, and C: experimentally observed and modeled reactive solute fronts (product shown in red) for A) Homogeneous media (mechanical-dispersion), B) Mildly heterogeneous (macro-dispersion), and C) Highly heterogeneous media (mass-transfer). The mass-transfer results are reactive simulations based on the conservative tracer for the $A+B\rightarrow P$ reaction; shown for $R_{AB} = 10$.

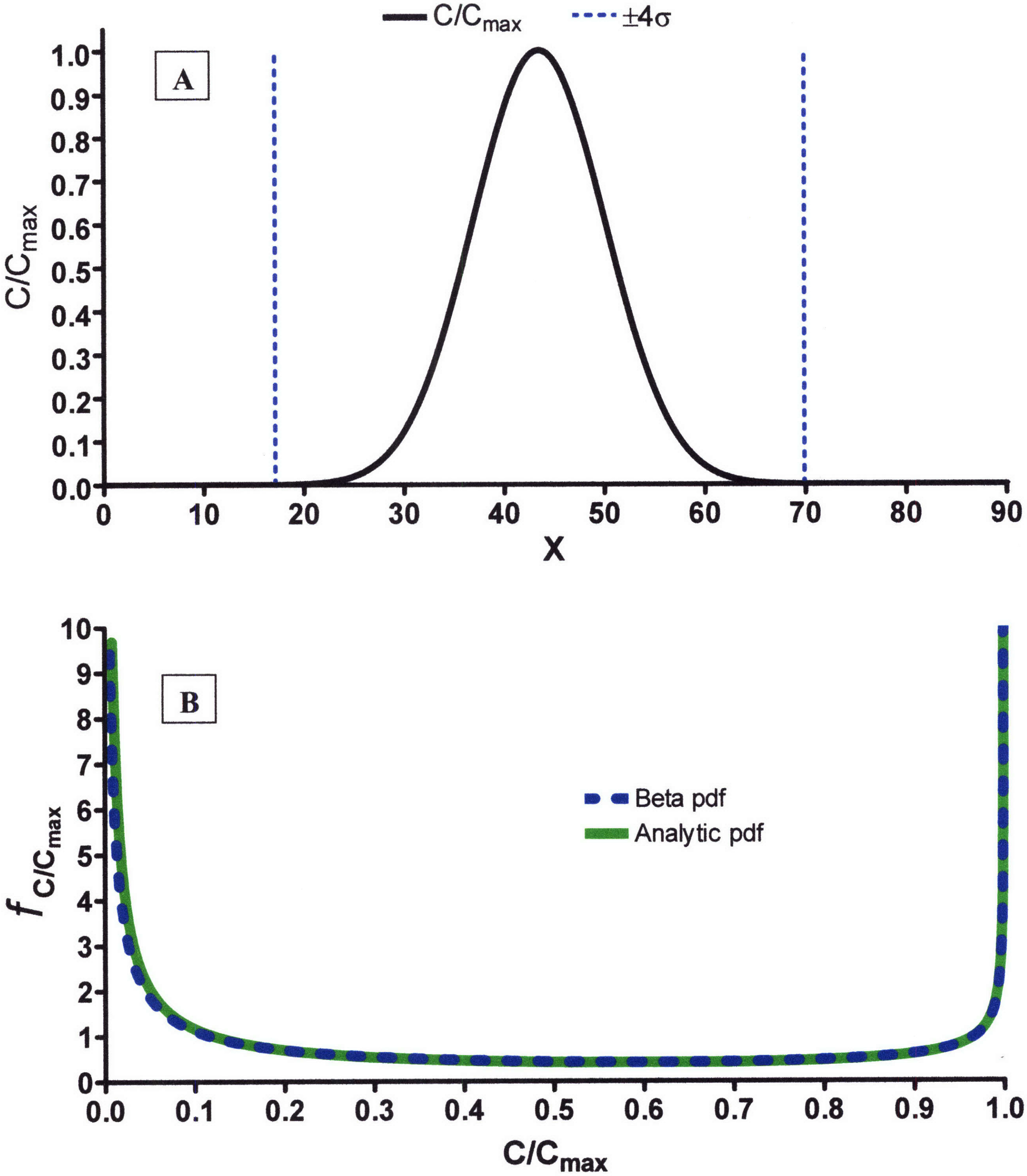

Figure 14. A) Gaussian concentration pulse normalized by maximum concentration. The dashed blue lines show domain for which the *pdf* is calculated. B) *pdf* of the concentration pulse compared to beta distribution with the same mean and variance.

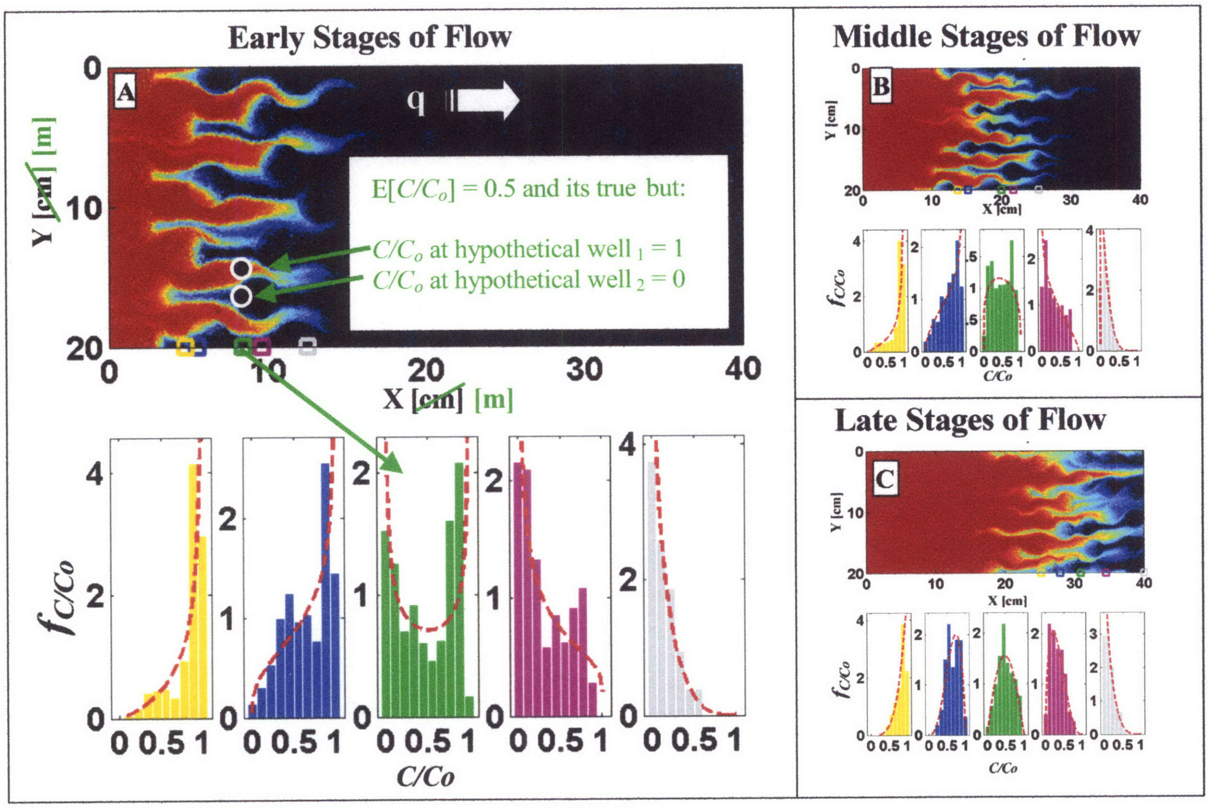

Figure 15. Observed concentration distributions for selected values of x compared to beta distributions at A) Early; B) Middle; and C) Late stages of flow. 9-A has also been hypothetically scaled (green units) to show how two well right next to each other would experience very different concentrations compared to the correctly predicted mean concentration because of lack of mixing.

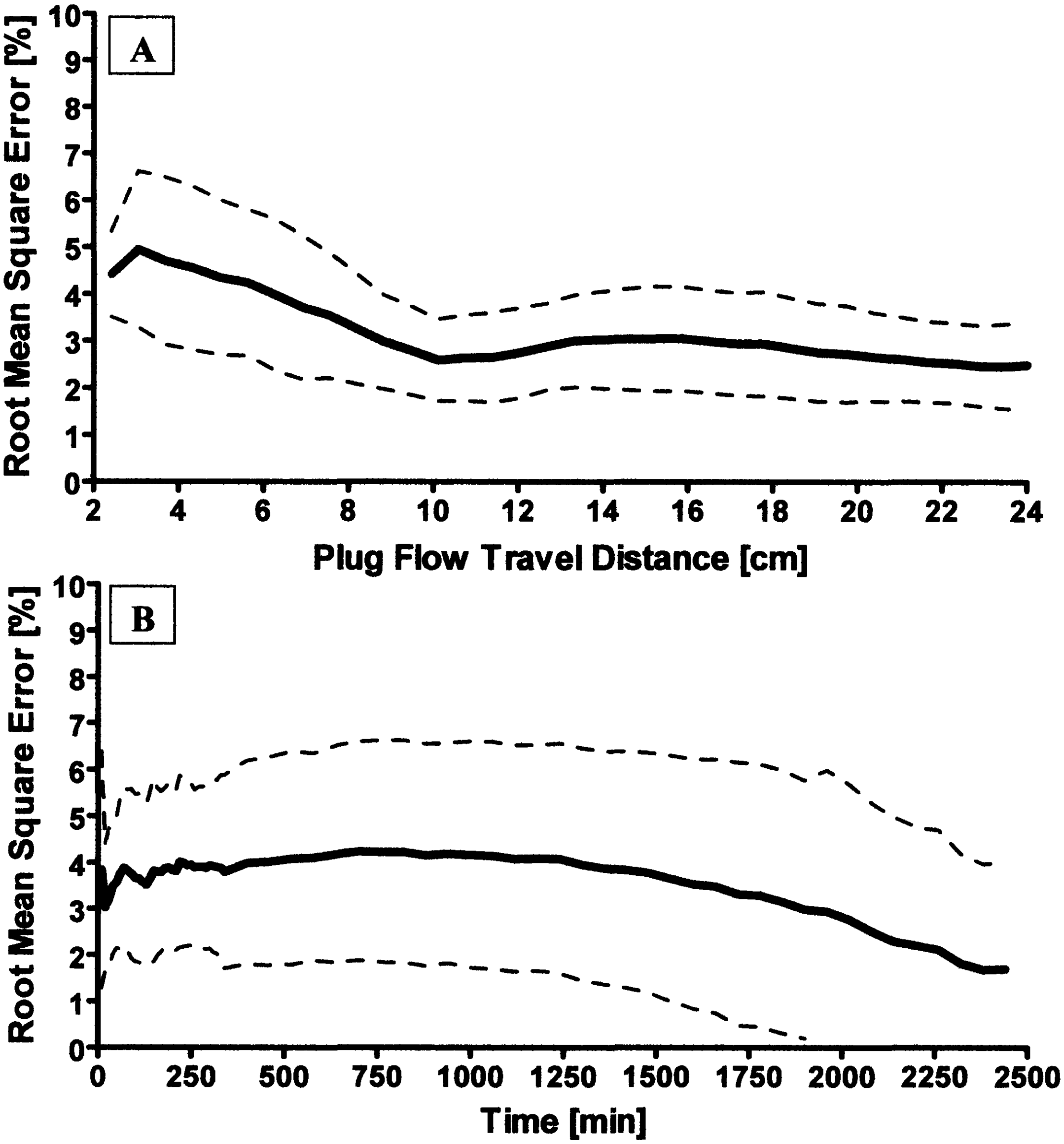

Figure 16. The average and standard deviation of the root-mean-square error between the beta *cdfs* and observed *cdfs* for A) the dispersion front in mild-heterogeneous porous media and B) the entire domain of the highly heterogeneous porous media.

Table 1. Calibration Curve Solutions.

Solution #	1	2	3	4	5	6
Tiron (M)	0.05	0.0053	0.043	0.017	0.033	0.025
Molybdate (M)	0.0	0.022	0.0033	0.016	0.0083	0.0125
A_l, at 580 nm	0.0	0.047	0.26	0.40	0.64	0.83

Table 2. A) Mean reactions not adequately modeled by mean concentrations: 1) Equilibrium reactions, 2) Rate-limited reactions higher than first order, 3) Microbial Michaelis-Menten utilization and Monod growth kinetics; 4) Freundlich and Langmuir sorption; 5) Rate-limited Freundlich and Langmuir sorption. B) Mean reactions adequately modeled by mean concentrations: 1) First-order decay; 2) Linear sorption; 3) Rate-limited linear sorption.

A) Mean Reactions Not Adequately Modeled by Mean Concentrations	B) Mean Reactions Adequately Modeled by Mean Concentrations
1) $aA + bB \rightleftharpoons cC + dD;\ K = \frac{[A]^a [B]^b}{[C]^c [D]^d}$ 2) $\frac{\partial C_N}{\partial t} = -\kappa \prod_{N>1} [C_N]^c$ 3) $\frac{\partial C_N}{\partial t} = -\prod_N \left(\frac{C_N}{K_{S,N} + C_N} \right) \mu_{\max}$ 4) $S = K_f C^n;\ S = \frac{k_1 k_2 C}{1 + k_1 C}$ 5) $\frac{\partial S}{\partial t} = \alpha \left(K_f C^n - S \right);\ \frac{\partial S}{\partial t} = \alpha \left(\frac{k_1 k_2 C}{1 + k_1 C} - S \right)$	1) $\frac{\partial C}{\partial t} = -\kappa C$ 2) $S = K_d C$ 3) $\frac{\partial S}{\partial t} = \alpha \left(K_d C - S \right)$

Chapter 4. Development and Experimental Validation of the Concentration Fluctuation Beta-*pdf* (*CF-β*) Model

Mixing-controlled non-linear reactions in porous media can be accurately upscaled by modeling concentration means and variances and assuming that reactants can be described by joint Beta distributions. This approach is verified for mildly heterogeneous media by modeling the product and reactant means, variances, and distributions from the experiments of Chapter 3 and for homogeneous media by modeling the product means from the experiments of Chapter 3, Gramling *et al.* (2002), and Raje and Kapoor (2000). This reactive transport approach works without maps of hydraulic conductivity fields or pore-structures but requires experimental calibration to determine the variance-length scale, a length scale that characterizes variance destruction and reactive mixing.

4.1. Introduction.

The ideal approach for modeling reactive transport in porous media would fully resolve heterogeneity at all scales, fully resolve the velocity field, and then use advection-diffusion equations coupled to a chemical reaction models to account for transport and reaction. Even if this were computationally possible, heterogeneity will likely never be fully resolved at a field site. As such, we must resort to upscaled modeling approaches that can capture the effects of heterogeneity without actually having to resolve heterogeneity. This can be done by viewing concentrations as random variables and taking spatial averages to yield mean or expected concentration values.

In stationary porous media with small log-conductivity fluctuations, macro-dispersion theory can accurately predict the spreading of mean conservative concentrations, but it overestimates mixing and reaction. To reduce the macro-dispersion predicted mixing, it is possible to choose a smaller dispersion coefficient that predicts the correct total amount of product formation, but reducing dispersivity still overestimates the peak concentration, underestimates spreading (Cirpka, 2002; Cirpka and Nowak, 2003), and will not capture the observed product variability (figure 1).

Figure 1.

More sophisticated approaches are needed to predict the space-time evolution of reactive flows in porous media. The crux of the upscaling challenge is that spatial averages have to be taken to approximate the average amount of the chemical reaction because heterogeneity cannot be resolved. The expected value, denoted by the over-bar, of chemical reaction, $\overline{r(C_1, C_2, \ldots C_n)}$, is only equal to chemical reaction based on the mean concentrations provided by macro-dispersion theory, $r\left(\overline{C_1}, \overline{C_2}, \ldots \overline{C_n}\right)$, under first-order decay and linear sorption. A different but related issue is that regulations are based on maximum contaminant levels (MCLs) and conventional transport models only provide average concentration values, and incorrectly when concentrations undergo non-linear reactions. A solute transport modeling framework is needed that addresses both the correct amount of chemical reaction and maximum contaminant levels.

Both Lagrangian and Eulerian approaches have been applied to upscale reactive transport. Lagrangian-based stream-tube models have been developed to predict reactive breakthrough curves such as the stochastic-convective-reactive transport model (Simmons *et al.*, 1995). Stream-tube models use a conservative tracer breakthrough curve to generate a residence-time distribution and then approximate mixing and reaction based on residence-times. This approach has been successfully applied to multi-component reactive transport situations (Ginn, 2001; Ginn *et al.*, 2001), but it only serves as a lower bound on the amount of mixing as it assumes flow in layered parallel media with different hydraulic conductivities (Cirpka and Kitanidis, 2000; Robinson and Viswanathan, 2003). A major limitation of this approach is it does not allow for local dispersion, which is what controls mixing and reaction for equally sorbing solutes. Ginn (2001) expanded the stream-tube approach to allow longitudinal dispersive mixing in individual stream-tubes but not transverse mixing between stream-tubes, which can be the dominant component of mixing (Cirpka *et al.*, 1999). A conceptual problem with stream-tube approaches is that the full space-time evolution of small-scale mixing cannot be captured from a single breakthrough curve of a conservative tracer. Robinson and

Viswanathan (2003) state that this approach can only treat mixing as a “black box" to be bounded. They were able to place an upper bound on the amount of mixing but only by using unrealistic conductivity fields.

Cirpka and Kitanidis (2000) propose that many conservative tracer breakthrough curves taken along the stream tubes can yield information about the evolution of transverse and longitudinal mixing, which is captured by apparent-dispersion coefficients. Apparent-dispersion coefficients essentially parameterize transverse exchange between independent stream-tubes as enhanced longitudinal dispersion within a stream tube. Measuring apparent dispersion coefficients at a field site requires a large number of point-source breakthrough curves (Jose and Cirpka, 2004; Jose *et al.*, 2004), which may not be feasible to measure in realistic field situations. The average apparent dispersion coefficients can be modeled as effective dispersion, which is the average dispersion coefficient for point-like injections (Dentz *et al.*, 2000; Cirpka, 2002; Jose and Cirpka, 2004; Jose *et al.*, 2004). Effective dispersion coefficients have been derived for specific conductivity statistics (Dentz *et al.*, 2000) and have shown good predictive abilities for reactive transport scenarios influenced by both mechanical-dispersion and differential sorption (Janssen *et al.*, 2006). However, studies have shown that apparent dispersion coefficients are highly variable. The numerical results of Cirpka and Kitanidas (2000) reported a coefficient of variation of 0.55 for apparent dispersion and the experimental results of Jose *et al.* (2004) reported apparent dispersion coefficients ranging from 1.8×10^{-7} to 3.4×10^{-5} m^2/s. This raises the question: is replacing such variable mixing rates with an average valid? Variable mixing rates will generate variable concentrations of reactants and since reactions can be non-linear, the average of all reactions can be substantially different then a reaction based on the average mixing. This is essentially the upscaling problem.

Eulerian analysis has yielded analytical results for bioreactive transport (Miralles-Wilhelm *et al.*, 1997; Miralles-Wilhelm and Gelhar, 2000), but the results are not applicable for dispersion-controlled mixing (Ginn, 1998). Kapoor *et al.* (1997) analyzed a generic bimolecular reaction using an Eulerian perturbation approach and focused on the cross-covariance term, which is difficult to determine. Furthermore, a perturbation analysis could prove extremely complex for complicated chemical reactions. For example, the chemical products for the Tiron/molybdate reaction (Oates and Harvey, 2006) have dozens of very non-linear terms such as: $\left(\sqrt{K_1\left(2Mo_T - Ti_T^{\,2}\right)^3 Ti_T} + K_2 Mo_T Ti_T\right)^{1/3}$, where Ti_T is the concentration of total Tiron, Mo_T is the concentration of total molybdate, and K_1 and K_2 are constants. If Ti_T and Mo_T were decomposed into a mean and perturbation, the terms were expanded, and expected value was taken, the solution could become extremely complicated and require knowledge of high-order moments. This means that applying a perturbation approach for complicated reactions may not be feasible. Complex chemical reaction models, valid at the lab-scale, need to be readily applicable to field scale reactive transport models.

In this paper, we present a new approach to upscaling reactive transport in porous media that models concentration mean and variance and assumes that mixed reactants can be modeled with a joint distribution with Beta marginal probability density functions (*pdfs*). First, we briefly review the derivation of the conservative mean and variance equations and discuss how to apply a mixing line to transform an assumed Beta *pdf* of a conservative tracer into a joint distribution of reactants. Next, we show that this approach can successfully model the space-time evolution of the means, variances, and distributions of both reactive and conservative concentrations observed in the heterogeneous experiments of Chapter 3 and finally, the product means from the homogeneous experiments of Chapter 3, Gramling *et al.* (2002), and Raje and Kapoor (2000).

4.2. Concentration Fluctuation Beta-*pdf* (*CF-β*) Model for Reactive Transport in Mildly Heterogeneous Media.

4.2.1 Conservative concentration mean and variance.

We used the advection-dispersion equation (*ADE*) for conservative mean concentrations and an equation for conservative concentration variances from the work of Kapoor and Gelhar (1994a) based on Eulerian linear stochastic theory. A Lagrangian concentration variance approach (*e.g.* Dagan and Fiori, 1997; Pannone and Kitanidis, 1999; Fiori and Dagan, 2000; Fiori, 2001; Fiori, 2003; Pannone and Kitanidis, 2004) could have been implemented, but we found it more convenient to work with equations that could be solved by conventional finite-difference techniques. Kapoor and Gelhar (1994a) applied Eulerian stochastic theory to obtain the governing differential equations for the mean and variance of a conservative tracer in heterogeneous porous media. Starting with the small-scale advection-mechanical-dispersion equation:

$$\frac{\partial C}{\partial t} = -\frac{\partial v_i C}{\partial x_i} + d_{ij}\frac{\partial^2 C}{\partial x_i \partial x_j} \tag{1}$$

where summation over repeated indexes is implied. Concentration C and velocity v are treated as random variables that can be decomposed into a mean and a zero mean fluctuation (Gelhar and Axness, 1983):

$$C = \overline{C} + c'; \qquad v = \overline{v} + v'_i \tag{2}$$

In this treatment, the diagonal mechanical dispersion tensor d_{ij} is assumed constant and to depend only on the mean velocity (e.g. Kapoor and Gelhar, 1994a; Dagan and Fiori, 1997). Substituting equation 2 into equation 1 and taking expectation denoted by the over-bar $\left(\mathrm{E}\left[C\right] = \overline{C}\right)$ yields the equation governing the mean concentration with flow aligned in the x_1 direction:

$$\frac{\partial \overline{C}}{\partial t} = -\overline{v}\frac{\partial \overline{C}}{\partial x_1} - \frac{\partial \overline{v'_i c'}}{\partial x_i} + d_{ij}\frac{\partial^2 \overline{C}}{\partial x_i \partial x_j} \tag{3}$$

Equation 3 is subtracted from the result of equation 2 substituted into equation 1 to yield the governing equation of a concentration perturbation. The governing equation for a concentration perturbation is multiplied through by another concentration perturbation, and taking expectation $\left(\mathrm{E}\left[(c')^2\right] = \sigma_C^2\right)$ yields the budget for concentration variance:

$$\frac{\partial \sigma_C^2}{\partial t} = -\overline{v}\frac{\partial \sigma_C^2}{\partial x_1} - \frac{\partial\left(\overline{v_i'(c')^2}\right)}{\partial x_i} + d_{ij}\frac{\partial^2 \sigma_C^2}{\partial x_i \partial x_j} - 2\overline{c'v_i'}\frac{\partial \overline{C}}{\partial x_i} - 2d_{ij}\overline{\frac{\partial c'}{\partial x_i}\frac{\partial c'}{\partial x_j}} \tag{4}$$

Assuming the heterogeneous porous medium is stationary with small log conductivity fluctuations, Kapoor and Gelhar (1994a) adopted the following closure approximations:

$$\overline{c'v_i'} = -\overline{v}A_{ij}\frac{\partial \overline{C}}{\partial x_j}; \qquad \left(\overline{v_i'(c')^2}\right) = -\overline{v}A_{ij}\frac{\partial \sigma_C^2}{\partial x_j}; \qquad 2d_{ij}\overline{\frac{\partial c'}{\partial x_i}\frac{\partial c'}{\partial x_j}} = \chi\sigma_C^2 \tag{5}$$

The first two terms are macro-dispersion closure approximations, which have been addressed in the literature. The last closure term of the equations in 5 is for variance destruction. The key to this term is approximating mean perturbation derivatives in terms of concentration variance. For 2-D flow and transport, which assumes no conductivity variations in the *z* direction as is true for our tanks, the perturbation derivatives can be approximated by introducing concentration micro-scales (Tennekes and Lumley, 1972):

$$\left(\Delta_L^C\right)^2 = \frac{\sigma_C^2}{\overline{\left(\partial c'/\partial L\right)^2}}; \quad \left(\Delta_T^C\right)^2 = \frac{\sigma_C^2}{\overline{\left(\partial c'/\partial T\right)^2}} \qquad (6)$$

where and Δ_L^C is the longitudinal micro-scale, Δ_T^C is the transverse micro-scale, *L* is the longitudinal direction, and *T* is the transverse direction. The micro-scales are length scales that characterize the small-scale separation behavior of a statistically stationary concentration perturbation covariance function (Kapoor and Gelhar, 1994a).

Perhaps a more intuitive approach to understanding concentration micro-scales can be gained by taking the square root of the equations in 6 and rearranging terms to show:

$$\overline{\left|\frac{\partial c'}{\partial L}\right|} = \frac{\sigma_C}{\Delta_L^C}; \qquad \overline{\left|\frac{\partial c'}{\partial T}\right|} = \frac{\sigma_C}{\Delta_T^C}; \qquad (7)$$

that the average perturbation derivatives are approximated as rise divided by run, where the rise is given by the standard deviation and the run is the micro-scale (figure 2).

Figure 2.

Consider a theoretical case where a concentration profile varies in a macro-dispersion front as a function of the transverse direction T and has the form of an arbitrary periodic function:

$$C = A * Cos\left(\frac{T}{\lambda}\right) + B \tag{8}$$

The mean of this function is found by taking expectation with a dummy variable ξ of integration:

$$\overline{C} = \frac{1}{T}\int_0^T \left(A * Cos\left(\frac{\xi}{\lambda}\right) + B\right) d\xi = \frac{BT + A\lambda Sin\left(\frac{T}{\lambda}\right)}{T} \approx B \tag{9}$$

For large T, the mean may be approximated as B. Subtracting B from equation 8 for large T, yields a perturbation and the expected value of a perturbation squared is the variance:

$$\sigma_C^2 = \frac{1}{T}\int_0^T \left(A * Cos\left(\frac{\xi}{\lambda}\right)\right)^2 d\xi = \frac{A^2\left(\frac{T}{2} + \frac{1}{4}\lambda Sin\left(\frac{2T}{\lambda}\right)\right)}{T} \approx \frac{A^2}{2} \tag{10}$$

The expected value of the squared perturbation derivatives is:

$$\overline{\left(\frac{\partial c'}{\partial T}\right)^2} = \frac{1}{T}\int_0^T \left(\left(\frac{\partial}{\partial \xi}\left(A * Cos\left(\frac{\xi}{\lambda}\right)\right)\right)^2\right) d\xi = \frac{A^2\left(\frac{T}{2} - \frac{1}{4}\lambda Sin\left(\frac{2T}{\lambda}\right)\right)}{\lambda^2 T} \approx \frac{A^2}{\lambda^2 2} \tag{11}$$

Therefore, according to equation 6, dividing equation 10 by equation 11, the transverse concentration micro-scale is equal to λ:

$$\Delta_T^C = \lambda \tag{12}$$

and most importantly has no relation to the amplitude of the periodic function. This shows that the amplitude of concentrations does not affect the concentration micro-scales because the variance changes proportional to the perturbation derivatives. The micro-scale is determined by the wavelength of the concentration profile which would be determined solely by the flow structure. For these reasons, the micro-scales do not vary much over the plume (Kapoor and Kitanidas, 1998; and we also verify this in section 3.1), which justifies using average longitudinal and transverse values. Furthermore, the length-scale that approximates the perturbation derivative where concentrations go from maximum to minimum is one-half the period of a Cosine function is given as $\lambda\pi$. This means the length scale that transverse dispersion has to mix over to destroy variance is characterized by a micro-scale that's a factor of π smaller. The micro-scale is always going to be smaller then the length-scale characterizing the distance it takes for concentrations to go from minimum to maximum because the standard deviation is always smaller than maximum minus minimum.

The variance destruction term can be rewritten in terms of micro-scales and variance (shown for 2-D):

$$2d_L\overline{\left(\frac{\partial c'}{\partial L}\right)^2} + 2d_T\overline{\left(\frac{\partial c'}{\partial T}\right)^2} = \left(\frac{2d_L}{\left(\Delta_L^C\right)^2} + \frac{2d_T}{\left(\Delta_T^C\right)^2}\right)\sigma_C^2 = \chi\sigma_C^2 \tag{13a}$$

$$\chi = \left(\frac{2d_L}{\left(\Delta_L^C\right)^2} + \frac{2d_T}{\left(\Delta_T^C\right)^2}\right) \tag{13b}$$

where d_L and d_T are the longitudinal and transverse mechanical-dispersion and χ is the first order variance decay term.

Essentially, χ is a mixing-rate, which implies mixing occurs at the rate that mechanical dispersion destroys concentration fluctuations over length-scales that characterize their spatial derivatives. The reciprocal of χ is called the "variance residence time" or *VRT*, and it is a characteristic time over which local dispersion destroys concentration variance. *VRT* asymptotically increases like macro-dispersion, albeit more slowly, until the micro-scales reach asymptotic values (Kapoor and Kitanidas, 1998). Temporally increasing VRT_t and hence χ_t as can be modeled as:

$$VRT_t = VRT_\infty(1 - e^{-\kappa_\chi t}); \qquad \chi_t = \frac{\chi_\infty}{(1 - e^{-\kappa_\chi t})} \tag{15}$$

where κ_χ is the rate at which the concentration micro-scales approach their asymptotic value and VRT_∞ and χ_∞ are the respective asymptotic values. This approach is able to reproduce the early time variance destruction behavior observed in Kapoor and Kitanidas (1998) (figure 3).

Figure 3.

Since local dispersion is assumed to depend on the mean velocity, we can simply factor out the mean velocity from the variance destruction term to group the unknowns into a single unknown we call the variance length scale χ_L:

$$\chi = \frac{2d_L}{(\Delta_L^C)^2} + \frac{2d_T}{(\Delta_T^C)^2} = \frac{2\bar{v}a_L}{(\Delta_L^C)^2} + \frac{2\bar{v}a_T}{(\Delta_T^C)^2} = \bar{v}\left(\frac{2a_L}{(\Delta_L^C)^2} + \frac{2a_T}{(\Delta_T^C)^2}\right) = \frac{\bar{v}}{\chi_L} \tag{16}$$

where a_L is the longitudinal mechanical-dispersivity and a_T is the transverse mechanical-dispersivity. Analogous to the *VRT*, χ_L can be thought of a characteristic distance a plume has to travel to destroy variance. We also assume that the rate at which χ_L approaches its asymptotic value should be proportional to how much of the porous medium the plume has experienced, which is in term proportional to the mean velocity such that:

$$\kappa_{\chi} = \frac{\bar{v}}{\chi_G} \tag{17}$$

where χ_G is the variance growth-scale and can be thought of a characteristic length that a plume has to travel in order to reach the asymptotic variance destruction rate or χ_L.

Making the appropriate substitutions allows us to rewrite the mean and variance equations in terms of length-scales and mean velocity (shown in 1-D as they will be used to model the 1-D mean transport in our tanks):

$$\frac{\partial \bar{C}}{\partial t} = -\bar{v}\frac{\partial \bar{C}}{\partial x} + \bar{v}A_x \frac{\partial^2 \bar{C}}{\partial x^2} \tag{18}$$

$$\frac{\partial \sigma_C^2}{\partial t} = -\bar{v}\frac{\partial \sigma_C^2}{\partial x} + \bar{v}A_x \frac{\partial^2 \sigma_C^2}{\partial x^2} + 2\bar{v}A_x \left(\frac{\partial \bar{C}}{\partial x}\right)^2 - \frac{\bar{v}}{\chi_L}\sigma_C^2 \tag{19}$$

Remembering that if early time behavior is of interest then:

$$\chi_{L,t} = \chi_{L,\infty}\left(1 - e^{-(\bar{v}t)/\chi_G}\right) \tag{20}$$

The equation for conservative mean concentration is the advection-dispersion equation with macro- instead of mechanical-dispersion. Concentration variance is advected and dispersed like the mean concentration, but it is also produced by macro-dispersion, and destroyed by mechanical-dispersion. It should be noted that the over-bar on the mean concentration is typically dropped. Dropping the over-bar means that the predicted concentrations are the only concentrations, i.e. there is zero variance, and these predicted concentrations can therefore be directly used in chemical reaction models. However, the over-bar means that these concentrations are spatial averages and not the small-scale concentrations that actually drive biogeochemical reactions. This could be why the upscaling problem has persisted in reactive transport modeling.

Variance production and destruction is directly analogous to reactive mixing. Essentially, macro-dispersion creates concentration variance and chemical segregation, but it enhances fluid-fluid interfaces and creates steep concentration gradients for mechanical-dispersion to create variance destruction and mixing. Mixing results in chemical reaction (Roshko, 1976). Now that the equations for conservative concentration mean and variance have been covered, we will assume conservative probability distributions and transform them into joint reactant distributions.

4.2.2 Transforming conservative Beta distributions into joint reactant distributions with a mixing line.

Recall in Chapter 3 we showed that conservative concentration distributions that are normalized by the maximum concentration are well approximated by Beta distributions:

$$f_{C/Co} = \frac{\Gamma(a+b)}{\Gamma(a)\Gamma(b)}(C/C_O)^{a-1}(1-C/C_O)^{b-1} \tag{21}$$

where $f_{C/Co}$ is the probability density function, Γ is the gamma function, and a and b are shape parameters calculated from the normalized concentration mean $\overline{C/C_O}$ and variance σ^2_{C/C_O}:

$$a = \overline{C/C_O}\left(\frac{\overline{C/C_O}\left(1-\overline{C/C_O}\right)}{\sigma^2_{C/C_O}}-1\right); \qquad b = \left(1-\overline{C/C_O}\right)\left(\frac{\overline{C/C_O}\left(1-\overline{C/C_O}\right)}{\sigma^2_{C/C_O}}-1\right) \tag{22}$$

The continuous distribution can be approximated as discrete to make calculations easier using a large number of discrete of c/c_o values with small grid spacing $\Delta c/c_o$:

$$P(C/C_o = c/c_o) \approx f_{C/Co} \Delta c/c_o \tag{23}$$

The essential jump from conservative concentration distributions to joint reactant distributions is applying a mixing line. Recall that the total amount of Tiron and molybdate or the total amount of A and B for the $A + B \rightarrow P$ reaction (Chapter 3) behave as conservative quantities. As long as nothing sorbs, a mixing line can be applied for any arbitrary value of a conservative quantity $C_1/C_{1,O}$ in a Beta distribution to calculate a corresponding conservative $C_2/C_{2,O}$ value. These two mixed concentrations have the same discrete Beta probability as $C_1/C_{1,O}$. Next, the reactant pairs are unormalized, run through a chemical reaction model that can be arbitrarily complex and non-linear, and the formed product and remaining reactants retain the original discrete Beta probability of $C_1/C_{1,O}$. This calculation is performed across the entire mixing line weighted by the Beta probabilities to generate a new product and remaining reactant distributions, which can then be integrated to calculate product and remaining reactant means and variances.

Forming joint distributions with Beta distributions and a mixing line creates joint distributions with perfect negative correlation. Consider two normalized concentrations C_1 and C_2 that are each decomposed into a mean and fluctuation: $C_1 = \overline{C_1} + c'_1$ and $C_2 = \overline{C_2} + c'_2$. If they fall on a mixing line then $C_1 + C_2 = 1$. Substituting in the decomposition:

$$\overline{C_1} + c'_1 + \overline{C_2} + c'_2 = 1 \tag{24}$$

Taking expectation:

$$\overline{C_1} + \overline{C_2} = 1 \tag{25}$$

Subtracting equation 25 from equation 24 yields: $c'_1 = -c'_2$. Using this relationship it is easily show that $\mathrm{E}\left[(c'_1)^2\right] = \mathrm{E}\left[(-c'_2)^2\right] = \mathrm{E}\left[-c'_1 c'_2\right]$ or that $\sigma^2_{C_1} = \sigma^2_{C_2} = -\sigma^2_{C_1C_2}$ and thus the correlation coefficient is -1 when a mixing line applies.

As an example of transforming conservative Beta distributions into joint reactant distributions, consider a normalized mean total molybdate, $Mo_T/Mo_{T,O}$ of 0.3 and from the mixing line the normalized mean total Tiron concentration, $Ti_T/Ti_{T,O}$, would be 1.0 - 0.3 = 0.7. Assuming that the conservative total molybdate distribution is Beta, the conservative total Tiron distribution can be calculated from the molybdate distribution by applying the mixing line, which forms a joint distribution (figure 4):

Figure 4.

The normalized Tiron and molybdate concentrations have the same variance, meaning that Tiron will have the mirror image Beta distribution of molybdate. With the joint *pdf* approximated, the potential normalized mixed reactant concentrations are unnormalized (all Tiron values are multiplied by 0.05 M and molybdate values are multiplied by 0.025) and reacted to calculate the potential product and remaining reactants (see Oates and Harvey, 2006 for more details on the Tiron/molybdate reaction). The discrete probability is conserved through the reaction yielding product and remaining reactant distributions. Essentially, all potential mixed reactant concentrations are considered, and the reactions are weighted by the probability that they are present. This means that by modeling the mean and variance of a conservative tracer it is possible to calculate any number of nonlinearly reacting reactant pairs as long as the reactants are not sorbing. It is important to point out that because all possible reactions are considered before any averaging is performed; the reaction can be extremely non-linear. This process explicitly calculates product and reactant distributions, which can account for the high variability reported for mixing controlled reactions (Cirpka and Kitanidis, 2000; Cirpka, 2002). An overview of the distribution chemical reaction calculations is given in the appendix.

The above process explicitly calculates product and reactant distributions prior to integration, but we wanted to investigate if the new distributions could also be approximated as Beta distributions based on new means and variances. Beta distributions range from 0 to 1 so product and reactant concentrations must be normalized to fall within this range. This can be done by dividing the product or reactants means by their maximum value and dividing the product or reactant variances by the maximum value squared. The maximum value of A is 1, C is 0.5 and, the Tiron/molybdate product is 0.8. These normalized means and variances can then be used to calculate shape parameters for Beta distributions.

4.3. Results.

4.3.1 Application of the *CF-β* Model to the Mildly Heterogeneous Experiments.

We will validate the *CF-β* approach to reactive transport modeling by investigating and modeling the space-time evolution of the conservative tracer variance; the means and variances of P, A, and Tiron/molybdate product; the space-time evolution of the conservative and reactive distributions. All results are compared to our experimental data. Then we use the *CF-β* approach to model how different grain sizes and a larger domain would have affected reactive transport for our experiments. These results demonstrate that the *CF-β* approach can model the correct amount of chemical reaction and provide probably density functions for use in regulatory compliance situations based on maximum contaminant levels.

4.3.1.1 Perturbation field analysis. Given the high resolution of our data (Chapter 3), we can directly compare the perturbation analysis to our perturbation field and apply equation 9 to study the concentration micro-scales. To do this, the mean concentration value along x are calculated by averaging over y and then this mean is subtracted from each pixel at a given x to reveal the concentration perturbation field (figure 5-A).

Figure 5.

To approximate the effects of transverse and longitudinal mechanical-dispersion, which act parallel and perpendicular to local stream tubes, respectively, we assumed that transverse dispersion is acting in the direction of the maximum local concentration gradient, and longitudinal dispersion acted perpendicular to this direction. This is based on the notion that transverse dispersion is much smaller than longitudinal dispersion and the direction of smallest dispersion would have the steepest gradient. Concentration gradients were calculated by considering a pixel and taking a central difference of the perturbation field from the neighboring pixels and then determining the transverse and longitudinal directions. This approach was used to calculate the squared transverse perturbation derivatives $(\partial c'/\partial T)^2$ (figure 5-B) and the squared longitudinal perturbation derivatives $(\partial c'/\partial L)^2$ (figure 5-C). Next, at a given x, the variance is divided by the average perturbation derivatives to yield the two concentration micro-scales (equation 6) (figure 5-E). Finally, to calculate χ_L from equation 16, we assumed longitudinal and transverse dispersivities $a_L \approx d/\pi$ and that $a_T \approx \alpha_L/10$ where d is the average bead diameter (Spitz and Moreno, 1996), which yield respective values of ~0.03 and 0.003 cm (figure 5-E). Looking at the concentration micro-scales across the dispersive-front, they remain fairly constant because when the variance is smaller the mean squared perturbation derivatives are smaller and vice versa so the ratio remains close (see equation 6). This constant behavior justifies using a spatially averaged value. Over time, the average longitudinal micro-scale shows substantial growth while the transverse micro-scale is very constant (figure 6-A).

Figure 6.

Considering this behavior, the relative mixing contribution of transverse and longitudinal mixing can be calculated as the percentage of the variance destruction term (see equation 13b) (figure 6-B). In agreement with other researchers (*e.g.* Fiori and Dagan, 1997; Cirpka, 1999; Cirpka and Kitanidas, 2000), transverse mixing dominates mixing and variance destruction. Initially, longitudinal mixing is strongest because concentration and concentration perturbation gradients are still steep, which produces a small micro-scale for a given variance. Longitudinal mechanical dispersion is much larger than transverse mechanical-dispersion so with a small micro-scale longitudinal mechanical-dispersion initially creates most of the mixing as shown by its large initial mixing percentage.

However, as soon as the plug-flow distance passes only one correlation length, heterogeneity stretches and distorts the mechanical-dispersive front creating very steep transverse gradients and a large surface area for transverse dispersion to act over. At the same time, the stronger longitudinal mechanical-dispersion decreases its perturbation gradient faster than variance decreases, which causes the longitudinal micro-scale to grow and lesson its mixing contribution. There are no mechanisms to sharpen the longitudinal mechanical-dispersion gradients while heterogeneity creates velocity fluctuations that shear the fluid interfaces and maintain relatively sharp transverse gradients. As time progresses, transverse mechanical-dispersion starts smoothing out the transverse concentration fluctuation derivatives and this is mainly what is responsible for reducing variance. Therefore, the ratio of variance to the average transverse fluctuation derivative remains fairly constant because they are both being decreased by the same process at the same rate. Calculating the behavior of χ_L as a function of the micro-scales (figure 7)

Figure 7.

shows good agreement with the modeled behavior of χ_L that was used to fit the conservative concentration variance (next section). These results show that the concentration micro-scales remain constant over the dispersion front validating the closure approximation for the variance destruction term, and that transverse mechanical-dispersion is the dominant mixing mechanism.

4.3.1.2 CF-β means and variances. It has already been shown that the *ADE* adequately models the mean conservative concentrations (figure 6-A, Oates *et al.*, Chapter 3). We calculated the space-time evolution of the variance of the conservative tracer data at every x by calculating the variance over y. Concentration variance was modeled with a Crank-Nicholson finite-difference approximation of equations 19 and 20 with the following boundary conditions:

$$\sigma_C^2 = 0 \qquad x = 0, t \tag{26}$$

$$\frac{\partial \sigma_C^2}{\partial x} = 0 \qquad x = L, t \tag{27}$$

and there was no variance initially in the domain. The concentration mean, and thus the variance production term in the variance equation, was calculated with a Crank-Nicholson finite-difference of the *ADE* (equation 18) with the following boundary conditions:

$$-\bar{v} A_x \frac{\partial \overline{C}}{\partial x} + \overline{v C} = \bar{v} C_O \qquad x = 0, t \tag{28}$$

$$\frac{\partial \overline{C}}{\partial x} = 0 \qquad x = L, t \tag{29}$$

where the macro-dispersivity and mean velocity were calculated from the breakthrough curve of the conservative tracer with values of A_x = 1.1 cm and $\bar{v}$ = 0.57 cm/min respectively (Chapter 3). Then, using a non-linear least squares optimization algorithm, χ_L and χ_G were fit to the space-time evolution of the variance. The fit values of χ_L and χ_G were used in *CF-β* model to predict the mean of P, A, and the Tiron/molybdate product. Additionally, χ_L and χ_G were fit to the observed mean Tiron/molybdate reaction using the *CF-β* modeled mean product. The $A+B \rightarrow P$ concentration field was simulated from the conservative tracer (Chapter 3; the *P* and the *A* field can be seen in figure 11) and the only difference between the simulated fields and actual reactive transport data is pore-scale mixing (Chapter 3).

Applying a finite-difference model of the mean and variance shows that the variance of the conservative tracer can be reasonably modeled by fitting χ_L and χ_G (table 1) and we would expect a smoother fit if our tanks contained more correlation lengths (figure 8-A).

Figure 8.

Using the values of χ_L and χ_G fit to the conservative variance, the *CF-β* model excellently predicts the *P*, *A*, and Tiron/molybdate product means (figure 8-B, 8-C, 8-D), the moments of the means and peak mean concentrations (figure 9), and the observed variability (figure 10) all with the same variance length-scales. This verifies the success of the *CF-β* approach for modeling the complex reactive transport observed in our tank experiments.

Figure 8.

Figure 9.

Fitting χ_L and χ_G (table 1) to the mean Tiron/molybdate product reaction shows a very similar behavior to predictions made from the conservative tracer except the mean product is slightly less (figure 8-D and 10-C solid and dashed line). Interestingly, the conservative variance profile predicted with the variance length-scales determined from the reaction experiment is slightly higher then the conservative tracer (figure 8-A solid and dashed line). We believe that this slight increase in variance is a result of the incomplete pore-scale mixing, which manifest itself in a slightly higher macroscopic variance. This idea is further supported when using the χ_L and χ_G values obtained from fitting the variance of the blue dye tracer to simulate the mean Tiron/molybdate product; it produces slightly higher mean values (figure 7-D and 9-C, dashed lines; and figure 7 from Chapter 3). As already stated, this difference is not much and not thought to be very important for field-scale application. However, it implies that variance serves as a global mixing parameter that can assess and weight the importance of mixing over different scales. Furthermore, the important implication of this comparison is that χ_L and χ_G can be very precisely inferred from the mean value of a reactive tracer; an idea that will be revisited later.

Looking at the left tail of the mean Tiron/molybdate product (figure 8-D) shows that for the two-step complexation reaction of Tiron and molybdate, the over prediction of mixing can result in less product. This is because mixing more molybdate into the reaction shifts the product from the highly colored species (two Tirons and one molybdate) to the less colored species (one Tiron one molybdate). Unfortunately, our concentration field was not smooth enough to verify this experimentally, but it does demonstrate that it is possible to underestimate a product species by overestimating the amount of mixing. The results in this section demonstrate that the *CF-β* approach can model the correct amount of chemical reaction by calculating the expected value of chemical reaction by explicitly integrating over product and remaining reactant distributions.

4.3.1.3 CF-β distributions. We also wanted to assess how well this approach could model the space-time evolution of the conservative, product, and reactant concentration distributions. To separate out the error introduced by modeling the mean and variance and the error caused by assuming a Beta distribution, we generated Beta distributions from the modeled mean and variance and also from the exact empirical mean and variance calculated at a given x for both conservative and reactant concentrations. We calculated the root-mean-square error of the Beta cumulative density function (*cdf*) compared to the observed *cdf*, which we consider a more useful measure of error compared to a *Kolmogrov-Smirnof-test* given our large sample size per distribution (n>1000).

For a bounded range of concentrations and a given mean and variance, the Beta distribution does a good job of describing the observed distributions (figure 11).

Figure 11.

Calculating the mean and variance from the observed distributions shows the Beta distribution was able to reproduce the distribution of tracer, reactant and both products consistently with around 2-5% error (figure 12).

Figure 12.

The difference in error between the modeled Beta *cdfs* and the empirical Beta *cdfs* implies that the largest part of the error when modeling the full distributions results from modeling the mean and variance especially at early times. The model and data thus far have demonstrated the usefulness and versatility of the Beta distribution approximation, but it cannot capture all the complexities of fluid mixing in porous media. For example, the Beta distribution cannot reproduce multi-modal distributions where the peaks occur towards the middle of a distribution. Instead, the extra variance that results from these peaks raises the tails around 0 and 1 of the Beta distribution to honor the same variance. As such, high probabilities in the tail region should be viewed with a degree of caution. It is likely if a heterogeneous field contained more correlation lengths than our tanks that some of these peaks would smooth out. The *CF-β* approach is capable of modeling the space-time evolution of conservative and reactive concentration *pdfs*, which can be used in regulatory compliance situations based on maximum contaminant levels.

4.3.1.4. Smaller grains and bigger tanks. The mean bead size of the grains outside the circular inclusions was approximately 2.1 mm; around the size of coarse gravel. Since mechanical dispersivity scales with grain size (Spitz and Moreno, 1996), the tanks have almost the highest mixing rates possible for the given conductivity field and produce mixing and reaction closest to the macro-dispersion prediction. The effects of mechanical dispersion on macro-dispersion have been previously investigated (e.g. Gelhar and Axness, 1983; Dagan, 1989; Neuman and Zang, 1990; Fiori, 1996) and have been found to reduce macro-dispersion for highly anisotropic heterogeneity but mechanical dispersion is generally considered to have negligible contribution to the macro-dispersive flux (e.g. Dagan, 1982; Gelhar and Axness, 1983; Graham and

McLaughlin, 1989). However, mechanical dispersion plays a critical role in variance destruction (e.g. Kapoor and Gelhar, 1994a; Dagan and Fiori, 1997) and therefore reactive transport. If our tank beads were smaller but maintained the same relative permeability, then macro-dispersion and hence variance production would remain virtually the same. However, variance destruction and reactive mixing would be significantly reduced. We will assume that the conductivity micro-scales would remain unchanged because they represent features of the small-scale flow structure for advection dominated situations (Kapoor and Kitanidis, 1996, 1998). Therefore, changing the mean grain size from gravel d_G to an arbitrary grain size d would change the longitudinal and transverse mechanical-dispersivities of gravel, α_{L,d_G} and α_{T,d_G} respectively, to new dispersivities $\alpha_{L,d}$ and $\alpha_{L,d}$. From Spitz and Moreno (1996), we assume the following relationships:

$$\alpha_{L,d_G} \cong d_G; \qquad \alpha_{T,d_G} \cong \frac{d_G}{10}; \qquad \alpha_{L,d} \cong d; \qquad \alpha_{T,d} \cong \frac{d}{10} \tag{30}$$

Solving for the dispersivities of a new grain size in terms of the old dispersivities yields the following relationships:

$$\alpha_{L,d} = \alpha_{L,d_G} \frac{d}{d_G}; \qquad \alpha_{T,d} = \alpha_{T,d_G} \frac{d}{d_G} \tag{31}$$

Consider the variance length scale, χ_{L,d_G}, we have determined for our course gravel tanks:

$$\chi_{L,d_G} = \left(\frac{2\alpha_{L,d_G}}{\left(\Delta_L^C\right)^2} + \frac{2\alpha_{T,d_G}}{\left(\Delta_T^C\right)^2} \right)^{-1} \tag{32}$$

A theoretical tank with the same relative conductivity field but with smaller grains would have the effect of replacing the gravel dispersivities in equation 32 with the new dispersivities in equation 31. This theoretical tank would have the new variance length scale, $\chi_{L,d}$:

$$\chi_{L,d} = \left(\frac{2\alpha_{L,d_G} d}{\left(\Delta_L^C\right)^2 d_G} + \frac{2\alpha_{T,d_G} d}{\left(\Delta_T^C\right)^2 d_G} \right)^{-1} \Rightarrow \quad \chi_{L,d} = \frac{d_G}{d} \left(\frac{2\alpha_{L,G}}{\left(\Delta_L^C\right)^2} + \frac{2\alpha_{T,G}}{\left(\Delta_T^C\right)^2} \right)^{-1} \tag{33}$$

Dividing equation 33 by equation 32 yields:

$$\chi_{L,d} = \frac{d_G}{d} \chi_{L,d_G} \tag{34}$$

which means that we can model the effects of smaller grain sizes by just scaling the variance length scale (note that the assumption of $\alpha_L / \alpha_T = 10$ can be relaxed).

We investigated the hypothetical situation of our tanks having beads with a mean diameter of 0.42 mm, a high value for medium sand ($d_G/d = 5$), and 0.21 mm an average value for fine sand ($d_G/d = 10$). With the new variance length scale values, the *CF-β* model was then applied to simulate *P* and *A*, for *A*+*B*→*P*, and the Tiron/molybdate product (figure 13).

Figure 13.

Smaller grains and hence smaller mechanical-dispersivities can have a large impact on the amount of mixing as shown for this physically plausible tank situation where reaction is dramatically over predicted. Conceptually, this situation would produce very fine ribbons of product stretched about in the macro-dispersion realm of predicted spreading.

An important point to raise is that lack of mixing and reaction could cause *A*, a theoretical contaminant, to travel much further and faster then predicted by conventional models (figure 12-B).

We also wanted to model the reactive transport behavior over a larger domain to investigate what would happen if we had the same stationary conductivity field but if our tank was longer. To do this we extended the domain to 250 [cm] and used the *CF-β* model to simulate the Tiron/molybdate product for the cases of gravel, medium sand, and fine sand and compared the moments of the mean to the conventional *ADE* prediction (figure 14).

Figure 14.

Even after solutes mix over hundreds of correlation lengths, which were assumed not to increase with scale in this case, there still exists significant upscaling error especially for small pore-scale dispersion, which can be accurately modeled by the *CF-β* modeling framework.

Mixing in natural porous media is a slow process that can control the overall rate of chemical reactions and the lack of mixing causes concentrations to be spatially variable. The *CF-β* modeling framework has been experimentally validated to approximate the correct amount of chemical reaction and provide concentration probability density functions, which are needed to address laws and regulations based on maximum contaminant levels.

4.3.2. Application of the *CF-β* to Homogeneous Experiments.

4.3.2.1. Overview. In Chapter 3 we demonstrated that incomplete pore-scale mixing was relatively unimportant for heterogeneous porous media. However, as reaction constants can be inferred from column experiments in homogeneous porous media, we wanted to see if the *CF-β* could also model pore-scale mixing in homogeneous porous media. This would be important so that reaction constants do not unknowingly have a degree of mixing imbedded in them. Essentially, there is no such thing as a perfectly homogeneous medium and as such, variance production (or reactant segregation) would result from solute movement through some pores but not others as described by the mechanical-dispersion coefficient. Variance destruction (or reactant mixing) would result from diffusion smoothing out concentration gradients over a large surface area created by pore-scale velocity fluctuations. We were not sure a priori whether variance destruction would have a linear relationship with velocity representing a smaller-scale mechanical-dispersive mixing process, a quadratic relation with velocity suggesting mixing follows a Taylor-Aris type of dispersion, or perhaps no relation with velocity implying diffusion is unaided by velocity fluctuations.

First, the homogenous Tiron/molybdate experiments were modeled to assess if the *CF-β* approach is applicable for homogeneous porous media. Next, we investigated the velocity dependence of variance destruction by applying the *CF-β* approach to model the copper sulfate/EDTA reaction from the work of Gramling *et al.* (2002). Finally, we analyzed the breakthrough curves of Raje and Kapoor (2000) by fitting the variance length-scales to their first breakthrough curve, and then using these fit values to predict their second breakthrough curve generated at a different velocity and different initial reactant concentrations for their non-linear reaction.

4.3.2.2. Tiron/Molybdate product. The *CF-β* approach does an excellent job of modeling incomplete pore-scale mixing in homogeneous porous media (figure 15-A).

Figure 15.

The observed product variance was significantly lower then the modeled variance (figure 15-B) because our experimental technique could not observe pore-scale variability. Even though the true pore-scale variance could not be observed, it had to be modeled to predict the correct mean of the non-linear reaction which our experimental technique did resolve. This means that by comparing the observed to the modeled mean we can actually predict the pore-scale concentration distributions. The distributions had lower variance than the heterogeneous tanks as a result of the lower variance production, but they were very far from Gaussian except near the center of the plume (not shown).

4.3.2.3. Analysis of Gramling et al. (2002) and velocity dependence of variance destruction. All experimental results of Gramling *et al.* (2002) which were run at different velocities, were analyzed with the *CF-β* approach and the results were similar to figure (15-A). The rate constants χ and κ_χ were fit at three different velocities, which allowed their velocity dependence to be assessed (figure 16).

Figure 16.

It is clear that these parameters have a linear dependence on velocity for the advection-dominated flow studied, implying there is a small local-scale mechanical-dispersive mixing process destroying variance and that the behavior of the variance destruction evolves proportionally to the amount of the porous media experienced. This means that velocity can be factored out and the same length-scale dependent equation that applies to heterogeneous porous media also applies for homogeneous media (table 1).

4.3.2.4. Analysis of Raje and Kapoor (2000) and measuring variance destruction from a reactive breakthrough curve. The rate-limited bimolecular reactive breakthrough curve for run 1 from Raje and Kapoor (2000) was modeled with the *CF-β* approach assuming that the chemical reaction rate (438 M^{-1} s^{-1}) was fast enough compared to the advective time-scales to model the reaction as instantaneous. Fitting χ_L and χ_G (table 1) did an excellent job of modeling the breakthrough curve (figure 17-A).

Figure 17

The fitted values were then used to predict run 2 from Raje and Kapoor (2000), which was run at a different velocity with different initial concentrations for the non-linear reaction and the results were found to be in good agreement (figure 17-B). Aside from demonstrating the validity of the *CF-β* approach, it demonstrates that the variance length scales can be reliably determined from a breakthrough curve of rate-limited bimolecular reaction. This could have very important implications: a breakthrough curve of a rate-limited bimolecular reaction might be an appropriate field technique for measuring these length-scales at a field site. As the reaction rate from Raje and Kapoor (2000) was very fast compared to the advective time scales across the tank, we treated it as instantaneous reaction. However, and very importantly, the reaction rate was slow enough not to react in the outflow tube, which allowed the effects of chemical segregation to be observed.

4.3.2.5. χ_L and χ_G in homogeneous media. χ_L and χ_G differed between the Tiron/molybdate and Gramling *et al.* (2002) experiments (table 1). For the Tiron/molybdate experiment, the mean grain size is much smaller but χ_L is almost an order of magnitude higher, meaning worse mixing (table 1). We believe the important difference in terms of mixing between these experiments is grain roughness. The Tiron/molybdate experiment used smooth spheres while Gramling *et al.* (2002) used freshly crushed cryolite grains. The freshly crushed cryolite would have highly irregular surfaces that would increase small-scale velocity fluctuations and produce mroe efficient mixing. Raje and Kapoor (2000) also used smooth spherical beads and the χ_L for their experiment (8.6 cm) is very similar to the χ_L from the homogeneous Tiron/molybdate experiment (8.3 cm) which also used smooth spheres. This similarity implies the importance of grain roughness for pore-scale mixing. However, the χ_G values are different between Raje and Kapoor (2000) and the Tiron/molybdate but similar between Raje and Kapoor (2000) and Gramling *et al.* (2002). This might be due in part to the similar grain sizes. Further research is necessary to determine the relationships between χ_L, χ_G, grain roughness, grain diameter, and perhaps porosity. This could be accomplished by determining the variance length scales for a variety of homogeneous media using reactive breakthrough curves similar to Raje and Kapoor (2000). The behavior of χ_L for all the homogeneous experiments is shown in figure 7. These results show that the *CF-β* modeling framework can upscale reactive transport in homogeneous porous media without resolving pore-structures.

4.4.4. *CF-β* Limitations.

We have verified the success of the *CF-β* approach for modeling reactive transport observed in our laboratory experiments. However, the *CF-β* approach currently requires two potentially limiting assumptions: 1) reactions can be viewed as instantaneous because reaction rates are much faster than mixing rates; and 2) reactants do not sorb to the porous media and therefore fall on a mixing line. While these assumptions may hold in some field situations such as the slow mixing of oxygen and ethanol, a more general frame-work needs to be developed to relax these assumptions. We propose and verify that production-destruction balances can allow for variance and covariance approximations by scaling the mean gradients by the macro-dispersivity and the variance-length scale in the final paper of this series. If the large time production-destruction balance is generally applicable, which it appears to be, it would provide the necessary statistical moments to construct multivariate distributions for when reactants sorb differently and/or the instantaneous reaction assumption does not hold.

Appendix.

Numerically implementing the Beta distribution can be difficult for high variance situations, where it is possible to have close to a dirac delta at 0 and/or 1. In these cases it is difficult to generate a distribution that numerically integrates back to 1, even though it is exact analytically. To overcome this issue we: 1) made the grid spacing exponentially smaller around 0 and 1, where the values and derivatives of the Beta distribution can be extremely large; 2) forced the distribution to integrate to 1 by normalizing by a numerical integrand; and 3) refit the shape parameters *a* and *b* to honor the input mean and variance.

The grid spacing $\Delta c/c_o$ was constant in log space where n_g is the number of grid points:

$$\Delta c/c_o = \left(\log(0.5) - \log\left(10^{-16}\right)\right)/\left(n_g/2\right) \tag{A-1}$$

Then a vector of numbers, $c/c_{o1/2}$, ranging from ~ 0 to 0.5 with spacing of $\Delta c/c_o$ was generated (using Matlab notation)

$$c/c_{o1/2} = \left[\log\left(10^{-16}\right) : \Delta c/c_o : \log(0.5)\right] \tag{A-2}$$

Next a mirror image of this vector was created using Matlab's *fliplr* (flip left to right) command and the two vectors where then combined into one vector and the whole vector was exponentiated to yield a grid $c/c_{o\beta}$ that ranges from 0 to 1 with exponentially smaller grid spacing around 0 and 1:

$$c/c_{o\beta} = \left[e^{c/c_{o1/2}} : e^{fliplr\left(1-c/c_{o1/2}\right)}\right] \tag{A-3}$$

The numerical Beta distribution was then integrated over all $c/c_{o\beta}$ to normalize the density and ensure it integrated to 1:

$$f_{C/Co} = \frac{\left(c/c_{o\beta}\right)^{a-1}\left(1-c/c_{o\beta}\right)^{b-1}}{\sum_{i=1}^{n_x-1}\left(f_{C/Co(i)} + f_{C/Co(i+1)}\right)/2\left(c/c_{o\beta(i+1)} - c/c_{o\beta(i-1)}\right)} \tag{A-4}$$

The mean $\overline{C_\beta}$ and variance $\sigma^2_{C,\beta}$ of any conservative or reactive concentration are calculated from the numerical Beta distribution by numerical integration as follows:

$$\overline{C_\beta} = \sum_{i=1}^{n_x-1}\left(f_{C/Co(i)} + f_{/Co(i+1)}\right)/2\left(C_{(i)} + C_{(i+1)}\right)/2\left(c/c_{o\beta(i+1)} - c/c_{o\beta(i-1)}\right) \tag{A-5}$$

$$\mu^2 = \sum_{i=1}^{n_x-1} \left(\left(f_{C/Co(i)} + f_{C/Co(i+1)} \right) / 2 \left(C_{(i)} + C_{(i+1)} \right) / 2 \right)^2 \left(c/c_{o\beta(i+1)} - c/c_{o\beta(i-1)} \right) \tag{A-6}$$

$$\sigma_{C,\beta}^2 = \mu^2 - \overline{C_\beta}^2 \tag{A-7}$$

After calculating the mean and variance of the conservative numerical Beta distribution (denoted by subscript β), the distribution was checked to ensure that it matched the input mean and variance (denoted by subscript M). If a match was not found, new shape parameters a and b where determined that minimized the following function:

$$f = \left(\left(\frac{\overline{C_M} - \overline{C_\beta}}{\overline{C_M}} \right)^2 + \left(\frac{\sigma_{C,M}^2 - \sigma_{C,\beta}^2}{\sigma_{C,M}^2} \right)^2 \right) \tag{A-8}$$

which ensured that the numerical mean and variances matched the input values. The numerical conservative Beta distributions can then be transformed into product and reactant distributions by applying the mixing line and running all possible reactant pairs through a reaction model. Finally, the product and reactant mean and variance can be calculated using equations A-5 - A-7 where C is the product or remaining reactant concentration.

References

1. Cirpka, O. 2002. Choice of dispersion coefficients in reactive transport calculations on smoother fields. *Journal of Contaminant Hydrology*. 58, 261–282.
2. Cirpka, O. A., and Nowak, W. 2003. Dispersion on Kriged Hydraulic Conductivity Fields. *Water Resources Research*. 39(2), 1027, doi:10.1029/2001WR000598, 2002.
3. Cirpka, O. A., Frind, E. O., and Helmig, R. 1999. Numerical simulation of biodegradation controlled by transverse mixing, Journal of Contaminant Hydrology. 40(2), 159–182.
4. Cirpka, O. and Kitanidis, P. K. 2000. An advective-dispersive stream tube approach for the transfer of conservative-tracer data to reactive transport. *Water Resources Research*. 36(5), 1209-1220.
5. Dagan, G. 1982. Stochastic modeling of groundwater flow by unconditional and conditional probabilities, 2, The solute transport. *Water Resources Research. 18*, 835–848.
6. Dagan, G., and Fiori, A. 1997. The influence of pore-scale dispersion on concentration statistical moments in transport through heterogeneous aquifers. *Water Resources Research*. 33(7), 1595-1605.
7. Dentz, M., Kinzelbach, H., Attinger, S., and Kinzelbach, M. 2000. Temporal behavior of a solute cloud in a heterogeneous porous medium: 1. Pointlike injection. *Water Resources Research*. 36, 3591– 3604.
8. Fiori, A. 2001. The Lagrangian concentration approach for determining dilution in aquifer transport: Theoretical analysis and comparison with field experiments. *Water Resources Research*. 37(12), 3105-3114.
9. Fiori, A. 2003. An asymptotic analysis for determining concentration uncertainty in aquifer transport. *Journal of Hydrology*. 284, 1-12.
10. Fiori, A., and Dagan, G. 2000. Concentration fluctuations in aquifer transport: a rigorous first order solution and applications. *Journal of Contaminant Hydrology*. 45, 139-163.
11. Gelhar, L. W., Axness, C. L. Three-Dimensional Stochastic Analysis of Macrodispersion in Aquifers. *Water Resources Research*. 19(1), 161-180.
12. Ginn T. R. 1998. Comment on "Stochastic analysis of oxygen-limited biodegradation in three-dimensionally heterogeneous aquifers" by F. Miralles-Wilhelm *et al. Water Resources Research*. 34 (9), 2423-2426.
13. Ginn, T. R. 2001. Stochastic-convective transport with nonlinear reactions and mixing: Finite streamtube ensemble formulation for multicomponent reaction systems with intra-streamtube dispersion. *Journal of Contaminant Hydrology*. 47, 1-28.
14. Ginn, T. R., Murphy, E. M., Chilakapati, A., Seeboonruang, U. 2001. Stochastic-convective transport with nonlinear reactions and mixing: Application to intermediate-scale experiments in aerobic biodegradation in saturated porous media. *Journal of Contaminant Hydrology*. 48,121-149.
15. Gramling, C. M. Harvey, C. F., Meigs, L. C. 2002. Reactive transport in porous media: A comparison of model prediction with laboratory visualization. *Environmental Science and Technology*. 36(11), 2508-2514.

16. Janssen, G. M., Cirpka, O.A., van der Zee, S.E.A.T.M. 2006. Stochastic analysis of nonlinear biodegradation in regimes controlled by both chromatographic and dispersive mixing. *Water Resources Research.* 42, W01417
17. Jose, S. C., and Cirpka, O. A. 2004. Measurement of mixing-controlled reactive transport in homogeneous porous media and its prediction from conservative tracer test data. *Environmental Science and Technololgy.* 38(7), 2089-2096.
18. Jose, S. C., Rahman, M. A. and Cirpka, O.A. 2004. Large-scale sandbox experiment on longitudinal effective dispersion in heterogeneous porous media. *Water Resources Research.* 40(12), W12415, doi: 10.1029/2004WR003363.
19. Kapoor, V. K., Gelhar, L. W. 1994a Transport in three-dimensionally heterogeneous aquifers 1. Dynamics of concentration fluctuations. *Water Resources Research.* 30(6), 1775-1788.
20. Kapoor, V., and Kitanidis, P. K. 1996. Concentration fluctuations and dilution in two-dimensionally periodic heterogeneous porous media. *Transport Porous Media.* 22: 91–119.
21. Kapoor, V., and Kitanidis, P. K. 1998. Concentration fluctuations and dilution in aquifers. *Water Resources Research.* 34(5), 1181–1193.
22. Kapoor, V., Gelhar, L. W., and Miralles-Wilhelm, F. 1997. Bimolecular second order reactions in spatially varying flows: Segregation induced scale-dependent transformation rates. *Water Resources Research.* 33(4), 527–536.
23. Miralles-Wilhelm, F., and Gelhar, L. W. 2000. Stochastic analysis of oxygen-limited biodegradation in heterogeneous aquifer with transient microbial dynamics. *Journal of Contaminant Hydrology.* 42(1), 69-97.
24. Miralles-Wilhelm, F., Gelhar, L. W., and Kapoor, V. 1997. Stochastic analysis of oxygen-limited biodegradation in three-dimensionally heterogeneous aquifers. *Water Resources. Research.* 33(6), 1251–1263.
25. Oates P. M. and Harvey, C.F. 2006. A colorimetric reaction to quantify fluid mixing. *Experiments in Fluids.* 41, 673–683. DOI 10.1007/s00348-006-0184-z.
26. Pannone, M., and Kitanidis, P. K. 1999. Large-time behavior of concentration variance and dilution in heterogeneous formations. *Water Resources Research.* 35(3), 623-634.
27. Pannone, M., and Kitanidis, P. K. 2004. On the asympototic Behavoir of Dilution Parameters for Gaussian and Hole-Gaussian Log-Conductivity Covairance Function. *Transport in Porous Media.* 56, 257-281.
28. Raje, D. S. and Kapoor, V. 2000. Experimental study of bimolecular reaction kinetics in porous media. *Environmental Science and Technology.* 34 (7), 1234-1239.
29. Robinson, B.A., Viswanathan, H.S. 2003. Application of the theory of micromixing to groundwater reactive transport models. *Water Resources Research.* 39(11), 1313.
30. Roshko, A. 1976. Structure of Turbulent Shear Flows: A New Look. AIAA Journal. 14(10), 1349-1357.
31. Simmons, C. A., Ginn, T. R., and Wood, B. D. 1995. Stochastic-Convective transport with nonlinear reaction: Mathematical framework. *Water Resources Research.* 31, 2675-2688.

32. Spitz, K. and Moreno, J. 1996. *A Practical Guide to Groundwater and Solute Transport Modeling.* Wiley-Interscience. New York, NY.
33. Tennekes, H., and J. L. Lumley. 1972. *A first course in Turbulence*. MIT Press. Cambridge, MA.

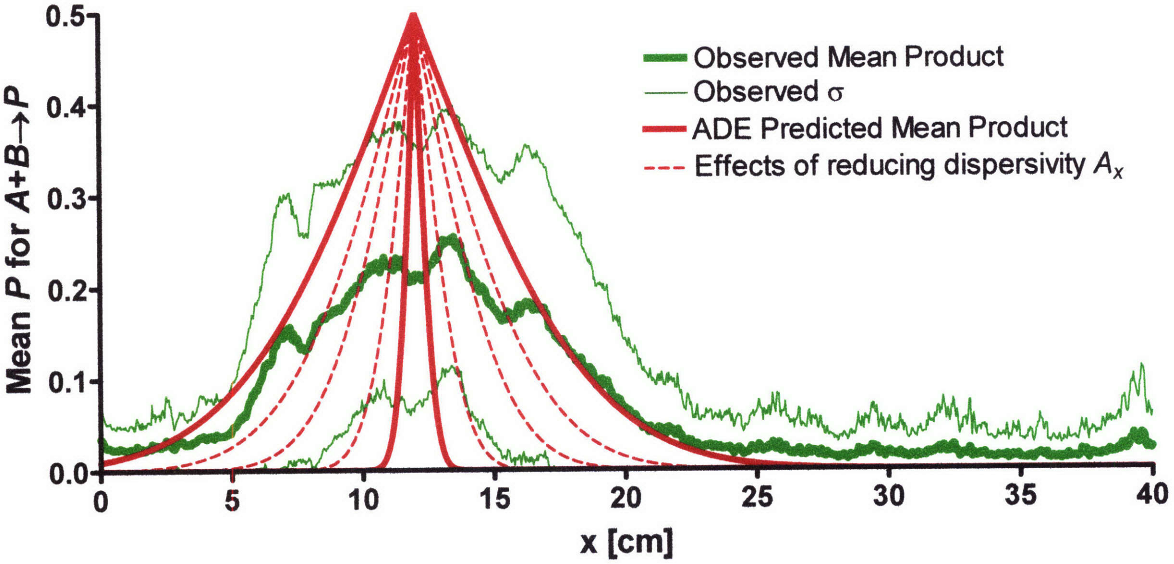

Figure 1. Effects of using a smaller dispersivity as an upscaled parameter to account for incomplete mixing. Reducing the dispersivity will always produce the same peak mean *P* for the *A*+*B*⟶*P* reaction and does not account for the for the unresolved-scale variability as indicated by the observed large standard deviation. Dispersivity could be chosen to match either the zeroth or the second product moment, but not both. *P* was simulated from the conservative tracer data in Chapter 3.

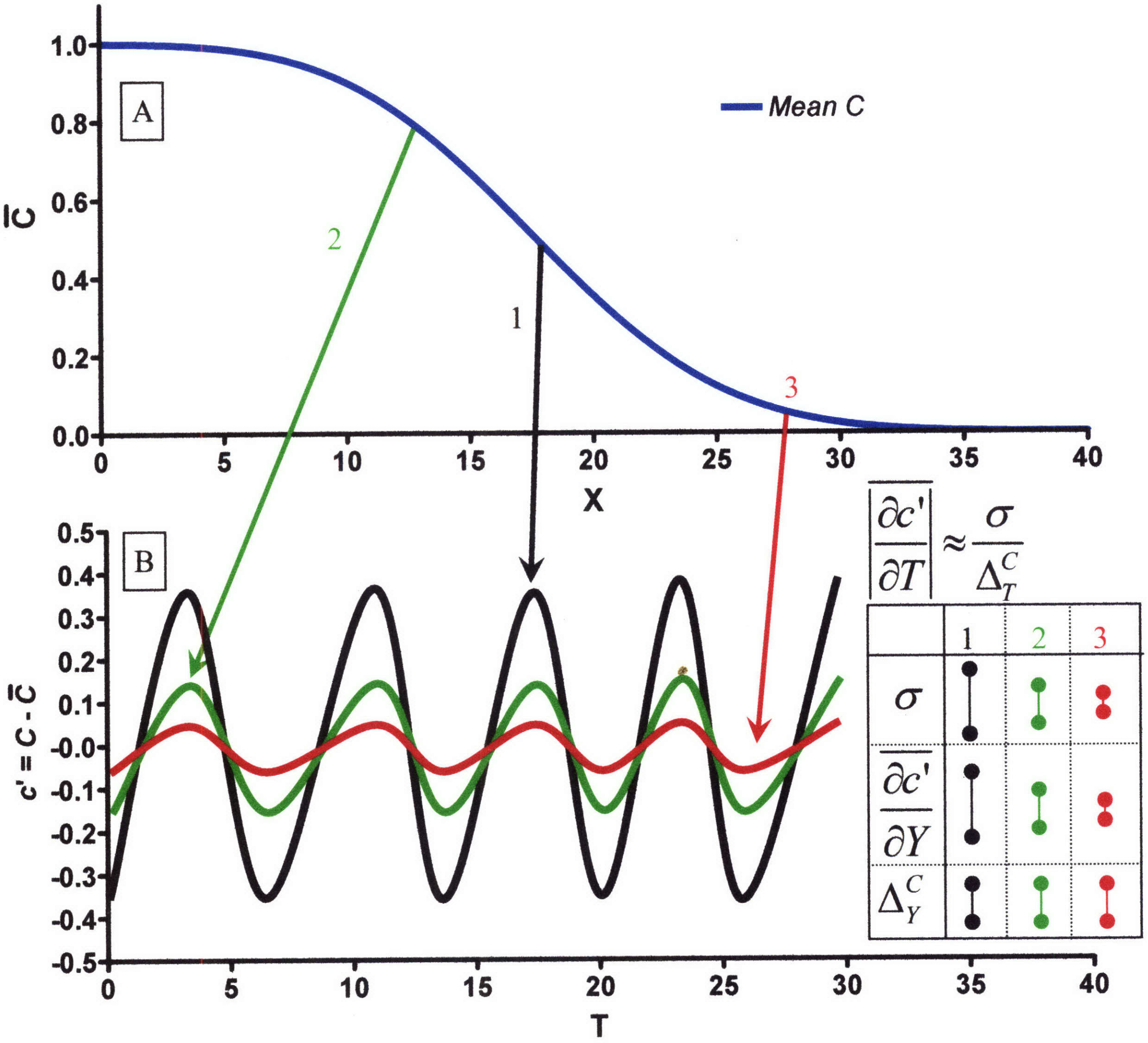

Figure 2. Average perturbation derivatives approximated as rise = standard deviation and run = concentration micro-scale. A) Hypothetical mean gradient. Three arbitrary spots are chosen and hypothetical transverse concentration profiles are plotted in panel B. Barbels in table show relative magnitude of each parameter for three different concentration profiles. The point to note is the standard deviation changes proportionally to the perturbation derivatives and concentration micro-scale stays the same, which justifies using an average value.

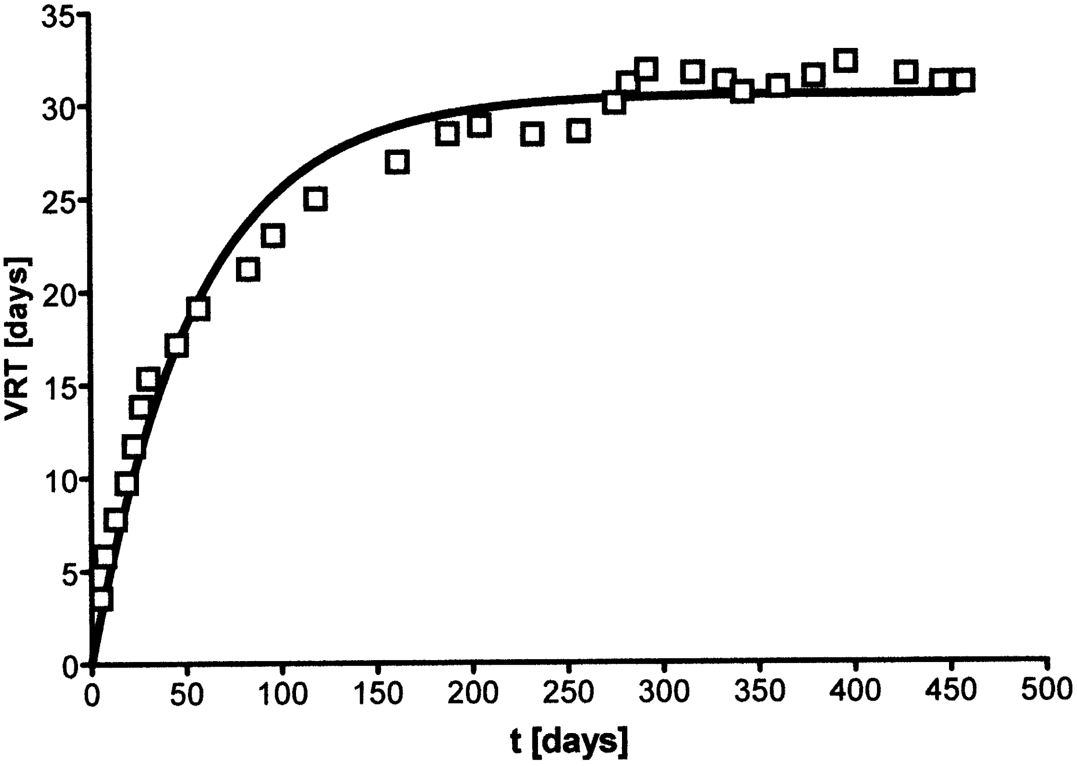

Figure 3. Exponential fit of temporally increasing variance residence time *VRT*. Data from numerical simulations of Kapoor and Kitanidas, 1998.

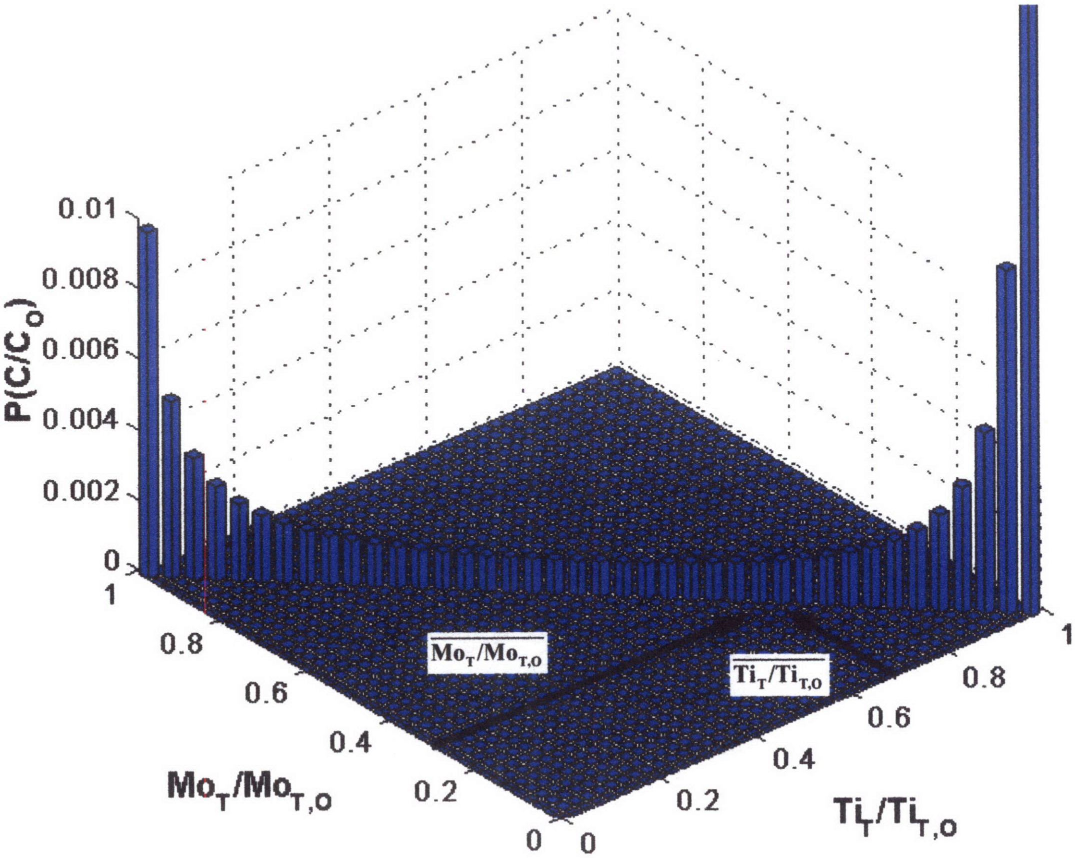

Figure 4. Joint beta distribution of total Tiron and molybdate before reaction.

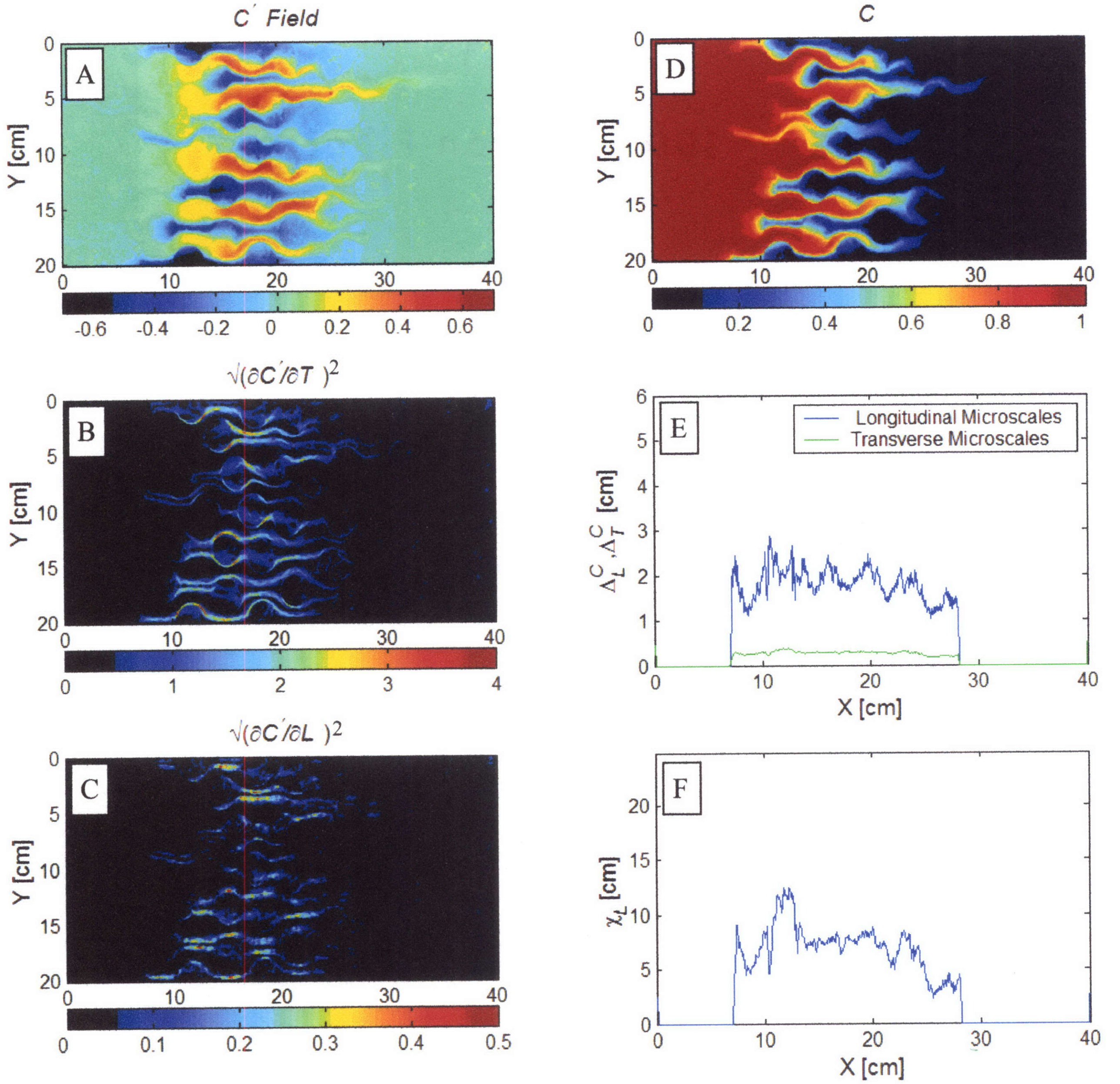

Figure 5. Time snap-shot of parameters relevant for modeling concentration variance: A) Concentration fluctuation field; B) Concentration fluctuation partial derivative in the transverse direction; C) Concentration fluctuation partial derivative in the longitudinal direction; D) Original concentration field; E) Longitudinal and transverse concentration micro-scales; F) Variance length-scale across the dispersion front.

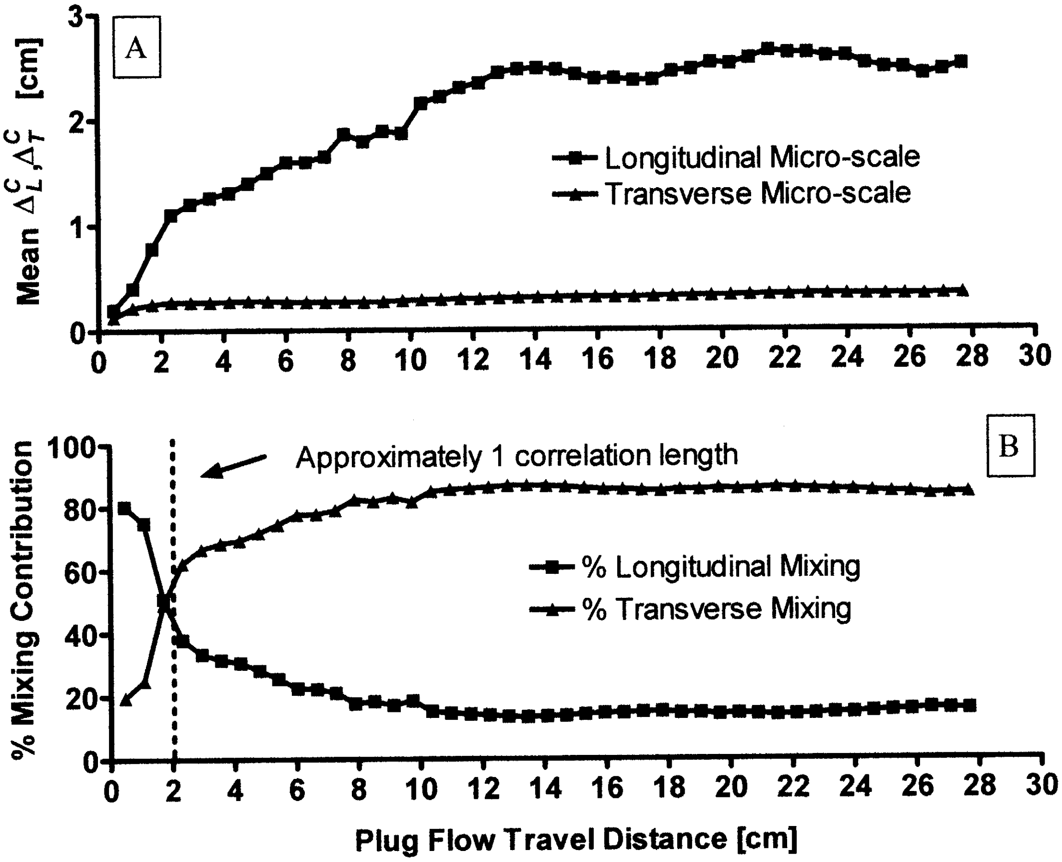

Figure 6. A) Evolution of the mean longitudinal and transverse concentration micro-scale; B) Percent mixing contribution calculated as the relative longitudinal and transverse components of χ (equation 9).

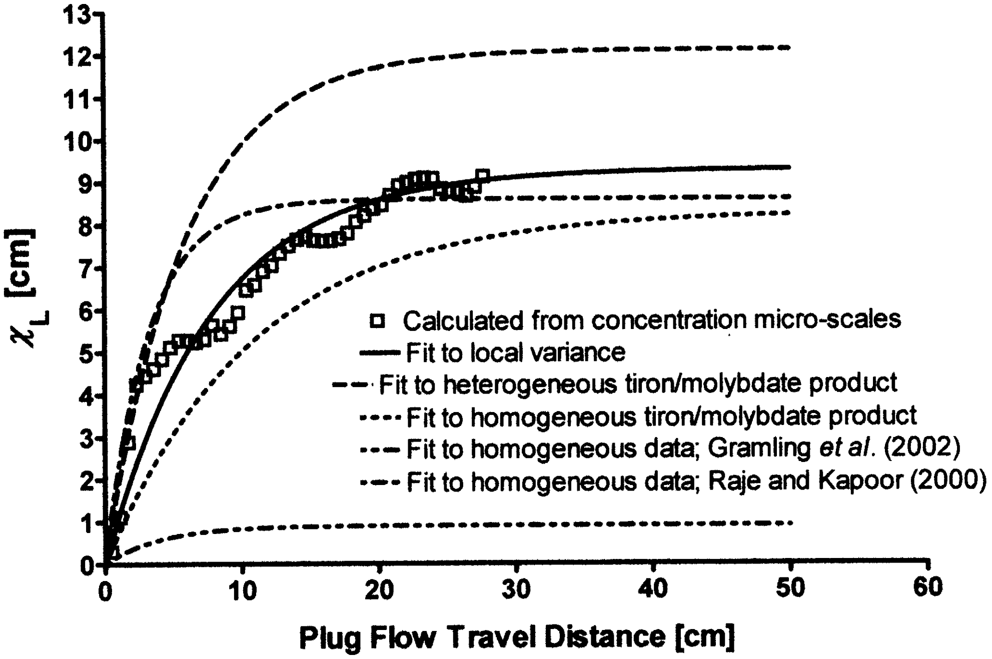

Figure 7. Evolution of the variance length-scale for different experiments.

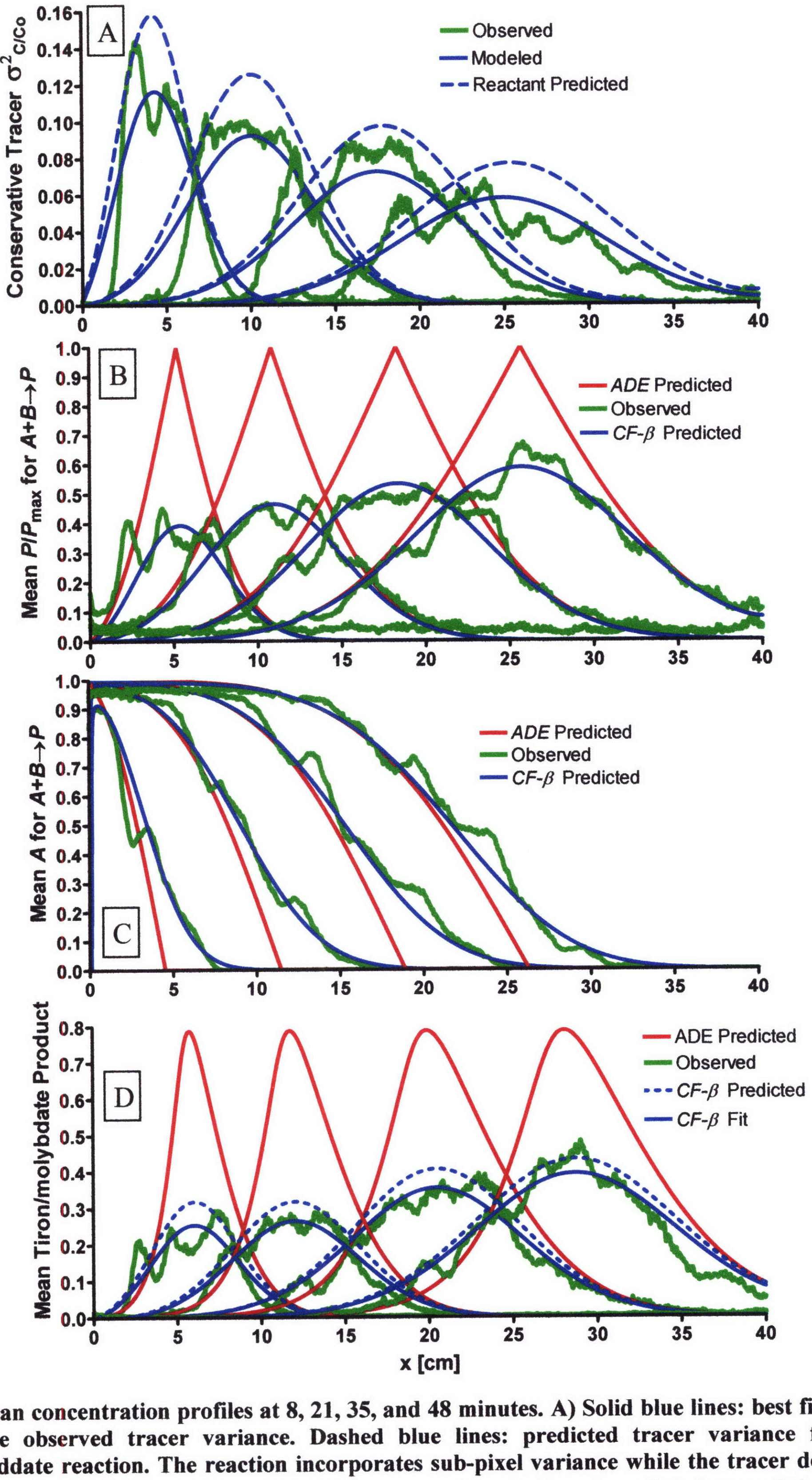

Figure 8. Mean concentration profiles at 8, 21, 35, and 48 minutes. A) Solid blue lines: best fit of the variance model to the observed tracer variance. Dashed blue lines: predicted tracer variance fit to the mean Tiron/molybddate reaction. The reaction incorporates sub-pixel variance while the tracer does not. B) *P* for the *A*+*B* → *P* reaction. Mean *ADE* predicted *P*, mean small-scale *P*, and predicted mean *P* from the *CF-β*. C) Mean *A* for the *A*+*B* → *P* reaction. Mean *ADE* predicted *A*, mean small-scale *A*, and predicted mean *A* from the *CF-β*. D) Tiron/molybdate product. Solid lines: mean *ADE* predicted product, observed mean small-scale product, and best fit mean product from the *CF-β*. Dashed Lines: mean product predicted by the *CF-β* model using variance parameters fit to the local dye tracer that do not account for pore-scale mixing.

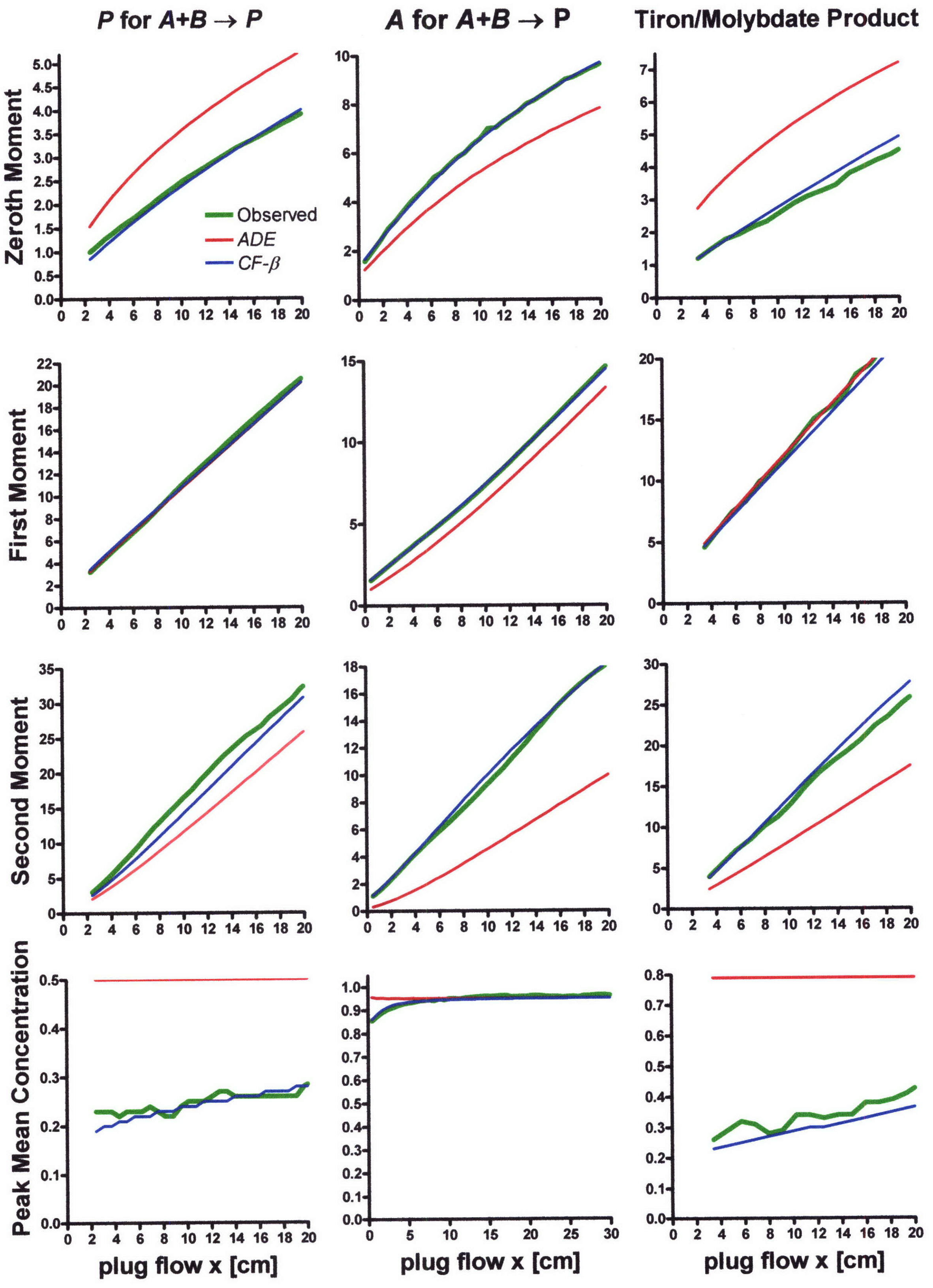

Figure 9. Zeroth moment, first moment, second moment, and peak of the mean *ADE* predicted product, observed product, and *CF-β* model over time.

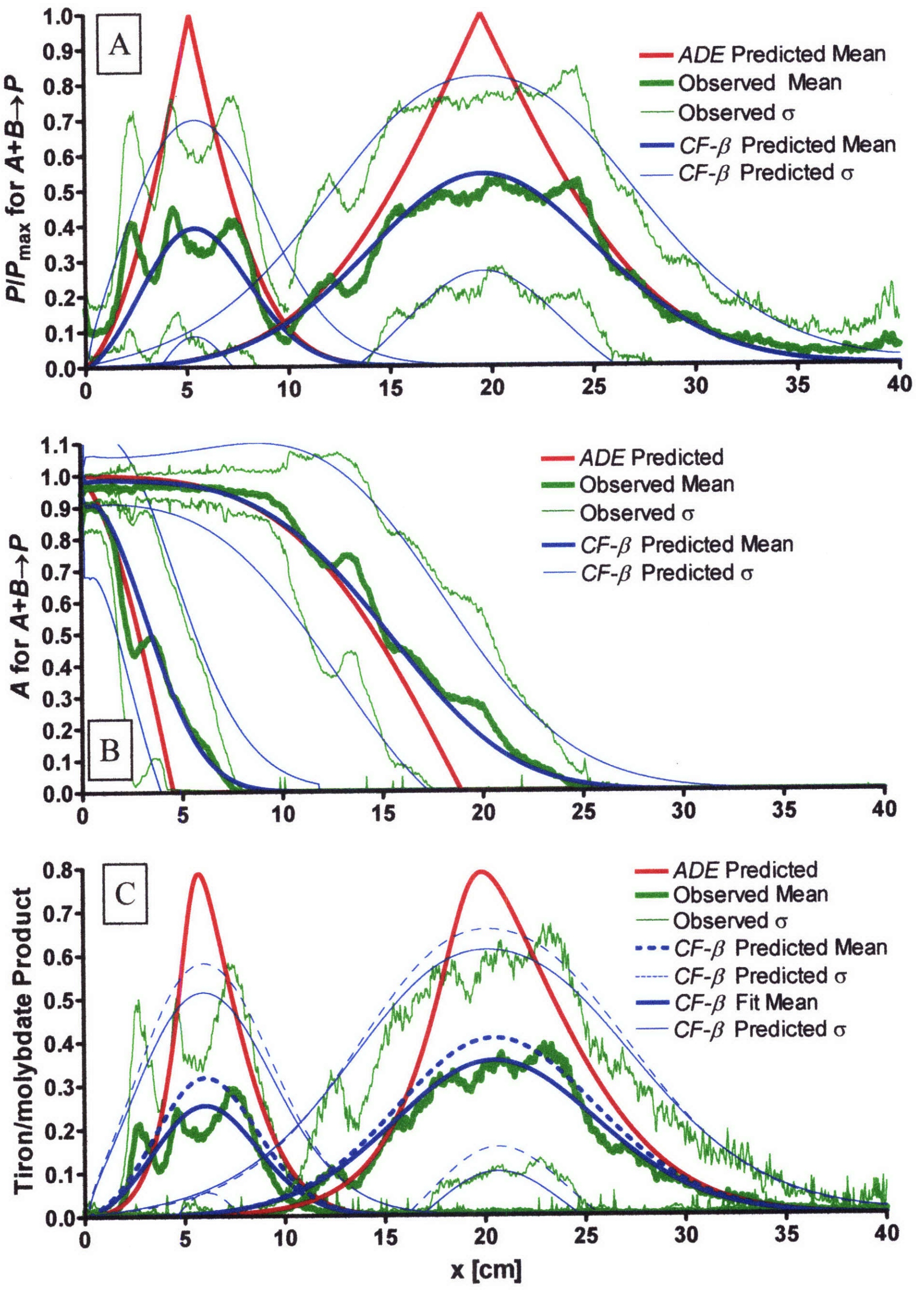

Figure 10. Mean concentration profiles ± 1 SD at 8 and 35 minutes. A) *P* for the *A*+*B* → *P* reaction. Mean *ADE* predicted *P* (implicitly assumed 0 SD), observed mean small-scale *P* ± 1 SD, and *CF-β* predicted mean *C* ± 1 SD. B) Mean *A* for the *A*+*B* → *P* reaction. Mean *ADE* predicted *A* (implicitly assumed 0 SD), observed mean small-scale *A* ± 1 SD, and *CF-β* predicted mean *A* ± 1 SD. C) Tiron/molybdate product. Solid lines: mean *ADE* predicted product (implicitly assumed 0 SD), observed mean small-scale product ± 1 SD, and best fit mean product from the *CF-β* model and associated ± 1 SD. Dashed Lines: mean *CF-β* predicted product ± 1 SD using variance parameters fit to the local dye tracer that do not account for pore-scale mixing.

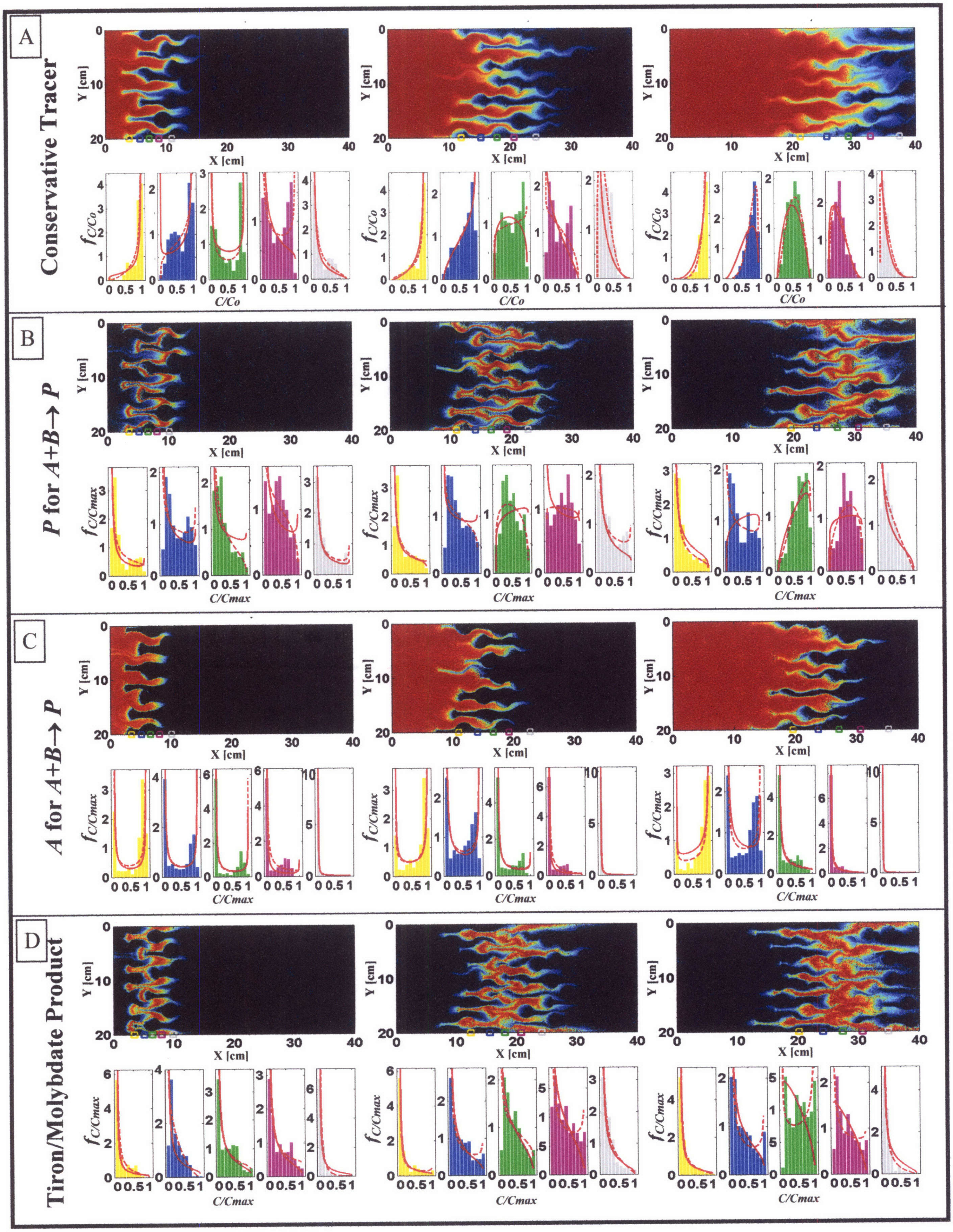

Figure 11. Observed, empirical beta (red dashed line), and *CF-β* beta (solid red line) modeled conservative and reactive distributions. Colored squares at the bottom of the concentration field show the location of the corresponding x-location of the corresponding colored distribution.

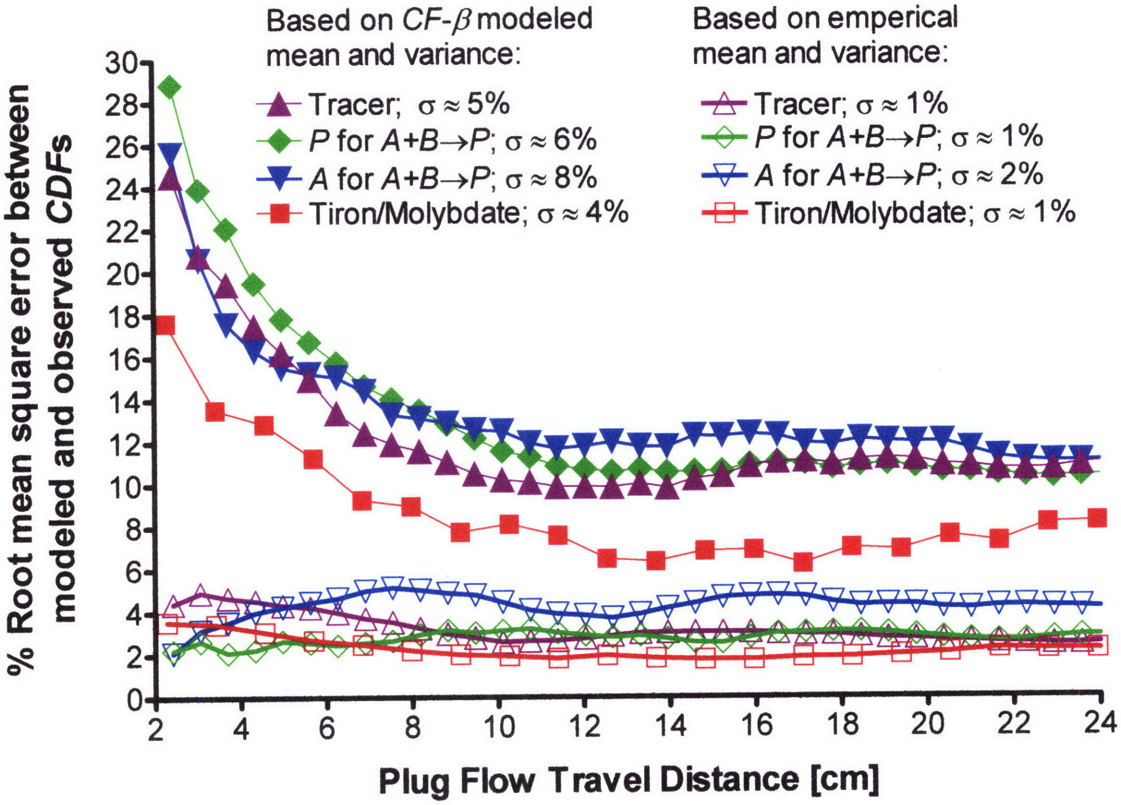

Figure 12. The root mean square error was calculated between the beta *CDF* and the empirical *CDF* across the dispersion front for a given plug flow distance. The mean behavior of this error is shown for beta distributions based on the modeled mean and variance (solid symbols) and empirical mean and variance (unfilled symbols).

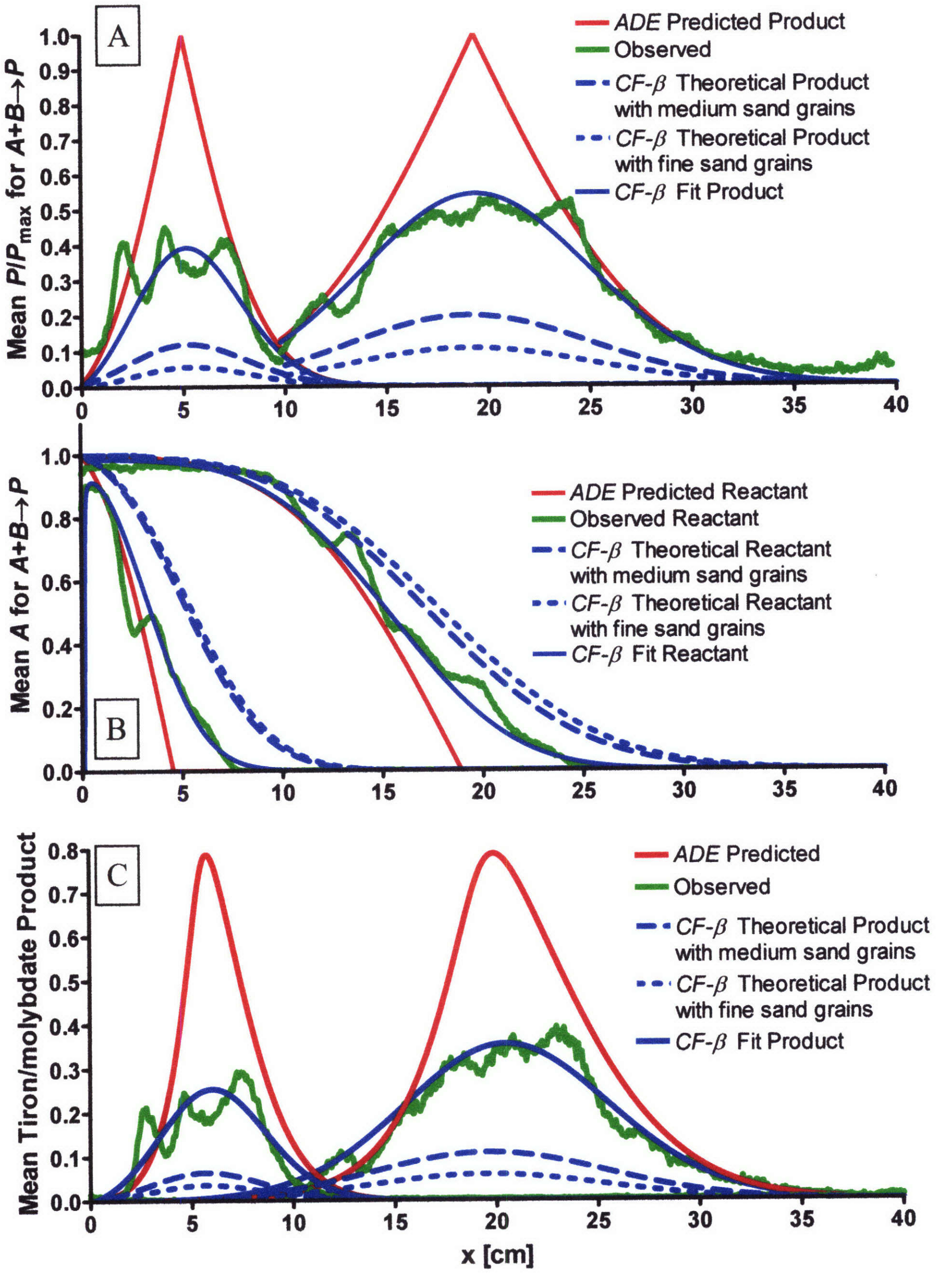

Figure 13. *ADE* and *CF-β* predicted mean concentration profiles at 8 and 35 minutes assuming finer grains and hence lower mechanical dispersivities for A) *P* for the $A+B \rightarrow P$ reaction. B) *A* for the $A+B \rightarrow P$ reaction. C) Tiron/molybdate product.

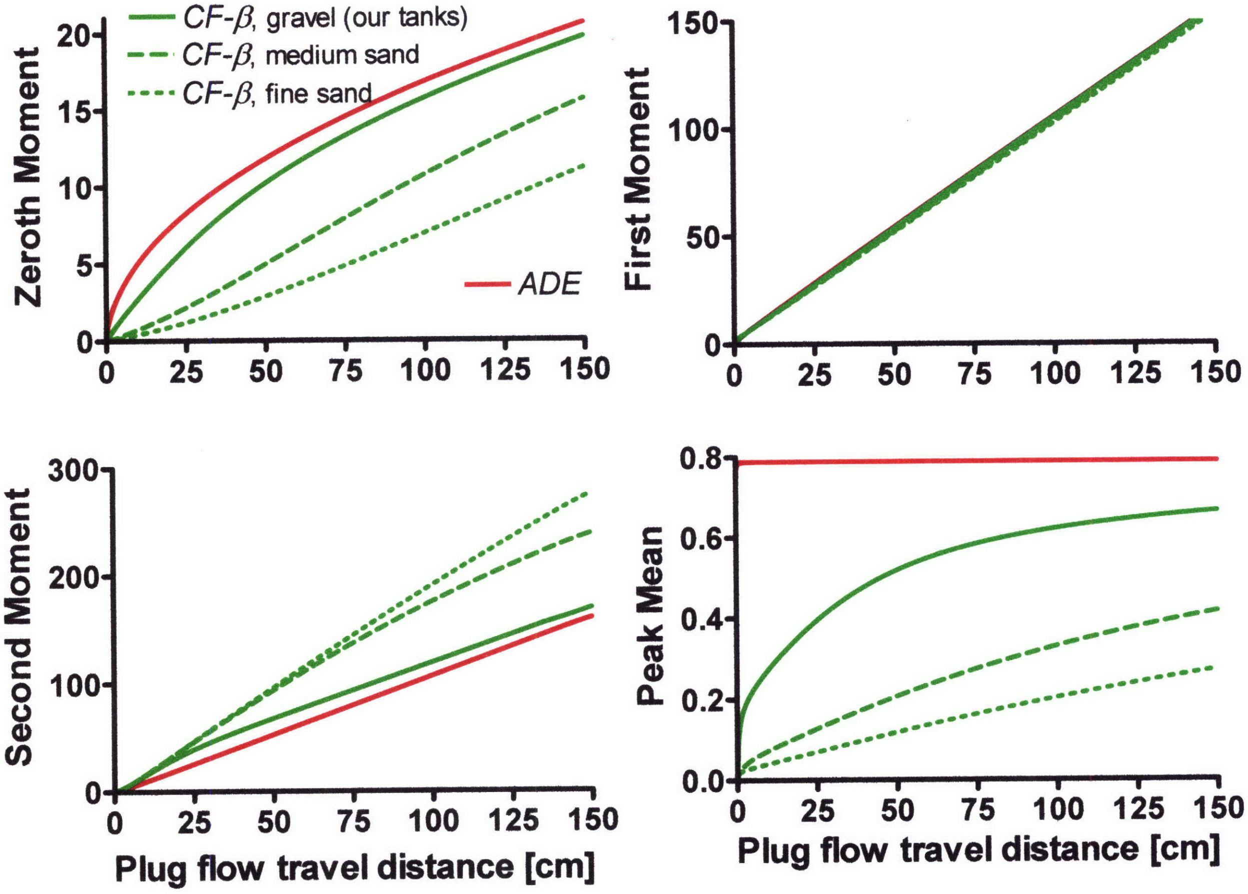

Figure 14. Zeroth moment, first moment, second moment, and peak of the mean *ADE* and *CF-β* predicted Tiron/molybdate product assuming finer grains and hence lower mechanical dispersivities in an extended domain.

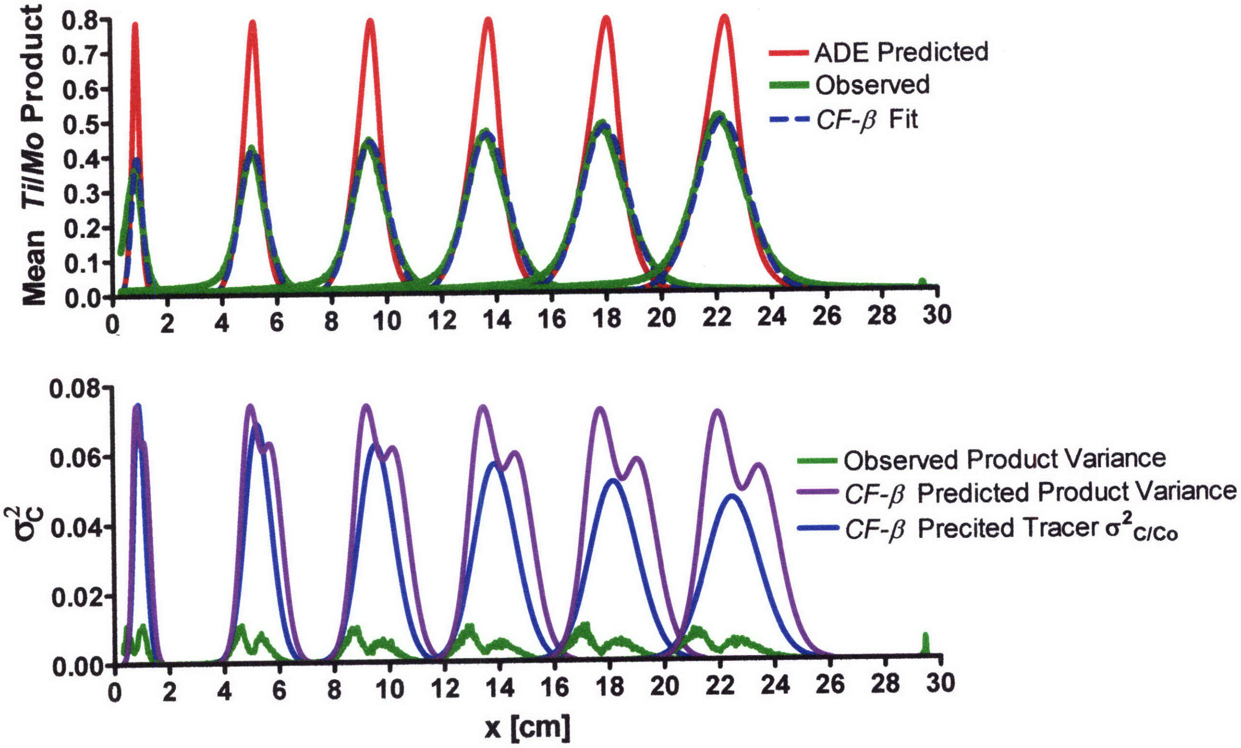

Figure 15. A) *ADE* predicted, *CF-β* fit, and observed mean Tiron/molybdate product in the homogeneous tank at 13, 58, 103, 178, 238, and 298 seconds. B) Observed pixel-scale product variance and *CF-β* predicted pore-scale variance for the same times as above. The blue line is the *CF-β* predicted variance with the same dispersivity and variance length scale of a conservative tracer with a constant source.

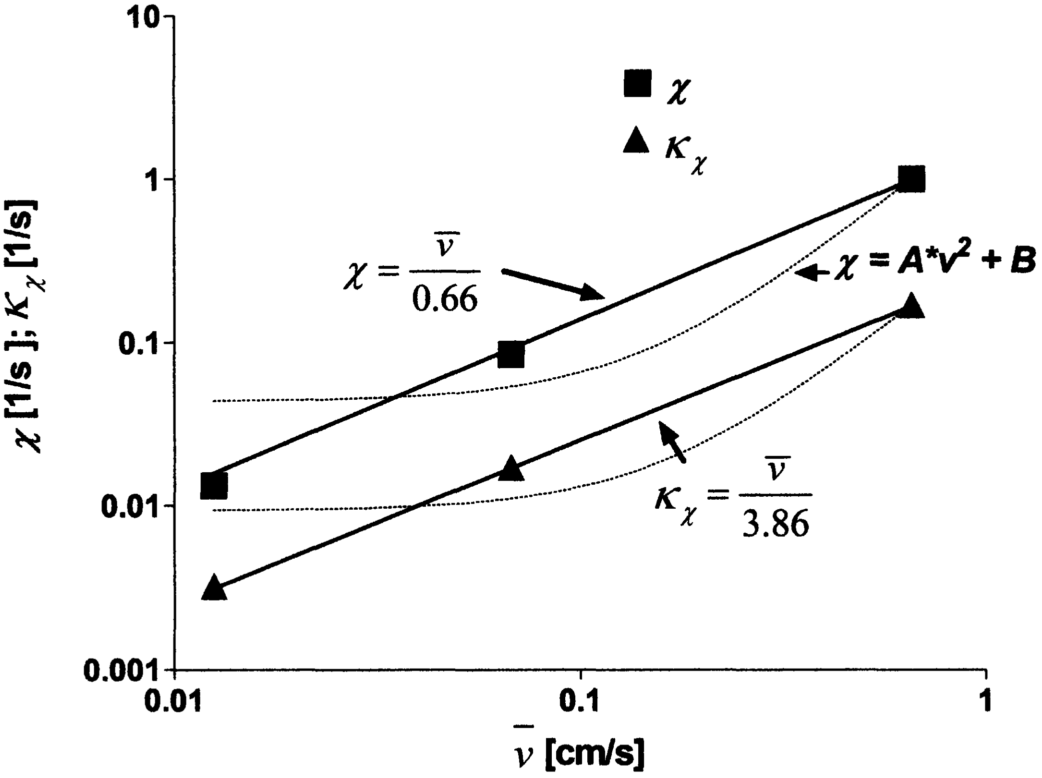

Figure 16. Variance destruction and pre asymptotic growth rate compared to mean velocity from the experiments of Gramling *et al.* (2002). χ is the rate of variance destruction and κ_χ is the rate that χ approaches its asymptotic value.

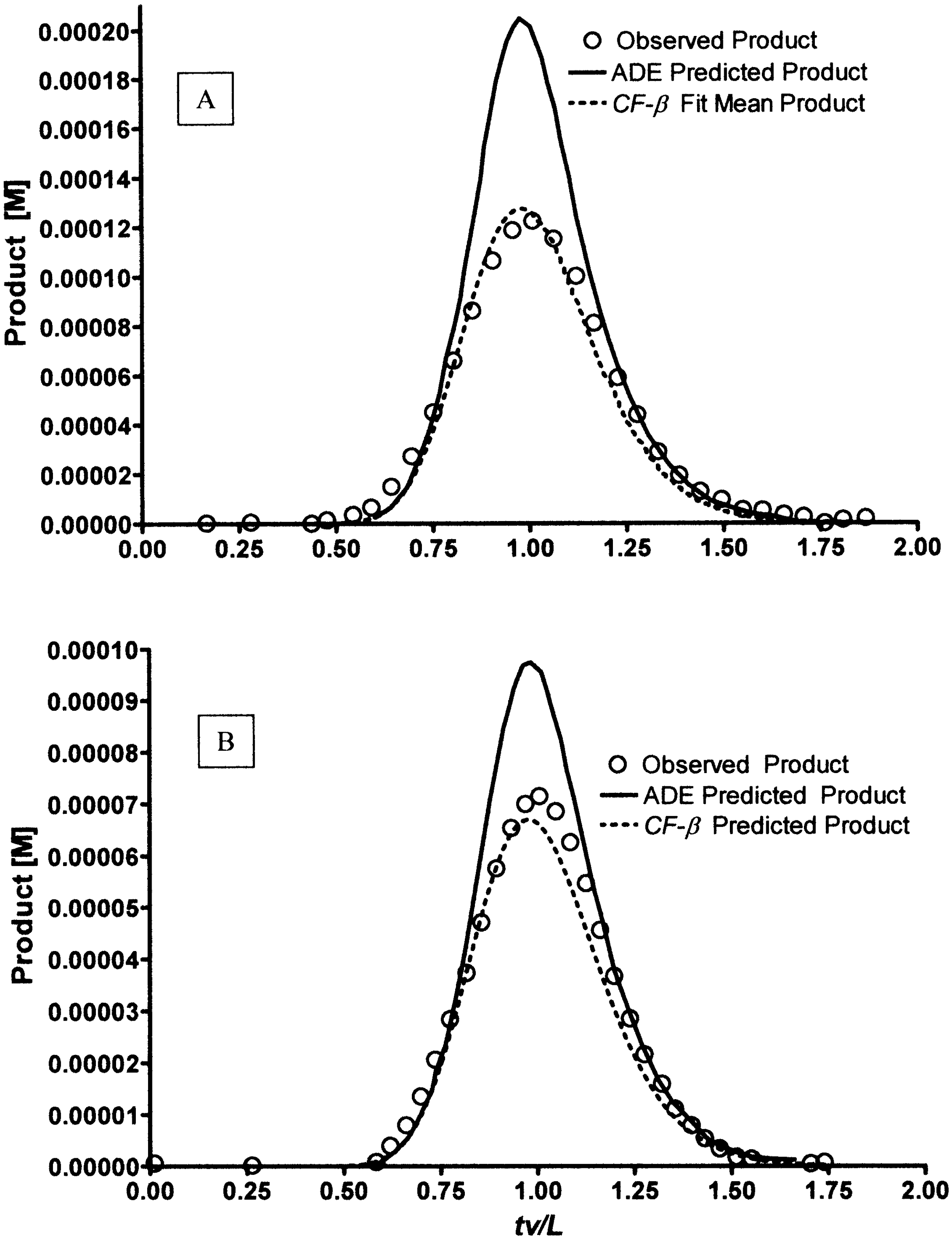

Figure 17. A) *CF-β* fit of the reactive breakthrough curve for run 1 of Raje and Kapoor (2000). B) *CF-β* prediction of the reactive breakthrough curve for run 2, which was at a different velocity and had different initial concentrations (Raje and Kapoor, 2000).

Table 1. Estimated Parameters for the Concentration fluctuation Model.

Experiment	$\bar{v}$ [cm/min]	A_x/a_x [cm]	θ [-]	d_{50} [cm]	χ_L [cm]	χ_G [cm]	$\overline{\Delta_L^C}$ [cm]	$\overline{\Delta_T^C}$ [cm]
Heterogeneous; $A+B \rightarrow P$	0.57	1.1	0.4	0.21/0.09	9.3	7.8	2.5	0.25
Heterogeneous; *Ti/Mo*	0.57	1.1	0.4	0.21/0.09	12.1	5.9	[2]NC	NC
Homogeneous; *Ti/Mo*	4.3	0.035	0.4	0.04	8.3	10.8	NC	NC
Homogeneous; Gramling *et al.* (2002)	39.6, 3.96, 0.78	0.27±0.1	0.35	0.13	0.7	3.9	NC	NC
Homogeneous; Raje and Kapoor (2000)	5.76, 4.2	0.33	0.45	0.15	8.6	3.2	NC	NC

[2] Not Calculated

Chapter 5. Production-Destruction Balances, Taylor Series, and Practical Considerations for the *CF-β* Model

Velocity fluctuations shear and distort fluid interfaces. This produces (co)variance and at the same time establishes mechanical-dispersive transverse concentration gradients that destroy (co)variance. The rates of (co)variance production and destruction asymptotically balance each another for both conservative and reactive flows. This balance leads to the following relationship to approximate an *m* by *n* aqueous species covariance matrix as a function of the variance length scale χ_L, macro-dispersivites A_{ij}, and species mean gradients:

$$\sigma^2_{C_m C_n} \approx 2\chi_L A_{ij}\left(\frac{\partial \overline{C_m}}{\partial x_i}\right)\left(\frac{\partial \overline{C_n}}{\partial x_j}\right)$$

We found this relationship to asymptotically hold for: 1) the following scenarios based on our experimental data: variance of a conservative tracer, covariance of two conservative tracers, covariance of two conservative species with differential sorption, variance of A and P for the A+B→P reaction, and the variance of the Tiron/molybdate product; and 2) the variances and covariance of oxygen and hydrocarbon undergoing a rate-limited double-Monod reaction where hydrocarbons sorbs with a retardation factor (R_H = 1.0, 1.2, 1.5, 4.0) from numerical simulations. The production-destruction balance can provide the necessary statistical moments to form multivariate reactant distributions to upscale complex reactive transport scenarios. Alternatively, we found that these second order moments can be used in an upscaled reaction expression derived from a second order Taylor series expansion. Incomplete mixing, parameterized by variance and covariance, caused the upscaled reaction rate of double-Monod kinetics to be almost an order of magnitude smaller compared to the conventional double-Monod reaction rate that implicitly assumes complete mixing. We propose the decisive variance length-scale can be measured in the field with a reactive breakthrough curve as it was for the work of Raje and Kapoor (2000), or possibly from a breakthrough curve of conservative concentration variance. Finally, manipulating the flow field to be perpendicular to its original direction would increase variance destruction and reactive mixing by an order of magnitude. Thus, generating a transient flow field would be a practical way to accelerate natural attenuation and bioremediation.

5.1. Introduction

So far in this series on upscaling reactive transport, we have presented a framework for solute transport modeling that approximates the correct amount of chemical reaction and concentration probability density functions. Probability density functions would aid in regulatory compliance situations based on the maximum contaminant levels (MCL) for example, to ensure there is a low probability that benzene would exceed its regulated probability of 5 ppb. Essentially, normalized conservative concentration distributions can be modeled as Beta distributions based on conservative mean and variance transport equations. Conservative distributions can then be transformed into joint reactant distributions with a mixing line as long as reactants sorb equally. Finally, as long as the reaction can be treated as instantaneous, all potential non-linear reactions can be calculated and the correct product and remaining reactant distributions can be formed.

A potentially important application of this approach is the mixing and reaction of oxygen and ethanol. The possibility of having a sustainable source of fuel has already led countries all over the world, notably Brazil, to have E10 or 10% ethanol fuel available (Niven, 2005) and General Motors (GM) has already produced over 2 million vehicles capable of running on E85 or 85% ethanol (GM, 2006). Even with current strict storage tank construction, monitoring, and regulations, spills have not been eliminated (Committee of Energy and Commerce, House of Representatives, 2003) and will likely never be eliminated (Niven, 2005). Ethanol itself is undesirable in groundwater and can severely limit the biodegradation of petroleum contaminants such as BTEX by preferentially reacting with oxygen and other electron acceptors. This effect hinders natural attenuation and extends contaminant plume lengths (e.g. Heermann and Powers, 1998; Molson *et al.*, 2002; Arey and Gschwend, 2005). Many numerical studies on the biodegradation of ethanol (e.g. Heermann and Powers, 1996; Stockholm *et al.*, 1998; Ulrich, 1999; McNab *et al.*, 1999) assume that ethanol biodegradation can be modeled as first order decay, which is incorrect. Ethanol biodegradation would result from a reaction where ethanol and an electron acceptor existed simultaneously (e.g. Molson *et al.*, 2002). Since ethanol and oxygen do not readily sorb and reaction rates are typically faster then mixing rates, the biodegradation of ethanol and electron acceptors would be mixing-limited and the $CF\text{-}\beta$ modeling approach would be suitable.

Currently, the $CF\text{-}\beta$ approach works for modeling equilibrium reactions, reactions with chemical kinetics much faster then mixing rates, and when there is no difference in chemical sorption. These restrictions arise because 1) we can currently only model the variance of total reactant because it is a conservative quantity and 2) because non-differential sorption allows for the covariance between species to be calculated from a mixing line. However, reactive transport situations with reactants having different retardation factors, such as oxygen and a non-polar organic contaminant in an aquifer with a significant fraction of organic carbon, is an important and practical scenario (Oya and Valocchi, 1998). Even with a large difference in retardation coefficients, reactive transport is still affected by small-scale dispersive mixing (Janssen *et al.*, 2006) and the $CF\text{-}\beta$ framework needs extension to handle this situation. Reactants with different retardation factors and rate-limited reactions would move concentrations off the mixing line and as such, the mixing line approach for forming joint reactant distributions would not apply. In order to form the yet to be determined multivariate distribution of reactants, or expand reaction terms with a Taylor series, the reactant variances and covariances need approximation.

Assuming that macro-dispersive (co)variance production balances mechanical dispersive (co)variance destruction affords simple mean gradient approximations for the space-time evolution of aqueous species covariance matrixes:

$$\sigma^2_{C_m C_n} \approx 2\chi_L A_{ij} \left(\frac{\partial \overline{C_m}}{\partial x_i} \right) \left(\frac{\partial \overline{C_n}}{\partial x_j} \right) \qquad (1)$$

where m and n are indices of the aqueous species and when $m = n$, the main diagonal of a species covariance matrix is the individual species variance. Using this assumption, which will be tested under a variety of conditions in this paper, more complex reactive transport situations might be modeled with following operator splitting approach: 1) at a time step transport the mean concentrations with standard software; 2) calculate the variances and covariances by scaling the mean gradients; 3) form a multivariate distribution (yet to be determined) based on these moments; 4) calculate all possible reactions in the multivariate distribution; 5) integrate the multivariate distribution and update all the mean concentrations. Alternatively, for some reactions, it could be possible to use these statistical moments in an upscaled reaction expression based on a truncated Taylor series about the mean concentrations. These approaches would avoid incomplete mixing error that exists in traditional approaches. Furthermore, scaling the mean gradients and assuming a Beta distribution would provide a complete statistical description for any species, which could aid in regulatory decisions based on maximum contaminant levels and calibrating transport models with field data.

In this paper, we test the production-destruction balance assumption for conservative and reactive transport from our tank experiments and from detailed numerical simulations. First, we investigate this assumption for conservative tracer variance based on transport parameters fit from our tank experiments. Next, we derive a governing equation for covariance of conservative species undergoing differential sorption and verify that the production-destruction balance holds for this scenario with our tank data. Then we cover some principles to show how the variance length-scale does not change because of chemical reactions and verify this and the production-destruction balance for the reactive flows in our tanks. Combining all these ideas, we verify the production-destruction balance for the mixing and rate-limited reaction of oxygen and hydrocarbon in a random conductivity field where hydrocarbon sorbs with a retardation factor of 1.0, 1.2, 1.5 and 4.0. We then cover some ideas about multivariate distributions, which still need further research before a full distribution approach can be applied to more complex reactive transport scenarios. As an alternative approach, we found that a second order Taylor series expansion of a reaction term about the mean concentrations produces an upscaled reaction rate as a function of mean concentrations and (co)variances. The second order approximation works well if the reaction can be approximated as quadratic. If a quadratic approximation is poor, higher order moments need to be included in the Taylor series. Next, we show empirical correlations between the decisive variance length-scale to other mixing parameters and propose how to measure it at a field site. Finally, we show that making the flow perpendicular to its original direction increases variance destruction and reactive mixing by an order of magnitude. This suggests that creating a transient flow field would be a practical way to accelerate mixing limited natural attenuation and bioremediation.

5.2. Production-Destruction Balances.

5.2.1. Conservative tracer variance.

The longitudinal velocity fluctuations of macro-dispersion create variance and covariance, but at the same time shear fluid packets setting up transverse concentration gradients that destroy variance and covariance. This implies that the rates of (co)variance production and destruction are intimately coupled because they are linked to the rate that macro-dispersive velocity fluctuations distort fluid interfaces. A common assumption in turbulence literature is that the production and destruction balance each other (e.g. Tennekes and Lumley, 1972; Shaw *et al.*, 2001). Gross and Nowell (1985) found production-destruction balances in a tidal channel; Trowbridge *et. al.* (1999) and Sanford and Lien (1999) found production-destruction balances in parts of a tidal estuary and tidal channel; and it its generally agreed that production-destruction balances exists in stable atmospheric boundary layers (e.g. Wyngaard and Cote; 1971, Wyngaard, 1992).

This concept has only recently begun to be applied to porous media research. Kapoor and Gelhar (1994b) and Kapoor and Kitanidis (1998) found a variance production-destruction balance for porous media for a Gaussian pulse at large times away from the center of mass; Kapoor and Kitandidis (1996) found this global balance to hold in two-dimensional periodic media; and Kapoor and Anmala (1998) found this true for rectilinear flows. Concentration variance is advected and dispersed like the concentration mean but is also produced by macro-dispersion and destroyed by mechanical dispersion:

$$\frac{\partial \sigma_C^2}{\partial t} = -\bar{v}\frac{\partial \sigma_C^2}{\partial x_1} + d_{ij}\frac{\partial^2 \sigma_C^2}{\partial x_i \partial x_j} - \frac{\partial\left(\overline{v_i'(c')^2}\right)}{\partial x_i} - 2\overline{c'v_i'}\frac{\partial \overline{C}}{\partial x_i} - 2d_{ij}\overline{\frac{\partial c'}{\partial x_i}\frac{\partial c'}{\partial x_j}} \qquad (2)$$

By equating production (second to last term of equation 2) to destruction (last term of equation 2) and adapting the closure approximations from Chapter 4, it is possible to obtain a very simple approximation for concentration variance (Kapoor and Gelhar, 1994b; Kapoor and Kitanidis 1998):

$$\begin{aligned} &-2\overline{c'v_i'}\frac{\partial \overline{C}}{\partial x_i} \approx 2d_{ij}\overline{\frac{\partial c'}{\partial x_i}\frac{\partial c'}{\partial x_j}} \Rightarrow 2\overline{v}A_{ij}\left(\frac{\partial \overline{C}}{\partial x_j}\right)\left(\frac{\partial \overline{C}}{\partial x_i}\right) \approx \frac{\overline{v}}{\chi_L}\sigma_{C'}^2 \Rightarrow \\ &\sigma_{C'}^2 \approx 2\chi_L A_{ij}\left(\frac{\partial \overline{C}}{\partial x_j}\right)\left(\frac{\partial \overline{C}}{\partial x_i}\right) \end{aligned} \tag{3}$$

Pannone and Kitanidis (2004) used a mixed Lagrangian/Eularian approach to find the variance of a conservative tracer is equal to the squared mean gradients multiplied by a constant as it is in the above expression. It is possible to derive simple analytic solutions for concentration variance using equation 3. The solution for mean concentration with remote boundaries (shown in 1-D) is:

$$\frac{\overline{C}}{C_O} = \frac{1}{2}erfc\left(\frac{x-\overline{v}t}{2\sqrt{\overline{v}A_x t}}\right) \tag{4}$$

This solution can be differentiated with respect to x to calculate the mean gradient, which is then squared and multiplied by the variance length-scale and macro-dispersivity to arrive at an approximate solution for the variance based on the production-destruction balance:

$$\sigma_{C/C_O}^2 = \frac{\left(1-e^{-\overline{v}t/(\chi_G)}\right)\chi_L e^{-\frac{(x-\overline{v}t)^2}{2A_x t\overline{v}}}}{2\pi t\overline{v}} \tag{5}$$

The first term on the right hand side of the equation has been included for early time behavior. Applying the parameters from our tank experiments, we can compare a finite difference solution of the full variance equation (see chapter 4) that includes all the terms in the variance budget with the solution based on the production-destruction balance (figure 1).

Figure 1.

During early times, even with the early time behavior of the variance length-scale accounted for, production is greater than destruction violating the balance assumption and variance is overestimated. Initially, production has to be greater then destruction or else there would never be any variance because there is no variance initially in the domain. For a hypothetical case of a larger variance length-scale (less mixing), the early time variance can be impossibly high and it takes longer to reach the correct values. However, the large time agreement is good and it should be kept in mind that the tanks are only about one-dozen correlation lengths long.

A 1-D production-destruction balance in terms of perturbation derivatives and recognizing that transverse dispersion is predominantly responsible for variance destruction (Chapter 4), yields:

$$\bar{v} a_T \overline{\left(\frac{\partial c'}{\partial T}\right)^2} \approx \bar{v} A_x \left(\frac{\partial \bar{C}}{\partial L}\right)^2 \qquad (6)$$

where T is in the transverse direction and L is in the longitudinal. For illustration and simplicity, we will assume that all the perturbation derivatives are equal, such that there would be a saw tooth transverse concentration profile along a transverse slice of a macro-dispersion front. Taking the square root of both sides of equation 6 shows that when the production-destruction balance holds, the absolute value of the transverse derivatives are proportional to the absolute value of the mean gradient:

$$\left|\overline{\frac{\partial c'}{\partial T}}\right| \approx \sqrt{\frac{A_x}{a_T}}\left|\frac{\partial \overline{C}}{\partial L}\right| \tag{7}$$

It is also easy to show that when the production-destruction balance holds, that the ratio of the macro-dispersive flux to the average transverse flux is proportional to the square root of the ratio of macro- to transverse mechanical-dispersivity. The dependence of the mean transverse gradient on the longitudinal mean gradient makes intuitive sense. The velocity fluctuations of macro-dispersion will shear and move packets of fluids past each other, which will establish transverse gradients between newly neighboring fluid packets as long as the packets have different concentrations. Therefore, on average, the magnitude of the transverse gradients should depend on the concentration difference between the newly neighboring sheared packets of fluid, which depends on the mean gradient (figure 2).

Figure 2.

This transference of mean gradients to transverse gradients shows how the production-destruction balance can occur locally. Generally, the velocity fluctuations control the rate of variance production and destruction, which leads to the balance.

As a conceptual example of how the production-destruction balance holds in flow fields with different conductivity and hence concentration structures, consider two flow fields with the same mean longitudinal concentration gradients, the same macro-dispersivity, and the same mechanical-dispersivity. However, the fields have different log conductivity variance and correlation lengths even though the product of the two is the same (figure 3).

Figure 3.

The mean concentration gradient and macro-dispersivities are the same for the two fields so variance production is occurring at the same rate. The field with the lower correlation length (figure 3-A) shows the solute fingers are closely spaced. As a result, it might be thought that variance destruction would occur faster in this field compared to the field with the solute fingers spaced further apart (figure 3-B). At large times, if variance destruction occurs at two different rates but is produced at the same rate, then the production-destruction balance cannot hold. However, panel C shows that the perturbation derivatives of the two fields are basically the same meaning that variance destruction is in fact occurring at the same rate. The difference of the two fields, is field *B* has more variance, which means that it would have a larger concentration micro-scale (recall the squared micro-scales are defined as the variance divided by the mean squared perturbation derivatives) and hence a larger variance length-scale. The last question to answer in this conceptual exercise, is with the same macro-dispersivity and if the production-destruction balance holds, how is it possible for one field to have more variance? Field *B* has a larger variance length scale and hence worse mixing compared to field *A*. This means that while the balance holds asymptotically, field *A* reached the production-destruction balance quicker then field *B*. As such, the early time condition of variance production being greater then variance destruction lasted longer for field *B* so it has more variance than field A at large times. This suggests that some function of the macro-dispersivity and the variance length-scale determines how quickly the production-destruction balance is achieved.

5.2.2 Conservative tracer covariance and differential sorption.

For the case of two conservative tracers mixing with no difference in sorption, the covariance can be directly calculated from a mixing line and it equals the variance but with opposite sign (Chapter 4). This means that since the rate of variance production balances the rate of variance destruction that the rate of covariance production has to balance the rate of covariance destruction and the following relation is also true

$$\sigma^2_{C_1C_2} \approx 2\chi_L A_{ij}\left(\frac{\partial \overline{C_1}}{\partial x_j}\right)\left(\frac{\partial \overline{C_2}}{\partial x_i}\right) \tag{8}$$

This relationship can be derived by applying a mixing line to equation 3, but it is explicitly derived for differential sorption below. Reactive transport situations with reactants having different retardation factors, such as oxygen and a nonpolar organic contaminant in an aquifer with a significant fraction of organic carbon, is an important and practical scenario. Species with different retardation factors would move concentrations off the mixing line and as such, the mixing line approach for calculating the covariance and for forming joint distributions would not apply.

To start to address this issue, consider two solutes ($C_n = C_1$, C_2) that do not react with each other and are subject to different equilibrium linear sorption ($R_n = R_1$, R_2), advection, and mechanical-dispersion:

$$R_n\frac{\partial C_n}{\partial t} = -\frac{\partial v_i C_n}{\partial x_i} + d_{ij}\frac{\partial^2 C_n}{\partial x_i \partial x_j} \tag{9}$$

Concentrations and velocities are decomposed into a mean and zero mean perturbation and a governing perturbation equation for each solute is derived as was done in Chapter 4. Next the two perturbation equations are added together and multiplied by (c_1'+ c_2'). Expectation is taken, and the individual solute variance equations (identical to equation 2 but with a retardation factor) are subtracted. Then making use of a symmetric dispersion tensor yields the governing equation for concentration covariance for two solutes undergoing different equilibrium sorption:

$$\begin{aligned}&(R_2+R_1)\frac{\partial \sigma^2_{C_1C_2}}{\partial t}+\overline{-R_2(c_2')\frac{\partial c_1'}{\partial t}-R_1(c_1')\frac{\partial c_2'}{\partial t}}=\\&-\frac{\partial \overline{v_i'c_1'c_2'}}{\partial x_i}-\overline{c_1'v_i'}\frac{\partial \overline{C_2}}{\partial x_i}-\overline{c_2'v_i'}\frac{\partial \overline{C_1}}{\partial x_i}-\bar{v}\frac{\partial \sigma^2_{C_2C_1}}{\partial x_1}+d_{ij}\frac{\partial^2 \sigma^2_{C_1C_2}}{\partial x_j \partial x_i}-2d_{ij}\overline{\frac{\partial c_1'}{\partial x_i}\frac{\partial c_2'}{\partial x_j}}\end{aligned} \tag{10}$$

Adopting the following closure approximations:

$$\overline{v_i'c_1'c_2'}=-\bar{v}A_{ij}\frac{\partial \sigma^2_{C_2C_1}}{\partial x_j}; \qquad d_{ij}\overline{\frac{\partial c_1'}{\partial x_i}\frac{\partial c_2'}{\partial x_j}}=\frac{\bar{v}}{\chi_L}\sigma^2_{C_1C_2} \tag{11}$$

yields the final form of the covariance equation with a new term still unclosed:

$$\begin{aligned}&(R_2+R_1)\frac{\partial \sigma^2_{C_1C_2}}{\partial t}=-\bar{v}\frac{\partial \sigma^2_{C_2C_1}}{\partial x_1}+\left(\bar{v}A_{ij}+d_{ij}\right)\frac{\partial^2 \sigma^2_{C_1C_2}}{\partial x_i \partial x_j}\\&+2\bar{v}A_{ij}\left(\frac{\partial \overline{C_1}}{\partial x_i}\right)\left(\frac{\partial \overline{C_2}}{\partial x_j}\right)-\frac{\bar{v}}{\chi_L}\sigma^2_{C_1C_2}+\overline{\left(R_2(c_2')\frac{\partial c_1'}{\partial t}+R_1(c_1')\frac{\partial c_2'}{\partial t}\right)}\end{aligned} \tag{12}$$

Concentration covariance is advected and dispersed like the concentration mean, produced by macro-dispersion, destroyed by mechanical-dispersion, and it is unclear exactly what the last term represents. When R_1 = R_2, the unclosed term disappears (after integration by parts) and the covariance equation collapses to the variance equation of a single solute, except with negative production term since the mean gradients of the two solutes will have opposite signs when one is leaving the domain and the other is entering. With no interaction and no difference in sorption, a mixing line holds, which means concentration variance equals negative covariance so the variance and covariance equations should be equal with opposite sign as they are.

Velocity fluctuations distort packets of fluids containing two species and create covariance proportional to the difference in concentrations of both species between fluid packets, which is captured by the mean gradients of both species. If there is no average concentration difference between distorted fluid packets of one species, i.e. the mean gradient is zero, then one species will not vary and no covariance will be produced. At the same rate, the velocity fluctuations distort fluid packets setting up transverse gradients of both species that controls mixing and covariance destruction. Again, we would expect the rate of production and destruction to balance each other because they are both controlled by the rate that the fluid interface is distorted. The only impact of differential sorption would appear in the mean gradients of the species. Assuming that macro-dispersive (co)variance production balances mechanical-dispersive (co)variance destruction in equation 12 leads to the following relation for solutes undergoing equilibrium linear sorption:

$$\sigma^2_{C_1C_2} \approx 2\chi_L A_{ij}\left(\frac{\partial \overline{C_1}}{\partial x_j}\right)\left(\frac{\partial \overline{C_2}}{\partial x_i}\right) \tag{13}$$

Note that this assumption allows us to ignore the unclosed term in 12. The solutions for mean concentrations with remote boundaries with C_1 in the domain and C_2 leaving the domain undergoing sorption are (shown in 1-D):

$$\frac{\overline{C_1}}{C_{1,o}} = \frac{1}{2} erfc\left(\frac{x - \bar{v}t / R_1}{2\sqrt{\bar{v}A_x t / R_1}} \right); \quad \frac{\overline{C_2}}{C_{2,o}} = 1 - \frac{1}{2} erfc\left(\frac{x - \bar{v}t / R_2}{2\sqrt{\bar{v}A_x t / R_2}} \right) \tag{14}$$

These solutions can be differentiated to obtain the gradient of the mean concentrations, which can then be multiplied and scaled by the variance length-scale and macro-dispersivity to arrive at approximate solutions for the variance:

$$\sigma^2_{C_n / C_{n,o}} = \frac{\left(1 - e^{-\bar{v}t / (R_n \chi_G)}\right) \chi_L R_n e^{-\frac{R_n \left(x - \bar{v}t / R_n\right)^2}{2 A_x t \bar{v}}}}{2\pi t \bar{v}} \tag{15}$$

and covariance:

$$\sigma^2_{C_1 / C_{1,o} C_2 / C_{2,o}} = -\frac{\left(1 - e^{-\bar{v}t / (R_2 \chi_G)}\right) \chi_L \sqrt{R_1 R_2}\, e^{-\frac{\frac{(R_1 + R_2) t \bar{v}}{R_1 R_2} + \frac{(R_1 + R_2) x^2}{t \bar{v}} - 4x}{4 A_x}}}{2\pi t \bar{v}} \tag{16}$$

where the first term on the right side of the equations have been included for early time behavior. While it was not clear a prori which retardation or average of retardation factors to use for the variance growth scale for covariance, we found the best agreement with our tank and numerical data was obtained with the larger of the two retardation factors. However, we did not test this for a difference in retardation factors greater than 4.

To assess the validity of the production-destruction balance assumption for covariance under differential sorption, we simulated the mixing of two non-interacting tracers with different retardation factors with the tracer data from out tank experiments. This was done by comparing images of our conservative tracer at different times. The C_1 field, which was entering the domain, followed the true temporal progression of the experiments. The C_2 field, which was initially in the domain, was calculated by applying a mixing line to a C_1 field from an earlier later time such that ratio of the C_1 time to the

C_2 time is equal to the retardation factor. Superimposing the C_1 and C_2 concentration fields allowed us to simulate three different scenarios where C_1 invaded C_2 and C_2 had retardation factors of R = 1.5, 2, and 3. The calculated variances of C_1, C_2, and covariance of C_1 and C_2 over y at a given x generally showed excellent agreement with the analytic solutions to the mean, variance, and covariance equations (14)-(16) for all three retardation cases (shown for R = 1.5; figure 4):

Figure 4.

We again found at early times that covariance was overestimated (similar to figure 1) but the large-time agreement was found to be excellent, and we were able to model the covariance of two non-interacting solutes that sorbed differently without accounting for the unclosed term. This demonstrates how the production-destruction balance holds under differential sorbing conditions and how various unclosed terms that arrive from a perturbation analysis can be neglected when applying the production-destruction balance assumption.

5.2.3 Instantaneous reactions.

There are three main issues to address for the production-destruction balance for reacting species: 1) How does the chemical reaction impact the expected value of the perturbation derivatives? 2) How does the chemical reaction affect the variance of reacting species as numerous new unclosed terms arrive from a perturbation analysis when reaction is included? 3) Does the chemical reaction affect the mean gradient in such a way that the velocity fluctuations produce variance at the same rate that they control the transverse gradients such that the production-balance still holds?

The fundamental issue of the first two questions is can the same concentration micro-scales, and hence variance-length scale, apply to both conservative and reactive transport? The only way that this is possible is if the chemical reaction changes the mean squared perturbation derivatives by the same amount it changes the variance. This would mean the ratio of the two would stay constant and the same length-scale would apply to variance destruction for both conservative and reactive concentrations. This is in fact what we find in both a simple theoretical exercise and with our tank data.

We first investigated a theoretical transverse concentration profile of total reactant *A* along a slice in a macro-dispersive front which was represented by a simple cosine function (figure 5).

Figure 5.

Next we calculated the corresponding profile of total reactant B_T by applying a mixing line. Then a reaction of $A+B \longrightarrow P$ was calculated where the amount of product *P* is equal to the limiting reactant and the amount of reactant *A* remaining is just what was there initially minus what was transformed into product. The squared concentration micro-scale is defined as a ratio of the variance to the mean squared perturbation derivatives:

$$\left(\Delta_T^C\right)^2 = \frac{\sigma_C^2}{\overline{\overline{\left(\partial c'/\partial T\right)^2}}} \qquad (17)$$

We see that the reaction increases the mean squared perturbation derivatives by the same amount as it increases the variances by essentially stretching the amplitude of the cosine function but not affecting the period. From equation 12 in the Chapter 4 the micro-scale has no relation to the amplitude. This shows that a chemical reaction can scale the amplitude of a periodic function and not change the micro-scale and hence the variance length-scale. To change the micro-scale, the reaction would have to change the wavelength which is unlikely as the average distance between similar concentrations is determined solely by the flow structure. This suggests that the micro-scales will not significantly change as a result of chemical reaction.

We tested this concept with out tank data. We calculated the longitudinal and transverse concentration micro-scales of the *A* and *P* fields for the $A+B \rightarrow P$ reaction with the approach described in Chapter 4. These results show that variance (figure 6-A) and the transverse perturbation derivatives (figure 6-B) are significantly affected by the chemical reaction. However, the ratio of the two, i.e. the transverse concentration micro-scale, remains almost constant before and after the reaction and across the dispersion front (figure 6-C).

Figure 6.

Overall, the mean micro-scales of *A*, *P*, and the conservative tracer behaved similarly (figure 7).

Figure 7.

The mean longitudinal micro-scale of *A* was slightly less than that for the conservative tracer and *P* but the transverse micro-scales, which is the micro-scale that controls mixing, are remarkably similar. This demonstrates that chemical reactions change the variance and the mean squared perturbation derivatives by roughly the same amount such that their ratio stays constant. This justifies using the same average micro-scale and hence variance length-scale for both conservative and reactive flows. Variance and covariance are controlled by the flow structure because the flow structure controls the average distance between solute fingers, which is characterized by the micro-scale. This can be observed in figure 9 from Chapter 4, where both conservative and reactive plumes have similar spatial patterns with tongues of solute separated by the same conductivity correlation scales.

The last requirement for the production-destruction balance to hold for reactive flows, is velocity fluctuations must produce variance at the same rate they control transverse gradients. To test this, we modeled the variance of reactant *A* and product *P* of the $A+B \rightarrow P$ reaction according to equation 1, which scales the respective squared mean gradients by the variance length-scale and macro-dispersivity that were obtained from the conservative tracer. The mean gradients were calculated using the *CF-β* model. The production-destruction-balance-predicted variance generally agreed well with the observed variance (figure 8).

Figure 8.

This implies that the production destruction balance holds for reactive flows when the concentration gradient is monotonic. However, the production-destruction balance approximation is poor in the center of the product plume *P* where the mean gradient is zero. Zero and almost zero concentration variance at points of zero-mean gradients have been observed and predicted (e.g. Vomvoris and Gelhar, 1997; Zang and Neuman, 1996; Kapoor and Anmala, 1998), but several studies have shown for pulse plumes, substantial variance can exist at points of zero-mean gradients (e.g. Graham and McLaughlin, 1989; Li and McLaughlin, 1991; Kapoor and Gelhar, 1994b; Kapoor and Kitanidis, 1998; Pannone and Kitanidis, 1999). This means the production-destruction balance has not been reached in the center where the mean gradient is zero and macro-dispersion is producing and/or transporting variance faster than local dispersion is destroying it. Fortunately, for pulse plumes, which are somewhat similar to a reaction product created by the mixing of two reactants, Kapoor and Gelhar (1994b) and Kapoor and Kitandis (1998) present a solution for variance of a conservative tracer. This solution has the basic production-destruction balance but also has a term that accounts for variance even when the mean gradient is zero (shown in 1-D)

$$\sigma_{C'}^2 \approx 2A_x\chi_L\left(\frac{\partial\overline{C}}{\partial x}\right)^2+\left(\frac{\chi_L}{vt}\right)^2\overline{C}^2 \tag{18}$$

The second term in equation 18 decays with the inverse of mean distance traveled relative to the variance length scale squared. We propose that it represents how long it takes for the production-destruction balance to be established at the center of the plume because it asymptotically approaches zero, which means the variance will eventually be solely determined by the production-destruction balance. Including this other term and applying it to our reaction product plume *P* (figure 9-A) and the Tiron/molybdate product (figure 9-B) the prediction is excellent.

Figure 9

We have shown that the production-destruction balance holds for the covariance of two solutes that sorb differently but do not react and for the variance of reactant plumes. The logical extension of these results is that the production-destruction balance holds for the variance and covariance of reactants that sorb differently but we could not test this with our tank data.

5.2.4 Rate-limited reactions and differential sorption.

Important reactive transport scenarios such as the rate-limited reactions between electrons acceptors (*e.g.* oxygen) and donors (*e.g.* hydrocarbons), where the electron donors sorb and the acceptors do not, needs to be addressed (e.g. Borden and Bedient, 1986; Borden *et al.*, 1986; Janssen *et al.*, 2006). In order to form the yet to be determined multivariate distribution of reactants or make Taylor series approximations, the reactant variances and covariances need approximation.

Detailed numerical simulations were used to test the hypothesis that production-destruction balances can approximate aqueous reactant variances and covariances under rate-limited reaction and differential sorption conditions. If the rate of macro-dispersive (co)variance production and mechanical (co)variance destruction balance one-another in the reactant species variance and covariance equations, then a species covariance matrix can be approximated as a function of the variance length-scale, macro-dispersivity, and mean gradients:

$$\sigma^2_{C_m C_n} \approx 2\chi_L A_{ij}\left(\frac{\partial \overline{C_m}}{\partial x_i}\right)\left(\frac{\partial \overline{C_n}}{\partial x_j}\right) \qquad (19)$$

where m and n are indices of the aqueous species and when $m = n$, the main diagonal of a species covariance matrix is the individual species variance. This assumption allows numerous unclosed terms to be neglected that arise from perturbation analysis in species variance and covariance equations.

MODFLOW was used to calculate a 2-D steady-state velocity field in a statistically-stationary, isotropic, lognormally-distributed, conductivity field with a Gaussian covariance structure created with GSLIB (table 1). Solute transport was run with MT3D and RT3D using the method of characteristics solution, which minimizes numerical dispersion and allows for small values of mechanical-dispersivity (Mehl and Hill, 2001). A conservative tracer was run through the domain and the mean velocity, macro-dispersivity, and the variance length-scales were fit to the observed conservative tracer mean and variance (figure 10).

Figure 10.

The fits are excellent and production almost balances destruction at early times for this case of large domain compared to correlation length (compare blue lines of finite difference solution which includes all the terms of the variance budget equation to the green lines based solely on the production-destruction balance). This field has a relatively low variance due to the small correlation length, which helps production balance destruction at early times. This was done to ensure that oxygen and hydrocarbon had a smooth mean gradient because the observed mean gradients will be used to test the production-destruction balance. In the section on Taylor series to follow, the production-destruction balance will be investigated for a higher variance situation.

Reactive transport was run with the hydrocarbon in the domain and oxygen entering (figure 11)

Figure 11.

where hydrocarbons undergoes equilibrium sorption and hydrocarbon and oxygen undergo a rate-limited double-Monod reaction governed by:

$$\frac{\partial O}{\partial t} = -\frac{\partial v_i O}{\partial x_i} + \frac{\partial}{\partial x_i}\left(v_i d_{ij} \frac{\partial O}{\partial x_j} \right) - \mu Y_{A/D}\left(M\right)\left(\frac{O}{k_O + O}\right)\left(\frac{H}{k_H + H}\right) \tag{20}$$

$$R_H \frac{\partial H}{\partial t} = -\frac{\partial v_i H}{\partial x_i} + \frac{\partial}{\partial x_i}\left(v_i d_{ij} \frac{\partial H}{\partial x_j} \right) - \mu\left(M\right)\left(\frac{O}{k_O + O}\right)\left(\frac{H}{k_H + H}\right) \tag{21}$$

where O is the concentration of oxygen [mg/l]; H is the concentration of hydrocarbon [mg/l]; μ is the contaminant utilization rate [s^{-1}]; $Y_{A/D}$ is the stochiometric yield coefficient [-]; M is the concentration of microorganisms, which are assumed immobile and non-prolific; k_O and k_H are the respective half saturation coefficients for oxygen and hydrocarbon; and R_H is the hydrocarbon retardation coefficient. The combination of reaction parameters was chosen such that the leading part of the oxygen front was fully consumed by the time it reached the end of the domain (table 1). It should be pointed out that applying a perturbation analysis to equations 20 and 21 to derive governing variance and covariance equations for oxygen and hydrocarbon would be extremely complex and contain numerous non-linear unclosed terms.

The oxygen and hydrocarbon means, variances, and covariances were calculated from the detailed 2-D concentration field after importing the results into Matlab. Then using the variance length-scale and macro-dispersivity fit to the conservative tracer, the observed mean gradients of oxygen and hydrocarbon were scaled according to equation 1 to predict the oxygen and hydrocarbon variances and covariance. The agreement between observed and predicted variances and covariances is excellent for the rate-limited reaction with no difference in sorption (figure 12),

Figure 12.

when hydrocarbon sorbs with $R_H = 1.5$ (figure 13),

Figure 13.

and when hydrocarbon sorbs with $R_H = 4.0$ (figure 14).

Figure 14.

This demonstrates that 1) macro-dispersive (co)variance production balances mechanical-dispersive (co)variance destruction under rate-limited and differentially sorbing conditions and 2) neither sorption or rate-limited reactions alter the variance length-scale for the parameters studied. The production-destruction balance assumption can provide the necessary statistical moments to construction multivariate distributions or Taylor series approximations.

5.3. Multivariate Distributions.

Multivariate Beta-distributions have been investigated and are still an active area of research (e.g. Mosimann. 1962; Michael and Schucany, 2002; Srivastava, 2003; Nadarajah, 2004). Girimaji (1991) developed a multivariate Beta distribution for mixing in turbulent flows which only requires transport equations for the concentration means and one additional transport equation for the sum of the species variance. This distribution has been used to investigate multiscalar mixing in turbulent flows (Girimaji, 1993), supersonic combustion (Baurle *et al.*, 1994), and this distribution has been shown to accurately model parts of the flow regime but poorly model other parts of the flow regime (Baurle *et al.*,1994). However, by using this assumed *pdf*, the species variances and covariances are no longer independent. This runs the danger of not forming the correct shape because the variances and covariances are incorrect (Gerlinger, 2003). We were unable to reproduce the mixing line case using any of the above referenced approaches.

As an alternative approach, it might be possible to numerically calculate the joint density without assuming a functional form but ensuring the following requirements are met: 1) the joint density integrates to 1; 2) the input means, variances, and covariances are honored; 3) concentrations are bounded between zero and the maximum; 4) the distribution is smooth. Consider a discrete joint density function P_{ij} of C_i and C_j. The moments are calculated:

$$1 = \sum_j \sum_i P_{ij} \tag{22}$$

$$\overline{C_i} = \sum_i C_i \sum_j P_{ij} \tag{23}$$

$$\overline{C_j} = \sum_j C_j \sum_i P_{ij} \tag{24}$$

$$\sigma_{C_i}^2 = \sum_i C_i^2 \sum_j P_{ij} - \left(\sum_i C_i \sum_j P_{ij} \right)^2 \tag{25}$$

$$\sigma_{C_j}^2 = \sum_j C_j^2 \sum_i P_{ij} - \left(\sum_j C_j \sum_i P_{ij} \right)^2 \tag{26}$$

$$\sigma_{C_{ij}}^2 = \sum_j \sum_i C_j C_i P_{ij} - \left(\sum_i C_i \sum_j P_{ij} \right)\left(\sum_j C_j \sum_i P_{ij} \right) \tag{27}$$

Calling the sum of the left of equations (22)-(27) f and the sum of the right g

$$f = g \tag{28}$$

The energy E of the distribution can be defined:

$$E = (f - g)^2 \tag{29}$$

At the solution, the energy is minimal or:

$$\frac{\partial E}{\partial P_{ij}} = 0 \tag{30}$$

This constraint should yield i times j equations to be solved simultaneously for all values of P_{ij}. Further, this produces values that honor the means, variances, and covariances, and by the very nature of the possible concentrations, the distribution is bounded. If this approach is computationally efficient, then n-dimensional multivariate distributions could be formed, all possible non-linear reactions could be calculated and weighted by their joint density, and the new product and reactant distributions could be integrated to update the new concentrations means. A computationally efficient way to calculate bounded multivariate distributions that honors the first two central moments is needed to extend the *CF-β* full distribution approach to more complicated reactive transport scenarios. Alternatively, it may be possible to use a Taylor series to upscale reactive transport.

5.4. Taylor Series Expansion for Mean Reactions.

5.4.1. Taylor series.

A general form of the upscaled reactive transport equation is:

$$\frac{\partial \overline{C_n}}{\partial t} = -\bar{v}\frac{\partial \overline{C_n}}{\partial x_1} + \left(\bar{v}A_{ij}\right)\frac{\partial^2 \overline{C_n}}{\partial x_i \partial x_j} - \overline{r\left(C_n\right)} \tag{31}$$

where $C_n = C_1, C_2$ for the mixing and reaction of two chemical reactants, and $\overline{r\left(C_n\right)}$ is the expected value of a reaction term. The upscaling approach discussed so far accounts for the expected value of the reaction term by: 1) approximating joint distributions of chemical reactants, 2) calculating all possible chemical reactions, and 3) integrating over the new distributions to obtain new concentration means and higher order moments.

An alternative approach to account for the expected value of the reaction term is to expand an arbitrary reaction term about the mean concentrations with a Taylor series and use the second order moments from the production-destruction balance. Concentrations are decomposed into a mean and zero mean perturbation:

$$C = \overline{C} + c' \tag{32}$$

and this relationship is used in a Taylor series expansion of a reaction that can be a function of one concentration:

$$r(C) = r(\overline{C}) + c'\left.\frac{\partial r}{\partial C}\right|_{\overline{C}} + \frac{1}{2}(c')^2 \left.\frac{\partial^2 r}{\partial C^2}\right|_{\overline{C}} + \ldots + \frac{1}{n!}(c')^n \left.\frac{\partial^n r}{\partial C^n}\right|_{\overline{C}} \tag{33}$$

or multiple concentrations:

$$r(C_1,\cdots,C_d) = \sum_{n_1=0}^{\infty}\cdots\sum_{n_d=0}^{\infty}\frac{\partial^{n_1}}{\partial C_1^{n_1}}\cdots\frac{\partial^{n_d}}{\partial C_d^{n_d}}\frac{r\left(\overline{C_1},\cdots,\overline{C_d}\right)}{n_1!\cdots n_d!}(c_1')^{n_1}\cdots(c_d')^{n_d} \tag{34}$$

Taking expectation of the Taylor series yields the expected value of the reaction in terms of mean concentrations and higher order moments.

5.4.2 First order second moment expansion for double-Monod kinetics.

Consider the rate-limited double Monod reaction for oxygen in equation 20:

$$r = \mu Y_{A/D}(M)\left(\frac{O}{k_O + O}\right)\left(\frac{H}{k_H + H}\right) \tag{35}$$

This reaction has the following Taylor series expansion about the mean concentrations truncated at second order terms:

$$\begin{aligned} r(O,H) \approx r(\overline{O},\overline{H}) &+ O'\left.\frac{\partial r}{\partial O}\right|_{\overline{O},\overline{H}} + H'\left.\frac{\partial r}{\partial H}\right|_{\overline{O},\overline{H}} + \frac{1}{2}(O')^2\left.\frac{\partial^2 r}{\partial O^2}\right|_{\overline{O},\overline{H}} + \frac{1}{2}(H')^2\left.\frac{\partial^2 r}{\partial H^2}\right|_{\overline{O},\overline{H}} \\ &+ (O'H')\left.\frac{\partial^2 r}{\partial H \partial O}\right|_{\overline{O},\overline{H}} \cdots \end{aligned} \tag{36}$$

All first order derivatives will by multiplied by zero after taking expectation. The second order derivatives taken at the mean concentrations are:

$$\left.\frac{\partial^2 r}{\partial O^2}\right|_{\overline{O},\overline{H}} = -2\mu Y_{A/D}(M)\left(\frac{k_O}{\left(k_O + \overline{O}\right)^3}\right)\left(\frac{\overline{H}}{\left(k_H + \overline{H}\right)}\right) \tag{37}$$

$$\left.\frac{\partial^2 r}{\partial H^2}\right|_{\bar{O},\bar{H}} = -2\mu Y_{A/D}(M)\left(\frac{\bar{O}}{\left(k_O+\bar{O}\right)}\right)\left(\frac{k_H}{\left(k_H+\bar{H}\right)^3}\right) \tag{38}$$

$$\left.\frac{\partial^2 r}{\partial O \partial H}\right|_{\bar{O},\bar{H}} = \mu Y_{A/D}(M)\left(\frac{k_O}{\left(k_O+\bar{O}\right)^2}\right)\left(\frac{k_H}{\left(k_H+\bar{H}\right)^2}\right) \tag{39}$$

Expectation of this Taylor series yields the mean reaction rate in terms of mean concentrations, variances, and covariance:

$$\begin{aligned}\overline{r(O,H)} \approx\; & \mu Y_{A/D}(M)\left(\frac{\bar{O}}{\left(k_O+\bar{O}\right)}\right)\left(\frac{\bar{H}}{\left(k_H+\bar{H}\right)}\right) - \mu Y_{A/D}(M)\left(\frac{k_O}{\left(k_O+\bar{O}\right)^3}\right)\left(\frac{\bar{H}}{\left(k_H+\bar{H}\right)}\right)\sigma_O^2 \\ & -\mu Y_{A/D}(M)\left(\frac{\bar{O}}{\left(k_O+\bar{O}\right)}\right)\left(\frac{k_H}{\left(k_H+\bar{H}\right)^3}\right)\sigma_H^2 + \mu Y_{A/D}(M)\left(\frac{k_O}{\left(k_O+\bar{O}\right)^2}\right)\left(\frac{k_H}{\left(k_H+\bar{H}\right)^2}\right)\sigma_{HO}^2\end{aligned} \tag{40}$$

The mean reaction rate $\overline{r(O,H)}$ only equals the conventional reaction rate of the mean concentrations $r(\bar{O},\bar{H})$ when there is no variance, i.e. in a beaker. Since the species variance is always positive and the covariance is always negative when one fluid displaces another, these terms that arise from incomplete mixing will always reduce the reaction rate based on the mean concentrations.

Combing this upscaled reaction rate with the macro-dispersive transport equations, the governing equations for mean oxygen and hydrocarbon undergoing rate-conventional limited reactions and differential sorption are:

$$\frac{\partial \bar{O}}{\partial t} = -\bar{v}\frac{\partial \bar{O}}{\partial x} - \bar{v}A_x\frac{\partial^2 \bar{O}}{\partial x^2} - \overline{r(O,H)} \tag{41}$$

$$R_H\frac{\partial \bar{H}}{\partial t} = -\bar{v}\frac{\partial \bar{H}}{\partial x} - \bar{v}A_x\frac{\partial^2 \bar{H}}{\partial x^2} - \overline{r(O,H)}/Y_{A/D} \tag{42}$$

The variances and covariances in the reaction term (equation 40) are provided by the production-destruction balance:

$$\sigma^2_{C_m C_n} \approx 2\chi_L A_{ij}\left(\frac{\partial \overline{C_m}}{\partial x_i}\right)\left(\frac{\partial \overline{C_n}}{\partial x_j}\right) \tag{43}$$

Furthermore, the full distribution of any species can be approximated using the modeled mean and variance and assuming a Beta distribution.

These upscaled equations and the production-destruction balance were tested against a second flow and transport scenario with a new set of parameters conducive to complex mixing and reaction (table 1). Hydrocarbon is initially in the domain, oxygen is entering, and product is calculated as a conservative tracer minus oxygen (figure 15).

Figure 15.

First, the mean velocity, macro-dispersivity, and variance length-scale and growth-scale were fit to a conservative tracer run through the conductivity field (figure 16).

Figure 16.

The concentration mean and variance equations showed good agreement, albeit production was greater than destruction for a significant part of the domain. Using the parameters fit from the conservative tracer, the upscaled reactive transport equations (40-43) did an excellent job of predicting the space-time evolution of the mean oxygen, hydrocarbons, and product concentrations (figure 17, top row).

Figure 17.

Intimately tied to the mean concentrations, the production-destruction balance provided a good approximation of species variances and covariance (figure 17, middle row). The incomplete mixing of the complex reactive fluid interface is captured by the variance and covariance, which manifests by lowering the mean reaction rate by almost an order of magnitude (figure 17, bottom row).

Initially in the domain, variance and covariance production is greater then destruction and variance and covariance are over predicted. This has the effect of under predicting the upscaled reaction rate and the mean amount of predicted reaction is less then the observed mean reaction. However, as production starts to balance destruction, the predicted and observed reactant concentrations agree. One potential way to overcome this problem is to fit the variance length-scale and variance growth scale using the production-destruction balance over the whole domain. This essentially forces the mathematical relationship to hold and the early time imbalance is imbedded within the variance length-scale and growth-scale. We found the fit to conservative variance with this approach to be equally as good as applying the full variance equation with all the terms in the variance budget. The variance length-scale remained virtually the same but the variance growth-scale increased significantly. We found in the last Chapter that the variance length-scale increased with travel distance because the longitudinal micro-scale increases with travel distance as the longitudinal contribution to variance destruction decreases. When forcing the mathematical relationship of the production-destruction balance to hold throughout the domain, the variance growth-scale also captures how far a plume has to travel to for the production-destruction balance to be obtained.

5.4.3 Tiron/molybdate reaction and higher order expansion.

We applied a second order Taylor series expansion to the Tiron/molybdate reaction analogous to equation 36. The second order derivatives were calculated at the mean concentrations with central finite differences. The variances and covariance of total Tiron and total molybdate were calculated by applying a mixing line to the variance of a conservative tracer modeled with parameters from the tank experiments. The second order approximation for the Tiron/molybdate reaction is poor when modeling the tank behavior (figure 18).

Figure 18.

There are areas of the Tiron/molybdate reaction, notably around the peak product, that are too non-linear to be approximated as quadratic (figure 19-A).

Figure 19.

Furthermore, the error in the quadratic approximation is amplified by the large derivatives of how the Tiron/molybdate product changes with respect to changes in Tiron because the molar absorbance coefficient multiplies the product concentrations by a factor of 80. This combined effect can be observed in figure 18. At the right side of the product front, the approximation is respectively better where the function is better approximated as quadratic. Where the product peaks, the function is highly non-linear with respect to total Tiron and molybdate, and we see that this is the area where the error is the largest. The second order approximation works well for the modeled double Monod kinetics because the reaction can be well approximated as quadratic (figure 19-B). With highly non-linear reactions, truncating the Taylor series at second order terms is inadequate and higher order approximations are needed.

For non-linear chemical reactions involving one chemical species or two chemical species that lie on a mixing line, higher order moments can be provided by assuming the chemical species are Beta distributed. The shape parameters of the Beta distribution are a function of the mean and variance:

$$a=\overline{C/C_O}\left(\frac{\overline{C/C_O}\left(1-\overline{C/C_O}\right)}{\sigma^2_{C/C_O}}-1\right);\qquad b=\left(1-\overline{C/C_O}\right)\left(\frac{\overline{C/C_O}\left(1-\overline{C/C_O}\right)}{\sigma^2_{C/C_O}}-1\right) \tag{44}$$

which can be provided from transport equations and production-destruction balances. The third and fourth moments of the Beta distribution are:

$$\frac{\overline{(c')^3}}{C_O^{\,3}}=\frac{2(b-a)\left(\frac{ab}{(a+b)^2(a+b+1)}\right)^{3/2}\sqrt{a+b+1}}{\sqrt{ab}\,(2+a+b)} \tag{45}$$

$$\frac{\overline{(c')^4}}{C_O^{\,4}}=\frac{a^2b^2\left(3+\frac{6\left(a^2+a^3-4ab-2\left(a^2+ab\right)b+b^2+b^3\right)}{ab(a+b+2)(a+b+3)}\right)}{(a+b)^4(1+a+b)^2} \tag{46}$$

The n^{th} moment can be calculated from the moment generating function for the Beta distribution given as:

$$\frac{\overline{(c')^n}}{C_O^{\,n}} = \left(-\frac{a}{a+b}\right)^n F_1\left(-n, a; a+b; \frac{a+b}{a}\right) \tag{47}$$

where F_1 is a hypergeometric function. For bimolecular reactions that lie on a mixing line the following relationship that was derived in Chapter 4 can be used to calculate higher order cross moments:

$$c'_1 = -c'_2 \tag{48}$$

For example to calculate a sixth order cross moment:

$$\frac{\overline{(c_1')(c_2')^5}}{C_{1,O}C_{2,O}^{\;5}} = -\frac{\overline{(c_1')(c_1')^5}}{C_{1,O}C_{1,O}^{\;5}} = -\frac{\overline{(c_1')^6}}{C_{1,O}^{\;6}} \tag{49}$$

where the sixth order moment can be obtained from the moment generating function of the Beta distribution. However, if a mixing line does not apply, then it is not clear how to calculate higher order cross moments. Like the multivariate distributions, they would likely need to be calculated as a function concentration means, concentration covariance matrixes and the under the conditions that concentrations are bounded and have a smooth multivariate distribution. Theoretically, this principle could be used to model the Tiron/molybdate reaction if enough higher order terms were included.

Combining a low order Taylor series expansion of a reaction term to upscaled transport equations is an attractive approach for upscaling complex mixing and reaction for its simplicity and computational efficiency. For some reactions, this approach coupled to the production-destruction balance is able to model the correct space-time evolution of the product and reactant means, variances, and assumed Beta *pdfs* without resolving heterogeneity or utilizing multivariate distributions that are yet to be determined. Furthermore, Taylor series provide a natural framework for expanding heterogeneous reaction parameters that could account for solid-phase chemical or microbial heterogeneity, if practical ways to calculate the covariance of between aqueous and solid phase concentrations are developed. However, as was demonstrated for the Tiron/molybdate product, when the chemical reaction is highly non-linear, low order approximations can yield poor predictions and higher order moments must be included. This area needs further research to determine what types of reactions have well behaved Taylor series and how to approximate higher order cross-moments. In regards to *CF-β* framework, two important issues that warrant discussion are: 1) how to obtain the variance length-scales for a given modeling situation and, 2) casting reactive mixing as variance destruction, is there a way to enhance favorable mixing in the subsurface?

5.5. Discussion

5.5.1. χ_L, the variance length-scale.

5.5.1.1. Empirical correlations. As far as we know, a first order approximation of the variance length-scale based on the traditional statistics of the conductivity field has not yet been achieved. Kapoor and Gelhar (1994a) were able to relate the concentration micro-scales to the micro-scales of the log conductivity field, which are defined as:

$$\left(\Delta_i^{\ln K}\right)^2 = \frac{\sigma_{\ln K}^2}{\overline{\left(\partial \ln K'/\partial x_i\right)^2}} \tag{50}$$

Unfortunately, to calculate the expected value of the derivatives of the log conductivity fluctuation field would require intensive characterization of the conductivity field (Kapoor and Gelhar, 1994b) and is not feasible in a real field situation. Kapoor and Kitanidas (1996) use calculus of variations to present an upper bound on the variance length scale; Kapoor and Anmala (1998) present three different bounds for rectilinear flow; and Kapoor and Kitandis (1998) apply the Schwartz inequality to give a lower bound to variance length scale as a function of the Lagrangian velocity integral timescale.

From the Lagrangian perspective of concentration variance, the statistical quantity that controls the rate of variance destruction is the transverse Peclet number defined as the transverse correlation length λ_T number divided by the transverse mechanical dispersivity a_T: $Pe_T = \lambda_T / a_T$ (e.g. Dagan and Fiori, 1997; Fiori and Dagan, 2000; Vanderbrought, 2001). To our knowledge, the transverse Peclet number and the variance length-scale have not been rigorously compared, but based on the limited work done to date, they appear highly correlated (figure 20-A).

Figure 20.

Another measure of mixing that has been applied to reactive transport is effective dispersion (Dentz etl al., 2000; Cirpka, 2002; Jose and Cirpka, 2004; Jose *et al.*, 2004). Effective dispersion contains the key term τ_{D_t}, which is the time-scale for transverse dispersion, and it determines how long it takes effective-dispersion to catch up to macro-dispersion. Assuming that local dispersion depends on the mean velocity, the time scale for transverse dispersion can be written as: $\tau_{D_t} = \lambda_T^2 / \left(\bar{v} \alpha_T \right)$. Multiplying both sides of the equation by the mean velocity produces a length-scale, which can be thought of as a distance that a plume has to travel before effective dispersion catches up to macro-dispersion. Comparing this distance to the variance length-scale shows that these quantities are also highly correlated (figure 20-B). Furthermore, Pannone and Kitanidis

(2004) found for an isotropic first type hole-Gaussian function (Vomvoris and Gelhar, 1990) that at large times and for a 1-D case, concentration variance can be written as:

$$\sigma_C^2 = 2A_x \frac{\lambda^2}{4\alpha}\left(\frac{\partial \overline{C}}{\partial x}\right)^2 \tag{51}$$

We have observed in this work that the production-destruction balance leads to a very similar relationship:

$$\sigma_C^2 = 2A_x \chi_L \left(\frac{\partial \overline{C}}{\partial x}\right)^2 \tag{52}$$

Equating the right hand sides of equations 51 and 52, $\chi_L = \lambda^2/4\alpha$, under the conditions that 51 is valid. This is also very similar to the distance of effective-dispersion.

Kapoor and Gelhar (1994) also state that the log conductivity microscales will generally be proportional to the log conductivity correlation scale. For scales of evolving heterogeneity (e.g. Dagan, 1994; Neuman, 1995; Bellin *et al.*, 1996) the log conductivity correlation scale increases with overall scale (e.g figure 6.5, Gelhar, 1993). Because the variance length-scale appears related to the correlation scale, there is a good possibility that like macro-dispersivity, the variance length-scale would exhibit scale dependency, which is supported by the very limited data available (figure 20-C). The scale dependence of correlation lengths could have very important implications for mixing and reaction. Larger correlation scales of conductivity would cause solute to flow in and around larger structures represented by larger macro-dispersion and hence a larger term of variance production. Concurrently, the transverse mechanical-dispersion that actually creates mixing will have larger and larger fingers to mix across and hence a slower variance destruction term. In the case of a fractal conductivity field, the upscaling problem from incomplete mixing could persist over very large spatial and temporal domains. The framework provided in this work should be suitable for handling this problem using scale-dependent parameters.

While an exact formulation for variance length-scale has yet to be derived as a function of standard geostatistical parameters, which are rarely available or practical to measure, there is always the possibility of directly measuring this parameter at a field site. This would also allow for the simultaneous measurement of macro-dispersivity. Tracer tests are much more practical than directly resolving the statistical parameters of the conductivity field, especially the log conductivity micro-scales. In fact, measuring the variance length-scale would yield information about the log conductivity micro-scales and the small-scale separation behavior of the log conductivity covariance structure, which would be useful for building new covariance structures for geostatistical simulations.

5.5.1.2. Measuring χ_L at a field site. Measurements of variance destruction rates are difficult because it requires resolution at small-scales. Destruction rates are measured in turbulence in three classic ways (Stewart and Huq, 2006): 1) Resolve all spatial gradients and use the exact definition of the expected value of the concentration perturbation derivatives. 2) Measure or model all the other terms in the variance budget to yield the destruction rate; this is likely difficult at a field site because it requires measuring concentration variance which may be possible (more below). 3) Compute the area under the destruction spectrum; this is also difficult because it requires probes with high resolution and the spectrum often has to be extrapolated to close the integral (Zhou and Antonia, 2000). The full conductivity spectrum at a field site, especially the high wave numbers, is difficult to determine (Kapoor and Kitanidas, 1998) and therefore it would be difficult to predict the full concentration spectrum. Nash and Moum (2002) used a fast-conductivity/temperature micro-probe to measure oceanic salinity microstructure and the destruction spectrum. Wain and Rehmann (2005) resolved the temperature spectrum and hence destruction rate in bubble plume with a self-contained autonomous microprofiler (SCAMP), which is capable of measuring small-scale temperature fluctuations. Alford *et al.* (2006) were able to resolve the salinity spectrum by using a fiber optic sensor to measure oceanic density fluctuations by refractive index signatures.

We propose a new approach to measure the variance length-scale and growth-scale: by measuring the breakthrough curve of a reaction product such as a rate-limited bimolecular tracer as we did in analyzing the work of Raje and Kapoor (2000). Our preliminary results suggest that the essential length scales, χ_L and χ_G, for this reactive transport modeling framework can be determined by observing the mean product of a bimolecular reaction downstream from their source. In fact, fitting these parameters to reactive tracer data was so sensitive that we were able to distinguish between complete and incomplete pore-scale mixing in the heterogeneous tank (Chapter 4). We propose that these length-scales can be determined from the measured breakthrough curves of a rate-limited bimolecular reaction, where the reaction rate is slow enough to prevent reaction during sampling (i.e. negligible reaction in the well-bore or sampling lines). Tiedeman and Hsieh (2004) showed that equal-strength forced-gradient well-to-well tests yield longitudinal dispersivities closest to natural flow and transport conditions. Consequently, we propose to use this type of well-to-well setup for a reactive tracer test.

The bimolecular reaction should have products and reactants that do not sorb, are non-toxic at aquifer concentrations, are easily detectable after significant dilution, and have a low molecular weight so significant concentrations can be added without creating density effects. Additionally, it would be convenient if one of the reactants were naturally present in the ambient groundwater and if there was little interference from other ambient chemical species. If this situation does not exist, the two reactants could be injected in sequence. SN2 methyl-halide reactions contain many of the desired attributes. For example, the widely studied reaction of methyl-bromide and chloride has a half-life on the order of days, the reactants do not significantly sorb, and bromide is a product, which is routinely measured as a quasi-conservative tracer (Schwarzenbach *et al.*, 2002).

As an alternative approach for determining the variance length-scale and growth-scale, it could be possible to directly measure and then model conservative variance. Theoretically, a "spiny well" could have dozens of fiber optic cables extend out of the well screen and measure point locations of fluorescent tracers such as fluorescein (Jose and Cirpka 2004; Jose *et al.*, 2004). These point concentrations could be used to construct a breakthrough curve of concentration variance, which could then be modeled to fit variance length-scale and growth-scale. Furthermore, this approach might provide the many breakthrough curves required to characterize apparent dispersion at a field site (Jose and Cirpka, 2004; Jose *et al.*, 2004). Every fiber optic probe could serve to sample a stream tube and be used to calculate an experimental breakthrough curve and yield an apparent dispersion coefficient. Then the relationship of Dentz *et al.* (2000) could be used to scale the apparent dispersion coefficient along each stream tube if a reactive breakthrough curve at different distances was required as long as the transverse correlation length and transverse mechanical-dispersivity is also known. The same type of field measurement is needed to provide information for two different approaches of reactive transport modeling.

5.5.2 A Practical Result of Variance Destruction: Transience-Enhanced Mixing.

For long thin contaminant plumes, the rate of natural attenuation and enhanced biodegradation is controlled by transverse mixing of electron acceptors/donors and the contaminant substrate (e.g. Cirpka *et al.*, 1999; Grathwohl *et al.*, 2000). Transverse mixing is very slow, and if mixing could be enhanced, it might greatly accelerate the rates of natural attenuation and biodegradation. One way to enhance mixing and reaction is by creating a transient flow field (Bagtzoglou and Oates, 2006). This concept can be verified simply by considering the variance destruction, or mixing term. If the flow field is suddenly perpendicular to its original direction, then longitudinal dispersion will mix over a series of steep concentration gradients characterized by the much smaller transverse micro-scale:

$$\chi = \frac{\bar{v}}{\chi_L} = \frac{2\bar{v}a_L}{\left(\Delta_L^C\right)^2} + \frac{2\bar{v}a_T}{\left(\Delta_T^C\right)^2} \quad \textit{create perpendicular flow} \Rightarrow \quad \frac{2\bar{v}a_T}{\left(\Delta_L^C\right)^2} + \frac{2\bar{v}a_L}{\left(\Delta_T^C\right)^2} \qquad (53)$$

Creating perpendicular flow for the concentration micro-scales and assumed mechanical dispersivities for our tanks decreases χ_L by almost an order of magnitude and therefore increases the rate of variance destruction and reactive mixing rate by an order of magnitude. Of course, the transverse micro-scale is now the longitudinal micro-scale and would be expected to grow as macro-dispersive velocity fluctuations create steep transverse concentration gradients for transverse dispersion to act over. Then after a given travel distance, perhaps after a distance of the variance growth scale, the flow could then be rotated again to create longitudinal mixing over the steeper transverse gradients, which would greatly accelerate natural attenuation and bioremediation.

5.6. Summary and Conclusions.

Over any unresolved scale such as a field site, numerical grid block, or lab column, the exact conductivity and/or pore structures will likely never be determined and concentration values cannot be modeled deterministically. In this work we have shown that the concentration distributions that result from incomplete mixing within a dispersion front can be approximated by modeling the mean and variance and assuming that concentrations are Beta-distributed. Concentration distributions represent the small-scale concentrations that drive biogeochemical reactions and help address laws and regulations set forth by maximum contaminant levels. Applying mixing lines to conservative distributions transforms them into joint reactant distributions, which are in turn transformed into product and reactant distributions according to the non-linear chemical reaction. We used our experimental data to validate our reactive transport approach by modeling the space-time evolution of the means, variances, and distributions of a conservative tracer and three reactant species. We also demonstrated that the same *CF-β* approach is valid for homogenous porous media by correctly modeling the mean product of different non-linear reactions for three independent data sets.

This modeling approach can be extended to more complex reactive transport scenarios by recognizing that macro-dispersive (co)variance production balances mechanical dispersive (co)variance destruction. This relationship leads to simple mean gradient approximations for the space-time evolution of aqueous covariance matrixes and allows numerous unclosed terms to be neglected. Using production-destruction approximations, more complex reactive transport situations might be modeled with following operator splitting approach: 1) at a time step, transport concentration means with standard software; 2) calculate the variances and covariances by scaling the mean gradients; 3) form a multivariate distribution (yet to be determined) based on these moments; 4) calculate all possible reactions in the multivariate distribution; 5) integrate the multivariate distribution and update all the mean concentrations.

An alternative approach to account for the expected value of the reaction term is to expand an arbitrary reaction term about the mean concentrations with a Taylor series and use the second order moments from the production-destruction balance. Combining a low order Taylor series expansion of a reaction term to upscaled transport equations is an attractive approach for upscaling complex mixing and reaction for its simplicity and computational efficiency. For some reactions, this approach coupled to the production-destruction balance is able to model the correct space-time evolution of the product and reactant means, variances, and assumed Beta *pdfs* without utilizing multivariate distributions that are yet to be determined. However, as was demonstrated for Tiron/molybdate product, when the chemical reaction is highly non-linear, low-order approximations can yield poor predictions and higher-order moments must be included. This area needs further research to determine what types of reactions have well behaved Taylor series and how to approximate higher order cross moments.

The *CF-β* full distribution and Taylor series approach avoids incomplete mixing upscaling error that exists in traditional approaches without resolving heterogeneity.

Furthermore, scaling the mean squared gradients and assuming a Beta distribution would provide a complete statistical description for any species, which could aid in regulatory decisions based on maximum contaminant levels and calibrating transport models with field data.

The key parameter controlling dispersive mixing for the *CF-β* approach is the variance length-scale. With the limited data from the literature, we found it to correlate to the transverse Peclet number and the time scale for transverse dispersion. It also appeared to correlate with domain and hence correlation length. While this relationship could be useful for first order approximation, it suggests that concentrations may never or very slowly become completely mixed because increasing correlation scales could cause increasing variance production and, at the same time, decreasing variance destruction. Variance production would increase from macro-dispersion increasing with scale and variance destruction would decrease from transverse dispersion having to mix over larger micro-scales created by larger correlation lengths.

As the variance length-scale can be used to model reactive transport, we propose that reactive tracers can be used to measure the variance length-scale. Specifically, following the experimental approach of Raje and Kapoor (2000), these length-scales could be determined from breakthrough curves of a rate-limited bimolecular reaction with a reaction rate slow compared to measuring time. We believe that this would be a good approach to measure these length-scales at a field site. Alternatively, it might be possible to calculate the variance length-scale at a field site by modeling a breakthrough curve of concentration variance measured by dozens of fiber optic probes coming out of a well screen. Measuring the variance length-scale with either of these approaches would also allow for the simultaneous measurement of macro-dispersivity. Tracer tests are much more practical than directly resolving the statistical parameters of the conductivity field. Furthermore, the parameter values measured with the tracer test would yield information about the conductivity field.

Viewing mixing and reaction as variance destruction and production might help us understand how to increase favorable mixing in the subsurface. If a system of wells suddenly switched the flow perpendicular to its original direction, the variance destruction and reactive mixing rate would increase by almost an order of magnitude because the larger longitudinal mechanical dispersion would then mix over very steep concentration gradients that are the result of macro-dispersive velocity fluctuations and small transverse dispersion. This could be a very practical way to accelerate natural attenuation and bioremediation.

The model development, experimental validation, and discussion presented in this work are meant to provide a foundation for distribution reactive transport modeling. Further research is needed to address reactive transport situations involving solid-fluid reactions, perhaps through Taylor series expansion. Li *et al.*, (2006) studied geochemical reaction rates relevant to CO_2 sequestration and found the upscaling error for heterogeneous reaction rates can not only differ by orders of magnitude but the reaction rates based on a spatial average can predict the opposite reaction direction compared to the true small-scale reaction. Finally, as pointed out by Kapoor *et al.* (1998), the same upscaling problem could also apply for reactive transport in surface waters such as rivers and estuaries and we feel the *CF-β* approach presented in these papers could be a potential solution.

References

1. Alford, M.H., D.W. Gerdt and C.M. Adkins (2006), An ocean refractometer: Resolving millimeter-scale turbulent density fluctuations via the refractive index. *J. Atmos. Ocean. Tech.*, 23, 121-137.
2. Alford, M.H., D.W. Gerdt and C.M. Adkins (2006), An ocean refractometer: Resolving millimeter-scale turbulent density fluctuations via the refractive index. *J. Atmos. Ocean. Tech.*, 23, 121-137.
3. Arey, S. J., and Gschwend, P. M. 2005. A physical–chemical screening model for anticipating widespread contamination of community water supply wells by gasoline constituents. *Journal of Contaminant Hydrology*. 76, 109-138.
4. Bagtzoglou, A.C., Oates, P.M. Chaotic Advection Enhanced Groundwater Remediation. ASCE J. Materials in Civil Engr: Advances in Physico-Chemical Stabilization of Geomaterials. (In press)
5. Baurle, R. A., Alexopoulos, G. A. and Hassan, H. A. 1994. Assumed Joint Probability Density Function Approach for Supersonic Turbulent Combustion. *Journal of Propulsion and Power*. 10(4).
6. Bellin, A., Pannone, M., Fiori, A., Rinaldo, A. On transport in porous formations characterized by heterogeneity of evolving scales. *Water Resources Research*. 32(12), 3485.
7. Borden, R. C., and Bedient, P.B. 1986. Transport of dissolved hydrocarbons influenced by oxygen-limited biodegradation: 1. Theoretical development. *Water Resources Research*. 13, 1973-1982.
8. Borden, R. C., Bedient, P. B., Lee, M. D., Ward, C. H., Wilson, J. T., 1986. Transport of dissolved hydrocarbons influenced by oxygen-limited biodegradation: 2. Field application. *Water Resources Research*. 13, 1983-1990.
9. Cirpka, O. 2002. Choice of dispersion coefficients in reactive transport calculations on smoother fields. *Journal of Contaminant Hydrology*. 58, 261–282.
10. Committee on Energy and Commerce, House of Representatives. 2003. The effectiveness of leaking underground storage tank cleanup programs. *Hearing before the Subcommittee on environment and hazardous materials.* U.S. Government Printing Office. Washington DC: March 5, Serial No. 108-16.
11. Dagan, G. 1994. The significance of heterogeneity of evolving scales to transport in porous formations. *Water Resources Research*. 30, 3327-3336.
12. Dagan, G., and Fiori, A. 1997. The influence of pore-scale dispersion on concentration statistical moments in transport through heterogeneous aquifers. *Water Resources Research*. 33(7), 1595-1605.
13. Dentz, M., Kinzelbach, H., Attinger, S., and Kinzelbach, M. 2000. Temporal behavior of a solute cloud in a heterogeneous porous medium: 1. Pointlike injection. *Water Resources Research*. 36, 3591– 3604.
14. Fiori, A., and Dagan, G. 2000. Concentration fluctuations in aquifer transport: a rigorous first order solution and applications. *Journal of Contaminant Hydrology*. 45, 139-163.
15. Gelhar, L.W. 1993. Stochastic Subsurface Hydrology. New Jersey, Prentice-Hall Inc.

16. Gerlinger, P. 2003. Investigation of an assumed pdf approach for finite-rate chemistry. *Combust. Sci. and Tech.* 175, 841-872.
17. Girimaji, S. S. 1991. Assumed *β*-pdf Model for Turbulent Mixing: Validation and Extension to Multiple Scalar Mixing. *Combust. Sci. and Tech.* 78, 177-196.
18. GM, 2006. "Live Green Go Yellow" http://www.gm.com/company/onlygm/livegreengoyellow/index.html
19. Graham, W., and McLaughlin, D. 1989. Stochastic analysis of nonstationary subsurface solute transport, 1, Unconditional moments. *Water Resources Research.* 25(2), 215–232.
20. Grathwohl, P., Klenk, I.D., Berhardt C., Maier U. (2000). "Steady state plumes: mechanisms of transverse mixing in aquifers". In: *Contaminant Site Remediation: From Source Zones to Ecosystems.* Proc. CRSC, Melbourne, Vic., 4–8 December, Centre for Groundwater Studies, CSIRO, Perth, Western Australia. p. 459–466.
21. Gross, T. F., and Nowell, A. R. M. 1985. Spectral Scaling in a tidal boundary-layer. *Journal of Physical Oceanography.* 15, 496.
22. Heermann, S. E., Powers, S. E. 1998. Modeling the partitioning of BTEX in water reformulated gasoline systems containing ethanol. *Journal of Contaminant Hydrology.* 34, 315–41.
23. Janssen, G. M., Cirpka, O.A., van der Zee, S.E.A.T.M. 2006. Stochastic analysis of nonlinear biodegradation in regimes controlled by both chromatographic and dispersive mixing. *Water Resources Research.* 42, W01417
24. Jose, S. C., and Cirpka, O. A. 2004. Measurement of mixing-controlled reactive transport in homogeneous porous media and its prediction from conservative tracer test data. *Environmental Science and Technololgy.* 38(7), 2089-2096.
25. Jose, S. C., Rahman, M. A. and Cirpka, O.A. 2004. Large-scale sandbox experiment on longitudinal effective dispersion in heterogeneous porous media. *Water Resources Research.* 40(12), W12415, doi: 10.1029/2004WR003363.
26. Kapoor, V., and Kitanidis, P. K. 1996. Concentration fluctuations and dilution in two-dimensionally periodic heterogeneous porous media. *Transport Porous Media.* 22: 91–119.
27. Kapoor, V., and Kitanidis, P. K. 1998. Concentration fluctuations and dilution in aquifers. *Water Resources Research.* 34(5), 1181–1193.
28. Kapoor, V., Anmala, J., 1998. Lower bounds on scalar dissipation in bounded rectilinear flows. *Flow Turbul. Combust.* 60 (2), 125–156.
29. Kapoor, V., Gelhar, L. W. 1994a Transport in three-dimensionally heterogeneous aquifers 1. Dynamics of concentration fluctuations. *Water Resources Research.* 30(6), 1775-1788.
30. Kapoor, V., Gelhar, L. W. 1994b Transport in three-dimensionally heterogeneous aquifers 2. Predictions and observations of concentration fluctuations. *Water Resources Research.* 30(6), 1789-1801.
31. Li, L. Peters, C. A., Celia, M.A. 2006. Upscaling geochemical reaction rates using pore-scale network modeling. Advances in Water Resources. 29. 1351-1370.
32. Li, S. and McLaughlin, D. 1991. A nonstationary spectral method for solving stochastic groundwater problems: Unconditional analysis. *Water Resources Research.* 27(7), 1589-1605.

33. McNab, W., Heermann, S. E., and Dooher, B. 1999. Screening model evaluation of the effects of ethanol on benzene plume lengths, in *Health and Environmental Assessment of the Use of Ethanol as a Fuel Oxygenate, Report to the Governor of the State of California in Response to Executive Order D-5-99, vol. 4, Potential Ground and Surface Water Impacts*, edited by D. W. Rice and G. Cannon, Rep. UCRL-AR-135949, 41– 4-21, Lawrence Livermore Natl. Lab., Livermore, Calif.
34. Mehl, S., Hill, M. C. 2001. A comparison of solute transport techniques and their effect on sensitivity analysis and inverse modeling results. *Groundwater*. 39(2), 300-307.
35. Michael, J. R., and Schucany, W. R. 2002. The mixture approach for simulating bivariate distributions with specific correlations. *The American Statistician*. 56, 48-54.
36. Molson, J. W., Barker, J. F., Frind, E. O. 2002. Modeling the impact of ethanol on the persistence of benzene in gasoline-contaminated groundwater. *Water Resources Research*. 38(1), 4-1 – 4-12.
37. Mosimann, J. E. 1962. On the Compound Multinomial Distribution, the Multivariate Beta Distribution, and Correlations Among Proportions. *Biometrika*, 49(1/2), 65-82.
38. Nadarajah, S. 2005. Reliability for some bivariate beta distributions. *Mathematical Problems in Engineering*. 101–111. doi: 10.1155/mpe.2005.101
39. Nash, J. D., Moum, J. N. 2002. Microstructure estimates of turbulent salinity flux and the dissapation spectrum of salinity. *Journal of Physical Oceanography*. 32, 2312-2333.
40. Neuman, S. P. 1995. On advective transport in fractal permeability and velocity fields. *Water Resources Research*. 31, 1455-1460.
41. Niven, R. K. 2005. Ethanol in gasoline: environmental impacts and sustainability review article. *Renewable and Sustainable Energy Reviews*. 9, 535-555.
42. Pannone, M., and Kitanidis, P. K. 1999. Large-time behavior of concentration variance and dilution in heterogeneous formations. *Water Resources Research*. 35(3), 623-634.
43. Pannone, M., and Kitanidis, P. K. 2004. On the asympototic Behavoir of Dilution Parameters for Gaussian and Hole-Gaussian Log-Conductivity Covairance Function. *Transport in Porous Media*. 56, 257-281.
44. Raje, D. S. and Kapoor, V. 2000. Experimental study of bimolecular reaction kinetics in porous media. *Environmental Science and Technology*. 34 (7), 1234-1239.
45. Sanford, T. B., and Lien, R. C. 1999. Turbulent properties in a homogeneous tidal bottom boundary layer. *Journal of Geophysical Research-Oceans*. 104, 1245.
46. Schwarzenbach, R. P., Gschwend, P. M., Imboden, D. M. 2002. Environmental Organic Chemistry. Wiley-Interscience. New York, NY
47. Shaw, W. J., Trowbridge, J. H., and Williams III, A. J. 2001. Budgets of turbulent kinetic energy and scalar variance in the continental shelf bottom boundary layer. *J. Geophys. Res.* 106(C5), 9551–9564.
48. Srivastava, M. S. 2003. Singular wishart and multivariate beta distributions. *The Annals of statistics*. 31(5), 1537–1560.

49. Stewart, E. J., and Huq, P. 2006. Destruction rate correction methods. *Experiments in Fluids*. 40, 405-421.
50. Stockholm, A., Deeb, R., and Kavanaugh, M. 1998. Evaluation of the fate and transport of ethanol in the environment. Report, Malcolm Pirnie, Inc., Oakland, California.
51. Tennekes, H., and J. L. Lumley. 1972. *A first course in Turbulence*. MIT Press. Cambridge, MA.
52. Tiedeman, C. R., and Hsieh, P. A. 2004. Evaluation of longitudinal dispersivity estimates from simulated forced- and natural-gradient tracer tests in heterogeneous aquifers. *Water Resources Research*. 40, W01512.
53. Trowbridge, J. H., Geyer, W.R., Bowen, M. M., Williams, A. J. 1999. Near-bottom turbulence measurements in a partially mixed estuary: Turbulent energy balance, velocity structure, and along-channel momentum balance. *Journal of Physical Oceanography*. 29, 3056.
54. Ulrich, G. 1999. The fate and transport of ethanol-blended gasoline in the environment. Report, Governor's Ethanol Coalition, Surbec-ART Environment.
55. Vanderborght, J. 2001. Concentration variance and spatial covariance in second-order stationary heterogeneous conductivity fields. *Water Resources Research*. 37(7), 1893-1912.
56. Vomvoris, E. G., and L. W. Gelhar. 1990. Stochastic analysis of the concentration variability in a three-dimensional heterogeneous aquifer. *Water Resources Research*. 26(10), 2591-2602.
57. Wain, D. J., and Rehmann, C., R. 2005. Eddy diffusivity near bubble plumes. *Water Resources Research*. 41, W09409, doi:10.1029/2004WR003896.
58. Wyngaard, J. C. 1992. Atmospheric-Turbulence. *Annual Review of Fluid Mechanics*. 24, 205.
59. Wyngaard, J. C., and Coté, O. R. 1971. Budgets of turbulent kinetic energy and temperature variance in atmospheric surface layer. *Journal of the Atmospheric Sciences*. 28, 190.
60. Zang, D. and Neuman, S. P. 1996. Effect of local dispersion on solute transport in randomly heterogeneous media. *Water Resources Research*. 32(9), 2715–2723.
61. Zhou, T., and Antonia, R. A. 2000. Approximation for turbulent energy and temperature variance destruction rates in grid turbulence. *Phys Fluids*. 12(2), 335-344.

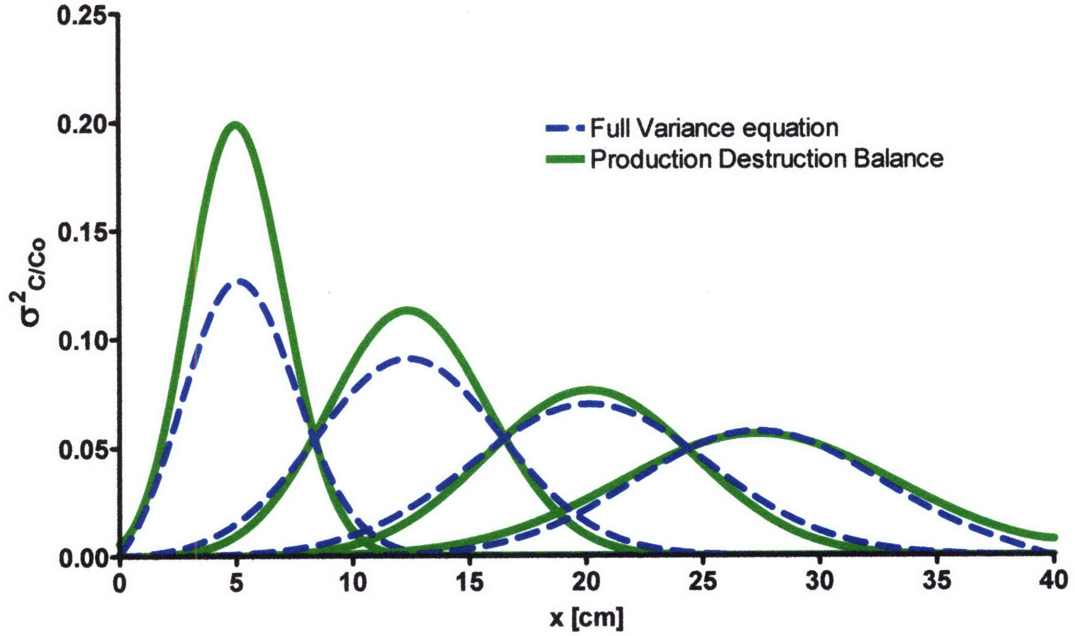

Figure 1. Comparison of finite difference solution of all the terms in the variance budget with the analytic solution based production-destruction balance for parameters from our tank experiments.

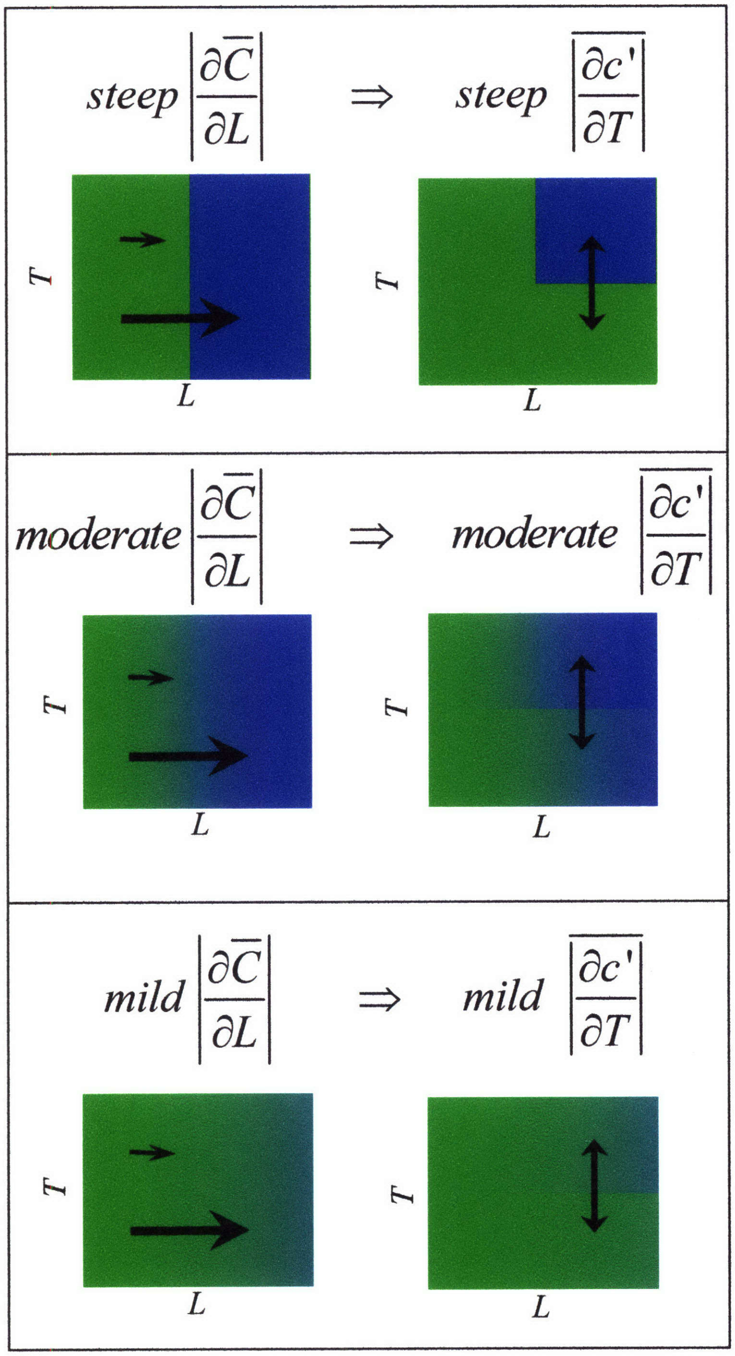

Figure 2. Zoom in on part of a macro-dispersion front showing how longitudinal gradients are transferred into proportional transverse gradients. The average of this effect on a larger scale is captured by the mean longitudinal gradient and the mean transverse gradients and shows how the production-destruction balance can occur locally.

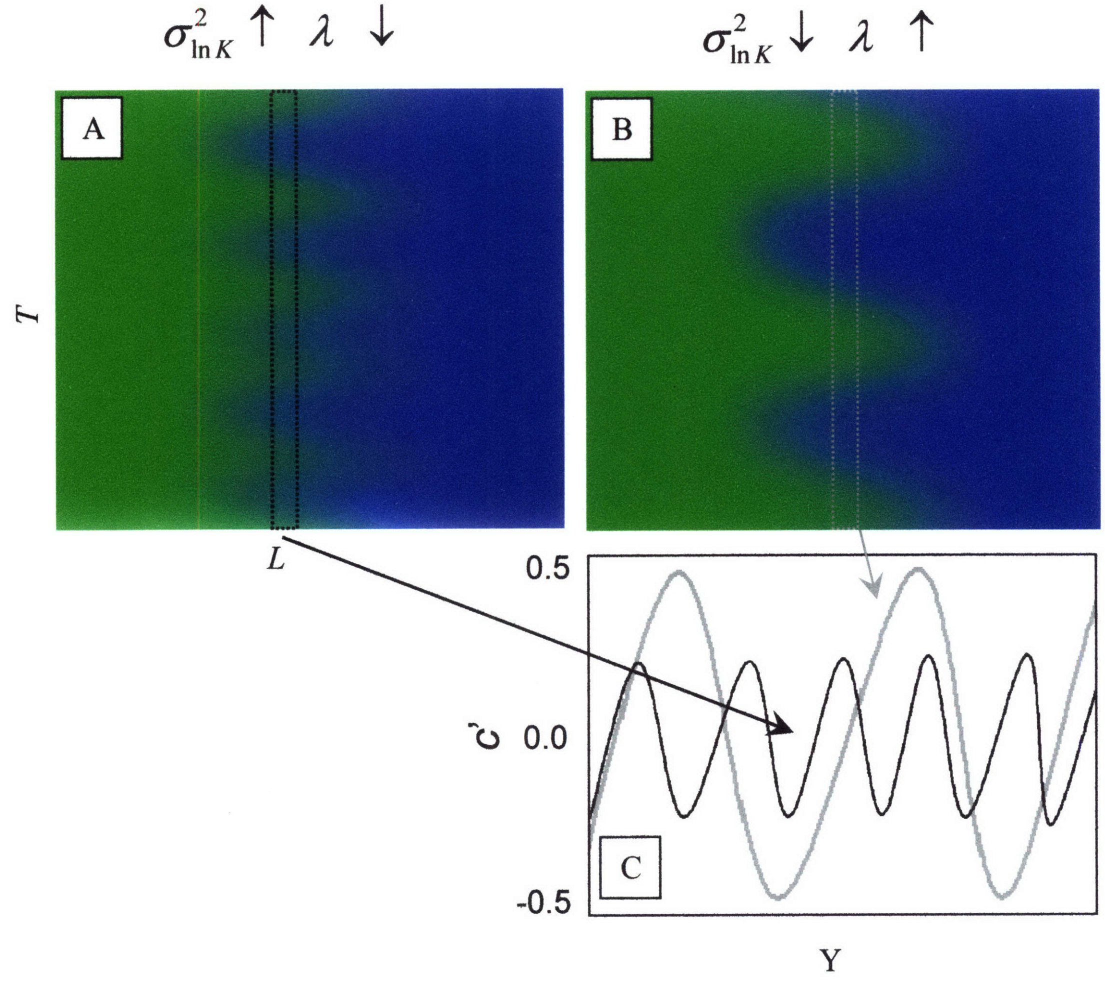

Figure 3. Production-destruction balance for two flow fields with the same mean longitudinal concentration gradient, macro-dispersivity, and mechanical-dispersivity. However, the fields have different log conductivity variance and correlation lengths even though the product of the two is the same. A) Flow field with higher log conductivity variance but lower correlation length; B) Flow field with lower log conductivity variance but higher correlation length. Variance production is the same for both fields. C) Transverse concentration profile along a slice of the macro-dispersive front showing perturbation derivatives are roughly equal for both fields, which means variance destruction is also occurring at the same rate. The difference between the two fields is field B has more variance and hence a larger variance length-scale.

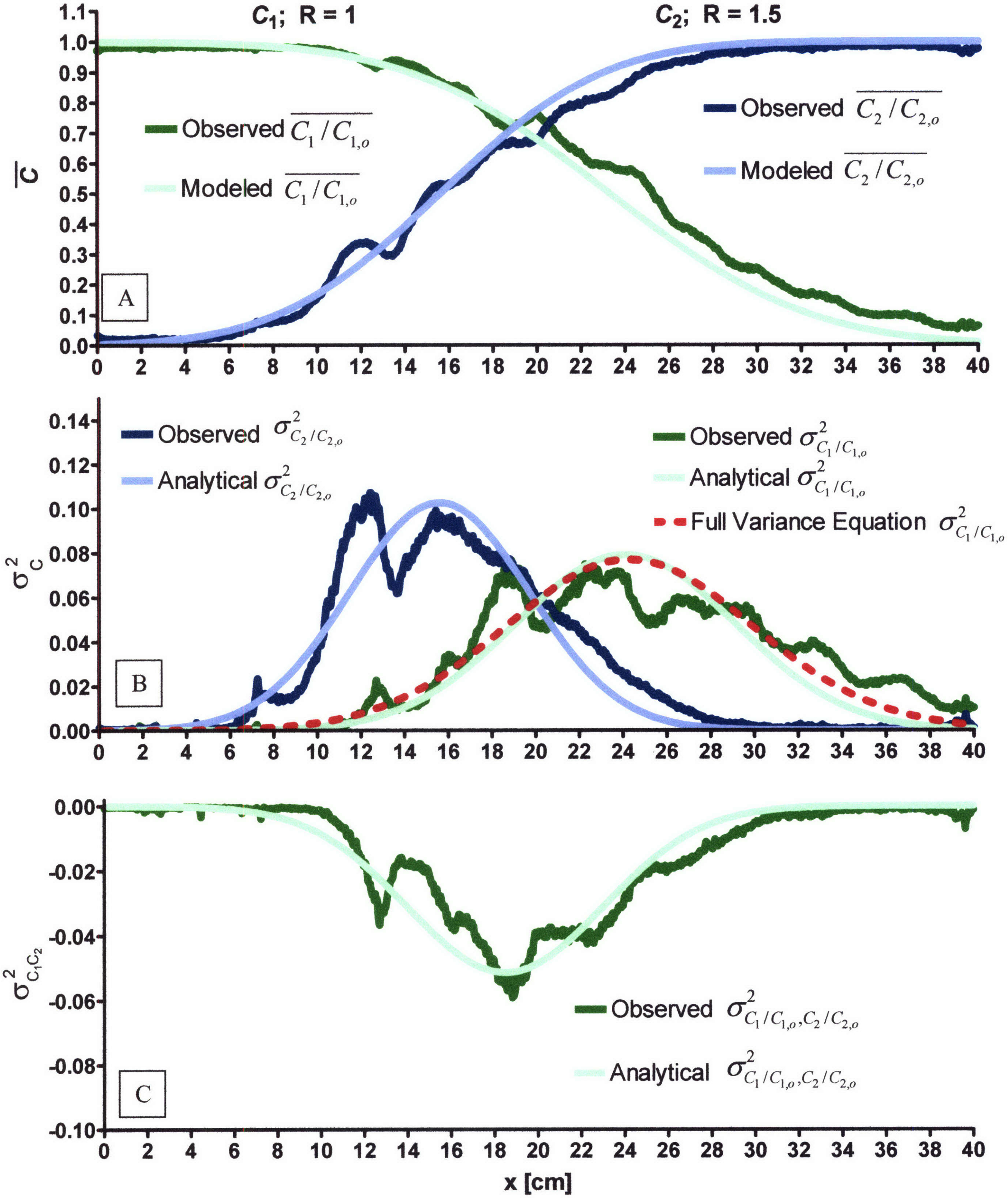

Figure 4. First and second order statistical moments of two non-interacting solutes with different retardation factors: A) Observed and modeled means. B) Observed variances, finite-difference solution to full variance budget, and analytical solutions based on production-destruction balance. C) Observed covariance and analytical solution based on production-destruction balance.

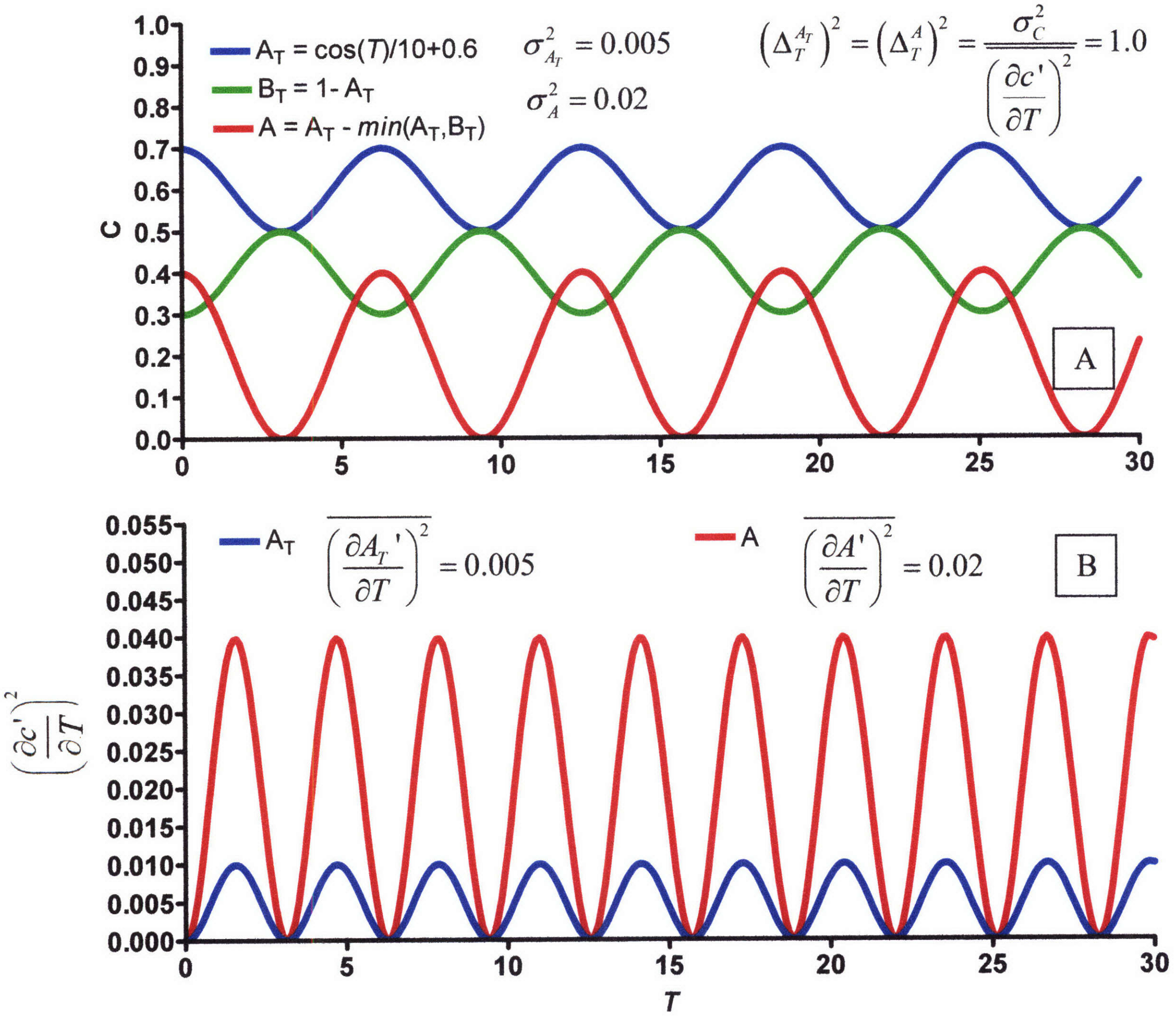

Figure 5. Transverse concentration micro-scales of A before and after $A+B \rightarrow P$ reaction of a theoretical transverse slice of a macro-dispersion front. The reaction does not change the micro-scales because the reaction increases the squared perturbation derivatives by the same amount as the variance: A) Concentration profiles of total reactant A_T and B_T and post reaction A. B) Squared perturbation derivatives of A_T and A.

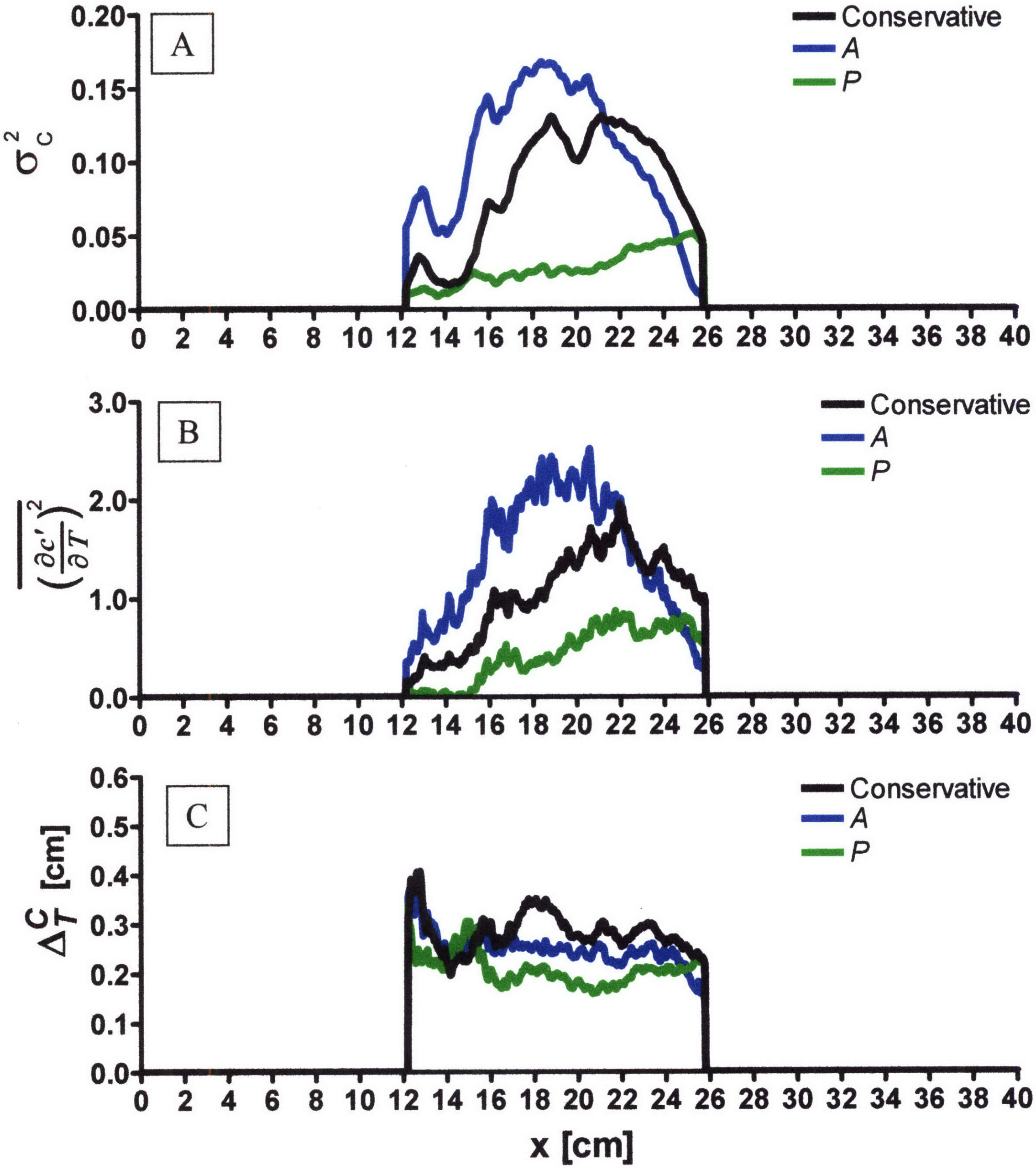

Figure 6. Micro-scales of conservative tracer and *A* and *P* from the *A*+*B*→*P* reaction. Looking over a part of the domain where the micro-scales are defined for the A) Variance, B) Expected value of the squared transverse perturbation derivatives, and C) transverse micro-scales.

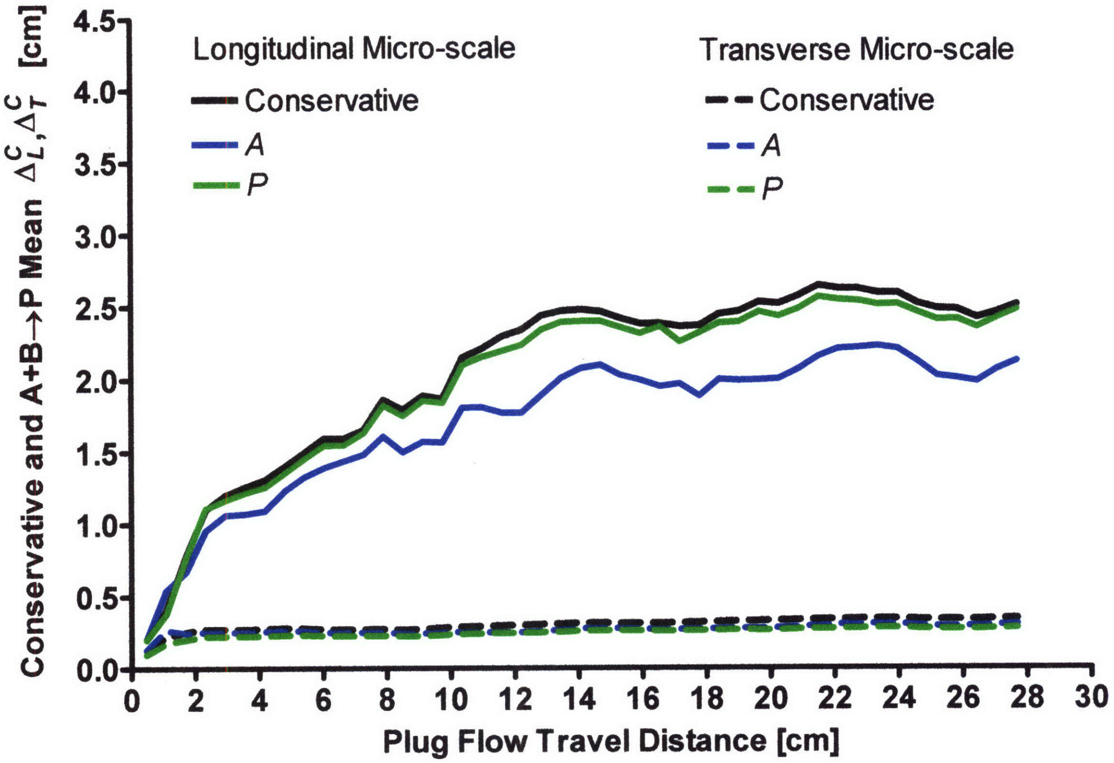

Figure 7. **Evolution of the mean longitudinal and transverse concentration micro-scales for the conservative tracer, *P* for the *A*+*B*→*P* reaction, and *A* for *A*+*B*→*P* reaction.**

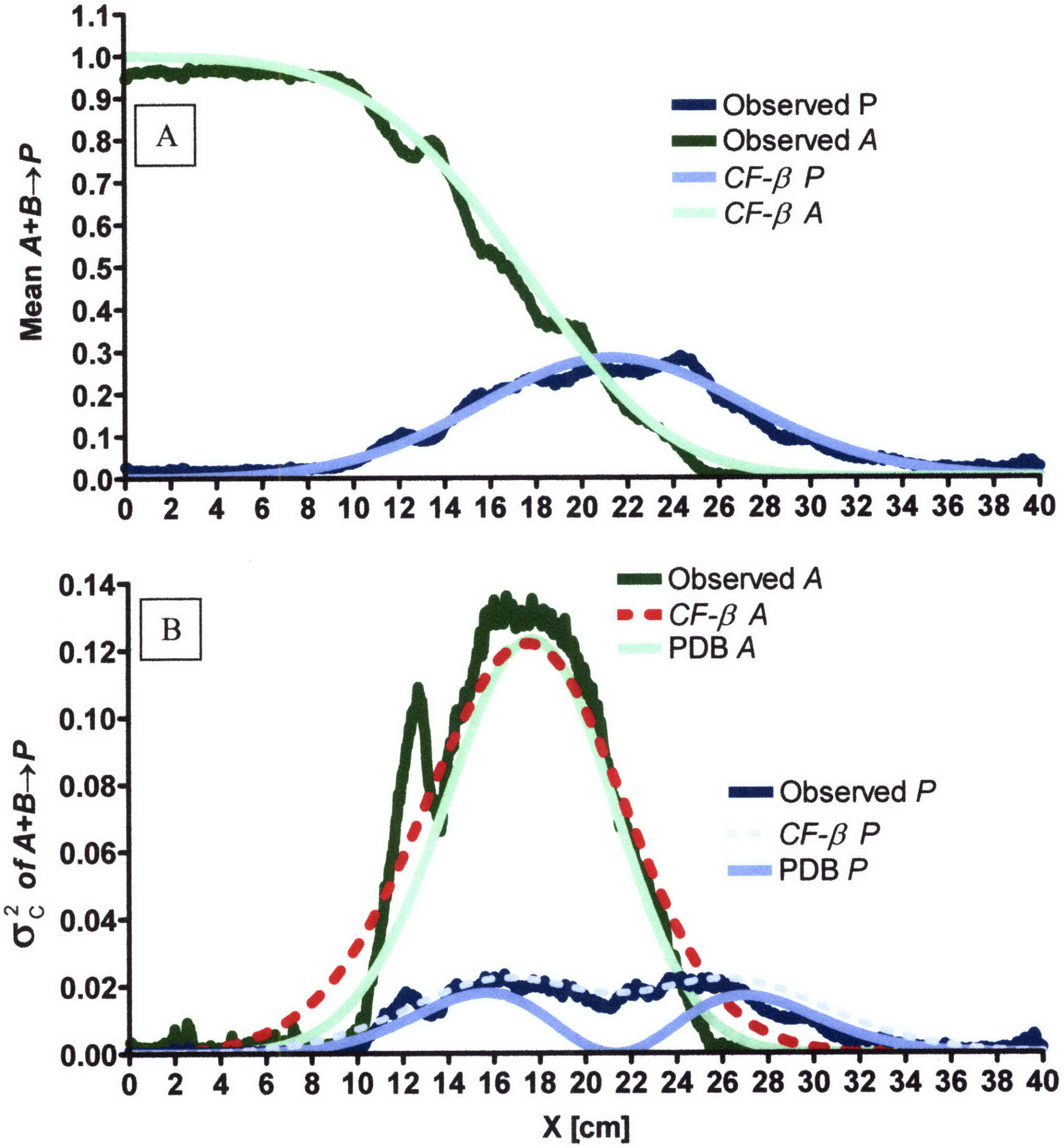

Figure 8. Mean and variance of A and P for the $A+B\rightarrow P$ reaction A) Observed and *CF-β* predicted mean A and P. B) Observed variances, *CF-β* predicted variance found from integrating across the A and P distributions, and variance prediction based on scaling the mean gradients from the production-destruction balance (PDB).

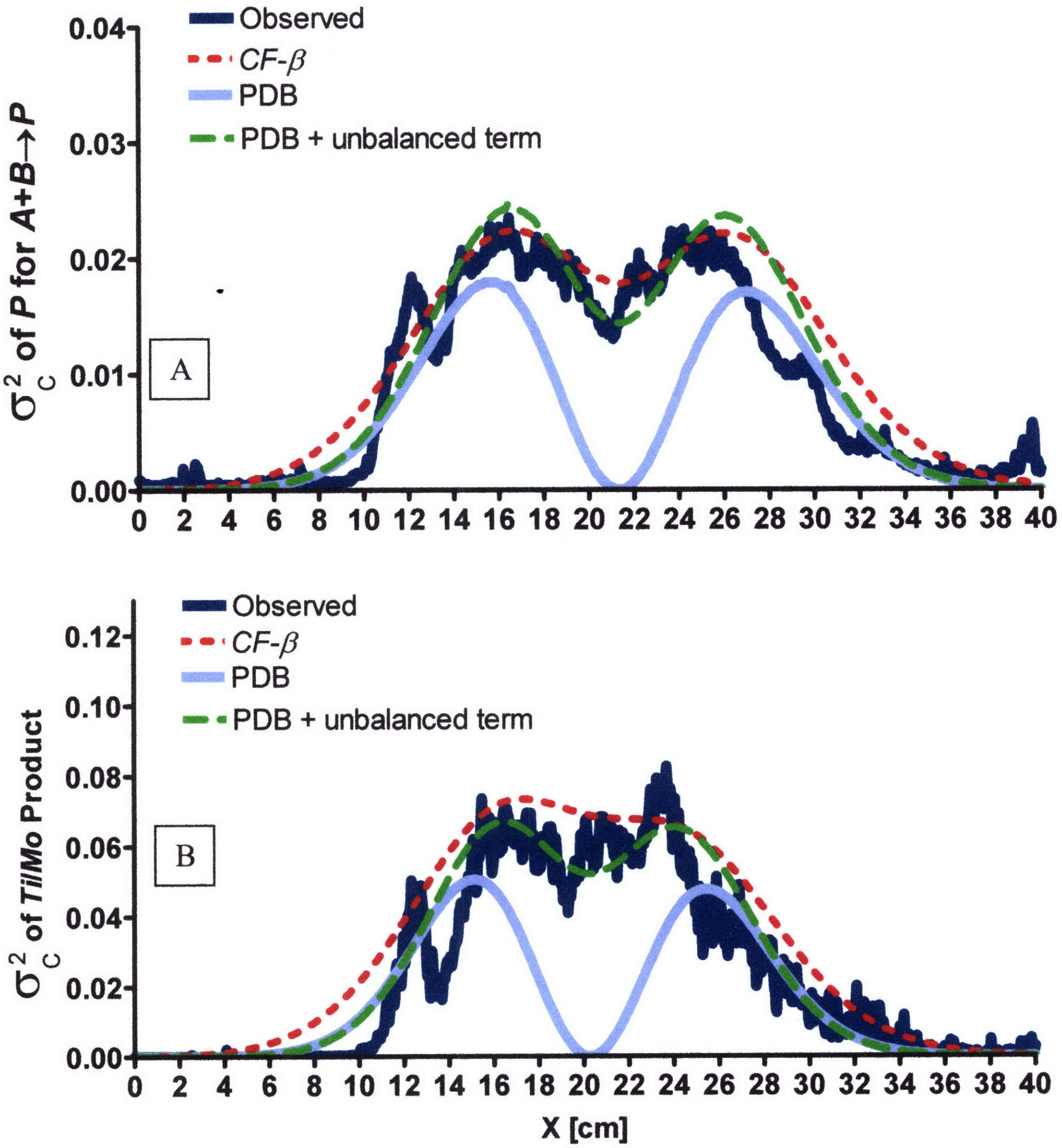

Figure 9. Observed variance, *CF-β* predicted variance found by integrating across the distribution, variance prediction based on scaling the mean gradients, and mean gradient prediction including the unbalanced term for A) *P* for *A*+*B*→*P* reaction B) Tiron/molybdate product.

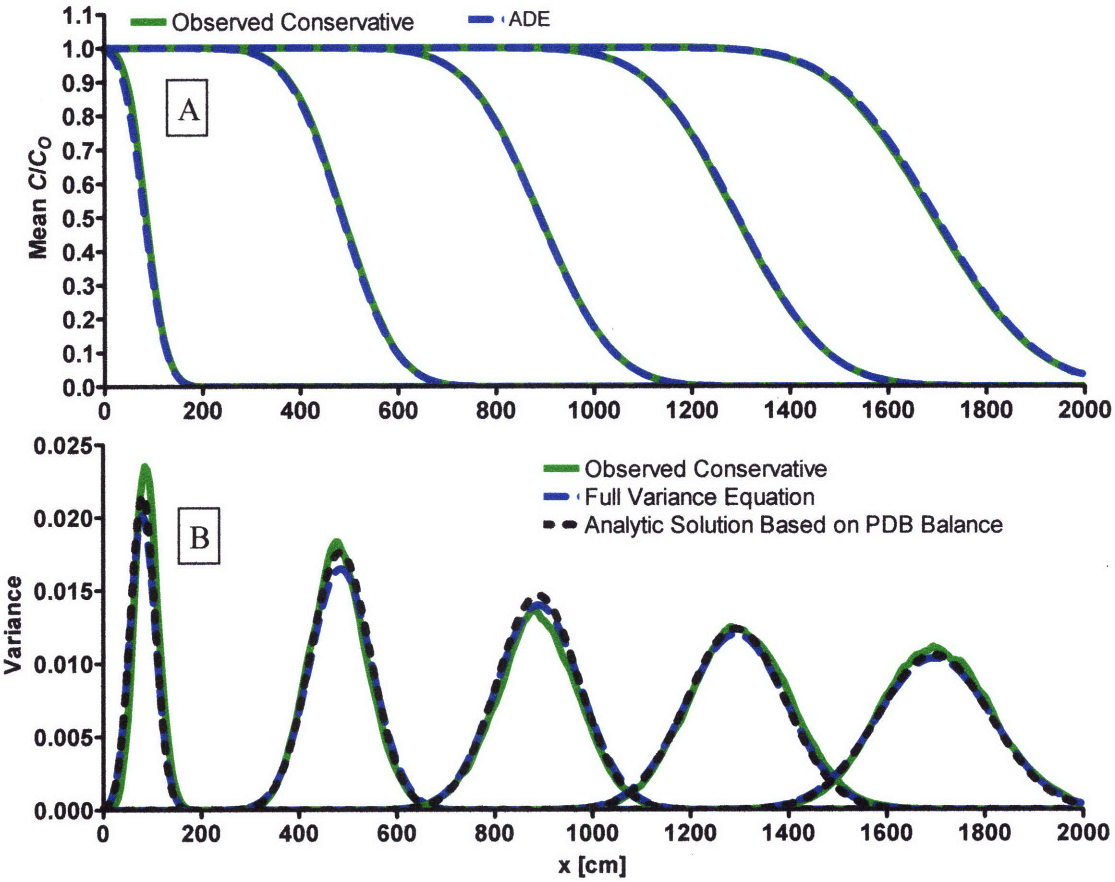

Figure 10. A) Mean conservative profiles and best fit to the advection dispersion equation and B) conservative tracer variance and modeled variance. Solid lines are the finite difference model of the full variance budget and dashed lines are the analytic solution based on the production-destruction balance. Times are 200, 1200, 2200, 3200, and 4200 s.

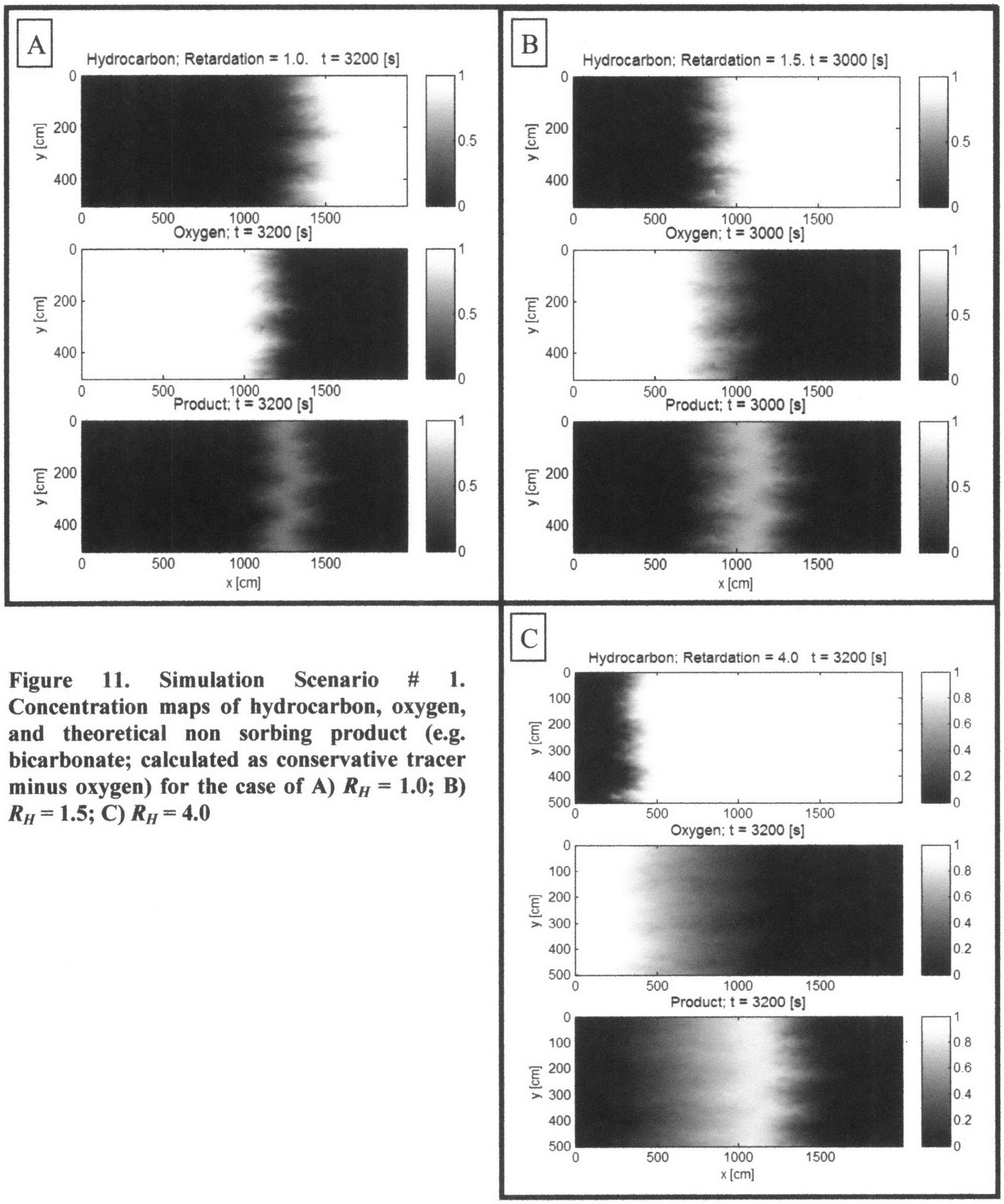

Figure 11. Simulation Scenario # 1. Concentration maps of hydrocarbon, oxygen, and theoretical non sorbing product (e.g. bicarbonate; calculated as conservative tracer minus oxygen) for the case of A) $R_H = 1.0$; B) $R_H = 1.5$; C) $R_H = 4.0$

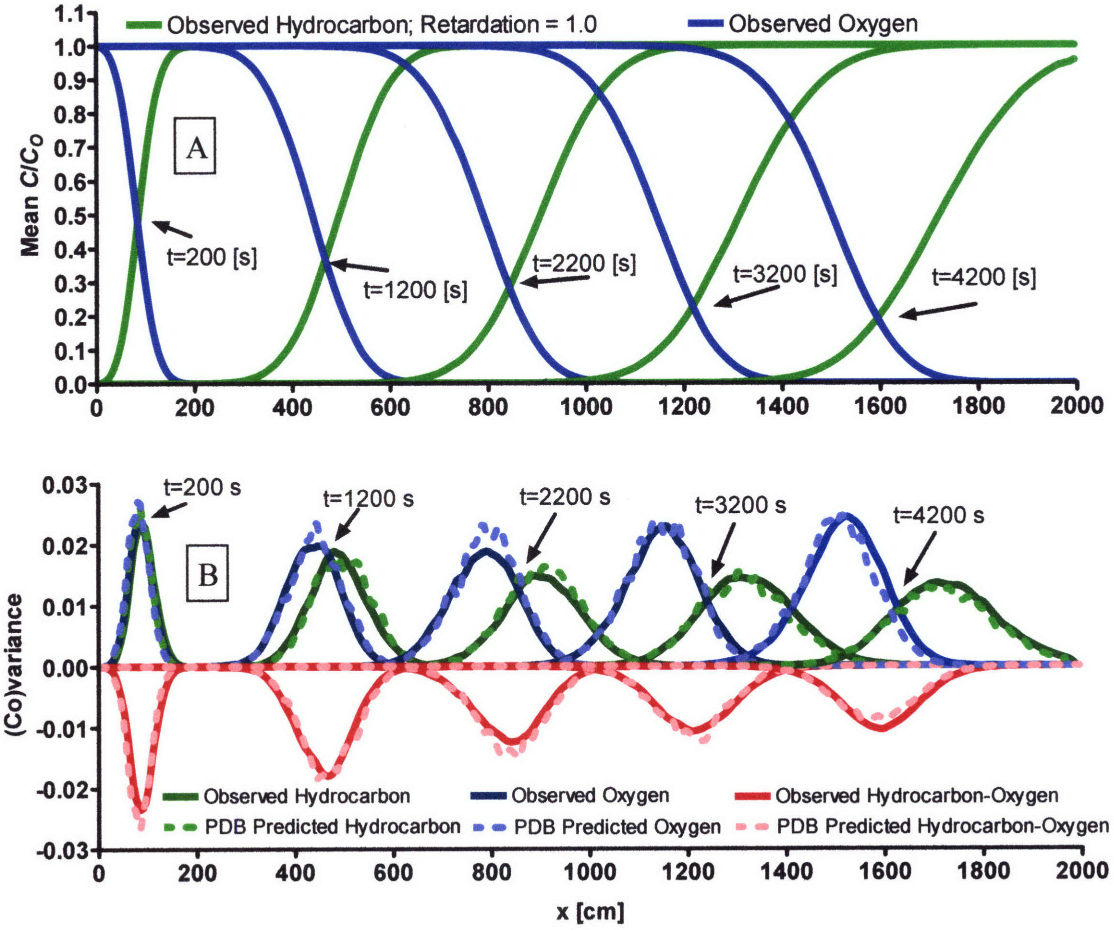

Figure 12. Reactive transport results with no difference in sorption. A) Observed mean hydrocarbon and oxygen concentration profiles. B) Hydrocarbon and oxygen variances and covariances. Solid lines are calculated from the detailed 2-D field and the dashed lines are predicted from the production-destruction balance.

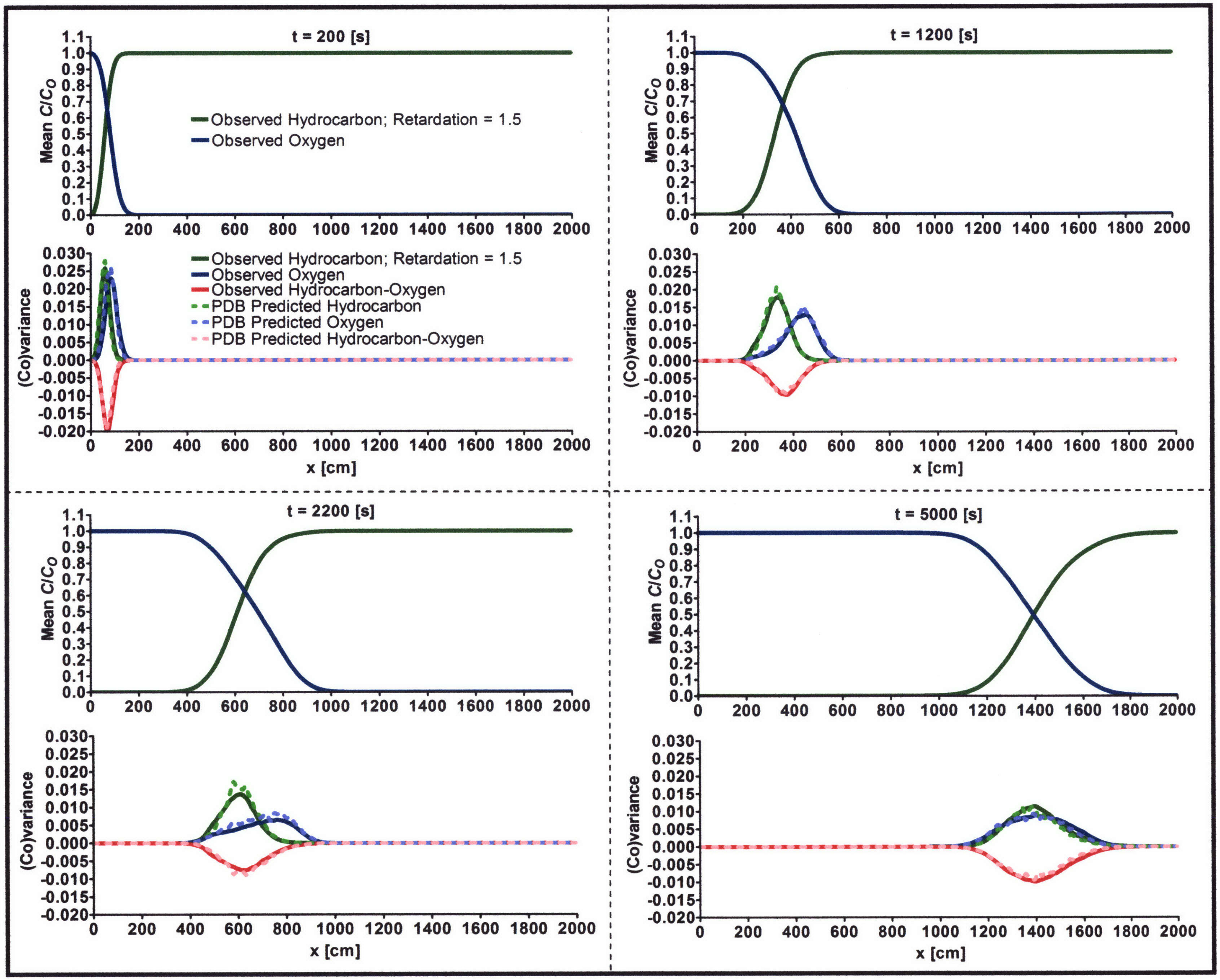

Figure 13. Reactive transport results with $R_H = 1.5$. A) Observed mean hydrocarbon and oxygen concentration profiles. B) Hydrocarbon and oxygen variances and covariances. Solid lines are calculated from the detailed 2-D field and the dashed lines are predicted from the production destruction balance.

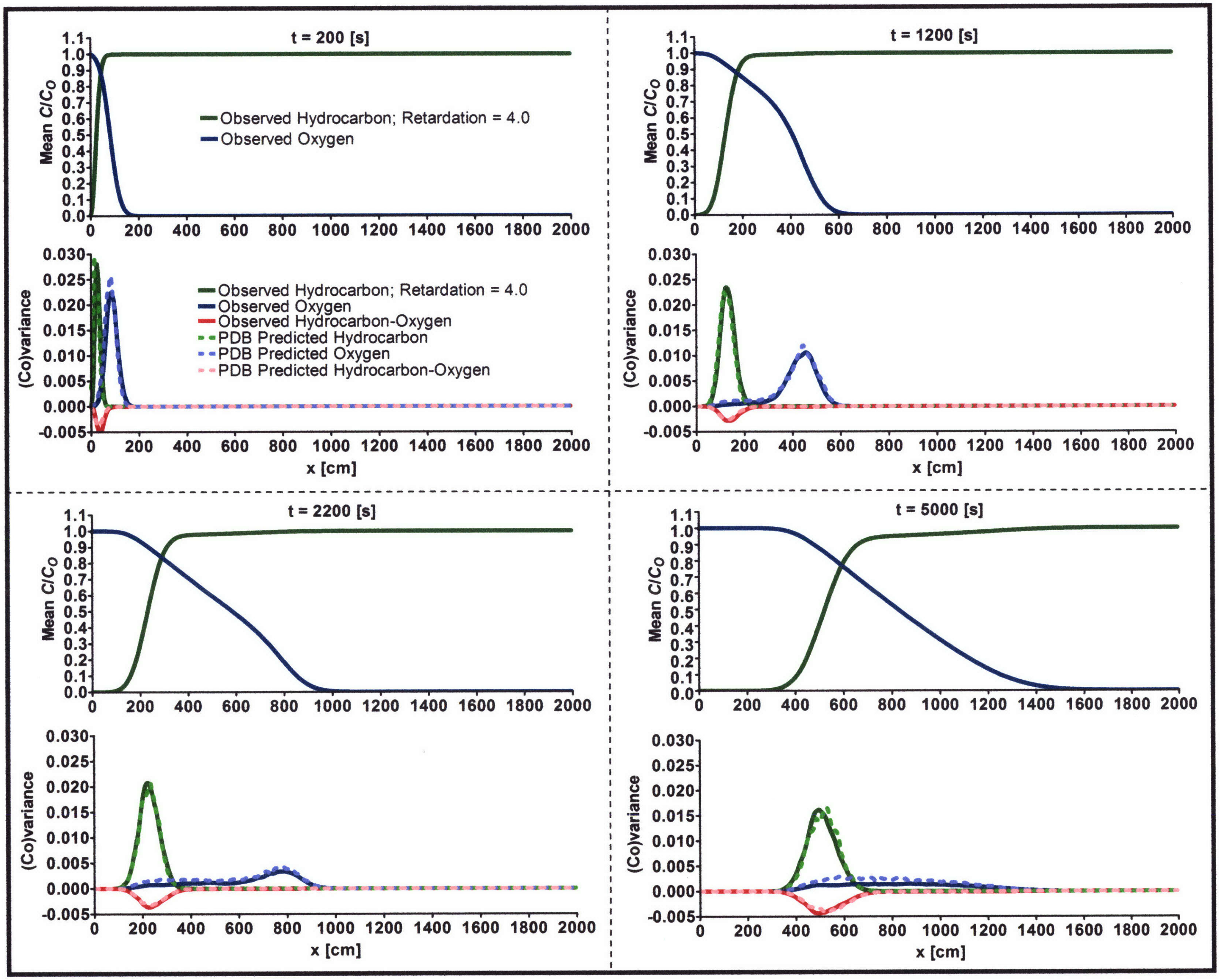

Figure 14. Reactive transport results with R_H = 4.0. A) Observed mean hydrocarbon and oxygen concentration profiles. B) Hydrocarbon and oxygen variances and covariances. Solid lines are calculated from the detailed 2-D field and the dashed lines are predicted from the production-destruction balance.

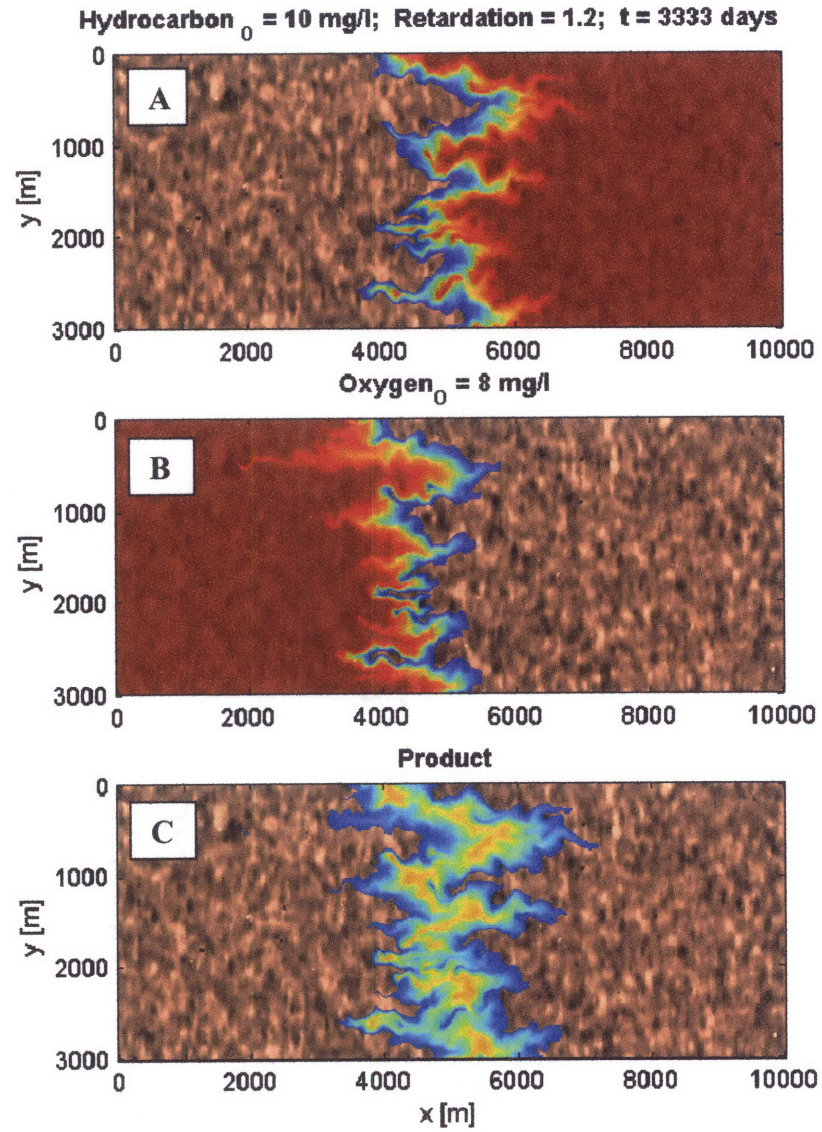

Figure 15. Simulation Scenario #2. Concentration maps of A) hydrocarbon, B) oxygen, and C) theoretical non sorbing product (e.g. bicarbonate; calculated as conservative tracer minus oxygen).

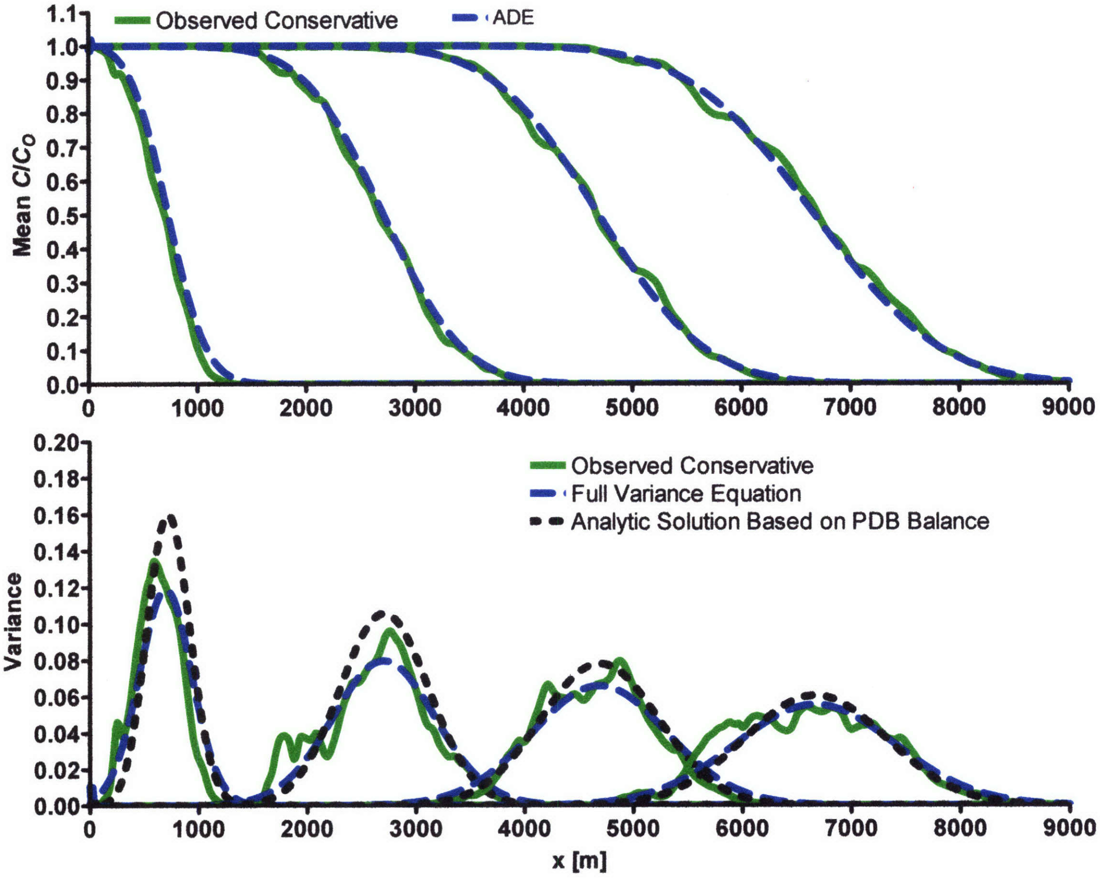

Figure 16. A) Mean conservative profiles and best fit to the advection dispersion equation and B) conservative tracer variance and modeled variance. Solid lines are the finite difference model of the full variance budget and dashed lines are the analytic solution based on the production destruction balance. Times are 1250, 2500, 3750, and 5000 days.

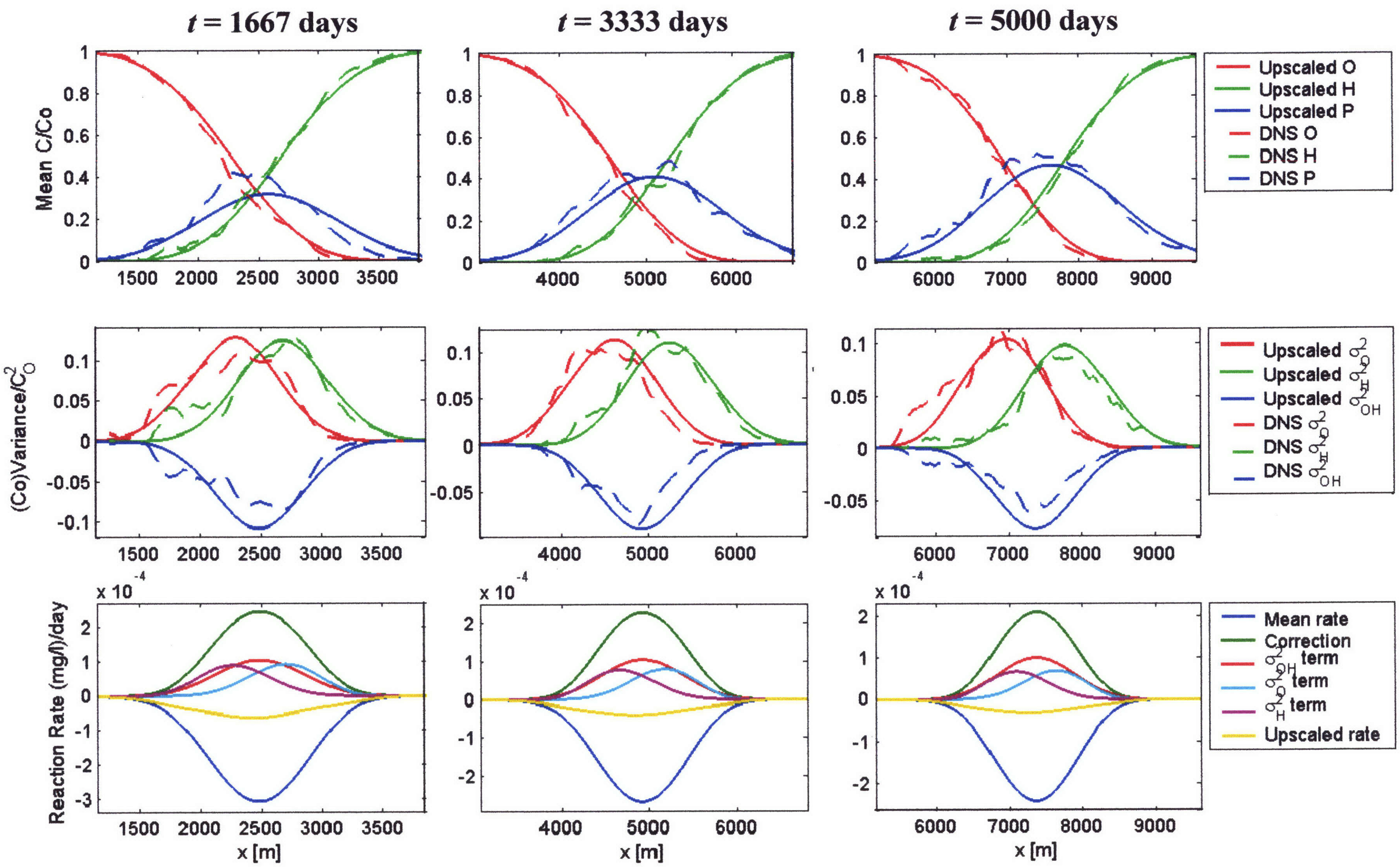

Figure 17. Top row: observed mean concentrations from direct numerical simulation (DNS) and upscaled mean concentrations based on Taylor series expansion and production-destruction balance. Middle row: observed variances and covariance and modeled variances and covariance based on the production-destruction balance. Bottom row: conventional reaction rate based only on the mean concentrations and upscaled reaction rate based on the second order Taylor series expansion and variances and covariance.

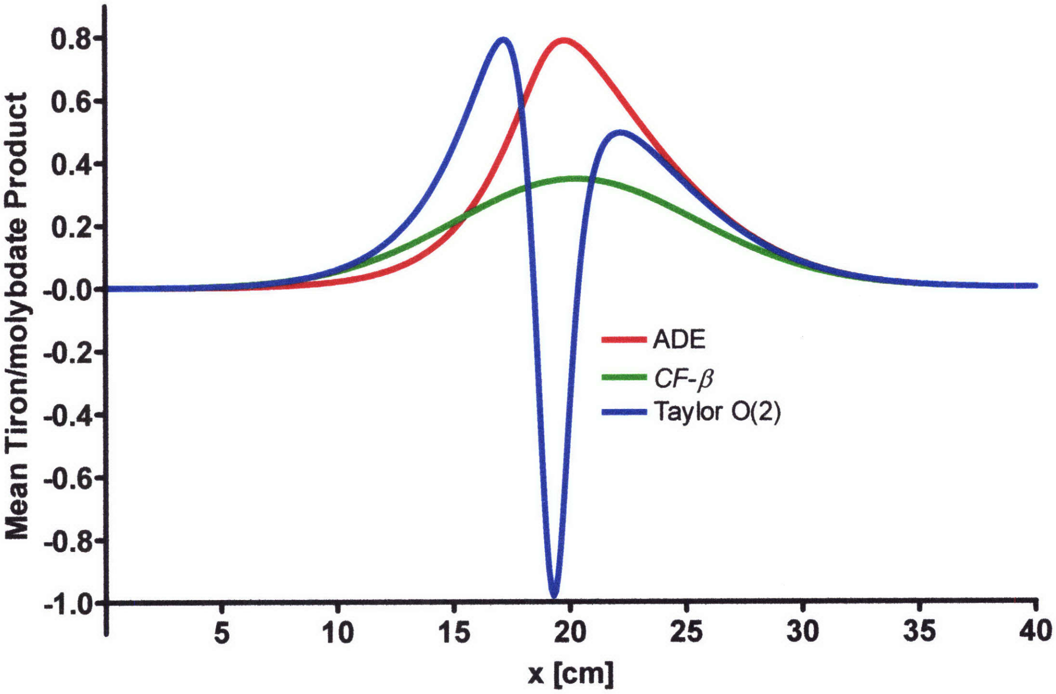

Figure 18. Mean concentration profile of the Tiron/molybdate reaction based on the ADE, *CF-β*, and a second order Taylor series approximation.

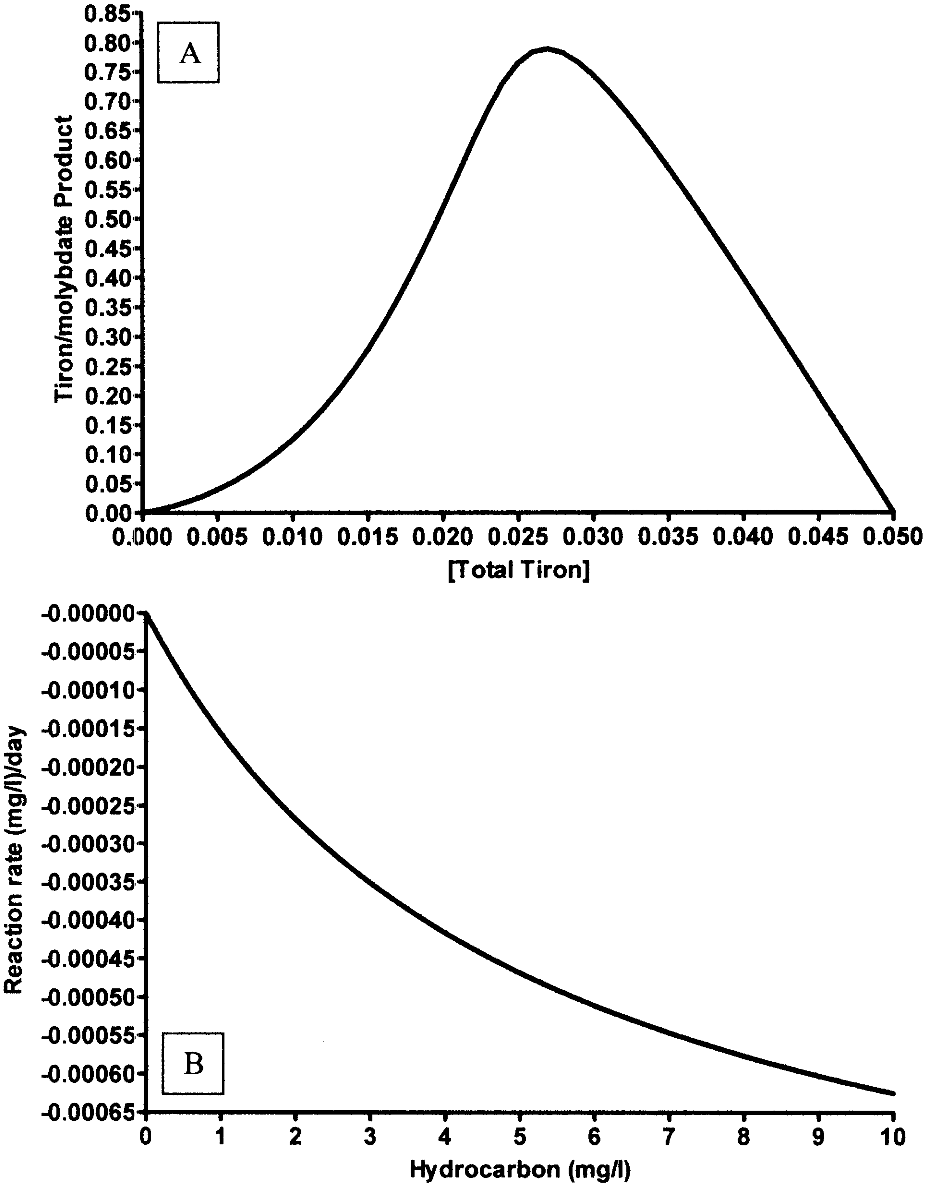

Figure 19. A) Tiron/molybdate product as a function of total Tiron and total molybdate. Total molybdate is calculated by applying a mixing line to total Tiron. B) Double Monod reaction rate as a function of Hydrocarbon concentration with Oxygen constant at 4 mg/l.

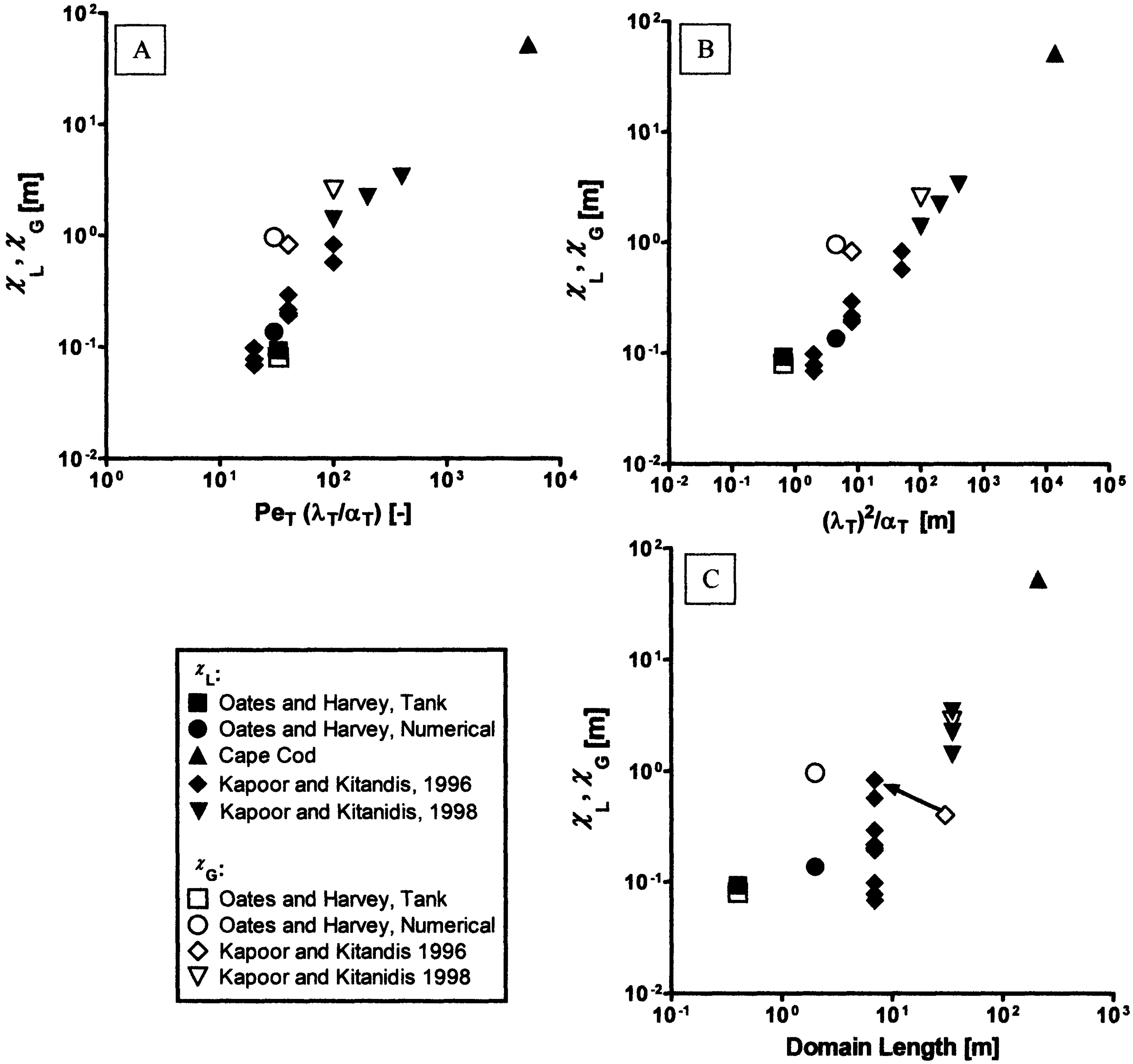

Figure 20. Comparison of the variance length and growth scales to: A) the transverse peclet number, B) the length scale of transverse dispersion; C) and the overall domain length. The variance length scale for Cape Cod was calculated from Kapoor and Gelhar (1994b). The correlation length from Kapoor and Kitanidis, 1998 was increased by a factor of 10 to approximate the average distance between high and low conductivity regions as determined by inspection of the conductivity field. This increased separation distance compared to the correlation length results from the hole-type covariance structure used to generate the random field, which results in structured correlation well beyond several correlation lengths.

Table 1. Model Parameter Values.

Parameter	Scenario # 1 Value	Scenario # 2 Value
Grid		
y	3000 [cm]	10,000 [m]
x	2000 [cm]	3000 [m]
Δx	2.5 [cm]	12.5 [m]
Δy	2.5 [cm]	5 [m]
Flow and Transport		
ln K structure	Gaussian	Gaussian
$\sigma^2_{\ln K}$	1.0	1.0
Correlation length	15 [cm]	100 [m]
Hydraulic Gradient	0.1 [-]	0.02 [-]
Porosity	0.3 [-]	0.3 [-]
$\bar{v}$	0.4 [cm/s]	1.6 [m/day]
A_x	7.7 [cm]	66.2 [m]
a_L	2.5 [cm]	2.5 [m]
a_T	0.5 [cm]	0.5 [m]
χ_L	136 [cm]	2697 [m]
χ_G	966 [cm]	2707 [m]
Reaction		
O_O	8 [mg/l]	8 [mg/l]
H_O	20 [mg/l]	10 [mg/l]
R_H	1.0, 1.5, 4.0 [-]	1.2 [-]
μ_{max}	0.00125 [s^{-1}]	0.03 [day^{-1}]
$Y_{A/D}$	3.0 [-]	1.5 [-]
M	1.0 [mg/l]	1.0 [mg/l]
k_O	0.8 [mg/l]	4.0 [mg/l]
k_H	2.0 [mg/l]	5.0 [mg/l]

Chapter 6. Future Work

There are numerous avenues that need exploration in order to implement and expand the *CF-β* modeling framework developed in this thesis.

6.1 Measuring χ_L at Cape Cod.

Cape Cod is an ideal site to test measuring χ_L in the field with the mean product of a rate-limited bimolecular reaction or a breakthrough curve of conservative concentration variance. First, numerical modeling needs to be conducted to ensure that this idea is tractable. Numerical simulations need to compare values of χ_L determined from forced gradient well-to-well tests to those calculated in a standard Cartesian coordinate system to determine what is the smallest-possible well spacing needed to obtain an accurate value of χ_L. To obtain sufficient statistical sampling of the heterogeneity such that ergodicity holds for macro-dispersion theory, a plume needs to travel about a 10 correlation lengths. I would expect this is also true for variance destruction so the wells would have to be about 26 m apart using the longitudinal correlation length of 2.6 m. However, both macro-dispersion and variance destruction were observed accurate in our tanks after only 2-3 correlation lengths. This needs to be further studied with numerical modeling.

Next, fluorescent conservative tracers (*e.g.*, fluorescein) for use with fiber optic spiny wells, which are wells that can provide dozens of point measurements to construct a breakthrough curve of conservative variance, and reactive tracers (*e.g.*, methyl bromide and sodium chloride) need to be tested with Cape Cod sediment for compatibility. After determining the experimental design with the numerical model, both reactive and conservative tests can be conducted. The values of χ_L found from the well-to-well tests could be compared to the value of χ_L reported in Kapoor and Gelhar (1994b) determined from hundreds of measurements at Cape Cod. This would demonstrate the validity of the proposed approaches for measuring χ_L at a field site.

We also found χ_L to correlate highly to the transverse correlation length squared divided by the mechanical transverse dispersivity. It would be useful if a theoretical relationship between χ_L could be derived from stochastic theory. This way, χ_L could be predicted from traditional conductivity statistics, or more practically, measuring χ_L would yield information about properties of the porous media.

6.2 Time for Production to balance Destruction.

The time for production to balance destruction was assessed for Cape Cod by comparing the production-destruction balance to the full variance budget using the following parameters $\bar{v}$ = 0.42 [m/day], A_x = 1.0 [m], χ_L = 53 [m] from Kapoor and Gelhar (1994b) and assuming that $\chi_G \approx \chi_L$ as it has for all other situations investigated (figure 1).

Figure 1.

The production-destruction balance holds after traveling about 75 [m] or after about traveling 30 correlation lengths using the longitudinal correlation length of 2.6 [m]. In order to establish when variance production balances variance destruction, more work needs to be done. This can be done by defining a measure for when production balances destruction such as when the difference between the peak variance profile from the full variance budget is less than 5% of the variance profile from the production-destruction balance or perhaps when the root-mean-square error between the two profiles is less then 5%. Using this measure, the time to achieve the production-destruction balance can be generated as a 2-D contour plot as a function of χ_L and A_x. Generally, the time to achieve the production-destruction balance should scale proportional to the product of χ_L and A_x. It is possible that the whole issue of when production balances destruction can be eliminated by redefining the variance-growth scale to include the early time imbalance, as discussed in chapter 5, which needs further exploration.

6.3 Enhancing Mixing with Transient Flow.

One practical result of viewing mixing and reaction in terms of variance production and destruction is that it gives key insight on how to increase favorable mixing in the subsurface. Creating flow perpendicular to its original direction would have increased the rate of variance destruction and reactive mixing by an order of magnitude in our tank experiments. This increase in mixing results because hydraulic conductivity variations cause velocity variations that sheer fluids and establish steep transverse gradients. Transverse-mechanical dispersivity acts slowly on these steep gradients. Rotating the flow field would result in the much larger longitudinal mechanical dispersion acting with the same steep gradients to cause a much larger mixing flux.

Small temporal variations (less than a 10 degree rotation) on the flow field and the resulting effects on macro-dispersion and reactive mixing have been discussed by Cirpka and Attinger (2003). However, there should be an optimum rotation angle which is likely 90 degrees and an optimum frequency between switching the flow field. These optimum conditions are very unlikely to occur under natural conditions and should be engineered to optimize remediation, which would save time and money.

First, the behavior of the conservative concentration micro-scales should be studied under conditions of creating perpendicular flow to see if the transverse micro-scale becomes the longitudinal micro-scale and vice versa when the flow is rotated. Do these conditions hold when the porous media is anisotropic? Then, the effects of rotating the flow field should be tested on reactive transport with detailed numerical simulations of mixing a contaminant plume and electron acceptors/donors with transient flow. Chromatographic mixing or the mixing between electron donors and acceptors due to the difference in sorption only works in the longitudinal direction. This minimizes its impact for long thin plumes and makes transverse mixing along the long edges of the plume still very important. However, if the flow field was made perpendicular, then chromatographic mixing would now act along the entire length of the plume which would greatly accelerate mixing in additional to the enhanced dispersive mixing.

Important issues such as the optimal well configuration and the optimal timing between alternating the flow field to induce the highest overall rate of reaction rate should be addressed. Furthermore the effects of dimensionality should be addressed as steep vertical concentration gradients are often observed in the field. Wells could be placed below the contaminant plume to induce vertical flow to enhance mixing in 3-D.

6.4 3-D.

In 3-D, a contaminant plume is surrounded by electron acceptors in all dimensions and mixing and reaction would be faster than a 2-D representation because there is a much larger surface over which for mechanical dispersion to mix. The *CF-β* equations are general and apply to 3-D settings. In 3-D, the steep vertical gradients that are often observed in the field would be characterized by a small vertical micro-scale, which would manifest by greatly increasing the variance-destruction term (or decreasing the variance-length scale). 3-D conservative and reactive mixing should be studied with detailed numerical modeling. How does χ_L change when the dimensionality of the problem changes? Dimensionality also needs to be considered for measuring χ_L at a field site. Does a reaction product of two reactants injected sequentially only measure mixing in 2-D? Does a breakthrough curve of conservative variance measuing mixing in 3-D?

6.5 Evolving Correlation Scales.

For scales of evolving heterogeneity (*e.g.*, Dagan, 1994; Neuman, 1995; Bellin *et al.*, 1996) the log conductivity correlation scale increases with overall scale (*e.g.*, figure 6.5, Gelhar, 1993). Because the variance length-scale appears related to the correlation scale, there is a good possibility that like macro-dispersivity, the variance length-scale would exhibit scale dependency. The scale dependence of correlation lengths could have very important implications for mixing and reaction. Larger correlation scales of conductivity would cause solute to flow in and around larger conductivity structures represented by larger macro-dispersion and hence a larger term of variance production. Concurrently, the pore-scale mechanical transverse dispersion that actually creates mixing will have larger and larger solute fingers to mix across and hence a slower variance destruction term. In the case of a fractal conductivity field, the upscaling problem from incomplete mixing could persist over very large spatial and temporal domains. Mixing and reaction in fractal conductivity fields should be studied with detailed numerical experiments. Whether or not the *CF-β* framework can model this situation with scale-dependent parameters should be assessed.

6.6. Taylor Series.

Combining a low-order Taylor series expansion of a reaction term to upscaled transport equations is an attractive approach for upscaling complex mixing and reaction for its simplicity and computational efficiency. For some reactions, this approach coupled to production-destruction balances is able to model the space-time evolution of the product and reactant means, variances, and assumed Beta *pdfs* without resolving heterogeneity or utilizing multivariate distributions. Furthermore, Taylor series provide a natural framework for expanding heterogeneous reaction parameters that could account for solid-phase chemical or microbial heterogeneity if practical ways to calculate the covariance between aqueous and solid phase concentrations are developed. When chemical reactions are highly non-linear, such as the Tiron/molybdate reaction, low-order approximations can yield poor predictions and higher-order moments must be included. Further research is needed to determine what types of reactions have well-behaved Taylor series, how to calculate the covariance between aqueous and solid phase concentrations, and how to approximate high-order cross moments.

For example consider Arsenic sorption. Taking a Langmuir isotherm

$$S = \frac{k_1 k_2 C}{1 + k_1 C} \tag{0.1}$$

Its retardation factor is calculated by:

$$R = 1 + \frac{\rho_b}{\theta}\frac{\partial S}{\partial C} = 1 + \frac{\rho_b}{\theta}\left(\frac{k_1 k_2}{\left(1 + k_1 C\right)^2}\right) \tag{0.2}$$

To study the effects of incomplete mixing, concentration C is decomposed into a mean and zero mean perturbation and the equation for retardation is expanded with a Taylor series about the mean concentration:

$$R = R(\overline{C}) + c'\left.\frac{\partial R}{\partial C}\right|_{\overline{C}} + \frac{1}{2}\left(c'\right)^2 \left.\frac{\partial^2 R}{\partial C^2}\right|_{\overline{C}} + \dots \tag{0.3}$$

Truncating the Taylor series after the second term and taking expectation (Note: We can include higher order terms by using the moments from the beta distribution based on the mean and variance):

$$\overline{R\left(C\right)} = R(\overline{C}) + \frac{1}{2}\sigma_C^2 \left.\frac{\partial^2 R}{\partial C^2}\right|_{\overline{C}} + \dots \tag{0.4}$$

calculating the second-order derivative:

$$\frac{\partial^2 R}{\partial C^2} = 6\frac{\rho_b}{\theta}\frac{k_1{}^3 k_2}{\left(1 + k_1 C\right)^4} \tag{0.5}$$

and taking expectation yields:

$$\overline{R\left(C\right)} = 1 + \frac{\rho_b}{\theta}\left(\frac{k_1 k_2}{\left(1 + k_1 \overline{C}\right)^2}\right) + 3\frac{\rho_b}{\theta}\frac{k_1{}^3 k_2}{\left(1 + k_1 \overline{C}\right)^4}\sigma_C^2 \tag{0.6}$$

This equation shows that any spatial variability in dissolved concentrations will result in more retardation than predicted by calculating retardation based on the mean values. Consider the Langmuir isotherm for arsenic sorption calculated in Harvey *et al* (2002) (figure 2).

Figure 2.

We see significantly more sorption when concentration variability is accounted for (figure 3).

Figure 3.

If macro-dispersive variance production balances mechanical dispersive variance destruction under equilibrium-non-linear-sorption conditions, which has not yet been verified, then scaling the mean gradients could supply the concentration variance. Non-liner sorption can have the effects of self sharpening fronts which results in steep mean gradients meaning that high levels of variance would be sustained at the lead edge of a plume and could result in significantly different transport behavior. More research such as through detailed numerical simulations of sorption is needed to verify if the production destruction balance holds for non-linear sorption and how accurate is the Taylor series expansion needs to be assessed.

References

1. Cirpk, O. A., Attinger, S. 2003. Effective dispersion in heterogeneous media under random transient flow conditions. *Water Resources Research.* 39(9), 1257.
2. Harvey, C.F., Swartz, C.H., Badruzzaman, A.B.M., Keon-Blute, N., Yu, W., Ali, M.A., Jay, J., Beckie, R., Niedan, V., Brabander, D., Oates, P.M., Ashfaque, K.N., Islam, S., Hemond, H.F., Ahmed, M.F. 2002. Arsenic mobility and groundwater extraction in Bangladesh. Science. 298 (5598): 1602-1606.
3. Kapoor, V., Gelhar, L. W. 1994b. Transport in three-dimensionally heterogeneous aquifers 2. Predictions and observations of concentration fluctuations. *Water Resources Research.* 30(6), 1789-1801.

Figures.

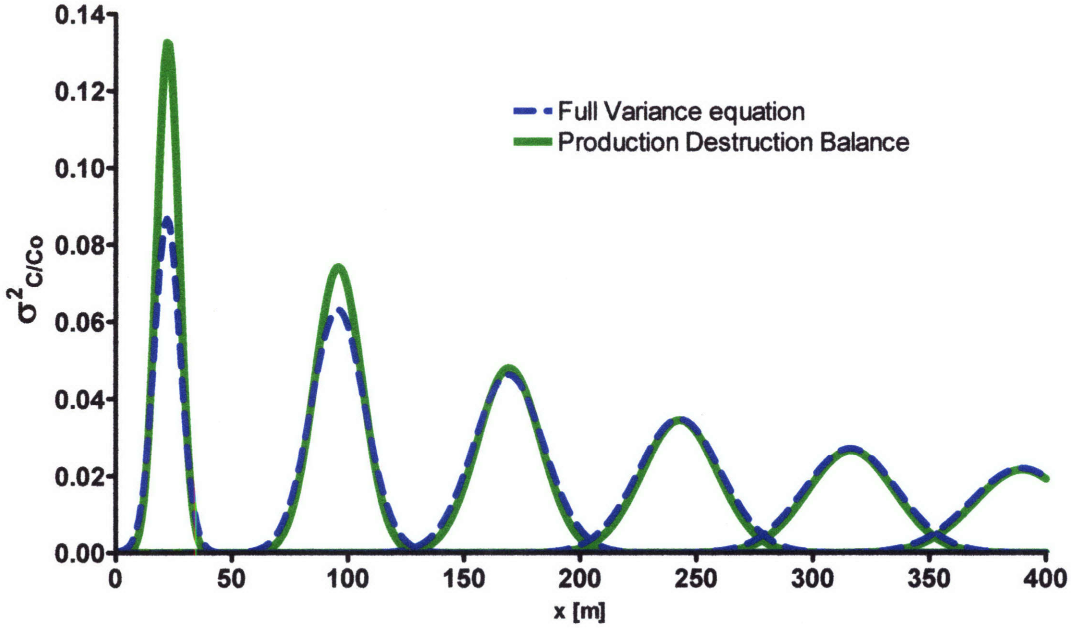

Figure 1. Production-destruction balance at Cape-Cod

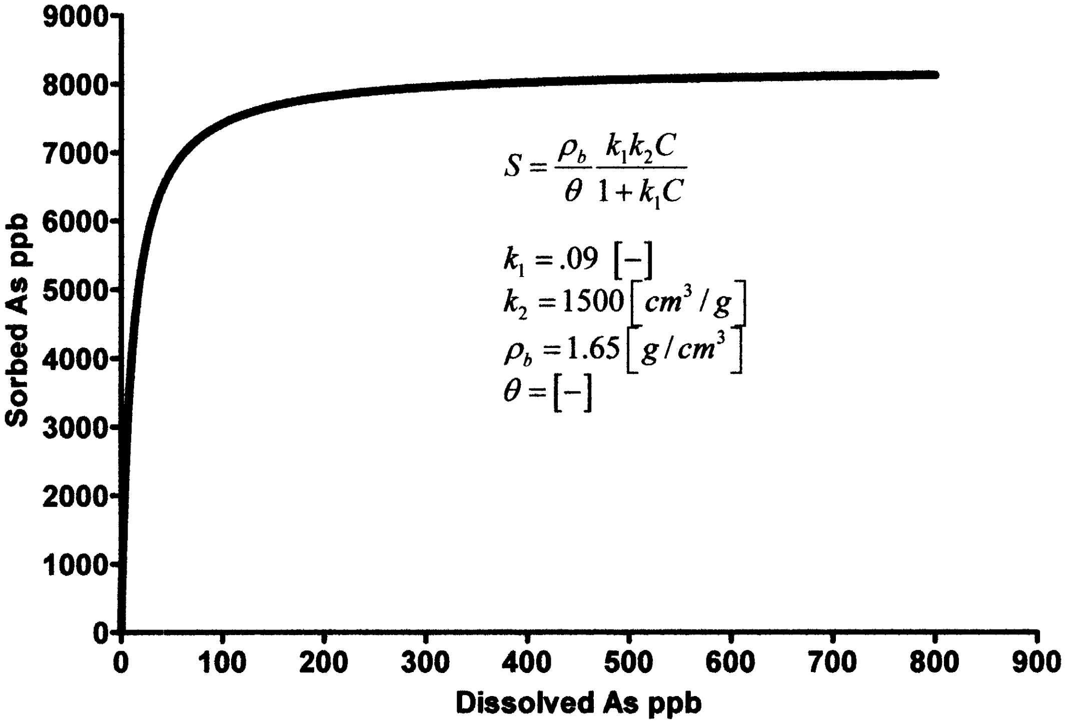

Figure 2. Arsenic sorption in Bangladesh (Harvey *et al.*, 2002)

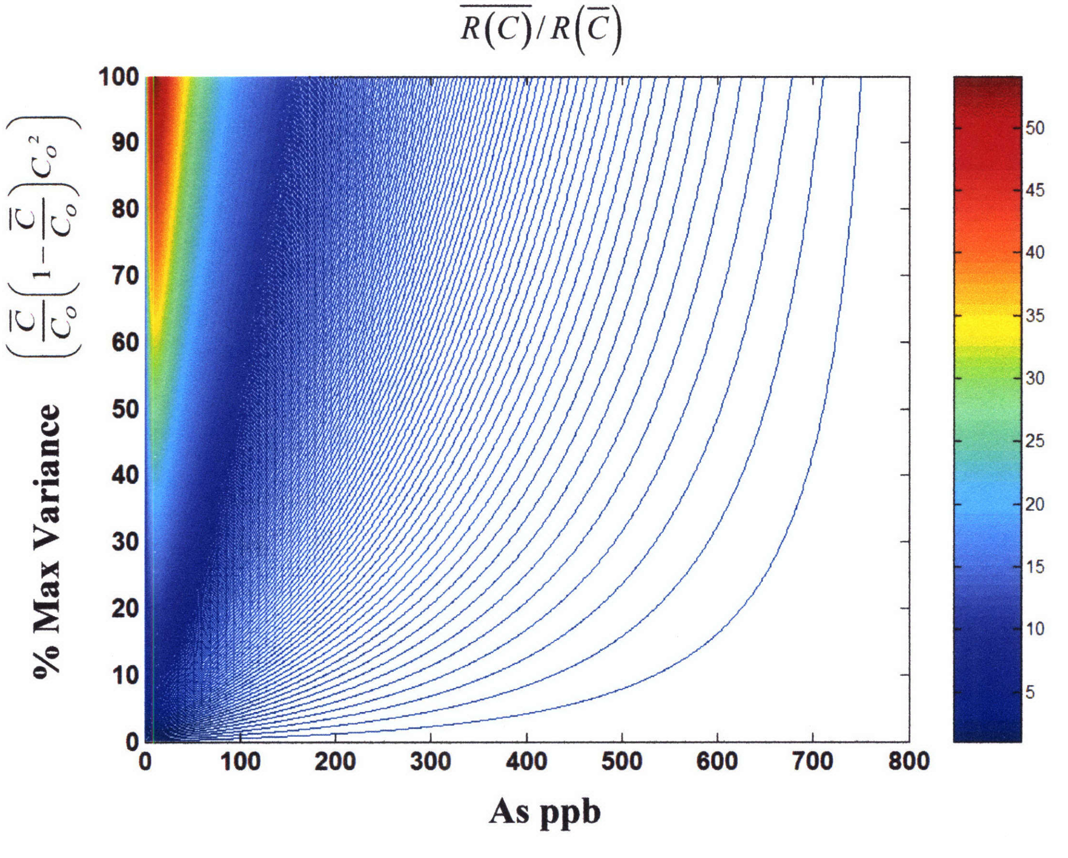

Figure 3. Effects of incomplete mixing on Arsenic sorption in Bangladesh.